GENERATION OF DYE-SENSITIZED TRANSITION METAL DOPED SEMICONDUCTORS FOR EFFICIENT SOLAR ENERGY HARVESTING – A LOW-COST METHOD

A thesis submitted to the Faculty of Science

KUVEMPU UNIVERSITY

for the award of degree of

DOCTOR OF PHILOSOPHY
IN
CHEMISTRY

By

Mr. YATHISHA R.O. M.Sc.

Under the guidance of

Dr. Y. ARTHOBA NAYAKA
Professor
Department of Chemistry

Department of P.G. Studies and Research in Chemistry
Kuvempu University
Jnana Sahyadri, Shankaraghatta - 577 451
Shivamogga Dist., INDIA

August-2019

GENERATION OF DYE-SENSITIZED TRANSITION METAL DOPED SEMICONDUCTORS FOR EFFICIENT SOLAR ENERGY HARVESTING – A LOW-COST METHOD

A thesis submitted to the Faculty of Science

KUVEMPU UNIVERSITY

for the award of degree of

DOCTOR OF PHILOSOPHY

IN

CHEMISTRY

By

Mr. YATHISHA R.O. M.Sc.

Under the guidance of

Dr. Y. ARTHOBA NAYAKA

Professor
Department of Chemistry

Department of P.G. Studies and Research in Chemistry
Kuvempu University
Jnana Sahyadri, Shankaraghatta - 577 451
Shivamogga Dist., INDIA

August-2019

Dr. Y. Arthoba Nayaka M.Sc., Ph.D.,

Professor
Dept. of PG Studies and
9448855078
Research in Chemistry
Kuvempu University
Shankaraghatta-577451

Phone: 08282-256308(O)
Mob :

Fax :08282-256255
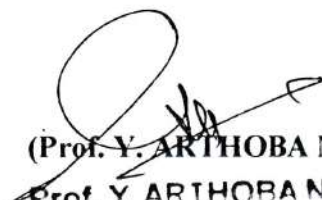E-mail: drarthoba@yahoo.co.in

KUVEMPU UNIVERSITY

CERTIFICATE

This is to certify that the work presented in the thesis entitled **"GENERATION OF DYE-SENSITIZED TRANSITION METAL DOPED SEMICONDUCTORS FOR EFFICIENT SOLAR ENERGY HARVESTING – A LOW-COST METHOD"** embodies the results of bonafide research work done by **Mr. Yathisha R.O.,** Research Scholar, Department of Chemistry, Jnana Sahyadri, Kuvempu University, Shankaraghatta - 577 451, Shivamogga, for the degree of Doctor of Philosophy in Chemistry, in the Faculty of Science, Kuvempu University, Shankaraghatta, under my guidance and supervision. I further certify that the results of this thesis have not previously formed the basis for the award of any degree or diploma.

Date: 28 - 08 - 2019

Place: **Shankaraghatta**

(Prof. Y. ARTHOBA NAYAKA)
Prof. Y. ARTHOBA NAYAKA
Dept. of Chemistry, Jnanasahyadri
Kuvempu Univeristy
Shankaraghatta-577 451
Shivamogga Dist.

KUVEMPU UNIVERSITY

YATHISHA R.O. M.Sc.,   Dept. of Chemistry
Research Scholar   Jnana Sahyadri, Shankaraghatta
E-mail- yathisharo@yahoo.com   Karnataka, **INDIA**

DECLARATION

I hereby declare that the matter embodied in the thesis entitled **"GENERATION OF DYE-SENSITIZED TRANSITION METAL DOPED SEMICONDUCTORS FOR EFFICIENT SOLAR ENERGY HARVESTING – A LOW-COST METHOD"** is based on the results of research work carried out by me in the Department of Chemistry, Kuvempu University, Jnana Sahyadri, Shankaraghatta - 577 451, Shivamogga District, under the guidance of **Dr. Y. Arthoba Nayaka**, Professor, Department of Chemistry, Kuvempu University, Jnana Sahyadri, Shankaraghatta - 577 451. I further declare that this thesis or any part of there has not been submitted elsewhere for any other degree or diploma in any other university.

(YATHISHA R.O.)

Date: 28 - 08 - 2019
Place: **Shankaraghatta**

Dedicated to Beloved

Parents, Teachers & Friends
for their love, support and encouragement
throughout my career….

Acknowledgements

This thesis of mine was possible due to the incessant prayers, guidance, support, co-operation, assistance, encouragement and good wishes of many people to whom I owe a great debt of gratitude.

I am immensely pleased to place on record my gratitude to my research Supervisor, **Dr. Y. Arthoba Nayaka,** Professor, Department of Chemistry, Kuvempu University, Shankaraghatta, for his invaluable, meticulous and untiring guidance, moral support, advice and constant encouragement.

I awhile this opportunity to thank, **Prof. J. Keshavayya, Prof. Yadav Bodke** and **Dr. T. Venkatesh,** Department of Chemistry, Kuvempu University, Shankaraghatta, for their timely advice and support.

I owe my special thanks and respect to all my **Teachers** who taught me in my **primary schooling,** whose blessings and encouraging words made me to move on.

This moment would never have been realized, without the blessings, guidance and support of my beloved parents **Sri. H.R. Onkarappa** and **Smt. Rathnamma**.

My special thanks to my lab seniors, **Dr. Venkatesha T.G., Dr. Vidyasagar C.C.** and **Dr. Vishwantha R.,** I sincerely thank them for their kind help in supporting and continuous encouragement throughout my work.

It's high time to acknowledge the support received from **Mr. Thippeswamy D., Mr. Basavarajappa K.V., Mr. Manjunatha P., Mr. Purushothama, H.T., Mr. Vinay M.M., Ms. Deepa K.,** Research Colleagues, for their kind support and continuous encouragement throughout my research work.

It would be incomplete if I do not thank all my **Friends** for their constructive comments, encouragement and invaluable support.

I would like to express my heartfelt thanks to all the **Teaching and Non-Teaching Staff,** Department of Chemistry, Kuvempu University, **Library Staff** of Kuvempu University, **UGC and DST-SERB,** New Delhi, for their help during the course of my research work.

Yathisha.....

LIST OF ABBREVIATIONS

Å	Angstrom
CV	Cyclic voltammetry
Cr-ZnO	Chromium doped zinc oxide
$Cr-TiO_2$	Chromium doped titanium oxide
°C	Degree Celsius
cm^{-1}	Per centimeter
CB	Conduction band
CdO	Cadmium oxide
DSSCs	Dye-sensitized solar cells
D	Average particle size
DEG	Di-ethylene glycol
EB	Evans blue
EDAX	Energy-dispersive X-ray spectroscopy
E_g	Optical band gap
et al.	And Others (Co-workers)
eV	Electron Volt
EG	Ethylene glycol
EJ	Electron Joule
FE-SEM	Field emission scanning electron microscope
FWHM	Full width at half maximum
GW	Giga Watt
HOMO	Highest occupied molecular orbital
JCPDS	Joint committee power diffraction standards
KeV	Kilo electron Volt
KCl	Potassium Chloride
LUMO	Lowest unoccupied molecular orbital
ml	Milliliter
mA	Milliampher

mM	Millimolar
nm	Nanometer
NHE	Normal hydrogen electrode
Ni-CdO	Nickel doped cadmium oxide
PCE	Power conversion efficiency
2-PL	2-Propanol
SPD	SPADNS
SAED	Selected area electron diffraction
SCE	Saturated calomel electrode
TB	Trypan blue
TWh	Terawatt hour
UV	Ultra-Violet
V_{oc}	Open circuit voltage
XRD	X-ray diffraction
X	Dopant concentration
W	Watt
Wt%	Weight percentage
$Zn(OH)_2$	Zinc hydroxide
ZnO	Zinc oxide
Zn-CuO	Zinc doped copper oxide
Zn-MgO	Zinc doped magnesium oxide
2θ	Bragg's angle
λ_{max}	Absorption maximum
%	Per cent
ε	Micro-strain
δ	Dislocation density

CONTENTS   Page No

SYNOPSIS

The look for renewable sources of energy is a most important thrust area as an alternative to conventional energy sources due to very high emission levels of environmental polluted gases (greenhouse gases) like carbon dioxide (CO_2), carbon monoxide (CO), nitrogen oxides (NO_x), sulphur dioxide (SO_2), phosphorous pentaoxide (P_2O_5) and other traditional fossil fuels like hydrocarbons [1]. Furthermore, the processing cost for the generation of electrical energy from conventional sources like fossil fuels and nuclear elements increases significantly. In addition to this, the social and environmental considerations, such as the cost for securing reliable oil supplies, process nuclear wastes, and to relief disasters caused by global climate changes, etc, are increasing day-by-day [2]. While the generation of electricity from non-renewable energy sources is released a large amount of CO_2 and nuclear radiations, which affects the big environmental issues like global warming and health issues for human beings. So it is necessary to replace these conventional sources with non-conventional one [3]. Among the various renewable energies, solar energy is considered as the most favourable for its usefulness. Moreover, the solar ultraviolet radiations striking on the earth's surface have no cost, clean, sustainable, eco-friendly and commonly dispersed over the entire global [4]. So the light conversion route of these solar radiations into electrical power by using the optical and electronic properties of appropriate materials shows to be a graceful energy conversion process and an ideal alternative to conventional energy sources. This clearly confirms the solar modules are the best solution for converting solar energy into useful electrical energy [5].

During the past few decades, nanomaterials have emerged as the new building blocks to construct solar energy harvesting assemblies. Nanotechnology is believed to revolutionize the industry in the coming years and will have a significant economic impact allowing a considerable cost reduction of the photovoltaic energy, both by reducing the cost of the devices and by increasing efficiencies [6]. Size-dependent properties such as size quantization effect in semiconductor nanoparticles and quantized charging effect in metal nanoparticles provide the basis for developing new and effective light energy harvesting systems [7]. These nanostructures provide innovative strategies for designing next-generation energy conversion devices. Tailoring the optoelectronic properties of metal oxide nanoparticles by organizing chromophores of specific properties and functions on nanoparticles can yield photoresponsive inorganic nanohybrid materials. Amongst the various types of nanomaterials, semiconductor nanoparticles have been widely investigated in recent years [8].

In order to improve the photo-efficiency of photovoltaic devices (solar cells), various methods are used such as doping of right dopant ions (transition and inner transition metal ions) into bare nanomaterial lattice [9]. Doping the impurity ion is known as one of the effective ways to manipulate the internal properties of host material such as crystalline structure and crystallite size. Many attempts have been made to tune the band gap by varying the composition of transition metal ions. It is possible to decrease the band gap by using right dopants [10]. In addition, a few reports of present years suggested that transition metal doped semiconductors could possess interesting optical properties. The origin of these improved photo-reactivities is clearly related to the efficiencies of the doping centers in trapping charge carriers and interceding in the

interfacial transfer. Trapping either an electron or hole alone is ineffective for the generation of photocurrent because immobilized charge species quickly recombines with mobile counterpart. Thus, metal ions can also serve as charge trapping sites and thus reduce electron-hole recombination rate [11]. In order to reduce the band gap of semiconductors, incorporation of certain amount of transition and rare earth metal such as Cr, Er, Ce, Cu, Gd, Mn and V has extensive importance. Doping of these metals essentially reduces the band gap of semiconductors for the photo-excitation and simultaneously reduces the recombination rate of photogenerated electron-hole pairs [12]. The effect of doping on the activity of semiconducting nanomaterials depends on number of key factors, e.g. the method of doping, synthesis route and the concentration of dopant [13]. Therefore, looking for a simple method and appropriate metal dopants are necessary for the large-scale synthesis of metal-doped nano semiconductors.

Recently, numerous methods, such as electrochemical [14], solvothermal [15], solid-state [16], hydrothermal [17], sol-gel [18] have been developed for synthesizing uniform nano-sized pure and doped metal oxide particles. The metal oxide nanoparticles exhibit novel electrical, mechanical, chemical and optical properties due to the larger surface area and quantum confinement effects [19]. Among these methods, the microwave-assisted synthesis has gained more importance due to its advantages of being fast, simple and more energy efficient [20-21]. Compared to the conventional heating process, (a) microwaves generate high power densities, enabling increased production speeds and decreased production costs, (b) microwave energy is precisely controllable and can be turned on and off instantly, eliminating the need for warm-up and cool-down, (c) microwave energy is selectively absorbed by areas of greater moisture resulting in more uniform temperature and moisture profiles, and d) microwave method gives

improved yields and enhanced product performance [22]. Therefore, the fabrication of transition metal oxides with different morphology for the solar energy harvesting has been the target of scientific interests in recent years because of their unique properties and fascinating applications in optoelectronics [23].

Dye-sensitized solar cells (DSSCs) are the most promising photovoltaic devices in the third generation solar cells for achieving good energy conversion efficiency at low cost [24]. It was firstly reported by the Michael Gratzel and Brian O'Regan in 1991, so it is also called as "Gratzel cell". After this invention, DSSCs have gained more importance in the various fields like chemistry, physics and materials science due to their low processing cost and easy fabrication method compared to Si-based conventional solar cells [25].

In DSSCs, the heart of the system is a mesoporous oxide layer composed of metal oxide nanoparticles sintered on a transparent conductive glass substrate, such as indium-doped tin oxide (ITO) or fluorine-doped tin oxide (FTO) glass. This mesoporous oxide film acts as a high surface area support for the sensitizer, a pathway for electron transportation and a porous membrane for the diffusion of the redox couple [26]. Specifically, nanocrystalline semiconductor oxide (typically TiO_2) nanoparticles, which adsorb dye molecules onto their surface and transport photo-generated electrons to the outer circuit, serve as electron conductors and state the efficiency of electron transport and collection [27]. By this, the solar energy-to-electricity conversion efficiency for the best DSSCs has now been enhanced from 12 to 14%, with various recent efforts directed mainly towards developing better inorganic electrode materials and organic sensitizers [28].

Zinc oxide (ZnO) is one of the significant metal oxide semiconductors with a wide energy gap of 3.31 eV and large excitation binding energy (60 eV) [29]. These unique characteristics make it suitable to various applications, such as optical coating, solar cells, gas sensors and photocatalyst [30]. In fact, doping of right dopant, structure, and size play a vital role in the optical and electrical properties of ZnO nanostructures, which can be controlled by the different routes of the nanostructure growth. Therefore, many methods have been created to synthesize ZnO nanostructures including microwave combustion method, solvothermal method, sol-gel method, hydrothermal method, an auto combustion method, ultrasonic and chemical vapor deposition methods [31]. As mentioned above, the doping of ZnO with right dopants offers an effective method to enhance and control its electrical properties. The elements such as Au^{2+}, Ce^{3+}, Eu^{3+}, In^{3+}, Cu^{2+} and Cr^{3+} have been doped in order to control the optical and electrical properties of host ZnO materials. Moreover, undoped and doped ZnO has considered being a potential commercial material due to its low-cost, non-toxicity, and abundant availability in nature. By this, ZnO is being used in the fabrication of third-generation dye-sensitized solar cells (DSSCs) [32].

Copper oxide (CuO) is an important semiconducting transition metal oxide with a monoclinic crystal structure and it has been studied as a p-type semiconducting metal oxide with a bandgap of 1.7 eV [33]. The CuO is being used as a novel material because of the ease of availability of raw materials, low processing cost, non-toxic nature, excellent thermal stability, good optical and electrical properties [34]. The unique physical, chemical and electrical properties of CuO nanoparticles have many potential applications in the fields of photocatalyst, batteries, gas sensing, solar cells and biosensors [35]. It has been highlighted that the crystal shape and size are the two

important considerations to control the optical and catalytic properties of CuO nanoparticles [36]. Furthermore, in the recent research the main focus is given to tune the energy gap of CuO. Doping of several metal ions into the host lattice of CuO is one of the significant routes to alter the energy gap of CuO [37]. Chiang *et al*. reported the effects of Ni doping on the photoelectrochemical properties of CuO thin film photo-electrode. They found that the photocurrent density was decreased with the improved conductivity [38], M. Iqbal *et al*. reported that the band gap of CuO increased upon Mn doping and they proved that the Mn-doped CuO nanowires are much photoactive than the undoped CuO nanowires [39].

Cadmium oxide (CdO) is transparent conducting oxides materials that hold both high electrical conductivity and high optical transparency (>80%) in the visible light region of the electromagnetic spectrum [40]. CdO is an *n*-type semiconductor with nearly metallic conductivity. Its indirect and direct bandgaps of are in the range of 2.2-2.5 eV and 1.3-1.98 eV respectively. Such a difference in both direct and indirect bandgaps is attributed to intrinsic cadmium and oxygen vacancies [41]. Due to its ionic nature coupled with its low electrical resistivity and high optical transmission in the visible region. Nanoscaled CdO has extensive applications as solar cells, windows, IR reflector, transparent electrodes, flat panel display and photo-transistor. It was proven that the structural, electrical and optical properties are very sensitive to the film structure and deposition conditions. Such transparent conductors are being used to comprehensively in thin films solar cells and optoelectronic devices [42].

Titanium oxide (TiO$_2$) nanoparticle is one of the promising materials for the fabrications of dye-sensitized solar cells (DSSCs). Because it has special properties like wide bandgap, suitable band edge levels for charge injection and extraction, the long

lifetime of excited electrons, exceptional resistance to photo-corrosion, non-toxicity and low cost [43]. TiO_2 occurs naturally in three different forms; anatase (tetragonal), rutile (tetragonal) and brookite (orthorhombic). For DSSCs, anatase is the most commonly used phase due to its superior charge transport. The tetragonal anatase crystal structure is made up of a chain of distorted TiO_6 octahedrons, which results in a unit cell containing four titanium atoms and eight oxygen atoms [44]. In addition, TiO_2 is one of the most attractive wide bandgap transition metal semiconductor, non-toxic, highly stable and low commercial cost. Due to these properties, TiO_2 gain more importance in the fabrication of photo-anode for dye-sensitized solar cells (DSSCs) with different structures such as nanotubes, nano-rods, nano-flower and nanofibers [45]. Most of the research focused on the modification of properties of TiO_2 by changing the morphology, tuning of the phase or external doping by different approaches. Also, morphology, specific surface area, crystal phase and crystalline structure of TiO_2 nanoparticles plays important role in solar cell performance [46].

Magnesium oxide (MgO) has a rock salt structure with Mg^{2+} and O^{2-} ions are octahedrally coordinated, making bulk magnesium oxide a diamagnetic material with a wide band gap of 7.8 eV [47]. Due to its wide band gap, inexpensiveness, and long term stability, MgO is used in potential applications of numerous disciplines. It can be extensively utilized in the fields of translucent ceramics, refractory, plasma display panel, absorbents in many pollutants and superconducting products [48]. Due to good photocatalytic properties of MgO, it is being used in the form of an ultra-thin shell on the surface of some metal oxides such as SiO_2, ZnO, and TiO_2 to improve the efficiency of dye-sensitized solar cells. Magnesium oxide (MgO) has been used as an insulating layer in the TiO_2 based DSSCs because of two important reasons: firstly, the MgO layer

protects the back electron transfer from the TiO₂ layer to the electrolyte solution and hence, reduces electron-hole recombination; secondly, the MgO coating layer improves the dye adsorption, leading to an improved efficiency. Also, it is an eco-friendly material and is extensively used in many medical, industrial and agricultural products [49].

Similar to photo-anode materials, many organic dyes are taking a significant role in the applications of dye-sensitized solar cells. The process of photosensitization play a vital role in absorbing some amount of visible light and photo exited electrons in the dye molecules that impinge into the conduction band of metal surfaces [50]. To achieve these functions, the dye molecules have to meet several conditions such as; the excited energy level (LUMO) of the dye should be slightly higher compared to conduction band of semiconductors, forming strongly bond with semiconductor surface, high absorption coefficient, wide spectrum of absorption in the visible region (redshift) and long term stability [51]. However, in past few years, most of the researchers have used ruthenium-based complexes as effective sensitizers, due to their intense charge absorption capacity in the whole visible range and more efficient in metal-to-ligand charge transfer rate. But, in recent days the metal-free organic dyes are used as a sensitizer in the alternative to ruthenium related complexes. Because the ruthenium complex includes heavy metal, which is undesirable from the point of view of eco-friendly aspects and it has high price [52]. By this, the metal-free organic dyes of Eosin-Y, Fast Sulphon Black-F, Solochrome Black-T, Orange IV, SPDANS and Evans blue are used as sensitizers with acceptable efficiency. These metals free organic dyes have more absorption coefficient compared to transition metal complexes due to π-π^* transition. Due to these features, most researchers have used metal-free organic dyes instead of metal complexes to improve the efficiency of DSSCs [53].

The present work is mainly focused on the synthesis and characterization of purely advanced semiconducting metal oxide nanoparticles, transition metal doped nanoparticles and their usage in low-cost dye-sensitized solar cells. The metal oxide nanostructures were synthesized by microwave combustion method with two different modes, such as solution and solid state mode. These metal oxide nanoparticles can exhibit an array of unique novel properties such as large surface area, high specificity, good reactivity and other properties, which can be an added advantages for industrial applications. The main aim of this work includes,

- Synthesis of undoped (ZnO, CuO, CdO, TiO$_2$ and MgO) and transition metal doped metal oxide (Cr-ZnO, Zn-CuO, Ni-CdO, Cr-TiO$_2$ and Zn-MgO) nanoparticles.

- Studies on the effect of doping on structural, optical and electrical properties of ZnO, CuO, CdO, TiO$_2$ and MgO nanoparticles.

- Sensitization of transition metal doped metal oxide nanoparticles (Cr-ZnO, Zn-CuO, Ni-CdO, Cr-TiO$_2$ and Zn-MgO).using Eosin-Y, SPADANS, Trypan blue and Evan's blue dyes.

- Evaluation of the consequence of dye sensitization on optical and electrical properties of synthesized transition metal doped semiconducting nanoparticles.

The thesis entitled **"Generation of dye-sensitized transition metal doped semiconductors for efficient solar energy harvesting - A Low-Cost method"** comprises five chapters.

Chapter-1 deals with the general introduction about nanomaterials and dye sensitized solar cells. It covers the literature review on history of solar energy conversion, DSSCs and their working principle, metal oxides for fabrication of DSSCs, nanomaterials

and their types, and various methods of synthesis of nanomaterials. At the end, the properties and applications of metal oxide nanomaterials were also described in detail.

Chapter-2 outlines the broad aim and scope of the work. It highlights the significance and comprehensive approaches to the synthesis of semiconducting nanoparticles and their applications for DSSCs.

Chapter-3 furnishes the methods and materials adopted in this work. This includes;

- Preparation of ZnO, CuO, CdO, MgO, TiO_2, Cr-ZnO, Zn-CuO, Ni-CdO, Cr-TiO_2, and Zn-MgO nanoparticles using microwave combustion method.

- Characterization of synthesized ZnO, CuO, CdO, MgO, TiO_2, Cr-ZnO, Zn-CuO, Ni-CdO, Cr-TiO_2 and Zn-MgO nanoparticles using X-Ray diffraction studies (XRD, Model: Bruker D8 Advance), Field-emission scanning electron microscopy (FE-SEM, Model: Nova Nano SEM600-FEI and FE-SEM Carl Zeiss AG-ULTRA 55), Energy dispersive X-ray diffraction spectroscopy (EDAX, Nova Nano SEM 600-FEI), Transmission electron microscopy (TEM, Model: Philips CM 200), Fourier transform infrared spectroscopy (FT-IR, Model: Bruker Alpha-T FT-IR Instruments), UV-Vis. spectroscopy (UV-Vis., Model: USB 4000, Ocean Optics) and photoconductivity method (I-V, Model: Kiethley Instruments Inc.2401).

- Calculation of Crystalline size, Micro-Strain, Dislocation density and lattice constants of nanomaterials using XRD data.

- Estimation of bandgap of nanomaterials using Tauc plot and Kubelka-Munk plot methods.

- Preparation of Eosin-Y, Trypan Blue, SPADANS and Evans blue dye solutions at different concentrations.

- Calculation of HOMO and LUMO of dye molecules using cyclic voltammetry.

- Fabrication of dye sensitized nanoparticle films using doctor blade method.

- Measurement of optical absorption of dye sensitized nanoparticle films using UV-Visible spectral data.

- Measurement of conductivity of dye sensitized nanoparticle films using Kiethley source meter.

Chapter-4 includes synthesis, characterization and properties of ZnO, Cr-ZnO, CuO, Zn-CuO, CdO, Ni-CdO, TiO_2, Cr-TiO_2, MgO and Zn-MgO nanoparticles. This chapter is sub-divided into chapter 4.1- 4.7.

Chapter-4.1 pertains to the synthesis, characterization and properties of ZnO and Cr-ZnO semiconducting nanoparticles. The lattice constants and band gap of synthesized ZnO and Cr-ZnO nanoparticles were calculated. The crystallinity of the samples was analyzed by X-ray diffraction studies (XRD). The doping property was analyzed by EDAX and UV-Visible spectrum for undoped and doped samples.

Chapter-4.2 deals with the characterization and properties of CuO and Zn-CuO nanoparticles by microwave combustion method. The surface morphology was studied by SEM and TEM techniques. EDAX confirms the presence of Zn in Zn-CuO lattice. Optical properties and photoresponse of these materials have been studied.

Chapter-4.3 presents the synthesis and characterization of CdO and Ni-CdO semiconducting nanoparticles synthesized by microwave combustion method. The prepared nanoparticles were characterized by XRD, FESEM, EDAX, UV-Vis. and I-V techniques. Effect of dopant on the optical and electrical properties of synthesized samples was studied.

Chapter-4.4 focused on the characterization of semiconducting TiO_2 and $Cr-TiO_2$ nanoparticles. The surface morphology was studied by FE-SEM and TEM. The optical and electrical properties synthesized TiO_2 and $Cr-TiO_2$ was studied using UV-Vis. spectroscopy and I-V characteristic studies.

Chapter-4.5 pertains to the characterization and properties of MgO and Zn-MgO nanoparticle synthesized by microwave combustion route. The structural, optical and electrical properties of these materials have been studied.

Chapter-4.6 describes the synthesis, characterization and results of synthesized ZnO nanoparticles using different solvents by microwave combustion route. The prepared ZnO nanoparticles were characterized by XRD, FE-SEM, UV-Vis. and I-V techniques. The effect of solvents on optical and electrical properties was studied.

Chapter-4.7 illustrates the structural, optical and electrical properties of synthesized ZnO nanoparticles under different microwave power via microwave combustion route. The structural morphology and elemental composition of synthesized ZnO samples were analyzed by FE-SEM and EDAX.

Chapter-5 focused on the study of optical and electrical characterization of dye-sensitized Cr-ZnO, Zn-CuO, Ni-CdO, $Cr-TiO_2$ and Zn-MgO nanoparticles. This chapter presents the selection of various dyes for sensitization of synthesized nanoparticles to enhance optical absorption band. The dyes Trypan blue, SPADANS and Evans blue were selected and their respective LUMO and HOMO levels were studied through cyclic voltametry. The synthesized doped nanoparticles were coated with these dyes and subjected for optical absorption studies. The optical and electrical properties of dye sensitized Cr-ZnO, Zn-CuO, Ni-CdO, $Cr-TiO_2$ and Zn-MgO were studied via UV-Vis. spectroscopy and I-V characteristic studies.

References

[1]   L. Fara and M. Yamaguchi, Advanced Solar Cell Materials, Technology, Modeling and Simulation, Engineering Science and Reference Publishing, 1st Edition, United States of America, **(2013)**.

[2]   L. Wei, P. Wang, Y. Yang, R. Fan, Y. Yanga and Y. Qiu, Sustainable Energy and Fuels, 1112, 1, **(2017)**.

[3]   B. Raj, M.V. de Voorde and Y. Mahajan, Nanotechnology for Energy Sustainability, Wiley-VCH Publishing, Germany, **(2017)**.

[4]   P. Wurfel and U. Wurfel, Physics of Solar cells: From Basic Principle to Advanced Concepts, Wiley-VCH Publishing, 1st Edition, Germany, **(2016)**.

[5]   A.L. Fahrenbruch, R.H. Bube, Fundamentals of Solar cells: Photovoltaic. Solar Energy Conversion, Academic Press, New York, London, **(1983)**.

[6]   R. Parthiban, D. Balamurugan, B.G. Jeyaprakash, Spectrochimica Acta Part A: Mol. Biomol. Spectro., 136, 986, **(2015)**.

[7]   Z. Zhang, J. Bao Yi, J. Ding, L. Mun Wong, H. Leng Seng, S. Jie Wang, J. Phys. Chem. C, 112, 9579, **(2018)**.

[8]   R.D. Tilley, Chem. Of New Zealand, 146, **(2018)**.

[9]   M. Anpo, M. Takeuchi, J. Catal., 216, 505, **(2019)**.

[10]   H. Ding, X. Zhang, M. K. Ram, C. Nicolini, J. Colloid Inter. Sci., 290, 166, **(2012)**.

[11]   K. Irshad, M.T. Khan, A. Murtaza, Physica B: Condensed Matter, 543, 3, **(2018)**.

[12]   N. Shanmugam, K. Dhanaraj, G. Viruthagiri, K. Balamurugan, K. Deivam, Arab.J. Chem., 9, S758, **(2016)**.

[13] M. Shatnawi, A.M. Alsmadi, I. Bsoul, B. Salameh, Results in Phys., 6, 1064, **(2016)**.

[14] S. Bazazi, N. Arsalani, A. Khataee, A.G. Tabrizi, J. Ind. Eng. Chem., 62, 265, **(2018)**.

[15] S. Rehman, J. Liu, R. Ahmed, H. Bi, J. Saud. Chem. Soc., 23, 385, **(2019)**.

[16] Y. Cao, D. Jia, R. Wang, J. Luo. Solid State Elect., 82, 67, **(2013)**.

[17] P. Shukla, J.K. Shukla, J. Sci.: Adv. Mat. Devices, 3, 452, **(2018)**.

[18] T.C. Bharat, Shubham, S. Mondal, H.S. Gupta, P.K. Singh, A.K. Das, Mater. Today: Proceedings, 11, 767, **(2019)**.

[19] M. A. Ciciliati, M. F. Silva, D. M. Fernandes, A.C. de Melo, Mater. Lett., 159, 84, **(2015)**.

[20] H. Ajamein, M. Haghighi, S. Alaei, Mat. Res. Bul., 102, 142, **(2018)**.

[21] Y. Cao, B. Liu, R. Huang, Z. Xia, S. Ge, Mat. Letters, 65, 160, **(2011)**.

[22] L.C. Nehru, V. Swaminathan, C. Sanjeeviraja, Powder Technol., 22, 30, **(2012)**.

[23] K. Patil, S. Rashidi, H. Wang, W. Wei, Inter. J. Photoenergy, 2019, 6, **(2019)**.

[24] A.M. Ammar, H. S. H. Mohamed, M.M.K. Yousef, J. Nanomaterials, 2019, 10, **(2019)**.

[25] J. Wu, Z. Lan, J. Lin, M. Huang, Y. Huang, Chem. Soc. Rev., 46, 5975, **(2017)**.

[26] X.F. Zhang, Z.G. Liu, W. Shen, and S. Gurunathan, Inter. J. Mol. Sci., 17, 1534, **(2016)**.

[27] K.K. Chattopadhyay, A.N. Banerjee, Introduction to Nanoscience and Nanotechnology, PHI Pvt. Limited Publishing, New Delhi, **(2009)**.

[28] S. Mourdikoudis, R. M. Pallares and N.T.K. Thanh, Nanoscale, 10, 12871, **(2018)**.

[29] T. Salim, S. Sun, Y. Abe, A. Krishna, A.C. Grimsdale and Y. M. Lam, J. Mater. Chem. A, 3, 8943, **(2015)**.

[30] W. Chen, M. P. Nikiforov and S. B. Darling, Energy Environ. Sci., 5, 8045, **(2012)**.

[31] J. Zhang, W. Peng, Z. Chen, H. Chen and L. Han, J. Phys. Chem. C, 116, 19182, **(2012)**.

[32] P. Wu, N. Du, H. Zhang, L. Jin, D. Yang, Mater. Chem. Phy., 124, 908, **(2010)**.

[33] Y.R. Sui, Y. Cao, X.F. Li, Y.G. Yue, B. Yao, X.Y. Li, J.H. Lang, J.H. Yang, Ceram. Int., 41, 587, **(2015)**.

[34] D. Rajesh, B. Varalakshmi, C.S.Sunandana, Phy. B, 407, 4537, **(2012)**.

[35] T. Jiang, M.B. Doeuff, Y. Farre, Y. Pellegrin, E. Gautron, M. Boujtita, L. Cario, S. Jobic and F. Odobel, RSC Advances, 6, 112765, **(2016)**.

[36] A. El-Trass, H.E. Shamy, I.E. Mehasse, M.E. Kemery, Appl. Surf. Sci., 258, 2997, **(2012)**.

[37] C. Chiang, Y. Shin, S. Ehrman, Appl. Energy, 164, 10319, **(2016)**.

[38] M. Iqbal, A.A. Thebo, A.H. Shah, A. Iqbal, K.H. Thebo, M.A. Mohsin, Inorg. Chem. Communicate, 76, 71, (**2017**).

[39] A. Sharma, M. Varshney, H.T. Kyun, K.H. Chae, H.J. Shin, Curr. App. Phys., 15, 1148, **(2015)**.

[40] X. Li, W. Guo, Y. Liu, W. He, Z. Xiao, Ele. Chim. Acta., 116, 278, **(2014)**.

[41] J. Lee, A. Katoch, J. Kim, S. Kim Sens. Actus B-Chem., 222, 307, **(2016)**.

[42]   H. Siddiqui, M.S. Qureshi, F.Z. Haque, Optik, 127, 3713, **(2016)**.

[43]   Y. C. Zhang, G. Lin Wang, Mat. Letts., 62, 673, **(2018)**.

[44]   D. M. Yufanyi, J. F. Tendo, A. M. Andoh, J. K. Mbadcam, J. Mats. Sci. Res., 3, 1, **(2014)**.

[45]   M. F. Elkady, M. A. Arafat, N. A. El Essawy, Beni-surf Uni. J. Basic Appl. Sci., 3, 229, **(2014)**.

[46]   L.S. Chougala, M.S. Yatnatti, R.K. Linganagoudar, R.R. Kamble, J.S. Kadadevarmath, J. Nano and Electronic Physics, 9, 04005, **(2017)**.

[47]   A. Arunachalam, S. Dhanapandian, C. Manoharan, G. Sivakumar, Spectrochim. Acta Part A: Mol. Biomol. Spectroscopy, 138, 105, **(2015)**.

[48]   D.V. Aware, S.S. Jadhav, Appl. Nanosci., 6, 965, **(2016)**.

[49]   U.G. Akpan, B.H. Hameed, Appl. Catalysis A: General, 375, 1, **(2010)**.

[50]   P.B. Devaraja, D.N. Avadhani, H. Nagabhushana, S.C. Prashantha, S.C. Sharma, B.M. Nagabhushana, H.P. Nagaswarupa, B. Daruka Prasad, J. Radiat. Res. Appl. Sci., 8, 36, **(2015)**.

[51]   K.S. Anantharaju, S.C. Prashantha, C. Shivakuamra, K. Gurushantha, Spectrochim. Acta Part A: Mol. Biomol. Spectroscopy, 149, 713, **(2015)**.

[52]   J. Jayaprakash, N. Srinivasan, P. Chandrasekaran, E.K. Girija, Spect. Acta Part A: Mol. Biomol. Spect., 136, 1803, **(2015)**.

[53]   Z.Q. Bai, Z.W. Liu, Scientific Reports, 11384, 11154, **(2017)**.

Chapter 1
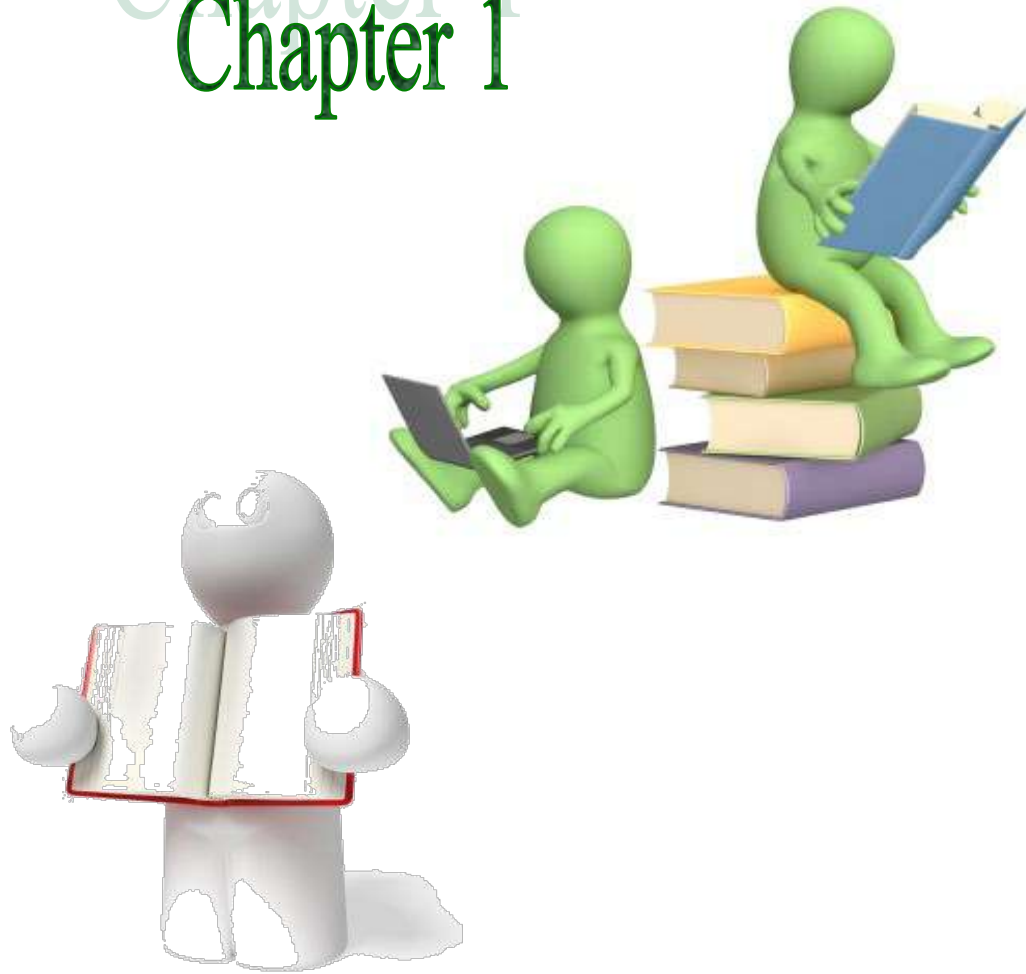
INTRODUCTION

1.1. Energy and Electricity

Today, energy is considered as one of the keystone in the economic growth of world. The continuous growth of world economy and industrialization across the world depends on the available natural resources which can be used as energy sources to power the machinery, heat homes and supply billions of individuals with electricity. Therefore, energy is one of the essential motivated sources for societal and world economies [1]. At present days world research is mainly focused on the reduction of future energy crisis across the global by using various conventional and renewable energy sources. Among these, fossil fuels, nuclear materials as well as hydroelectric power are the most accepted energy sources. The fossil fuels such as oil, coal and gas are extensively used for the production of energy and transportation, which releases more and more CO_2 in to atmosphere. This causes effect of global warming and also responsible for automatic climate change. Nuclear fuel is also used an alternative energy source for fossil fuels due to reduction of CO_2 emission. But, the storage of high energy radioactive waste is a difficult task in recent years [2]. Nowadays, increase in world population leads to the increase in global energy demand, environmental pollution and dependency on fossil fuels. At present situation 80% of fossil fuels (primary energy) consumed in the world, whereas only 58% of fossil fuels are used for transport sector [3]. On the other hand, a substantial portion of natural gas and coal are being used for the production of electrical power because no other conventional energy sources are even close to meet coal and natural gas potential over the next few years [4].

Electricity is regarded as most adoptable and versatile form of energy. It is also called as secondary source of energy because it can be converted from the primary energy

sources such as coal, natural gas, oil, nuclear power and other natural sources. Increase in the demand of electricity may be attributed to the increase in consumer electronics, the related industrial activity and access of large quantity of electricity to consumer in the technologically developing world [5]. According to global energy and CO_2 report of 2018, the generation of electricity increased by 3.1% (780 TWh) compared to the year 2017. The total electricity production in the world from coal, oil, nuclear power, natural gas and other renewable energies is 9566 TWh (37%), 997 TWh (4%), 2637 TWh (10%), 5944 TWh (23%) and 6426 TWh (25%), respectively [6].
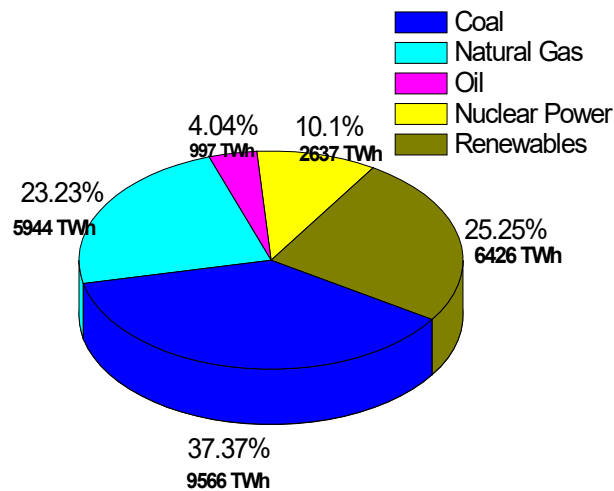
According to South Asian Energy (SAE-2018) survey, the worldwide economic growth and development gradually increasing by the production of electricity. Hence, it is necessary to fulfill the energy needs of the world by producing electricity double the normal usage. It could be done by increasing electricity upto 66% in between the years 2015 and 2040. This alters the global energy landscape and also offers new challenges with better opportunities [7]. As electricity significance increases, the energy conversion to generate electricity around the world also increases drastically by the usage of natural resources such as nuclear energy, natural gas and renewable resources [8].

1.2. Solar Energy

Solar radiation is the natural energy resource which is continuously supplied by the sun. It is the most significant non-conventional energy source so it is one of the highly sustainable, eco-friendly and non-polluting energy sources. In addition to these, solar energy helps to control global warming from greenhouse gases (through photosynthesis process). The energy supply from the sun is truly enormous and the solar energy received from earth's surface is about 1.08×10^8 GW. The total amount of energy that falls onto the earth from the sun in each year is about 3,400,000 EJ or 7000 to 8000 times of global energy consumption. The solar energy received by the earth per hour may produce current of annual energy demand. Only a small amount of solar energy is required to produce electricity of the power of 5000 to 6000 GW which is now accessible across the globe. For this reason solar energy is considered to be one of the best and most valuable renewable energy resources [9].

1.3. Generation of Solar Cells

The solar energy conversion is a one-step process which converts sunlight into electrical energy. Basically, the principle of photoelectric effect is responsible for the development of first photovoltaic devices. It was first noticed by Edmund Becquerel in 1839. Forty years later (in 1876) the first solid-state solar cell (photovoltaic device) was built by William Adams and Richards Day. They established that a photocurrent could generate in a sample of selenium when two heated platinum contacts [10]. Afterward, solar energy technologies were developed three generation solar cells. These can be represented in the Figure 1.
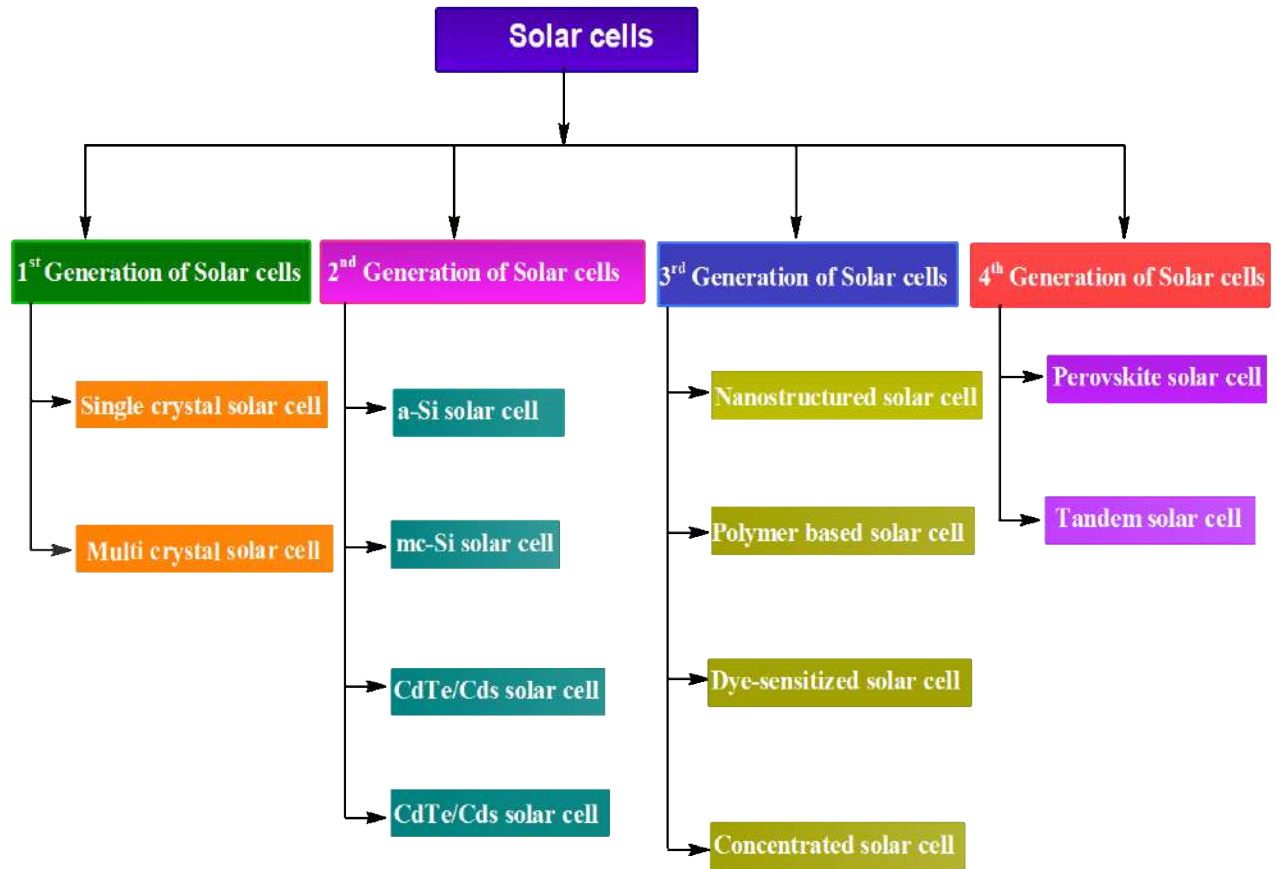
Figure 1. Generation of solar cells

Traditionally, the first generation solar cells are commonly based on the crystalline silicon technologies, either a monocrystalline or a polycrystalline Si-wafers and on gallium arsenide. These photovoltaic cells are single-junction devices with the theoretical efficiency of 33% and the energy conversion efficiency is only 15-25%. The majority of solar cells that exist in the market belong to first generation solar cells and it is extensively used amongst the other solar cells [11]. Although these solar cells were proven to be highly efficient, they encounter some disadvantages such as high time consumption, high-cost of silicon, high temperature requirement, high energy manufacturing processes and high processing cost. These limitations of the first generation solar cells seek to build efficient and low-cost new generation solar cells,

4

i.e., second generation solar cells [12]. These are mainly based on polycrystalline silicon or different semiconductors thin films like CdTe, CuIn and Se. The processing cost of these cells are lesser compared to the silicon based first generation solar cells. Second-generation solar cells were fabricated by depositing the thin films of semiconductors on the Silicon (Si), glass or ceramics (substrates) using molecular beam epitaxy (MBE), chemical vapour deposition (CVP) and spin-coating technique [13]. The 13-19% of power conversion efficiency was achieved by these solar cells. The main drawbacks of second generation solar cells are: i) environment contamination starts from the fabrication process and ii) difficult to find suitable semiconductor materials [14]. The third generation solar energy technologies are mainly focused on the improvement of light absorption coefficient and energy conversion efficiency of second-generation solar cells. But there is no variation in the processing cost of the third generation and second generation solar cells. The improvement of the light conversion efficiency of third generation solar cells can be achieved by fabricating the multi-junction solar cells, enhancing the absorption coefficient of materials and using the methods to increase the charge carrier collection. The energy conversion efficiency of these cells is greater than 15% [15]. Recent trends of commercialization provoke the fabrication of these types of solar cells because of high energy conversion efficiency, easily available raw materials, easy steps of fabrication and low-cost [16]. Over the development of solar cell technology, researches focus on the generation of the new type of solar cells and trying to enhance the light conversion efficiency. By this side, the fourth generation solar cells were introduced, which are also known as hybrid solar cells. This is the combination of low-cost, high flexible polymer films (organic materials) and high stable semiconductor

materials (inorganic materials). Such technological oriented inorganic to organic hybrid solar cell improves the conversion of solar light into electricity, which offers very good photo conversion efficiency than the present third generation solar cells [17].

1.4. Need of Third Generation Solar Cells

The third generation solar harvesting systems are one of the promising alternative types of photovoltaic devices. This aims to develop high conversion efficiency device with very low processing cost in comparison with expensive crystalline Si-based solar cells (1st generation solar cells) and less photo conversion efficiency of thin film solar cells (2nd generation solar cells). It is also one of the important types of nanostructure and polymer based (3rd generation) solar cells which generate from thin film route, abundant and non-toxic materials. These solar harvesting systems are potentially able to overcome the Shockley-Queisser limit 30-41% efficiency for single band gap solar cells. Moreover, the majority of solar industries are not interested in releasing such type of solar cells but researchers are focusing on the considerable improvement of such cells (only for study purposes). By use of size and shape dependent properties of nanostructured materials, dye-sensitized solar cells (DSSCs) have the potential to become third generation solar cells and are mainly focused on the low cost of fabrication compared to other types of solar cells [18].

1.5. Dye-Sensitized Solar Cells (DSSCs)

The history of DSSCs starts in the late 1960's with the work of organic dye sensitization on ZnO single crystal carried out by Gerischer and Tributsch. Subsequently, Tributsch and Calvin further demonstrated that the dye (chlorophyll) sensitized ZnO

nanostructures are play a vital role in the power conversion efficiency (PCE) of solar harvesting systems [19]. However, due to the poor anchoring of dye molecules on the semiconductor surface, the PCE was poor. Approximately, ten years later (1977), Spitter and Calvin were used TiO_2 nanostructured material instead of ZnO nanoparticles for the improvements of cell performance [20]. All these innovative experiments eventually lead to the invention of dye sensitized solar cells in 1991 by O' Regan and Gratzel. At that time, they achieved the photo conversion efficiency of about 7.1-7.9% [21]. Thereafter, this type of photo-electrochemical cell was named as the dye sensitized solar cells (DSSCs) because of the use of mesoporous TiO_2 semiconductor with a large specific surface area. This innovative and revolutionary third generation solar cell (especially thin film solar cells) created a new era in the field of research and development with less processing cost and better performance of DSSCs [22]. Generally, the DSSCs are collected of dye coated mesoporous metal oxide semiconductor photoanode, an iodide/ tri-iodide redox couple electrolyte and a platinized or carbon based counter electrode. Each constituent of DSSCs performs a definite tasks and the whole performance of DSSCs strongly depends on optimization of every single cell components in DSSCs system [23]. Over the past few decades, a great progress was made in technological applications and fundamental research of DSSCs. In current researches, an alternative sensitizer was used as counter electrode catalyst (N719, Z907, N3, D35, Y123) and redox couple has been used as a electrolytes (I_3^-/I^-, Co^{2+}/Co^{3+}, Cu^{2+}/Cu^+) for improvements of the cell performance. So, the photo conversion efficiency (PCE) was increased from 7.9% in 1991 to 13% in 2014 and an achieved PCE value of 14.3% in 2015 for cobalt mediated DSSCs [24].

1.6. Important Components of DSSCs

The DSSCs have mainly five important components, which are selected based on the role of charge carrier collection and enhancement in the efficiency of solar cell devices. The five main components are [25]:

1) Transparent conductive glasses

2) Wide band gap semiconducting nanomaterials (photoanode)

3) Dyes (photo sensitizers): a) Metal-free organic dyes

b) Inorganic dyes

c) Natural Dyes

4) Electrolyte

5) Counter electrode or auxiliary electrode

In DSSCs, the dyes sensitized nanostructured materials were commonly used as working electrode. The indium doped tin oxide (ITO) or fluorine doped tin oxide (FTO) substrates are commonly used transparent conductive glasses in solar devices. Various semiconductors with wide-bandgap were used for dye sensitization such as SnO_2, TiO_2, ZnO, ZnS, In_2O_3 etc., among them TiO_2 and ZnO nanoparticles showed a crucial role in DSSCs [26]. On the other hand, the organic dyes with anchoring groups (-COOH, $-PO_3H$, $-SO_3H$,-OH and $-NO_2$ groups), inorganic dyes (Ru, Zn, Cu, Co contained complexes) and natural dyes (Anthocyanins, Rose Bengal) were used as a sensitizer in DSSCs [27]. The electrolyte of DSSCs presents in between the auxiliary and working electrodes and shows the redox reaction. The commonly used electrolytes are potassium iodide and iodine, lithium iodide and iodine-like tri-iodide/iodine redox couples [28]. The auxiliary electrodes like platinized sheet and graphene or carbon coated glass were seen in the majority of DSSCs [29].

1.7. Working Principle of DSSCs

The DSSCs works basically on the principle of photosynthesis and the process involves the following steps [30]:
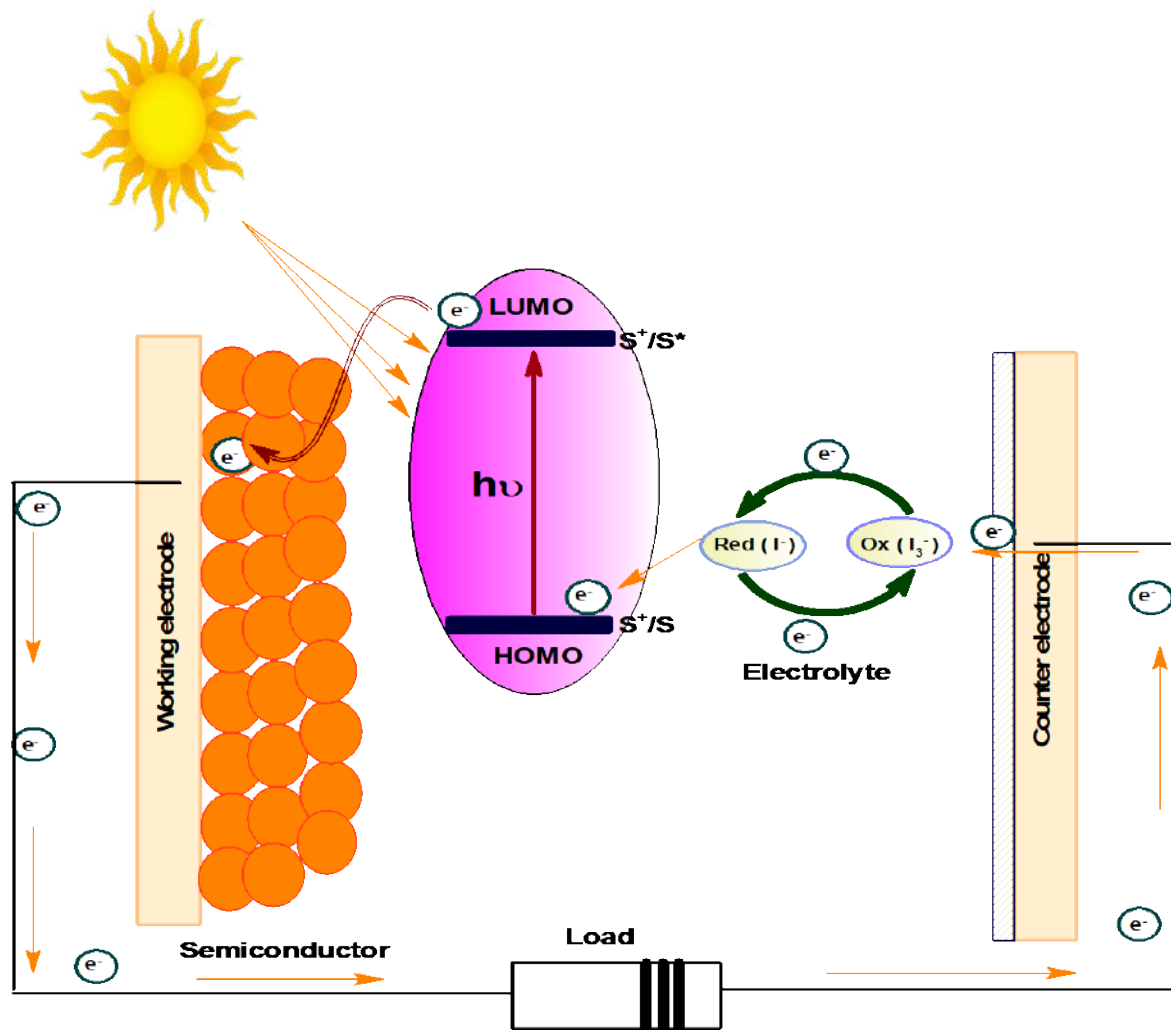
Step-1: When the light is illuminated on the surface of dye sensitized mesoporous semiconductor films, electrons in the dye are gets excited. Electrons tend to move from HOMO energy level (ground state) to LUMO energy level (exited state) of the dye molecule.

Step-2: The electrons in the higher energy state of dye molecule are inserted into conduction band of nanomaterial which lies below the excited energy level of

the dye, where the semiconductor nanoparticles absorbs solar light from UV region and the dye gets oxidized.

Step-3: The oxidised dye molecule is regenerated (reduced) due to the acceptance of electrons from tri-iodide ion (I_3^-)/iodide ion (I^-) redox couple.

Step-4: The inserted electrons travel through the semiconducting nanomaterial to reach the transparent conductive glass (back contact) and then through the external circuit to the counter electrode.

Step-5: At the counter electrode, iodide is regenerated by the reduction of tri-iodide ion.

1.8. Photoanode Materials for DSSCs

In DSSCs the photoanode materials are used as an electrons collector and this function of photoanode depends on the size, shape and band gap of the materials. Hence, it must have some significant characteristics such as: i) perfect pore size for efficient diffusion of dye; ii) large surface area for anchoring of high quantity of dye [31]; iii) suitable conduction band to improve the electron injection from LUMO level of the dye to the semiconductor [32]; iv) photo corrosion resistance [33]; v) excellent light scattering ability [34]; vi) electrons acceptor ability; vii) surface roughness; and viii) good adhesiveness with conductive glass [35].

1.9. Metal Oxide Semiconductors for DSSCs

The semiconducting metal oxide electrodes have more interested in the upcoming years for their applications in various solar harvesting and storage devices, such as solar cells, fuel cells, Li-ion batteries, electrochromic devices and photo-electrochemical cells [36]. To accomplish better performance of the devices, the electrodes used in these

applications must show good electron transfer properties and a high surface area even though the working principle of the devices is different from each other. Therefore, semiconducting metal oxide nanoparticles are appeared as a major class of versatile materials with various properties and great potentiality towards several device applications [37]. Till now, the majority of DSSCs works were employed on the basis of wide-bandgap semiconductors (TiO_2, ZnO, SnO_2, Nb_2O_5, CeO_2 and NiO). Because the characteristic properties of semiconducting nanomaterials shows proper conduction band position relative to dye sensitizers and also increased surface area of nanoparticles assisted the enhancement of light absorption [38]. There are two types of nanostructured semiconductors were used in the fabrication of DSSCs and they exhibits significant role in the enhancement of power conversion efficiencies. Generally, the n-type semiconducting nanoparticles such as ZnO, TiO_2, CdO and SnO_2 have been extensively studied and used as photoanode materials for DSSCs. Because of transparency in the solar spectrum and good electrical properties of these semiconductors provides wide applications towards the fabrication of photo voltaic and optoelectronic devices. Dye-sensitization of these types of semiconductors is an effective way to extend the photo response into visible light region and even into the near IR region [39]. A. Al-Kahlout *et al.* were used the ZnO nanoparticle films for the fabrication of DSSCs. They used them as photoanode material and achieved the maximum photocurrent of 7 $mAcm^{-2}$ [40]. A. Taleb *et al.* have been reported that the TiO_2 films prepared by spin coating were used as a photoanode material for DSSCs [41]. D.B. Kuang *et al.* were used hot reflux method for the synthesis of SnO_2 nanoparticles. They employed SnO_2 nanoparticles as photoanode material which has got photo conversion efficiency of 5.78% [42]. S.H. Han *et al.* have been reported that the CdO nanocrystalline thin film could be

used as anode materials for DSSCs with the photo conversion efficiency of 2.98% [43].

The p-type semiconductors were used in the fabrication of photocathode for DSSCs.

The reasons for use of these semiconductors in the application of DSSCs are:

a) wide-bandgap with photo corrosive resistant nature; b) simple synthetic procedure to

generate nanoparticles; c) suitable valence band position of these semiconductors so as to

enhance the open circuit voltage [44]. Among the variety of semiconducting

nanoparticles only a few metal oxides display the p-type semi-conductivity. Nickel oxide

(NiO) nanoparticles have been extensively used as p-type semiconductor for the

production of DSSCs. Because NiO is an intrinsic p-type semiconductor with energy

gap of 3-4 eV and it exhibits good thermal stability. The valence band potential of NiO

(0.54 V versus NHE at pH 7.0) shows the better electron donor properties for various

photo-sensitizers because the reductive quenching of different sensitizers is a strongly

allowed process. But small valence band potential shows the difficulties to obtain higher

open circuit voltage (V_{oc}) [45-46]. Furthermore, p-type semiconductors are known to be

poor conductors as compared to n-type semiconductors that is why transparent

conducting substrates are commonly of n-type. The photo induced absorption

spectroscopy is used for the measurement of hole diffusion coefficient in NiO films and

shows the electron diffusion coefficient of NiO is smaller than TiO_2 [47]. The long time

delay between injection of holes and their collection was caused by the slow diffusion of

holes into the NiO and this slow diffusion may be increased by redox mediator.

Therefore, new p-type semiconductors with high conductance than the NiO are

favourable for the development of efficient p-type DSSCs [48]. L. Pleux *et al*. showed a

NiO films prepared by hydrothermal method found particularly suitable for the

fabrication of efficient p-type DSSCs [49]. T. Jiang *et al*. and R. Bajpai *et al*. reported the fabrication of p-type DSSCs by using CuO and NiO nanoparticles [50-51].

1.10. Doped Metal Oxide Semiconductors for DSSCs

Doping of semiconducting nanoparticles is a significant approach in energy gap engineering because it changes the optical properties of semiconductors. Generally, it can be achieved by incorporating impurity ions (non-metal, transition and inner transition metal ions) to modify the optical and electrical properties of semiconducting metal oxides [52]. The main objective of substitution (doping) of impurity ions into host lattice of semiconducting nanoparticles is to induce a bathochromic shift or ref shift (shift a band to lower energy or higher wavelength), i.e., reduction of energy gap of pristine metal oxide semiconducting nanoparticles or to develop impurity energy states in between the valance and conduction bands, which results in the absorption of light in the visible region. Incorporation of impurity ions may lead to photo electronic systems that exhibit enhanced efficiency. This is due to the transfer of electron from one of these energy levels to the conduction band which requires very less energy than in the bare semiconducting nanoparticles [53]. Recently, majority of research works were carried out to synthesize undoped and doped TiO_2 nanoparticles with various size and structures for DSSCs applications [54]. The doping with suitable n-type or p-type elements leads to modify the electronic system and morphology towards smaller energy gap for fast charge transfer and very high light absorption. Incorporation of right dopants in TiO_2 crystal lattice may influence the several factors such as, initiation of surface defects for systematic trapping of charge carriers, reduction in recombination rate, production of oxygen vacancies, erection of grain boundaries, reduction of grain size, improvement in the dye sensitization

leading to better electron insertion, shifting of flat band gap resulting in a greater open circuit voltage (V_{oc}), decrease in the energy gap for absorption of light in visible region and also generation of radicals for the enhancement of dye-metal oxide attachment to inject electrons [55]. The overall particle to particle charge transport in the bulk is regulated by the distribution and concentration of localized energy states (traps), and also in the surface to environment charge transport in the interfaces has been suggested to be the main cause of above effects [56]. The non-metals such as nitrogen (N), carbon (C), boron (B), sulphur (S), fluorine (F) and chlorine (Cl) having more ionization energy and electronegativity shows efficient enhancement in the optical properties of semiconductors. This exhibits the better photo-response in the visible region owing to the reduction of energy gap and the shift in the optical absorption peak to higher wavelength. The non-metal ion doping introduces the impurity states in the above valence band and helps to realize the visible light photo activity of semiconductors [57]. J.Y. Park *et al.* reported the efficiency about 11.35% by using Cu/N-doped TiO_2 nanoparticles [58]. Y.Z. Zheng *et al*. were used I-doped ZnO nanoparticles for the improvement of the efficiency of DSSCs [59]. The various properties of 3d or 4d transition metals are affected by several factors, such as the number of d-electrons on transition metal ions, oxygen defects, crystalline structures and preparation routes [60]. Usually, the incorporation of transition metal ions could modify the band gap energy, fermi energy level and d-electronic configuration in the electronic structure of host semiconducting nanomaterials. Consequently, it produces new impurity states below the conduction band (CB) which is arisen due to partially filled d-orbital [61]. This exhibits the reduction of bandgap (red shift) of semiconducting nanomaterials and enhances its visible light

harvesting character. Therefore, transition metal ions like Cu^{2+}, Ni^{2+}, Zn^{2+}, Cr^{3+} and Fe^{2+} were used to change the optical, electrical and structural properties of host semiconducting nanomaterials [62]. Bodo *et al*. have studied the optical properties of Mn doped ZnS nanoparticles synthesized by chemical co-precipitation method [63]. Y.S. Wang *et al.* have reported the preparation and characterization of Cd, Mn and Fe doped ZnO nanoparticles [64]. The achievement of modulation the energy gap of metal oxides is the difficult task in recent days. By this reason, the researchers of materials science are introducing the new dopants like rare earth (4f, 5d, and 6s) and moderate the structural, optical and electrical properties of nanomaterials. Therefore, the rare earth-like Ce, Sm, Eu, Gd and Dy metal ions are widely used for the enhancement of photoactivities [65]. J. Anuntahirunrat *et al.* have reported the efficiency of DSSCs by using Nb-ZnO films [66]. A. Evcin *et al*. have studied the optical and electrical properties of Dy/Eu/Ag co-doped TiO_2 nanoparticles [67].

1.11. Recent Developments of Photoanode Materials

The device DSSC is a molecular system in which the properties of individual components are more important for understanding the functions of whole device. Therefore, the optimization of each component is more significant for the enhancement of quality of DSSCs [68]. Basically, the traditional DSSCs are mainly composed of four components such as photoanode, sensitizer, counter electrode and electrolyte [69]. The recent researchers achieved the power conversion efficiency of DSSCs upto 14-15% by several modifications but till now the conversion efficiency has not been bypassed that of silicon based solar cells. Therefore the optimization of these electrode materials to

improve the power conversion efficiency with good thermal stability is very much needed [70].

The photoanode materials play an important role in the enhancement of power conversion efficiency of DSSCs. The framework of photoanode is mainly composed of semiconducting nanomaterials. These materials show dual functions in DSSCs: a) as a support of dye loading; b) to transfer of photo exited electrons from dye molecules to external circuit [71]. Therefore, a nanostructured material with large surface area is necessary for the improvement of dye loading. The recent technological developments take a certain steps for the modification of photoanode materials such as doping of impurity ions into semiconductor lattice, decoration with nobel metals, synthesis of different nanostructure materials, modification with metal oxides and coating with up/down conversion materials. Improvement of photoanode materials by these modification steps have been addressed by specific aspects of DSSCs such as light absorption, electron-hole transport and reducing the charge recombination [72]. S. Ameen *et al*. were reported the optical band gap of ZnO nanomaterials which was decreased upon Sn doping [73]. A. Neshat *et al*. were reported the colloidal core-shell Au/SiO$_2$ nanoparticles as suitable material for decorating DSSCs [74]. V. Dhas *et al*. were reported the synthesis of anatase TiO$_2$ nanowires by hydrothermal method and achieved the efficiency of 4.12% by using salinization [75]. H.S. Jung *et al*. were studied the effect of surface modification of TiO$_2$ by insulating MgO nanoparticles in order to enhance the efficiency of DSSCs [76].

The sensitizer is a significant part of DSSCs because it absorbs the natural or artificial light and generates the photo-exited charge carriers at the surface of

semiconducting nanomaterials. To improve the performance of DSSCs, the sensitizer have certain properties such as very high molar excitation co-efficient, suitable HOMO and LUMO energy levels, appropriate band gap, good solubility and photo-stability [77]. Till now, more efforts were applied for the synthesis of variety of sensitizers which are categorized into ruthenium polypyridyl dyes, porphyrin dyes, quantum dot dyes, metal free organic dyes and pervoskite based dyes [78]. Ru (II) polypyridyl dyes are most popular sensitizer in DSSCs due to excellent light absorption capacity from UV light to near IR light and having suitable energy level for TiO_2 electrode and I^-/I_3^- electrolyte [79]. Upto 11.7% (2010) of energy conversion efficiency was achieved by using the Ru(II) complex based dyes. The recent development of DSSCs is more focused on the use of Ru(II) based dyes with different ligands to enhance the efficiency and stability of devices. For example, replacing the thiocyanate ligands with other chelating anions, substitution of ancillary ligand and using hydroxamate instead of corboxylate and phosphonate groups [80]. T. Jella *et al*. were synthesized benzimidazole functionalized ancillary ligands based Ru(II) complexes. They used these dye as sensitizer for semiconducting materials with the power conversion efficiency of 7.88% [81]. C. Dragonetti *et al*. were used pyrid-2-yltetrazolate ligand in place of thiocyanate in Ru(II) sensitizer and they achieved the power conversion efficiency of 6.1% [82]. S.J. Konezny *et al*. were used the hydroxamate based Ru(II) complex as a sensitizer for DSSCs [83]. Similarly, the metal free organic dyes with their smaller energy gap play a crucial role in the DSSCs. The high molar coefficient and high flexibility in the molecular structure of such organic dyes shows applicability towards the modern DSSCs [84]. Now, researchers developed the new metal free organic dyes with D-π-A, D-A-π-A

and D-D-π-A groups for DSSCs [85]. L. Han *et al*. were used new D-D-π-A triphylamine coumarin dye as a sensitizer for DSSCs and which has got a photo conversion efficiency of 4.99% [86]. Y. Shen *et al*. achieved 9.5% conversion efficiency for D-π-A structured phorphyrin based dye sensitized solar cells [87]. W. Zhu *et al*. fabricated a novel D-A-π-A indoline based DSSC with a conversion efficiency of 9.04% [88]. The Zn(II) porphyrin dyes have got more interest due to their properties like high molecular stability, suitable energy levels with flexible structure and intense absorption in the region of 400-500 nm and 500-700 nm. The efficiency of DSSCs recorded upto 12.3% (2011) using YD2-oC8 (D-π-A Zn (II) porphyrin dye) co-sensitized with Y123 (D-π-A organic dye) organic dye [89]. Quantum dot and pervoskite based sensitizers were also developed for the fabrication of efficient DSSCs. The most commonly used quantum dot sensitizers are CdS, CdTe, PbS, PbSe and Sb_2S_3 which show photo conversion efficiency of 7.4% [90]. Recently, the halide pervoskite based sensitizer gained considerable attention due to their excellent characteristics of light harvesting. The efficiency of these pervoskite sensitized DSSCs are increased year by year i.e., 3.81% (2009) to 20.1% (2014) [91].

In this present work, undoped and transition metal doped semiconducting metal oxide nanoparticles were prepared using microwave combustion method. The consequences of doping with different transition metals were studied through XRD, UV-Vis., FE-SEM, TEM and I-V techniques. The redox potentials of all the selected dyes were determined by cyclic voltammetry (CV). The absorption and photoconductivity of dye sensitized transition metal doped semiconducting nanoparticles have been examined through UV-Vis and I-V studies.

References

[1]   E. Colombo, S. Bologna, D. Masera, Renewable Energy for Unleashing Sustainable Development, Springer, Heidelberg, **(2013)**.

[2]   H. D. Yoo, E. Markevich, D. Salitra, Mater. Today, 17, 110, **(2014)**.

[3]   M.M. Rathore, Thermal Engineering, Tata McGraw Hill, New Delhi, **(2010)**.

[4]   S. A. Sarkodie, P.A. Owusu, Cogent Eng., 3, 5, **(2016)**.

[5]   One technology is already changing in future of energy (http:// www. wired. com/ insights), July, (**2013).**

[6]   Global Energy and CO_2 Status Report 2017, International Energy Agency, March, **(2018)**.

[7]   Southeast Asia Energy Outlook 2018*,* International Energy Agency, **(2018)**.

[8]   D. Steven, E. O'Brien, B.Jones, The Booking Institution, Washington, **(2015)**.

[9]   P. Breeze, Solar Power Generation, Elsevier, London, **(2016)**.

[10]   F. Sauvage, Advances in chemistry*,* Hindawai Publishing Corporation, **(2014)**.

[11]   N. Tetreault, M. Gratzel, Energy and Environmental Science*,* 5, 8506, **(2012)**.

[12]   M. Grubb, J.W. Bialek, Future Electricity technologies and systems, Cambridge University press, Cambridge, **(2018)**.

[13]   S.K. Nayaka, S. Mohanty, Trends and Applications in Advanced Polymeric Materials, Scrivener publishing, Baverly, USA, **(2017)**.

[14]   A. Pandikumar, R. Ramaraj, Rational Design of Solar Cells for Efficient Solar Energy Conversion, John Wiley & Sons, Inc. Hoboken, USA, **(2018)**.

[15]   M.I. Ahamed, A. Habib, S.S. Javaid, Inter. J. Photoenergy, 2015, 1, **(2015)**.

[16]   A. Khatibi, F.R. Astaraei, M.H. Ahmadi, Energ. Sci. Technol., 7, 312, **(2015).**

[17]   K.D.G.I. Jayawardena, L.J. Rozanski, C.A. Mills, S.R.P. Silva, Nanoscale, 5, 8412, **(2013)**.

[18]   M.A. Green, Third Generation photovoltaics: Advanced Solar Energy Conversion, Springer, Heidelberg, **(2003)**.

[19]   H. Gerischer, M.E. Michel- Beyerle, H. Tributsch, Electrochem. Acta, 13, 1509, **(1968)**.

[20]   H. Tributsch, M. Calvin, Photochem. Photobiol., 14, 95, **(1971)**.

[21]   K. Sharma, V. Sharma, S.S. Sharma, Nanoscale Res. Lett., 13, 2, **(2018)**.

[22]   Y. Luo, D. Li, Q. Meng, Adv. Mater., 21, 4647, **(2009)**.

[23]   S. Thomas, T.G. Deepak, G.S. Anjushree, T.A. Arun, A. Kumaran Nair, J. Mater. Chem., 2, 4474, **(2014)**.

[24]   I. B. Karki, J.J. Nakarmi, P.K. Mandal, S. Chatterjee, Appl. Sol. Energy, 49, 43, **(2013)**.

[25]   N. A. Karim, U. Mehmood, H.F. Zahid, T. Asif, Sol. Energy, 185, 166, **(2019)**.

[26]   M. Yang, B. Dong, X. Yong, W. Xiang, Z. Ye, E. Wang, L. Wan, L. Zhao, S. Wang, RSC Adv., 7, 41738, **(2017)**.

[27]   P. Chowdhury, H. Gomaa, A.K. Ray, Sustain. Nanotechnology Environ. Adv. Achievements, 1124, 240, **(2013)**.

[28]   G. Cassone, G. Calogero, J. Sponer, F. Saija, Phys. Chem. Chem. Phys., 20, 13038, **(2018)**.

[29]   D. Susanti, M. Nafi, H. Purwaningsih, R. Fajarin, G.E. Kusuma, Procedia Chem., 9, 4, **(2014)**.

[30]   M. Soroush, K.K.S. Lau, Dye-Sensitized Solar Cells, Mathematical Modeling, and Materials Design and optimization, Academic Press, London, **(2019)**.

[31]   C. P. Lee, C.T. Li, K.C. Ho, Mater. Today, 20, 268, **(2017)**.

[32]   K. Fan, J. Yu, W. Ho, Mater. Horiz., 4, 320, **(2017)**.

[33]   S. Sharma, B. Siwach, S.K. Ghoshal, D. Mohan, Renew. Sust. Ener. Rev., 70, 532, **(2017)**.

[34]   P. Zhang, Z. Hu, Y. Wang, Y. Qin, X.W. Sun, W. Li, J. Wang, Appl. Surf. Sci., 368, 403, **(2016)**.

[35]   M. Buchalska, J. Kuncewicz, E. Swietek, T. Baran, W. Macyk, Coord. Chem. Rev., 257, 769, **(2013)**.

[36]   J. Bisquert, Phys. Chem. Chem. Phys., 10, 50, **(2008)**.

[37]   N.K. Elumalai, C. Vijila, R. Jose, A. Uddin, S. Ramakrishna, Mater. Renew. Sustain. Energy, 11, 3, **(2015)**.

[38]   L. Benesperi, H. Michaels, M. Freitag, J. Mater. Chem. C, 6, 11905, **(2018)**.

[39]   C. Cavallo, F.D. Pascasio, A. Latini, M. Bonomo, D. Dini, J. Nanomaterials, 2017, 2, **(2017)**.

[40]   A. Al-Kahlout, Thin solid films, 520, 1820, **(2012)**.

[41]   A. Taleb, F. Mesguich, A. Herissan, C.C. Justin, X. Yanpeng, P. Dubot, Sol. Energy Mater. Sol. Cells, 148, 59, **(2016)**.

[42]   D.B. Kuang, K.N. Le, Y.F. Wang, Y.F. Yu, H.Y. Chen, Appl. Mater. Interfaces, 5, 5110, **(2013)**.

[43]   S.H. Han, R.S. Mane, H.M. Pathan, C.D. Lokhande, Sol. Energy, 80, 189, **(2005)**.

[44]   X. Xu, J. Cui , J. Han, J. Zhang, Y. Zhang, L. Luan, G. Alemu, Sci. Reports, 4, 2, **(2014)**.

[45]   H. Sun, S.C. Chen, S.W. Hsu, C.K. Wen, T.H. Chuang, X. Wang, Ceram. Int., 43, S369, **(2017)**.

[46]   F. Odobel, L.L, Pleux, Y. Pellegrin, E. Blart, Acc. Chem. Res., 43, 1066, **(2010)**.

[47]   S. Power, D. Xiong, T. Daeneke, M.T. Ma, A. Gupta, W. Chen, U. Bach, J. Phy. Chem. C, 118, 16375, **(2014)**.

[48]   S. Mori, S. Mukuda, S. Sumikura, Y. Takeda, Y. Tamaki, E. Suzuki, T. Abe, J. Phy. Chem. C, 112, 16134, **(2009)**.

[49]   L.L. Pleux, B. Chevillon, Y. Pellegrin, E. Blart, L. Cario, S. Jobic, Inorg. Chem., 48, 8249, **(2009)**.

[50]   T. Jiang, Y. Wang, D. Meng, X. Wu, J. Wang, J. Chen, Appl. Surf. Sci., 311, 608, **(2014)**.

[51]   R. Bajpai, S. Roy, N. Koratkar, D.S. Misra, Carbon, 56, 62, **(2013)**.

[52]   R. Vishwanatha, Praman- J. Phys., 84, 1056, **(2015)**.

[53]   F. Huang, A. Yan, H. Zhao, Semiconductor Photo-catalysis-Materials, Mechanisms and Applications, Intech Open, Croatia, **(2016)**.

[54]   H. F. Mehnane, C. Wang, K.K. Kondamareddy, W. Yu, S. Guo, X.Z. Zhao, RSC Adv., 7, 2358, **(2016)**.

[55]   R.T. Ako, P. Ekanayake, D.J. Young, J. Hobley, V. Chellappan, A.L. Tan, G.S. Subramanian, Appl. Surf. Sci., 351, 950, **(2015)**.

[56]   S.P. Lim, A. Pandikumar, H.N. Lim, R. Ramaraj, N.M. Huang, Sci. Reports, 5:11922, 2, **(2015)**.

[57]   S.Z. Islam, S. Nagpure, D.Y. Kim, S.E. Rankin, Inorganics, 5, 2, **(2013)**.

[58]   J.Y. Park, C.S. Kim, K. Okuyama, H.M. Lee, H.D. Jang, S.E. Lee, T.O. Kim, J. Powd. Source, 306, 771, **(2016)**.

[59]   Y.Z. Zheng, X. Tao, Q. Hou, D.T. Wang, W.L. Zhou, J.F. Chen, Chem. Mater., 23, 3, **(2011)**.

[60]   J. Pan. R. Wang, X. Zhou, J. Zhong, X. Xu, J. Hu, Phys. Chem. Chem. Phys., 19, 24594, **(2017)**.

[61]   Q. Meng, T. Wang, E. Liu, X. Ma, Q, Geac, J. Gong, Phys. Chem. Chem. Phys., 15, 9549, **(2013)**.

[62]   N.F. Djaja, D.A. Montja, R. Saleh, Adv. Mater. Phys. Chem., 3, 33, **(2013)**.

[63]   B. Bodo, D. Prakash, P.K. Kalita, Inter. J. Appl. Phys. Maths., 2, 183, **(2012)**.

[64]   Y.S. Wang, P.J. Thomas, P. O'Brien, J. Phy. Chem. Lett., 110, 21415, **(2006)**.

[65]   W. Li, Influence of electronic structures of doped TiO2 on their photocatalysis, Phys. Status Solidi R, 12, **(2014)**.

[66]   J. Anuntahirunrat, Y.M. Sung, P. Pooyodying, Mater. Sci. Eng. (IOP Conference Series), 229, 5, **(2017)**.

[67]   A. Evcin, N.C. Bezir, R. Kayali, M. Kasikci, A. Oktay, Acta Phy. Polonica A, 128, B-305, **(2004)**.

[68]   J. Gong, K. Sumathy, Q. Qiao, Z. Zhou, Renew. Sustain. Energ. Reviews, 68, 236, **(2017)**.

[69]   J. Wu, Z, Lan, J. Lin, M. Huang, Y. Huang, L. Fan, G. Luo, Y. Lin, Y. Xie, Y. Wei, Chem. Soc. Rev., 46, 5980, **(2017)**.

[70]   S. Yun, Y. Qin, A.R. Uhl, N. Vlachopoulos, M. Yin, D. Li, X. Han, A. Hagfeldt, Energy Environ. Sci., 11, 478, **(2018)**.

[71]   H. Wang, J. Lin, Z.X. Shen, J. Sci.: Adv. Mater. Devices, 1, 225, **(2016)**.

[72]   J. Macaira, L. Andrade, A. Mendes, Renew. Sustain. Energy Rev., 27, 337, **(2013)**.

[73]   M. Ye, X. Wen, M. Wang, J. Locozzia, N. Zhang, C. Lin, Z. Lin, Mater. Today, 18, 156, **(2015)**.

[74]   S. Ameen, M. S. Akhtar, H.K. Seo, Y.S. Kim, H.S. Shin, Chem. Eng. J., 187, 351, **(2012)**.

[75]   A. Neshat, R. Safdari, Energy Technol. Environ. Sci. (Chemistry Select), 4, 5000, **(2019)**.

[76]   V. Dhas, S. Muduli, S. Agarkar, A. Rana, B. Hannoyer, R. Banerjee, S. Ogale, Sol. Energy, 85, 1219, **(2011)**.

[77]   H.S. Jung, J.K. Lee, M. Nastasi, Langmuir, 21, 10335, **(2005)**.

[78]   I.B. Karki, S. Chatterjee, J.J. Nakarmi, D. Sinha, D. Goswami, P.K. Mandal, J. Nepal Chem. Soc., 30, 56 **(2012)**.

[79]   S. Zhang, X. Yang, Y. Numata, L. Han, Energy Environ. Sci., 6, 1446, **(2013)**.

[80]   A. Carella, F. Borbone, R. Centore, Frontier Chem., 6, 4, **(2018)**.

[81]   T. Jella, M. Srikantha, R. Bolligarla, Y. Soujanya, S.P. Singh, L. Giribabu, Dolton Trans. 44, 14702, **(2015)**.

[82]   C. Dragonetti, A. Colombo, M. Magni, P. Mussini, F. Nisic, D. Roberto, R. Ugo, A. Valore, A. Valsecchi, P. Salvatori, M. G. Lobello, F. D. Angelis, Inorg. Chem. 52, 10724, **(2013)**.

[83]   T.P. Brewster, S.J. Konezny, S.W. Sheehan, L.A. Martini, C.A. Schmuttenmaer, V.S. Batista, R.H. Crabtree, Inorg. Chem., 52, 6759, **(2013)**.

[84]   I.B. Karki, S. Chatterjee, J.J. Nakarmi, D. Sinha, D. Goswami, P.K. Mandal, J. Nepal Chem. Soc., 30**,** 56 **(2012)**.

[85]   S. Ahmada, E. Guillena, L. Kavan, M. Gratzel, M.K. Nazeeruddin, Energy Environ. Sci., 6, 3442, **(2013)**.

[86]   J. He, Y. Liu, J. Gao, L. Han, Photochem. Photobiol. Sci., 16, 1095, **(2017)**.

[87]   Y. Shen, J. Lu, X. Xu, K. Cao, J. Cui, Y. Zhang, Y. Shen, X. Shi, L. Liao, Y. Chenga,   M. Wang, J. Mater. Chem. A, 1, 10013, **(2013)**.

[88]   W. Zhu, Y. Wu, M. Marszalek, S.M. Zakeeruddin, Q. Zhang, H. Tian, M. Gratzel, Energy Environ. Sci., 5, 8261, **(2012)**.

[89]   N. J. Jeon, H. G. Lee, Y. C. Kim, J. Am.Chem. Soc., 136, 7839, **(2014)**.

[90]   P.V. Kamat, J. Phys. Chem. Lett., 4, 908, **(2013)**.

[91]   J. Cui, H. Yuan, J. Li, X. Xu, Y. Shen, H. Lin, M. Wang, Sci. Technol. Adv. Mater., 16, 1, **(2015)**.

Chapter 2
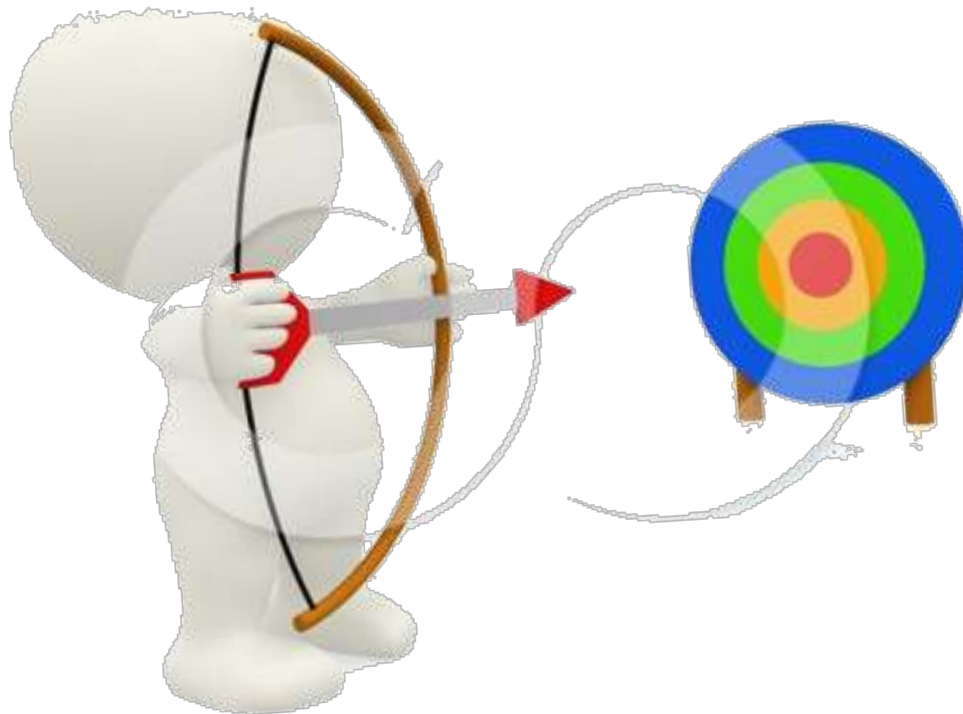
AIM AND SCOPE

The generation of global energy from conventional sources increases in the recent years. Subsequently, the demand and consumption of energy also increases with increase in the population of the world. In the coming days the supply of energy is one of the significant problems in the world. Between 2004 and 2030 the annual global consumption of energy is estimated to rise by more than 40-50%. Assuming current policies and practices remain in place, maximum amount of energy generation is expected to come from the burning of fossil fuels, such as oil, ethanol, natural gas and coal. Emission of CO_2 increases day by day due to extensive industrialization and over transportation. This causes serious impact on living system by releasing CO_2 (green house gas) to the atmosphere (especially from coal). So, there is a required security for sustainability of the increasing world population. The extensive use of fossil fuels has facing several significant challenges in the last few decades such as environmental pollution, large amount of CO_2 emission, global warming, depletion of fossil fuel reserves and ongoing increase of fuel cost. These problems will be forced to seek ecofriendly and sustainable alternative energy resources. Thus, the renewable energy sources are the only alternative solution for resolving the current environmental problems and energy crisis. Renewable energy sources such as solar, wind, biomass, wave and tidal energy systems have great potential. Among these sources, solar energy has got more prominence in the concern of energy generation.

The main objective of the recent research works on photovoltaic devices is to reduce the processing cost and to improve the energy production efficiency of solar cells. In order to achieve this considerable enhancement in the photo conversion efficiency of solar cells is required. Generally, the efficiency of solar cells is depends on two major

factors such as: a) choosing a suitable n-type or p-type semiconducting nanomaterials with wide band gap to match the solar spectrum; and b) innovative device engineering, which facilitates more effective charge collection as well as better consumption of the solar spectrum via single and multi junction approaches. However, in the recent developments it is feasible to randomly categorized a select assembly of semiconducting nanomaterials into various power conversion efficiency regimes: a) ultrahigh-power conversion efficiency devices ($\eta > 30\%$) are the multi-junction tandem solar cells devices consisting of GaAs and $GaInP_2$ semiconductors; b) high power conversion efficiency devices ($\eta > 20\%$) are the single crystal silicon solar cells; c) ultra-moderate power conversion efficiency devices ($\eta = 12$-20%) are the thin-film solar cells consisting of amorphous Si, $CuGaInSe_2$ (CIGS) and CdTe semiconducting materials d) moderate power conversion efficiency devices ($\eta < 12\%$) are the dye sensitized TiO_2 semiconductor solar cells, which are very low cost devices. Today the DSSCs are gained more interest due to their good photovoltaic performance, specifically under low-light conditions, flexibility in terms of colors and appearance, simple preparation procedures and low processing cost. But the long term stability is one of major drawbacks in the DSSCs. Leakage of electrolyte solution, degradation and desorption of dyes are the important key factors affecting the stability of DSSCs. Due to these factors current research is mainly focused on the modification of each component of DSSCs to improves the efficiency of power conversion. For instance, in order to fabricate most effective photo anodes of DSSCs, various shape of semiconducting nanomaterials are used such as nanoprisms, nanoplates, nanoflowers and nanorods. During the past few decades, the semiconducting nanoparticles have emerged as new building blocks to construct the efficient photovoltaic

devices. The film of semiconducting nanostructures is used as a photoanode material for DSSCs. This photoanode material provides the two important functions: 1) it facilitates for dyes (sensitizer) coating; and 2) it acts as a transporter of photo-excited charge carriers from dyes to external circuit. Thus, a nanostructured semiconducting material with high surface area is needed to ensure the effective dye loading. Moreover, a fast charge transport rate is required to ensure high electron collection efficiency. These two properties are the required ideal characteristic features of a photoanode. Current technological research work is mainly focused on the fabrication of effective photoanode films for DSSCs. A variety of thin film preparation techniques, such as sol–gel, hydrothermal, electrochemical anodization, spin coating, vapour deposition, spray pyrolysis, and atomic layer deposition have been employed.

At present to improve the efficiency of photovoltaic devices doping of suitable metal ions into bare semiconductors has been found to more fruitful. Recently, doping of two or more elements instead of single elements has also been adopted to enhance the photo conversion efficiency. The existence of two or more transition metal ions simultaneously in the host material helps to increase the impurity states between the valence and conduction band. The metal ions incorporation depends on various significant factors such as the way of incorporation, difference in the ionic radius of metal ions and concentration of dopant solution. Number of research reports has revealed that the efficiency of solar harvesting systems is significantly dependent on the optical and electrical properties of semiconducting nanoparticles.

In the present work, ZnO, Cr-ZnO, CuO, Zn-CuO, CdO, Ni-CdO, Ni-CdO, TiO_2, Cr-TiO_2, MgO and Zn-MgO nanoparticles were prepared using microwave combustion

method. The structural, optical and electrical properties of synthesized ZnO, Cr-ZnO, CuO, Zn-CuO, CdO, Ni-CdO, Ni-CdO, TiO_2, Cr-TiO_2, MgO and Zn-MgO nanoparticles were characterized through XRD, FE-SEM, TEM, EDAX, UV-Vis. and I-V characteristics studies. The micro-strain, lattice constants, dislocation density, crystalline size of synthesized metal oxide nanoparticles was calculated. The energy gap of all the samples was estimated using diffused reflectance spectra.

The various concentrations of Trypan blue (TB), SPADNS (SPD) and Evans blue (EB) dye solutions were used to sensitize the synthesized Cr-ZnO, Zn-CuO, Ni-CdO, Cr-TiO_2 and Zn-MgO nanoparticles. The main goal of this experiment was to analyze the optical and electrical properties of TB, SPD and EB sensitized Cr-ZnO, Zn-CuO, Ni-CdO, Cr-TiO_2 and Zn-MgO nanoparticles. The optical band gap and molecular orbital energy levels (HOMO, LUMO) of dyes were calculated using UV-Visible (UV-Vis.) spectroscopy and cyclic voltametry (CV), respectively. The dye adsorption saturation limit on the surface of nanoparticles was also studied. Measurement of current intensity of TB, SPD and EB dyes sensitized nanoparticles has been carried out using Kiethley source meter. The measured current intensity and optical absorption of TB, SPD and EB dyes sensitized Cr-ZnO, Zn-CuO, Ni-CdO, Cr-TiO_2, Zn-MgO nanoparticles indicated the possibility of using these materials for the fabrication of dye sensitized solar cells.

Chapter 3
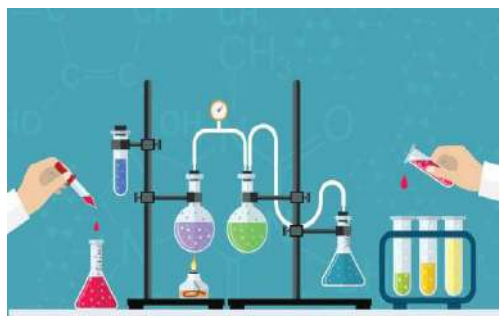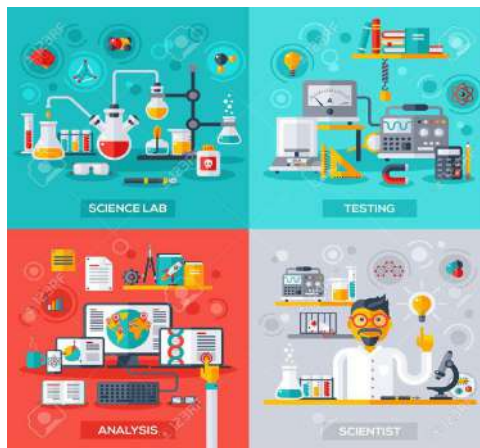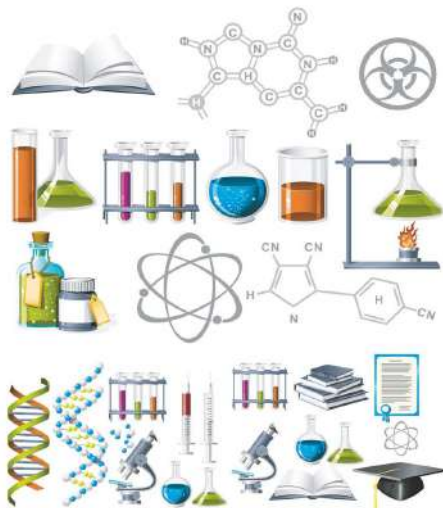
METHODS AND MATERIALS

Semiconducting metal oxide nanomaterials have been extensively studied from both experimental and theoretical viewpoints because of their potential applications in solar energy conversion, photocatalysis and in optoelectronic devices [1]. The main goal of the recent researchers in the field of nanotechnology is to develop different type of semiconducting nanoparticles with special properties compared to those of bulk counterpart. The development of these nano scaled metal sulphides, oxides and composites are able to show the unique structural and optical properties due to their small crystalline size and high density sites at corners and edges [2]. The desire for miniaturation is the driving force behind nanoparticles synthesis. Since the shape, size and dimensionality of semiconductor nanoparticles are vital parameters for their properties, development of facile methods for the preparation of well defined semiconducting nanostructures have got more importance. One dimensional nanostructure of semiconducting nanomaterials has received much attention because they offer superior opportunities for both fundamental research as well as technological applications [3]. More recently, the transparent semiconducting nanomaterials have attracted attention due to their excellent properties arising out of large surface-to-volume ratio and quantum confinement. Further, these properties of semiconducting nanoparticle are dependent upon crystalline size, shape and their surface conditions. These properties can be achieved by variety of experimental techniques [4]. Current innovative science and technology provided new advanced analytical tools for the characterization of nanomaterials. These tools provide the detailed information about physical and chemical properties of developed materials at nanoscale level [5].

In the present work, the synthesis of ZnO, Cr-ZnO, CuO, Zn-CuO, CdO, Ni-CdO, TiO_2, Cr-TiO_2, MgO and Zn-MgO nanoparticles were described in details. The

29

microwave combustion method was used for the synthesis of ZnO, Cr-ZnO, CuO, Zn-CuO, CdO, Ni-CdO, TiO$_2$, Cr-TiO$_2$, MgO and Zn-MgO nanoparticles. The various instrumental techniques (XRD, FE-SEM, TEM, UV-Vis. and I-V studies) have been used for the characterization of synthesized nanoparticles. The experimental procedure followed during the sensitization of TB, EB and SPD dyes on surface of Cr-ZnO, Zn-CuO, Ni-CdO, Cr-TiO$_2$ and Zn-MgO nanoparticles has also been discussed.

3.1. Materials

Zinc nitrate hexahydrate [Zn(NO$_3$)$_2$·6H$_2$O, 98% Merck], ethylene glycol [C$_2$H$_6$O$_2$, Merck], chromium (III) chloride hexahydrate [CrCl$_3$·6H$_2$O, 93%, Loba Chemie PVT. Ltd.], copper sulfate pentahydrate [CuSO$_4$·5H$_2$O, 99.5%, Hi-Media], sodium hydroxide [NaOH, 98%, Hi-Media], urea [NH$_2$CONH$_2$, 99.5%, Hi-Media] and zinc sulphate heptahydrate [ZnSO$_4$.7H$_2$O, 98%, Loba Chemie], acetone [CH$_3$COCH$_3$, 99%, Merck], absolute ethanol [C$_2$H$_5$OH, 99.9%, Changshu Yangshu Chemicals], cadmium nitrate hexahydrate [Cd(NO$_3$)$_2$·6H$_2$O, ≥99%, Merck], nickel nitrate hexahydrate [Ni(NO$_3$)$_2$·6H$_2$O, 99.99%, Hi-media], magnesium nitrate hexahydrate [Mg(NO$_3$)$_2$·6H$_2$O, 99.99%, Merck], titanium isopropoxide [C$_{12}$H$_{28}$O$_4$Ti, 98%, Hi-Media], 2-propanol [C$_3$H$_8$O, 99.5%, Merck], digol [C$_4$H$_{10}$O, 98.5%, Merck], trypan blue [C$_{34}$H$_{24}$N$_6$Na$_4$O$_{14}$S$_4$, Dye content 60%, Hi-Media], SPADNS [C$_{16}$H$_9$N$_2$Na$_3$O$_{11}$S$_3$, Dye content 79%, Merck], evans blue [C$_{34}$H$_{24}$N$_6$Na$_4$O$_{14}$S$_4$, Dye content 85%, Loba Chemie] were procured and used for the experiments. All the chemicals and reagents used in the present work were of analytical grade. Double distilled water was used for the preparation of solutions. Domestic microwave oven (Model: ONIDA POWER SOLD 17D, Power output-700 W, Frequency-2450 MHz) was used for the heating purpose.

3.2. Preparation of Undoped and Doped Metal Oxide Nanoparticles

3.2.1. Microwave combustion synthesis

Microwave combustion method has gained more popularity compared to conventional heating methods, due to its advantages like rapid heating, efficient energy transfer, low-cost processing, less reaction time, eco-friendly approach, high yield and formation of pure homogeneous product [6]. During the microwave assisted reaction, the heat is generated inside the sample by the interaction of microwave energy with reactive substance. The microwave energy can penetrate into the reactant material at molecular level and uniformly distribute among the surface and bulk material. This results in the formation of nanostructured materials within few minutes. Further, the microwave energy is converted into thermal energy throughout the material by rapid mechanisms of dipolar rotation and ionic conduction. This accelerates the reaction rate, which improves the yield and purity of the material with a proper size distribution and stoichiometry [7].

3.2.2. Preparation of ZnO, CdO and MgO nanoparticles

In the present method, 30 g of zinc nitrate hexahydrate was taken in a dry beaker and 6-8 drops of ethylene glycol was added and kept in a microwave oven for dissolution for 10 sec. Then the above solution was heated in a domestic microwave oven of power 480 W (60%) for 8 min. First the solution was converted into paste in a few seconds and further undergoes dehydration followed by decomposition with the evolution lot of heat and gases (O_2, NO_2) with orange colour fumes. The combustion was completed within 8 min resulting in the formation of white porous powder of ZnO. The resulting solid was subsequently annealed at 500 ºC in a muffle furnace and finally a fine crystalline powder

of ZnO was obtained. The similar procedure has been followed for the preparation of CdO and MgO nanoparticles. Similarly, the same procedure was also followed by the synthesis of ZnO nanoparticles under different microwave power (160, 320, 480, 640 and 800 W) and by using different solvents (water, ethylene glycol, digol and 2-propanol).

3.2.3. Preparation of Cr-ZnO, Ni-CdO and Zn-MgO nanoparticles

To synthesis Cr-ZnO (2-15 wt%) nanoparticles, zinc nitrate hexahydrate $[Zn(NO_3)_2.6H_2O]$ and Chromium (III) chloride hexahydrate $[CrCl_2 \cdot 6H_2O]$ were mixed in dry beaker and 6-8 drops of ethylene glycol was added and kept in a microwave oven for dissolution for 10 sec. Then the above solution was heated in a microwave oven of power 480 W (60%) for 8 min. First the solution was converted into paste in a few seconds and further undergoes dehydration followed by decomposition with the evolution lot of heat and gases (O_2, NO_2) with orange colour fumes. The combustion was completed within 8 min resulting in the formation of white porous powder of Cr-ZnO. The resulting solid was subsequently annealed at 500 ºC in a muffle furnace and finally a fine crystalline powder of Cr-ZnO was obtained. The similar procedure has been followed for the preparation of Ni-CdO and Zn-MgO nanoparticles at different dopant concentration.

3.2.4. Preparation of CuO and Zn-CuO nanoparticles

In a typical synthesis, undoped CuO and Zn-CuO nanoparticles (0.0, 2.0, 4.0, 6.0, 8.0 and 10.0 at mol% of Zn) were prepared via microwave combustion method. For the preparation of CuO nanoparticles, an equimolar concentration (0.8 M each) of copper sulphate pentahydrate $[CuSO_4 \cdot 5H_2O]$ and urea $[NH_2\text{-}CO\text{-}NH_2]$ were dissolved in 100 ml of double distilled water. A 100 ml of 0.4 M sodium hydroxide solution was

added drop-wise to the above mixture and kept stirring for 30 minutes at room temperature. When the solution turned blue to light green, 5 ml of this solution was taken in a china dish and placed in a domestic microwave oven. The solution was exposed to the microwave energy of 60% power (480 W) for 8 minutes. Initially, the reaction solution was boiled and subsequently it underwent dehydration with the evolution of gases. The so obtained solid product was washed with double distilled water and absolute ethanol followed by acetone to remove the impurity ions like Na^+, SO_4^{2-} and NH_4^+ and dried at 80 ºC for 5 hours. It was finally calcinated at 600 ºC for 2 hours. The above procedure has been followed for the synthesis of Zn-CuO nanoparticles with the addition of $ZnSO_4·7H_2O$ at different molar concentration.

3.2.5. Preparation of TiO_2 and Cr-TiO_2 nanoparticles

The TiO_2 and Cr-TiO_2 nanorods were prepared through microwave combustion method. In a typical synthetic procedure, 30 ml of ethylene glycol was taken in a dry beaker and kept into stirring for 20 min. A 10 ml of titanium isopropoxide ($C_{12}H_{28}O_4Ti$) added to the above solution drop wise using syringe. The resulting transparent solution was heated in a microwave oven of power 60% for 10 min. Initially, the reaction mixture boiled and subsequently underwent dehydration with the liberation of water vapour and CO_2 gas. The white powder of TiO_2 was settled down at the bottom of the beaker. The obtained product was cooled and washed for three to four times with water followed by alcohol. The resultant solid was subjected for calcination at 500 ºC for 2 h. Similar procedure was followed for the preparation of anatase Cr-TiO_2 nanoparticles by the addition of increasing amount (2-8 wt%) of chromium (III) chloride hexahydrate [$CrCl_3·6H_2O$] to the mixture of ethylene glycol and titanium isopropoxide.

3.3. Effect of Doping on Metal Oxide Nanoparticles

Doping is the process of addition of suitable impurity metal ions into host lattice of semiconductor. The doping of different metal ions into the host oxide materials improves the electrical, optical and structural properties. The significant change in such properties upon doping is ascribed to the modification of electron transfer characteristics due to the change in crystalline structure of pristine metal oxide nanoparticles [8]. Such changes lead to an increase or a decrease of energy gap resulting in a shift of the position of conduction band of semiconductor. In addition, other properties like crystal size and shape of nanoparticles also affected by doping of right dopants [9].

3.4. Characterization Techniques

3.4.1. X-ray diffraction (XRD) studies

XRD is one of the promising, powerful and nondestructive experimental techniques used for the analysis of single as well as polycrystalline materials. It provides the useful information on structure of the materials, orientation of crystal planes, lattice parameters, micro-strain, stress, crystalline size, unit volume and whether the synthesized nanomaterials posses single or multi-phase [10]. The crystalline nature of all the synthesized undoped and doped metal oxide nanomaterials were evaluated using high resolution X-ray diffractometer provided with Cu-Kα/30 kV/15 mA radiation at wavelength λ = 0.154060 nm from an angle 2θ = 30-80º. Basically XRD is obtained as the scattered X-rays from atoms, ions or molecules present in the parallel and equally spaced atomic planes as explained in the Bragg's law. The determination of structural properties of given materials is based upon the position of the peaks and their relative intensities [11].

From XRD data the following parameters have been calculated,

a)   Average crystallite size of synthesized undoped and doped metal oxide nanoparticles was calculated using Debye-Scherrer equation [12];

$$\text{Average crystallite size (D)} = 0.9 \, \lambda / \beta \, \cos\theta$$

where, λ = Wavelength of X-rays (0.154 nm), β = FWHM (radians), θ = Bragg's diffraction angle (degree).

b)   The lattice constants a, b and c for all the synthesized undoped and doped nanoparticles were determined using the following equations [13].

Cubic: $\dfrac{1}{d_{hkl}^2} = \dfrac{h^2 + k^2 + l^2}{a^2}$

Hexagonal: $\dfrac{1}{d_{hkl}^2} = \left[\dfrac{4}{3}(h^2 + k^2 + hk) + l^2 \left(\dfrac{a}{c}\right)^2 \right]$

Tetragonal: $\dfrac{1}{d_{hkl}^2} = \dfrac{h^2 + k^2}{a^2} + \dfrac{l}{c^2}$

Monoclinic: $\dfrac{1}{d_{hkl}^2} = \dfrac{1}{\sin^2 \beta} \left(\dfrac{h^2}{a^2} + \dfrac{k^2 \sin^2 \alpha}{b^2} + \dfrac{l^2}{c^2} - \dfrac{2h \cos \beta}{ac} \right)$

where, a, b, c = Lattice constants (Å), α, β = Interfacial angles (degree) and d = Inter atomic spacing (Å), h, k, l = Miller indices of a crystal plane.

c)   The micro-strain and dislocation density of synthesized nanoparticles were calculated from following equations [14-15]:

$$\text{Micro-strain } (\varepsilon) = \frac{\beta \cos\theta}{4}$$

$$\text{Dislocation density } (\delta) = \frac{1}{D^2}$$

where, β = FWHM (radians), D = Crystallite size (nm).

d) The unit volume of all the synthesized undoped and doped metal nanoparticles was determined using the following equations [16-19]:

Cubic: $V = (a)^3$

Hexagonal: $V = 0.866 \times a^2 \times c$

Monoclinic: $V = a\,b\,c\,(\sin\beta)$

Tetragonal: $V = a^2\,c$

where, V = Unit cell volume $(\text{Å})^3$, a, b, c = Lattice constants (Å), β = Interfacial angle (degree).

In the present work the phase purity and crystallite size of synthesized undoped and doped metal oxide nanoparticles were characterized through XRD (Model: Bruker D8 Advance) with Cu-Kα radiation ($\lambda = 0.154$ nm).

3.4.2. Field-emission scanning electron microscopic (FE-SEM) studies

FE-SEM is one of the important instrumental techniques for morphological study of nanomaterials. It gives the important information regarding the growth mechanism and shape of the synthesized nanoparticles [20]. In a typical FE-SEM instrument, the emitted electrons from the source are focused into a beam having energy in the range of few 100 eV to 40 keV, and impinge over the surface of the specimen by deflection coils. As the electrons bombards and penetrate the surface of the sample, ejection of electron from the sample is observed. The FE-SEM photomicrographs are obtained from cathode ray tube by collecting the ejected electrons [21].

The studies on structural morphology of synthesized undoped and doped metal oxide nanoparticles were carried out using FE-SEM (Model: Nova Nano SEM600-FEI and FE-SEM Carl Zeiss AG-ULTRA 55) technique.

3.4.3. Energy-dispersive analysis using X-rays (EDAX)

EDAX is a valuable experimental technique used for the determination of elements present in the synthesized materials. Sometimes it is also called as energy dispersive X-ray spectroscopy (EDX or EDS) and energy dispersive X-ray microanalysis (EDXMA). When an electron beam strikes on the surface of a sample, the electrons present in the inner shell of the atom are ejected by generating vacant positions (holes) and these vacant positions are occupied by the outer shell electrons. Energy difference between the outer and inner energy levels directs to emission of X-rays in the sample and energy of the X-rays discharged from a given material can be measured. The peak position and peak area of EDAX spectral analysis indicates the nature and amount of elements present in the given sample [22]. The elemental composition of undoped and doped metal oxide nanoparticles was determined by EDAX [Model: JSM-6300 (LA)] technique.

3.4.4. Transmission electron microscopic (TEM) studies

TEM is a versatile microscopic technique being used for the study of morphology, crystallinity and average crystalline size of materials. The main source of TEM is the electron gun which generates high energy beam of electrons. These electrons are bombarded on materials (thin films) of thickness less than 200 nm. The well focused beam has an adequate amount of energy for the electrons to be transmitted via the ultra thin specimen and the signal of scattered or transmitted electron is significantly magnified by a sequence of electromagnetic objective lenses. Finally, the magnified lenses produce desired TEM image of the sample [23]. The Selected area electron diffraction (SAED) is a well established crystallographic experimental technique used to

investigate the phase purity, orientation of diffraction planes, d-spacing and crystalline nature of a given material [24]. SAED was performed inside the TEM. It provides different type of ring pattern depends upon the crystalline nature of the samples: a) the spot ring pattern indicates the well-defined single phase crystalline materials and b) the concentric ring or diffused ring pattern represents the polycrystalline nature of the material [25].

In the present work TEM and SAED studies for the synthesized undoped and doped metal oxide nanoparticles were carried out using TEM (Model: Philips CM 200) technique.

3.4.5. UV- Visible absorbance (UV-Vis.) studies

The UV-Visible absorption spectroscopy is one of the important non-destructive tools used to find out the energy gap of semiconducting materials. The energy gap of host materials changes as the dopant creates the crystal imperfection. Usually, three forms of spectra are being used to analyze the absorption maxima of synthesized pristine and doped nanoparticles i.e., absorbance, reflectance and transmittance [26]. The plot of absorbance or reflectance or transmittance versus wavelength in the UV-Visible spectra depicts the electronic transition between lower to higher energy states of the molecules as a result of light absorption. The band gap of material could be estimated by using the position of absorption peaks in absorption spectra [27]. The optical properties of nanomaterials can also investigate by the diffuse reflectance spectrum (DRS), which is also adopted as standard analysing technique in recent years. Reflectance spectroscopy and UV-Vis. spectroscopy are closely related techniques because in both the methods visible light was used for the excitation of valence electrons to the vacant orbitals. The

relative change in transmittance of light when it passes through the solution gives the UV-Vis. spectra whereas in diffuse reflectance spectra the relative change in the amount of reflected light from the material surface is measured [28].

In the present work, UV-VIS-NIR spectrophotometer (model: Ocean optics, USB 4000, USA) was used to study the absorbance and reflectance spectra of metal oxide nanoparticles. The UV-Visible spectra have been recorded in the wavelength range 300-800 nm.

The band gap of synthesized semiconducting nanoparticles has been calculated using the following methods:

a) General method

The optical band gap of undoped and doped nanoparticles was calculated using the following equation [29]:

$$E = \frac{hc}{\lambda}$$

where, h = Planck's constant (J s),   c = Velocity of light (m/s) and λ = Photon wavelength (nm).

b) Tauc plot method

A Tauc plot is another method used for the determination of energy gap of undoped and doped nanomaterials. The Tauc relation is given by the following relation [30]:

$$(\alpha h\nu)^{1/n} = A\,(h\nu - E_g)$$

where, h = Planks constant (6.626×10^{-34} J s), A = Energy-independent constant, α = Absorption coefficient, E_g = Optical bandgap of valence and conduction band (eV),

n = Constant, which determines the type of optical transition. For direct allowed transition, n = 1/2; for indirect allowed transition, n = 2.

On plotting the values of $(\alpha h\nu)^2$ versus $h\nu$, a better linearity has been observed for the direct transition. The band gap energy has been obtained by extrapolating the linear part of the curves to energy axis (X-axis).

c)   Kubelka-Munk plot method

In this method, the optical band gap measurement was carried out by diffused reflectance spectroscopy. The Kubelka-Munk relation is expressed as [31]:

$$F(R) = (1-R)^2/\ 2R$$

where, F(R) = Kubelka-Munk function, R = Reflectance of the sample

d)   The conduction bands of synthesized metal oxide nanoparticles were calculated using the following equations [32]:

$$E_{CB} = \chi - E^e - 0.5\ E_g$$

$$E_g = \frac{1240}{\lambda_{max}}\ eV$$

$$E_{(AVS)} = -E_{NHE} - 4.5$$

where, χ = Absolute electronegativity of semiconductors, E^e = Energy of electrons in hydrogen scale (4.5 eV), E_g = Energy gap of semiconducting nanoparticles, λ_{max} = Optical absorption maxima of nanoparticles.

3.4.6. Cyclic voltammetric (CV) studies

CV is a versatile, prominent and widely used electroanalytical technique for investigating the oxidation and reduction behavior of electro-active species [32]. A three

electrode system comprising working or indicator electrode, counter or auxiliary electrode and reference electrode has been used. The electrode potential is varied in a desired fashion with reference to a suitable reference electrode and the current that flows between counter and auxiliary electrode is measured [33]. The oxidizing and reducing capacity of the electrode is controlled by the applied potential. Scanning towards the negative potential makes the electrode a stronger reductant whereas, scanning towards the positive potential makes it a better oxidant [34]. In the present work the electrochemical work station (Model: CH Instruments 660D, USA) was used for the voltammetric studies of dyes. For cyclic voltammetric studies, 0.1 mM solutions of commercial TB, SPD and EB dyes in 0.1 M of KCl solution were used. The potential range for all the dyes was set between -1.4 to 1.4 V. A three electrode cell consisting standard calomel, platinum wire and pencil graphite as reference, auxiliary and working electrode, respectively was used for CV studies. The ferrocene/ferocenium (Fc/Fc$^+$) system has been used as internal reference. In the present study, a scan rate of 100 mV/s was employed. The band gap, LUMO and HOMO energy levels were calculated by the following equations [35]:

$$E_{LUMO} / E_{HOMO} = -(4.8 + E_{onset}^{red} / E_{onset}^{oxd}) \ eV$$

$$E_g = E_{LUMO} - E_{HOMO} \ eV$$

$$E_g = \frac{1240}{\lambda_{max}} \ eV$$

where, E_{onset}^{red} = Onset oxidation potential (V), E_{onset}^{oxd} = Onset reduction potential (V), 4.8 eV = Internal reference of ferrocene in vacuum level, λ_{max} = Optical absorption maxima (nm).

3.4.7. Current-voltage (I-V) characteristic studies

The I-V characteristic study is the most adoptable experimental technique for the measurement of current, voltage and resistance in the photovoltaic cells. It provides the information regarding the photo conversion efficiency, short circuit current and open circuit voltage [36]. The photoconductivity (I-V) studies of undoped and doped transition metal oxide nanoparticles were carried out using Keithley source meter with USB GRIB adaptor (Model: Keithley source meter- 2401, USB-888, USA). The I-V measurements were performed under dark as well as UV-light conditions. The silver paste was used to make good electrical contact.
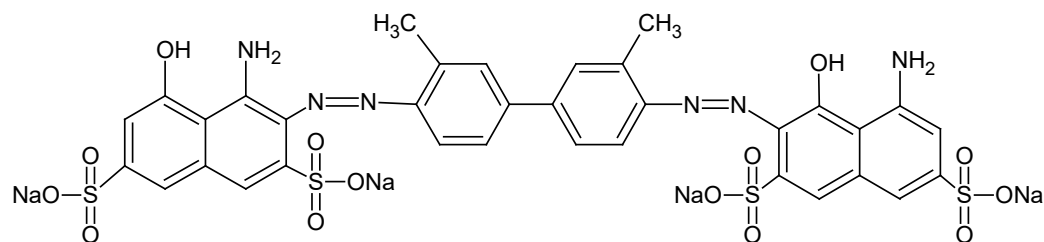
3.5. Dye Sensitization of Transition Metal Doped Semiconducting Nanoparticles

The transition metal doped nanoparticles films were prepared by using doctor blade method. Transparent glass plate of 1.5 x 1.5 cm^2 dimension was used as support. The glass plate were cleaned in double distilled water, ethanol and acetone for 10 min each with ultra sonication to remove contaminations, and finally dried at room temperature. The 1 g of synthesized transition metal doped oxide nanoparticles was dispersed in ethanol by sonication (for about 5-10 min) until a gelatinous paste of appropriate viscosity was obtained. The obtained paste was loaded on a pre-cleaned transparent glass plate by doctor blade method using scotch tape as spacer. The paste was dispersed uniformly with a glass rod and then dried at 60 ^{o}C for 10 min under air to eliminate ethanol. Different concentrations of dye solutions (Trypan blue, SPADNS and Evans blue) were prepared in a 25 ml (1:3 ratio of water: ethanol) conical flask. As prepared nanoparticle films by doctor blade method were dipped in the respective dye solutions for 30-45 min, dried in an oven (50-60 ^{o}C) for 30 min and used for I-V studies.

42

3.6. Physical Characteristics of Dyes

Trypan Blue

Type	:	Azo dye
Colour	:	Blue
Melting point	:	$\geq 300\ ^oC$
Absorption maxima (λ_{max})	:	600 nm
Solubility	:	water soluble (10 mg / ml) and partially soluble in ethanol
Molecular formula	:	$C_{14}H_{24}N_6O_{14}S_4Na_4$
Molecular structure	:	

SPADNS

Type	:	Azo dye
Colour	:	Red to brown
Melting point	:	$\geq 300\ ^oC$
Absorption maxima (λ_{max})	:	570 nm
Solubility	:	water and ethanol soluble
Molecular formula	:	$C_{16}H_9N_2O_{11}S_3Na_3$
Molecular structure	:	
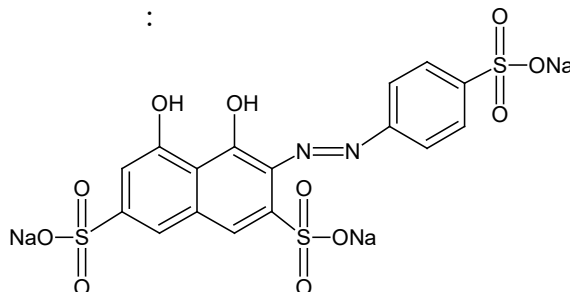
Evans Blue

Type   :   Azo dye

Colour   :   Dark brown to block

Melting point   : $\geq 300\ ^{\circ}C$

Absorption maxima (λ_{max})   :   620 nm

Solubility   :   Water, alcohol and acid soluble

Molecular formula   : $C_{14}H_{24}N_6O_{14}S_4Na_4$

Molecular structure   :
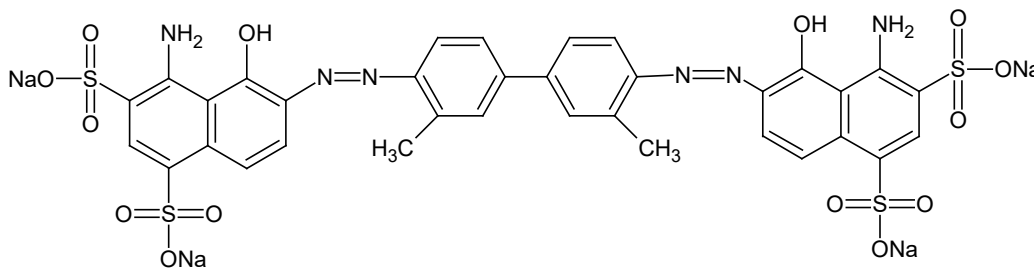
References

[1]   M.M. Hassan, W. Khan, A. Azam, A.H. Naqvi, J. Ind. Eng. Chem., 21, 283, **(2015)**.

[2]   J.P. Reece, New Nanotechnology Research, Nove Science Publishers, New York, **(2006)**.

[3]   A.K. Singh, U.T. Nakate, Adv. Nanopart., 2, 171, **(2013)**.

[4]   Y.C. Zhang, G.L. Wang, Mater. Lett., 62, 673, **(2008)**.

[5]   E. Mansfield, D. L. Kaiser, D. Fujita, Metrology and Standardization for Nanotechnology, Wiley-VCH, Germany, **(2017)**.

[6]   G.T. Anand, L.J. Kennedy, J.J. Vijaya, J. Mol. Struct., 1084, 244, **(2015)**.

[7]   A. Manikandan, J.J. Vijaya, L.J. Kennedy, M. Bououdina, J. Mol. Struct., 1035, 332, **(2013)**.

[8]   S. Phokha, D. Prabhakaran, A. Boothroyd, S. Maensiri, Microelectron. Eng., 126, 93, **(2014)**.

[9]   N.A. Bunaciu, E.G. Udristioiu, H.Y. Aboul-enein, Anal. Chem., 45, 289, **(2015)**.

[10] Bob B. He, Two-Dimensional X-ray Diffraction, 2nd Edition, John Wiley & Sons, Inc. USA, **(2018)**.

[11] V. Petkov, Mater. Today, 11, 28, **(2008)**.

[12] C.C. Vidyasagar, Y.A. Naik, T.G. Venkatesh, R. Vishwantha, Powder Technol., 214, 337, **(2011)**.

[13] M. Jurczyk, Handbook of Nanomaterials for Hydrogen Storage, Pan Stanford Publishing, Singapore, **(2018)**.

[14] I. Singh, R.K. Bidi, Appl. Surf. Sci., 257, 7592, **(2011)**.

[15] R.T. Ravichandran, A.R. Xavier, K. Pushpanathan, B.M. Nagabhushana, J. Mater. Sci. Mater. Electron., 27, 2693, **(2016)**.

[16]   N.S. Sabri, A.K. Yahya, N.A. Jani, M. Kamal, Inter. J. Inst. Mater. Malaysia, 1, 107, **(2013)**.

[17]   K. Raja, P.S. Ramesh, D. Geetha, Spect. Acta Part A: Mol. Biomol. Spectroscopy, 131 185, **(2014)**.

[18]   S.S. Juliet, S. Ramalingom, C. Ravidhas, IOSR-J. Appl. Phys., 9, 32, **(2017)**.

[19]   Q. Ahsanulhaq, J.H. Kim, J.S. Lee, H.B. Jahn, Electrochem. Commun., 12, 475, **(2010)**.

[20]   B.J. Inkson, Materials Characterization Using Nondestructive Evaluation (NDE) Methods**,** 17, **(2016)**.

[21]   C.A. Andrei, Towards Efficient Photovoltaic Devices: Key Facts and Experiments on Dye-Sensitized Solar Cells, Cambridge Scholars Publishing, United Kingdom, **(2017)**.

[22]   Energy-dispersive X-ray Spectroscopy (http://en.wikipedia.org), **(2019)**.

[23]   A.U. Amid, A Beginners Guide to Scanning Electron Microscopy, Springer Nature, Switzerland, **(2018)**.

[24]   S. Honglong, Z. Guling, Z. Bin, L. Minting, W. Wenzang, Microscop. Res. Tech., 76, 643, **(2013)**.

[25]   M. Nehfeh, Fundamental and Applications of Nano Silicon in Plasmonics and Fullerines, Elsevier, **(2018)**.

[26]   R.O. Yathisha, Y.A. Nayaka, J. Mater. Sci., 53, 678, **(2018)**.

[27]   UV-Visible Spectroscopy, Royal Society of Chemistry (http://www.rsc.org/learn-chemistry/content/filerepository/CMP/00/001/304/UV-Vis), **(2009)**.

[28]   D. Sarkar, Nanostructured Ceramics: Characterization and Analysis, Taylor & Francis, New York, London, **(2019)**.

[29]   R. Viswanatha, Y.A. Nayaka, C.C. Vidyasagar, T.G. Venkatesh, J. Chem. Pharm. Res., 4, 232, **(2012)**.

[30]   U. Ozgur, Y.I. Alivov, C. Liu, S. Dogan, J. Appl. Phys., 98, 100, **(2005)**.

[31]   C. Ayadin, K. Zheng, I.S. Yahia, F. Yakuphanoglu, Opt. Laser Technol., 48, 447, **(2013)**.

[32]   C.G. Zoski, Hand Book of Electrochemistry, 1st Edition, Elsevier, Netherland, **(2007)**.

[33]   P. Chooto, Cyclic Voltammetry and Its Applications, Intech Open (www.intechopen.com), **(2019)**.

[34]   H. Kaur, Instrumental Methods of Chemical Analysis, Pragathi Prakashan, New Delhi, **(2008)**.

[35]   M. Mao, Q.S. Li, X.L. Zhang, G.H. Wu, C.G, Dai, Q.H. Song, Dyes Pigments, 141, 153, **(2017)**.

[36]   F. Lasnier, T.G. Ang, Photovoltaic Engineering Handbook, IOP Publishing, Thailand, **(1990)**.

Chapter 4
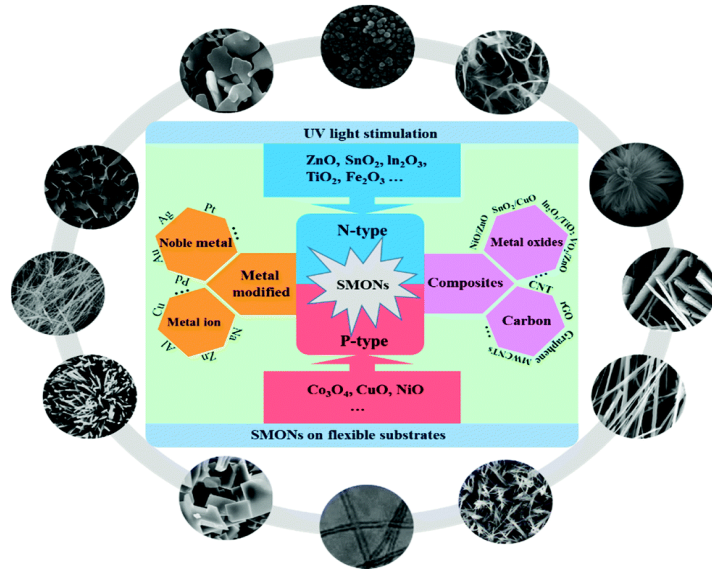
TRANSITION METAL DOPED SEMICONDUCTING NANOPARTICLES

Nanotechnology is an emerging field with its varied applications in science and technology for the manufacturing of new materials at the nanoscaled level. The development of nano-sized metal oxide semiconductors have attracted considerable attention because of their special properties such as large surface-to-volume ratio, electronic properties and unique optical properties as compared to bulk counter parts. Further, the properties of these materials are dependent upon their crystallite size, structure and surface conditions. These properties are achieved by variety of experimental methods as used in the synthesis of semiconducting metal oxide nanoparticles. Because of the extensive research, metal oxide likes zinc oxide (ZnO), tin oxide (SnO$_2$), copper oxide (CuO), cadmium oxide (CdO), titanium oxide (TiO$_2$), zinc sulphide (ZnS), indium oxide (In$_2$O$_3$) nanoparticles both in pure and doped forms have been investigated in the recent years. In addition, these metal oxide semiconductors are the key factor for various energy harvesting related technologies included dye sensitized solar cells, solid oxide fuel cells, Li-ion batteries and photo-catalysis (due to photo-stability and biocompatibility properties). Therefore, in this chapter the synthesis, characterization and properties of ZnO, Cr-ZnO, CuO, Zn-CuO, CdO, Ni-CdO, TiO$_2$, Cr-TiO$_2$, MgO and Zn-MgO nanoparticles were discussed in details. This chapter is sub-divided into chapter 4.1 to 4.7.

4.1. Structural, Optical and Electrical Properties of ZnO and Cr-ZnO Nanoparticles

4.1.1. Introduction

Zinc oxide (ZnO) is an important n-type semiconductor nanoparticle, which shows unique optical and electronic properties due to its wide bandgap of 3.37 eV and the large exciton binding energy (60 eV) at room temperature [1]. Moreover ZnO is a commercially available material with the advantage of non-toxicity, low-cost, high chemical stability and environmental friendly [2]. Because of these properties, ZnO nanoparticles possess many interesting applications in transparent conductive coatings [3], electrode materials for dye-sensitized solar cells [4], gas sensors [5] and electro-photo luminescent materials [6].

Doping of various transition metal ions such as Cu^{2+}, Ni^{2+}, Cd^{2+}, Mn^{2+} and Cr^{3+} offers feasible means of tuning physical properties, especially optical, electrical and magnetic properties with suitable applications. Among these metal ions, chromium has been used to enhance the optical properties, magnetic properties and luminescent properties of ZnO [7]. Chromium Oxide is the one of the important semiconductor, which exists in different phases of chromium oxide, such as Cr_2O, CrO, Cr_3O_4, Cr_2O_3, CrO_2, Cr_8O_{11} and CrO_3. Among these, Cr_2O_3 is the most stable phase under normal conditions. Amorphous and polycrystalline Cr_2O_3 has got an increasing interest in a wide variety of applications, such as solar absorber for thermal collectors, protective coating layers, various catalytic systems [8]. Hence, it is possible to modify the conducting properties of ZnO upon doping with Cr.

In this chapter, the synthesis of hexagonal prism shaped ZnO and Cr-ZnO $(0.00 \leq x \leq 0.15)$ using microwave combustion method. The main goal of this work is to discuss the consequence of Cr doping on crystal structure and morphology, optical properties and electrical properties with the help of X-ray diffraction studies (XRD), Field emission scanning electron microscopy (FE-SEM), Transmission electron microscopy (TEM), UV-Visible spectroscopy (UV-Vis) and I-V characterization technique.

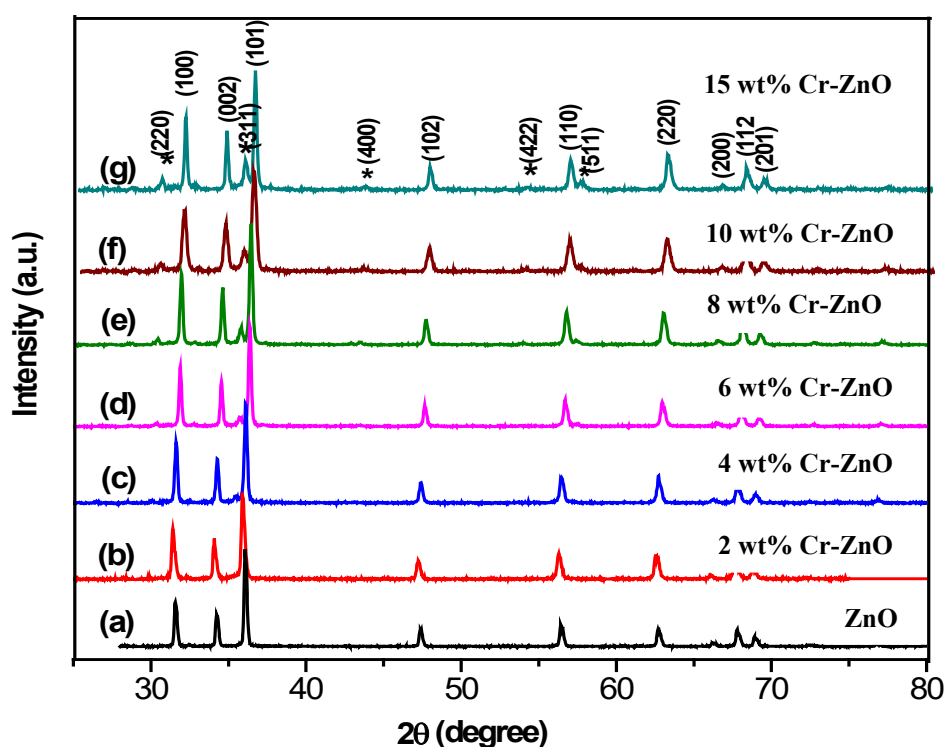### 4.1.2. Results and discussion

4.1.2.1. XRD analysis

Figure 4.1.1. XRD pattern of ZnO and Cr-ZnO $(0.00 \leq x \leq 0.15)$ calcinated at 500 °C. (*) represents the secondary phase i.e. Spinel $ZnCr_2O_4$.

Figure 4.1.1 shows the powder XRD patterns of synthesized ZnO and Cr-ZnO nanoparticles. The figures indicated phase purity and structural parameters of ZnO and Cr-ZnO ($0.00 \leq x \leq 0.15$). All the diffraction peaks could be indexed to hexagonal structure of ZnO, which further confirmed from the JCPDS No.79-0208 ($a = 0.3264$ nm and $c = 0.5219$ nm) and no peaks corresponds to chromium phase was detected upto 2 wt% doping of Cr. However, further increase in Cr concentration (above 2 wt %) some additional peaks corresponding to Cr phase were observed. These additional peaks were attributed to (220), (311), (400), (422) and (511) planes of secondary phase $ZnCr_2O_4$. This obviously shows that the incorporation limit for Cr in ZnO is below 4 wt%. At higher concentration of Cr (greater than 2 wt%) the probable residence of some Cr atom on octahedral interstitial site would increase and results in the formation of secondary phase $ZnCr_2O_4$ [9]. In addition, diffraction model displayed that Cr-ZnO peaks were widened as compared to ZnO peaks and the widening was found to be dependent on the Miller indices of the crystal plane. For our synthesized samples, the Bragg's reflection plane (002) is narrower as compared to (100) plane, which in turn is broader than (101) peak. This clearly indicated the presence of asymmetry in the crystalline shape and synthesized materials are in the nanometre range [10]. To confirm the probable incorporation of Cr instead of Zn in Cr-ZnO, the shift of angle (2θ) for the ZnO along (100) and (002) planes as a function of doping was observed (Figure 4.1.2 (a)). The peaks position was first slightly shifted towards lower angle (left) as Cr doping content increased from 0 to 2 wt% and on further doping of Cr, the peaks positions were slightly shifted towards higher angle (right). The variation in the diffraction angle shows that the microstructure and crystallite size are affected by Cr doping. Moreover, the intensity of XRD peak (100) was increased for doped sample upto a concentration of 2 wt% of Cr and above 2 wt% but below 8 wt% of Cr, FWHM found to be narrowed down with an

increase in intensity. Above 8 wt% of Cr doping in to ZnO lattice resulted in an increase in FWHM. This shown that, noticeable changes in lattice parameter *a*, but observable decreases in lattice parameter '*c*' [11].
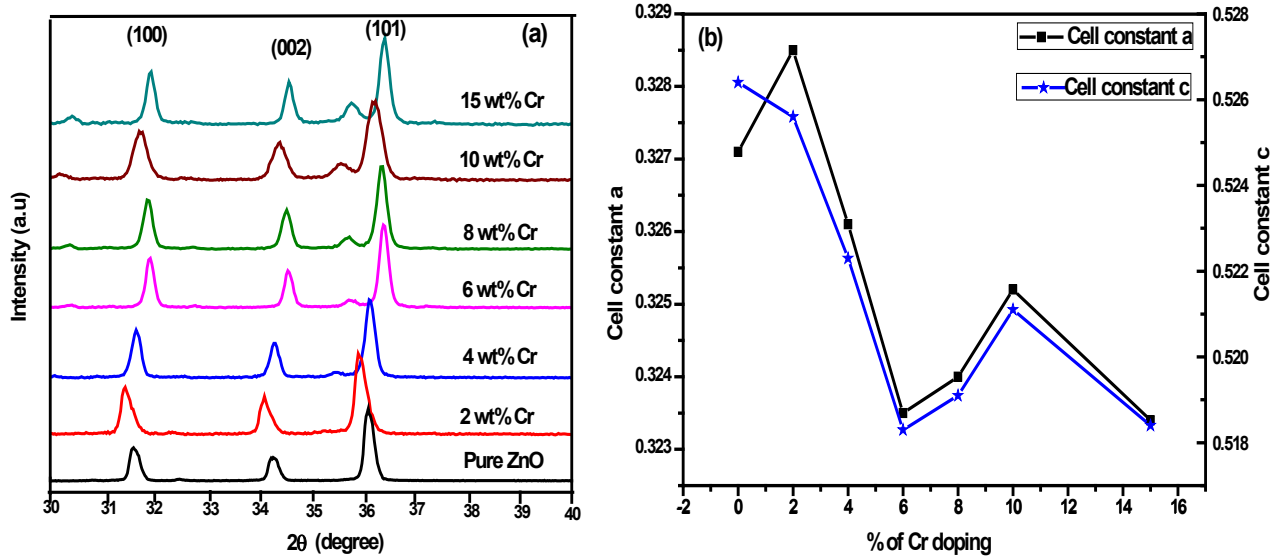

Figure 4.1.2: **(a)** Shifting of peak position of ZnO and $Zn_{1-x}Cr_xO$ $(0.00 \leq x \leq 0.15)$ nanoparticles. **(b)** The change in the cell constants *a* and *c* of ZnO with different Cr concentrations.
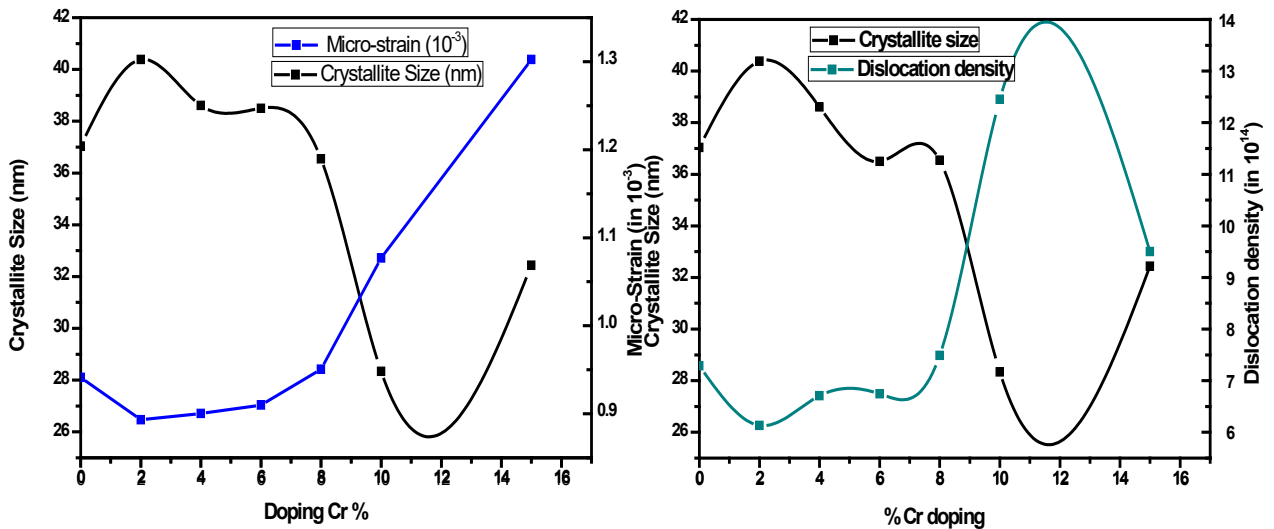

Figure 4.1.3: Dislocation density, micro strain and crystallite size of undoped ZnO and Cr-ZnO $(0.00 \leq x \leq 0.15)$ calcinated at 500 °C.

Figure 4.1.2(b) shows that the lattice parameters '*a*' and '*c*' have no systematic variation with increase in Cr content. This is due to mismatch in ionic radius between Zn^{2+} and Cr^{3+}. However, the *c*/*a* ratio of unit cell parameters reveals the hexagonal structure of ZnO which is not affected by Cr doping [12].

Figure 4.1.3 depicts the relations between dislocation density, micro-strain and crystallite size for undoped and Cr-ZnO nanoparticles, which are calculated from the XRD data. This revealed that the dislocation density is directly proportional to micro-strain and inversely proportional to crystallite size, i.e., for all the samples, as the dislocation density was increased simultaneously in the micro-strain and decrease in crystallite size or vice-versa [13]. The calculated values of crystallite sizes, dislocation density and micro-strain of ZnO and Cr-ZnO are tabulated in Table 1.

Table 1. Lattice constant, cell volume, average crystallite size and micro-strain of ZnO and Cr-ZnO nanoparticles

Property	ZnO	2% Cr	4% Cr	6% Cr	8% Cr	10% Cr	15% Cr
a (Å)	3.271	3.285	3.261	3.235	3.240	3.252	3.234
c (Å)	5.264	5.256	5.223	5.186	5.191	5.211	5.184
Cell volume (Å)^3	48.789	49.118	48.099	47.000	47.190	47.724	46.952
Average Crystallite size (nm)	37.04	40.38	38.61	38.50	36.54	28.34	32.44
Micro-strain (ε) in x 10^{-3}	9.9412	0.8932	0.9002	0.9100	0.9507	1.0769	1.3024
Dislocation density in x 10^{14}	7.28888	6.1329	6.7081	6.7465	7.4896	12.4509	9.5025

4.1.2.2. FE-SEM and EDAX analysis

The surface morphologies of undoped ZnO and doped $Zn_{1-x}Cr_xO$ ($0.0 \leq x \leq 0.15$) nanoparticles are shown in Figure 4.1.4(a-f). Figure 4.1.4(a) shows the surface morphology of undoped ZnO nanoparticles. It has a hexagon-prism like structure with uneven grain size of ~ 30-66 nm and having a better crystalline quality. The doping of 2 wt% of Cr, ZnO nanoparticles were turned into hexagon like structure. On further doping of Cr to 4-8 wt% in the Cr-ZnO lattice resulted in the mixture of hexagon and needle like structure. This shows that the needle like structure of secondary phase was developed on the surface of ZnO. However, some rods like structures were appeared at 10-15 wt% of Cr doping. The decrease in the crystallite size is attributed to the suppression of nucleation and subsequent growth of ZnO nanoparticles upon Cr doping, while increase in the grain size was due to the secondary phase formation [14]. Figure 4.1.4(h) shows the EDAX spectrum of 8 wt% Cr-ZnO. The EDAX spectrum of 8 wt% of Cr-ZnO shows an evidence for the presence of Cr, Zn and O. The C and Al peaks in the spectrum are due to the carbon tape used on the copper grids [15] and the Au peaks are due to the gold coating deposited on the specimens for FE-SEM study [16].
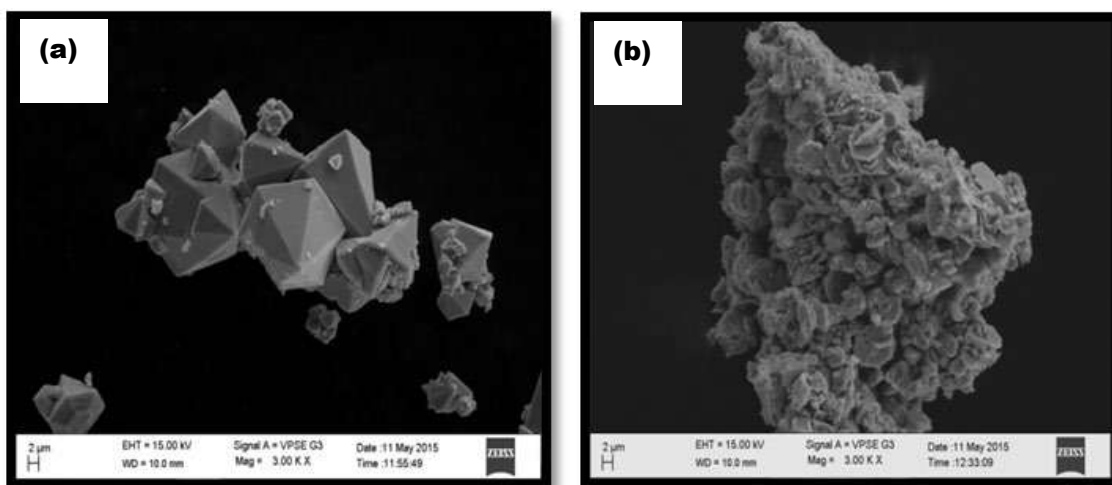
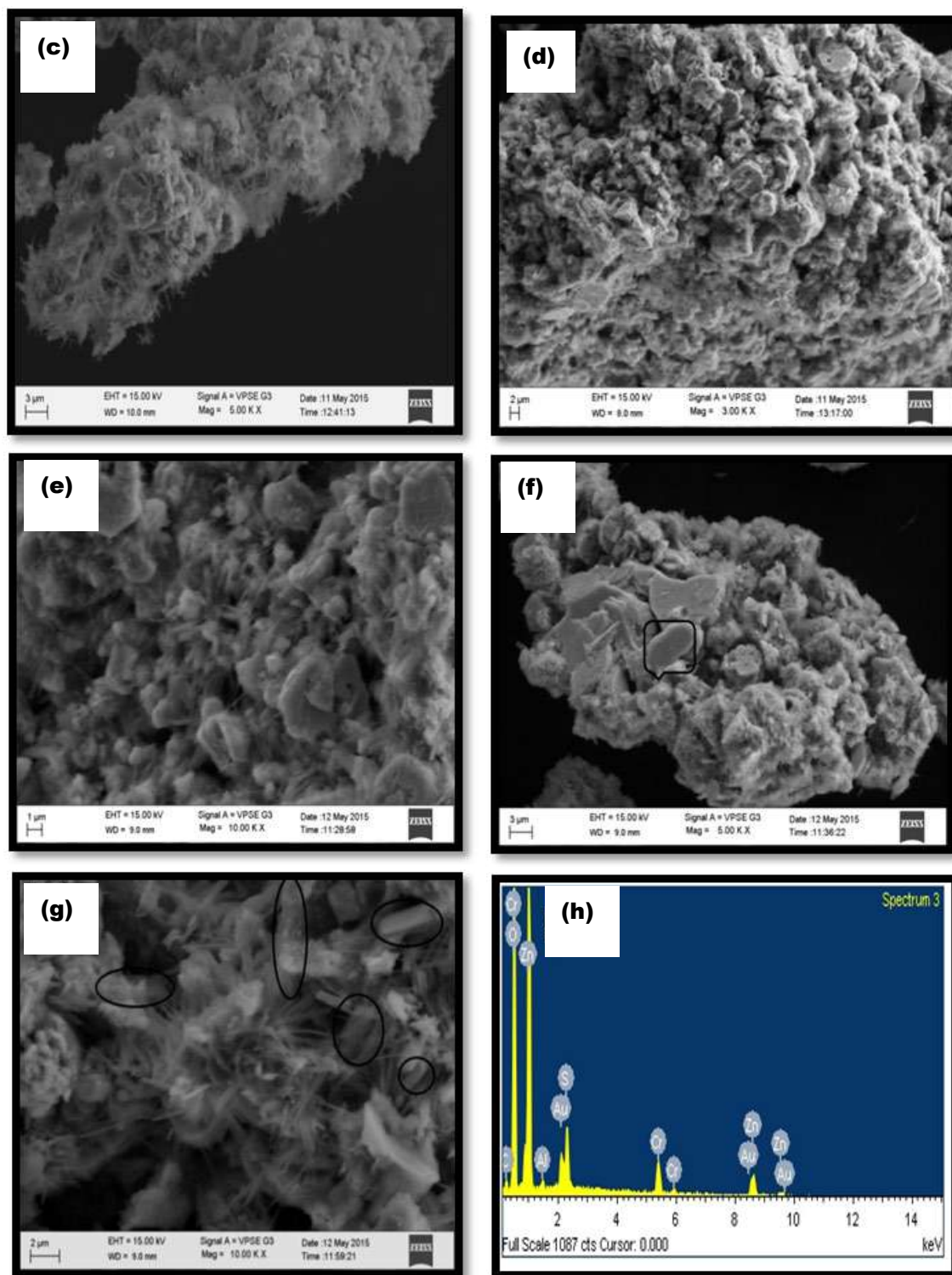**Figure 4.1.4:** FE-SEM images of (a) Undoped ZnO, (b) 2 wt% of Cr-ZnO, (c) 4 wt% of Cr- ZnO, (d) 6 wt% of Cr-ZnO, (e) 8 wt% of Cr-ZnO, (f) 10 wt% of Cr-ZnO, (g) 15 wt% of Cr-ZnO, (h) EDAX image of 8 wt% of Cr-ZnO.
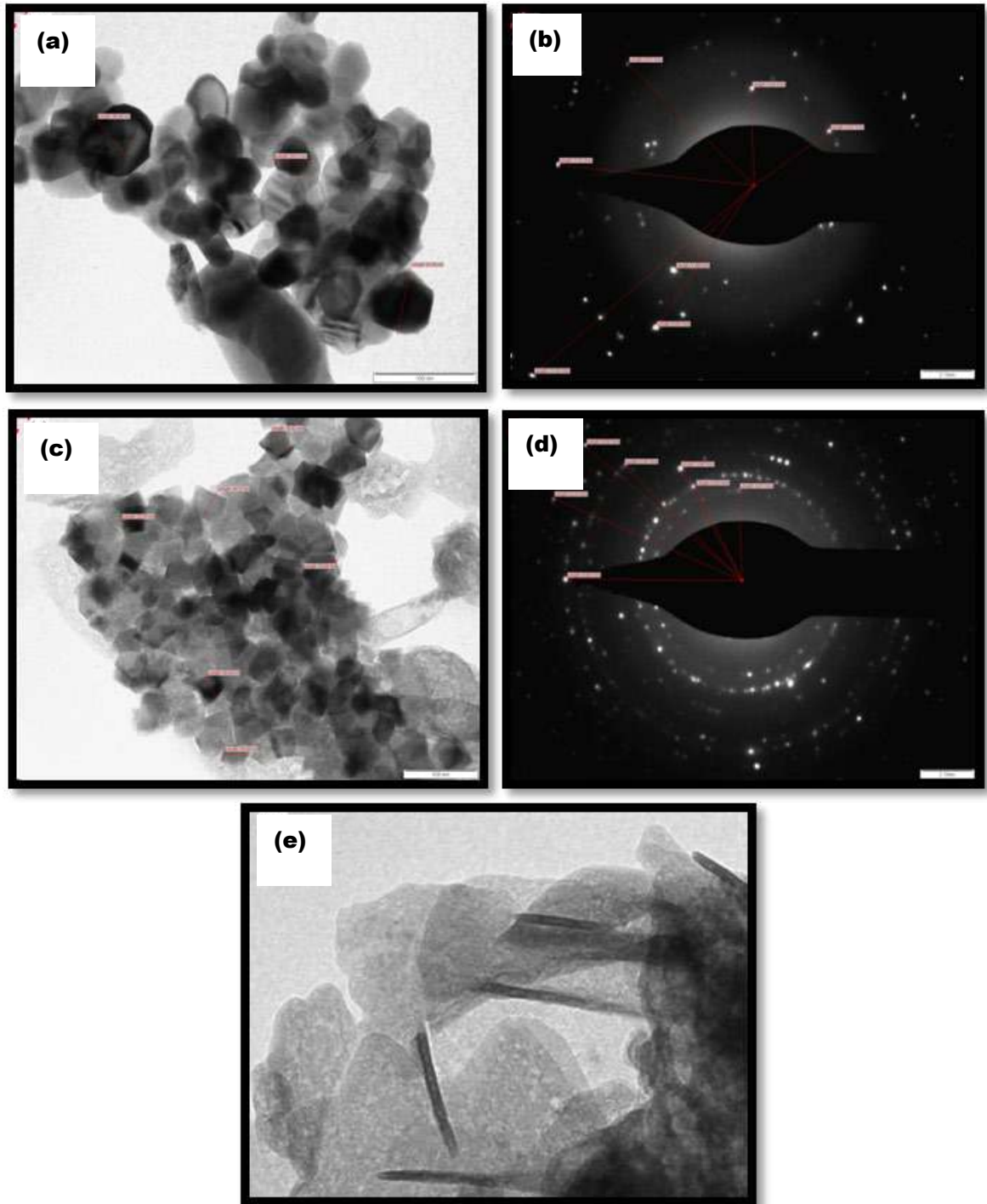
4.1.2.4. TEM analysis

Figure 4.1.5: TEM image and SAED pattern of undoped ZnO (a), (b), TEM image and SAED Pattern of Cr-ZnO (4 wt%) (c), (d) and TEM image of needle shaped secondary phase at 8 wt% of Cr-ZnO (e).

Figure 4.1.5(a-e) shows the TEM images and selected area of electron diffraction (SAED) patterns of the ZnO and Cr-ZnO (4 wt%) prepared by simple microwave combustion method and calcinated at 500 °C. The micrographs shows good crystalline nature and reveals particle size ranges from 38-62 nm for ZnO and 30-50 nm for Cr-ZnO. This is well matched with the crystallite size calculated from XRD using Scherrer formula [17]. The SAED patterns reveal the qualitative difference between the samples ZnO and Cr-ZnO. Figure 4.1.5(b) confirmed the formation of a well-defined single phase crystals and the wurtzite phase of ZnO. Figure 4.1.5(d) clearly demonstrated the polycrystalline type ring structure, which confirms the formation of secondary phase at 4 wt% of Cr-ZnO. TEM images also reveal the formation of hexagonal prism like structure. On doping of 4 wt% of Cr into ZnO lattice, there is no change in the shape of ZnO nanoparticles but needle like structure of secondary phase (i.e., Cr_2O_3) developed simultaneously on the surface of the ZnO as shown in the Figure 4.1.5(e). The formation of secondary phase has already been confirmed by the XRD pattern and SEM images of 4-15 wt% of Cr incorporated into ZnO lattice. TEM images of Cr-ZnO also confirmed the solubility of Cr in the ZnO lattice when the Cr content was below 4 wt% [18].

4.1.2.5. UV-Visible spectral analysis

The UV-Vis. absorption spectroscopy is one of the important tools used to study the optical properties and to examine the doping effects of the host metal oxide nanoparticles. Figure 4.1.6(a) shows the UV-Vis. spectra of doped and undoped ZnO nanoparticles with different concentration of Cr calcinated at 500 °C. This reveals the optical absorption edge of Cr-doped samples show a red shift compared undoped ZnO nanoparticles. Figure 4.1.6(b) shows the optical band gap of ZnO and Cr-ZnO was

calculated using Tauc plot method [(hv) v/s $(\alpha hv)^2$] [19]. Energy band gap can be obtained by extrapolating the linear part of the curves to the photon energy axis. The measured optical band gap E_g values were found to be 3.31 eV for ZnO, 2.82, 2.81, 2.80, 2.74, 2.80 and 2.81 eV for Cr-ZnO at different concentration of dopant. Since the decrease in the bandgap is due to the secondary electronic states which are formed by doping of Cr and from transition between partially forbidden valence band and conduction band [20]. The increase in the band gap can also be studied on the basis of Moss-Burstein effect. The fermi-level shifts close to the conduction band on increase in the carrier concentration. Then the low energy level of transition was prevented and increases the bandgap at 10-15 wt% [21].
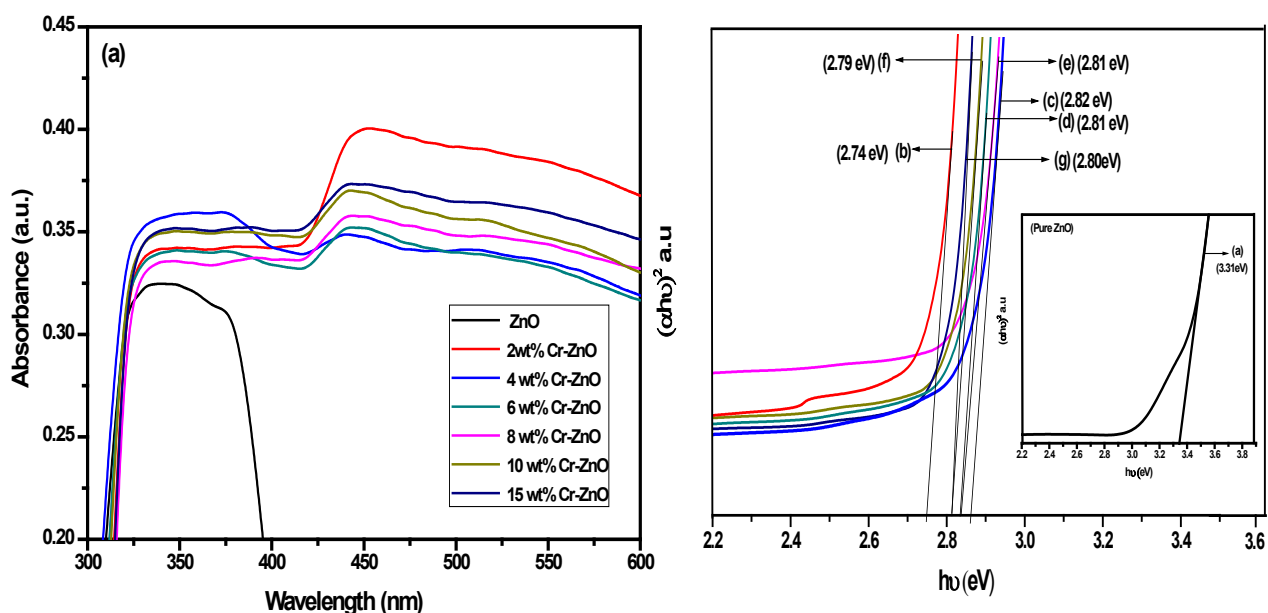

Figure 4.1.6: (a) UV-Vis spectra, (b) Tauc plot of undoped and Cr doped ZnO $(0.0 \leq x \leq 0.15)$ nanoparticles.

4.1.2.6. Electrical properties of ZnO and Cr-ZnO nanoparticles

The I-V characteristics studies of ZnO and Cr-ZnO nanoparticles have been carried out using silver paste to make good electrical contact. Figure 4.1.7(a-b) show the

I-V characteristics of ZnO and Cr-ZnO under the dark and UV-light condition. The electrical conductance and resistance are the two important parameters to investigate the function of ZnO and Cr-ZnO nanoparticles [22]. From these curves, it can be seen that the pure ZnO nanoparticles show poor conductivity in the dark condition. This is due to the effect on the mobility of charge carriers present in the grain boundaries. These boundaries act as dissemination sites and potential walls which lead to reduce the carrier mobility by increasing resistance and decreasing the current intensity [23]. The resistivity was decreased by doping of Cr into ZnO lattice (2-8 wt%). In the case of doping, the replacement of Zn by Cr which introduces the large number of electrons in the doped samples, thereby increase in the charge carriers. Thus increases the current intensity of doped nanoparticles. However, with further incorporation of Cr in to ZnO lattice the resistivity was increases results in the segregation of Cr takesplace in the grain boundaries or interstices. Moreover, at higher doping concentration of Cr the neutral defects may be observed. So these defects neutralize the excess charge carriers. This may enhance the resistivity [24]. Under suitable condition, the UV-light illuminated on the prepared samples of ZnO and Cr-ZnO increases the current intensity due to increase the mobility of charge carriers. Which is significantly improves the current intensity and decreases the resistivity of the pure and Cr-ZnO nanoparticles [25]. In the present work, I-V curves were analyzed simultaneously with the optical band gaps for the synthesized samples. This shows the significant relationship between the variation of resistance and current intensity of the pure ZnO and Cr-ZnO nanoparticles. The remarkable increase in the current intensity by these samples may results in higher efficiency of the solar cells [26].
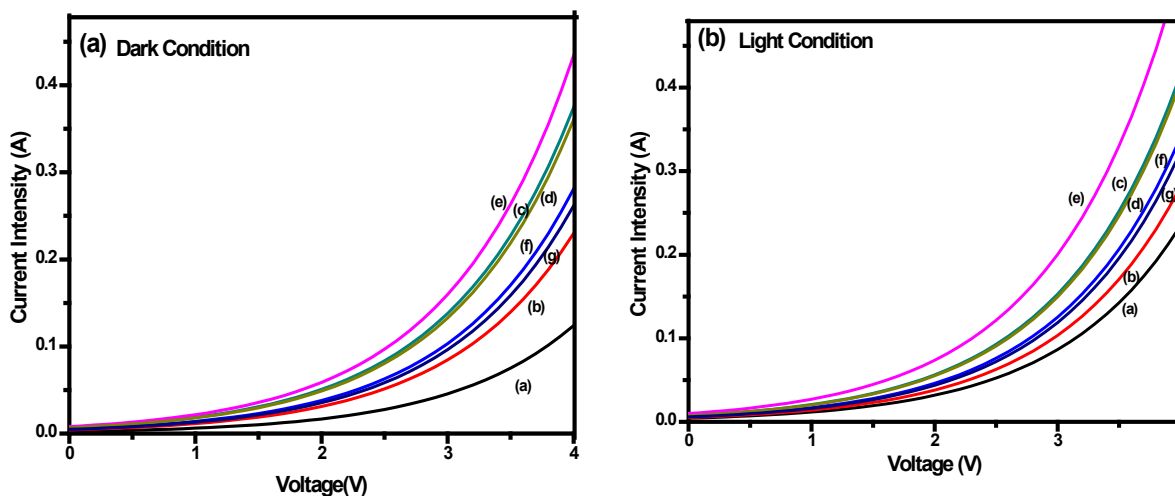
Figure 4.1.7: I-V characteristics of undoped ZnO and Cr-ZnO in dark (a) and UV-light (b) conditions.

4.1.3. Conclusions

In this study, a simple microwave combustion method was used to synthesize pure ZnO and Cr-doped ZnO nanoparticles. The effect of Cr doping on the structure, optical and electrical properties of ZnO were studied. The particle size of the synthesized nanoparticles was found to be ~ 30-66 nm. The SEM and TEM analyses were showed that the crystal structure of ZnO and Cr-ZnO. The optical properties of synthesized nanoparticles were studied by measuring of band gap energy. This reveals that with increasing the doping concentration of Cr upto 8 wt%, the band gap edge shifted to longer wavelength region. The I-V characteristics of the ZnO and Cr-ZnO nanoparticles in dark and under UV-light illumination showed that, the band gap of ZnO found to be decreased with increase in Cr content upto 8 wt%. Therefore estimated optical band gap energy, conductance, resistance are also very useful for application of Cr-ZnO in the solar cells and optical devices. The proposed microwave method is simple, easy to operate, less time consuming and inexpensive.

4.2. Structural, Optical and Electrical Properties of CuO and Zn-CuO Nanoparticles

4.2.1. Introduction

Copper oxide (CuO) is an important semiconducting transition metal oxide with a monoclinic crystal structure and it has been studied as a p-type semiconducting metal oxide with a bandgap of 1.7 eV [27]. The CuO is being used as a novel material because of the ease of availability of raw materials, low processing cost, non-toxic nature, excellent thermal stability, good optical and electrical properties [28]. The unique physical, chemical and electrical properties of CuO nanoparticles has many potential applications in the fields of photo catalyst [29], batteries [30], gas sensing [31], solar cells [32] and biosensors [33]. It has been highlighted that the crystal shape and size are the two important considerations to control the optical and catalytic properties of CuO nanoparticles.

The doping is used to modify the optical and electrical properties of the host material by the addition of impurity ions into the lattice of the host material. Currently, an extensive research has been carried out to investigate the effect of doping elements such as $Ni^{2+,}$ $Co^{2+/3+}$, Zn^{2+}, Cd^{2+}, $Cr^{2+/3+}$ and $Fe^{2+/3+}$ on the electrical, optical and magnetic properties of CuO nanoparticles. Of all the transition metal ions, Zn^{2+} causes more effective doping with CuO since the ionic radius of Zn^{2+} (0.60Å) and Cu^{2+} (0.57 Å) are similar to each other. Hence Zn^{2+} ion can be easily incorporated into the CuO lattice without destroying the crystal structure [34]. The conducting property of the nanomaterials depends upon the energy gap or band gap between the valence band and conduction band. It is possible to modify the conducting properties of CuO upon doping with Zn.

In this chapter, the synthesis of CuO and Zn-CuO nanoparticles (0.00 ≤ x ≤ 0.10) via microwave combustion method has been reported. The main goal of this work was to study the consequences of Zn doping on crystal structure, optical and electrical properties of CuO. The synthesized CuO and Zn-CuO nanoparticles were characterized with the help of X-ray diffractometry (XRD), Field emission scanning electron microscopy (FE-SEM), Transmission electron microscopy (TEM), UV-Visible spectroscopy (UV-Vis.) and Photoconductivity techniques. The obtained results were discussed in terms of optical and electrical properties in correlation with crystal shape and size.

4.2.2. Results and discussion
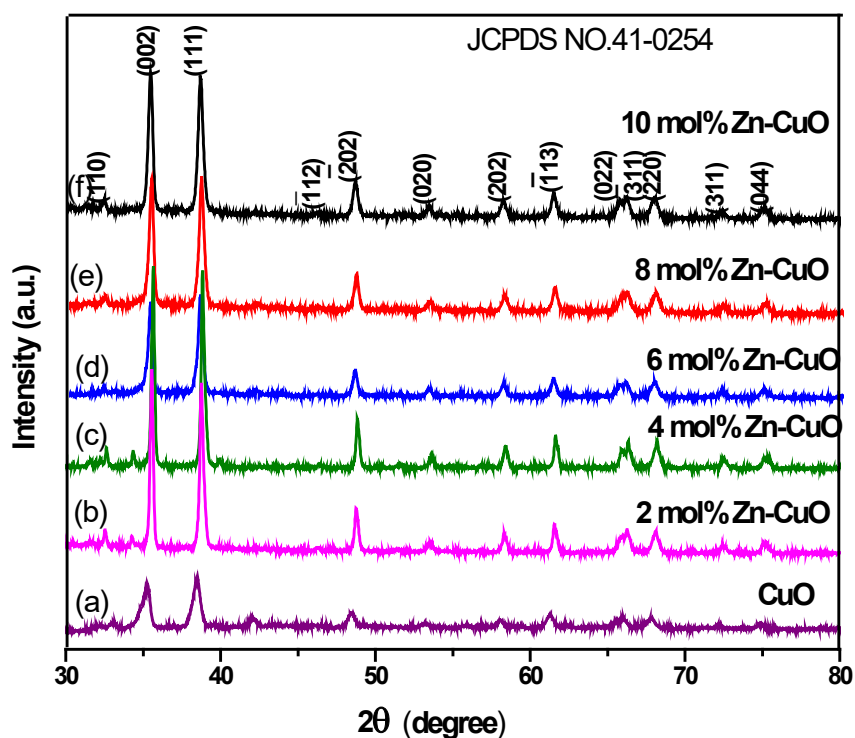
4.2.2.1 XRD analysis

Figure 4.2.1: X-ray diffraction pattern of CuO and Zn-CuO (0.00 ≤ x ≤ 0.10) nanoparticles calcinated at 600 °C.

The Figure 4.2.1 displays X-ray diffraction pattern (XRD) of the CuO and Zn-CuO nanoparticles. The figure shows the phase purity and structural parameters of CuO and Zn-CuO nanoparticles ($0.00 \leq x \leq 0.10$, where 'x' represents molar concentration of dopant). The result shows a typical diffraction peaks at $2\theta = 32.52°$, $35.45°$, $38.76°$, $48.76°$, $53.50°$, $58.31°$, $61.56°$, $66.25°$, $68.12°$, $72.42°$ and $75.25°$, which correspond to (110), (002), (111), ($\bar{2}$02), (020), (202), ($\bar{1}$13), (311), (220), ($\bar{3}$11) and (044) Bragg's reflection planes of monoclinic (Tenorite) crystalline CuO (C_2/c symmetry group) according to JCPDS file no: 41-0254. A careful analysis of diffraction pattern shows that there is no trace of Zn related phases (metallic zinc, zinc oxide or binary zinc copper phases) or clusters for all Zn-CuO samples. This suggested that the dopants are well-integrated into the CuO lattice sites during the growth process. But the peak appeared in the 2θ range 40-45° may be attributed to the hydrated CuO according to JCPDS no. 42-0746. The appearance and disappearance of the peak positioned between 40-45° may be due to poorly differentiated (122) plane in the doped samples [35]. The CuO peaks were found to be broader as compared to Zn-CuO peaks. The diffraction plane (202) was narrower than (002) plane, and (002) in turn was narrower than (111) plane. This clearly indicated the existence of asymmetry in the crystalline shape and synthesized materials were in the nanometre range [36]. To confirm the substitution of Zn^{2+} ions in place of Cu^{2+} ions in Zn-CuO nanoparticles, the shift of angle (2θ) along major (111) and (002) diffraction planes as a function of doping was observed. These data reveals that, the positions of peaks slightly shifted towards the right side upto

4 mol% of Zn and on further increase in the doping percentage, the peaks were slightly shifted towards the left side of the graph. The deviation in the diffraction angle indicated that the microstructure and crystallite size of Zn-CuO nanoparticles are dependent on the percentage of Zn doping. Also, with increase in Zn content upto 4 mol% the peak intensity of (111) and (002) planes has been increased and above 4 mol% of Zn in CuO lattice has resulted in the broadening of FWHM with a subsequent decrease in the peak intensity [37]. The lattice parameters for CuO and Zn-CuO were calculated from XRD data. It reveals that, there is no linear dependence of the lattice parameters with the concentration of Zn content [38]. This can be explained on the basis of the replacement of larger ionic radius Zn^{2+} ion (0.60 Å) with smaller ionic radius Cu^{2+} ion (0.57 Å) [39].
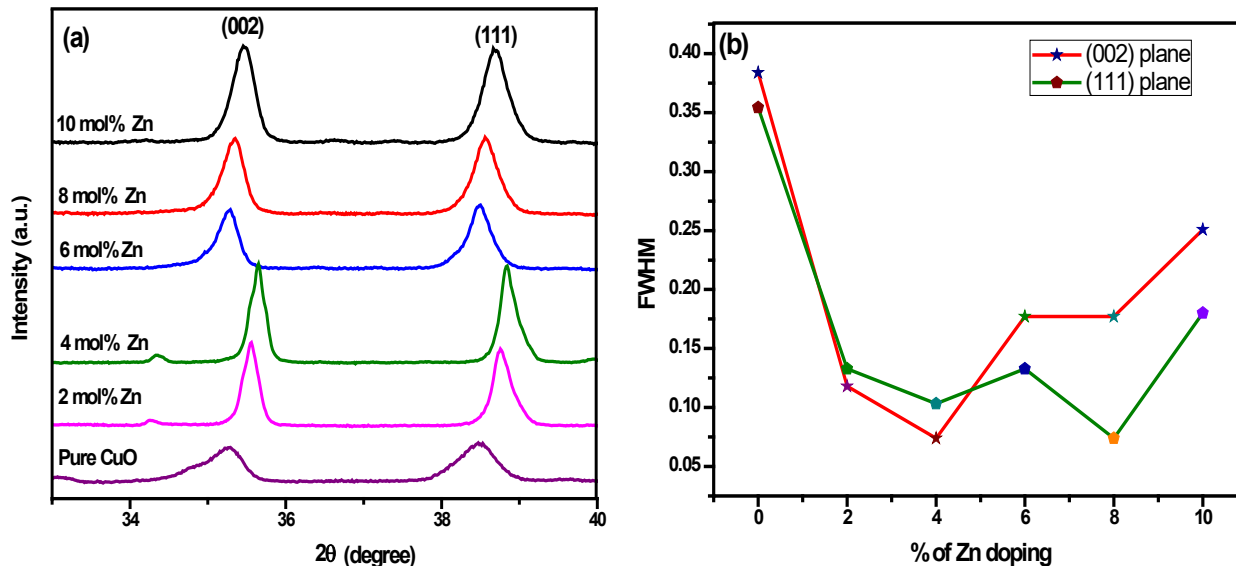

Figure 4.2.2: (a) The shift of peak position of CuO and Zn-CuO (0.00 ≤ x ≤ 0.10) nanoparticles, (b) The change in the FWHM of CuO with different Zn concentration.

Figure 4.2.2(b) shows the decrease in full width at half maxima (FWHM) for Zn-CuO nanoparticles as compared to pure CuO nanoparticles. This is due to the crystallite size induced or micro-strain induced reduction, since (111) and (002) peaks positions almost have changed as shown in Figure 4.2.2(a) [40]. Figure 4.2.3 clearly indicates that the micro-strain is directly proportional to the dislocation density and inversely proportional to the crystallite size. Dislocations are the irregularity in a crystal which arises due to the lattice mismatch from one part of the crystal to another part. In this case, the dislocation densities were found to vary along with micro-strain as shown in Figure 4.2.3(a) and 4.2.3(b) [41]. The crystallite size (D), dislocation density (δ) and micro-strain (ε) of CuO and Zn-CuO nanoparticles were calculated and are given in Table 2.

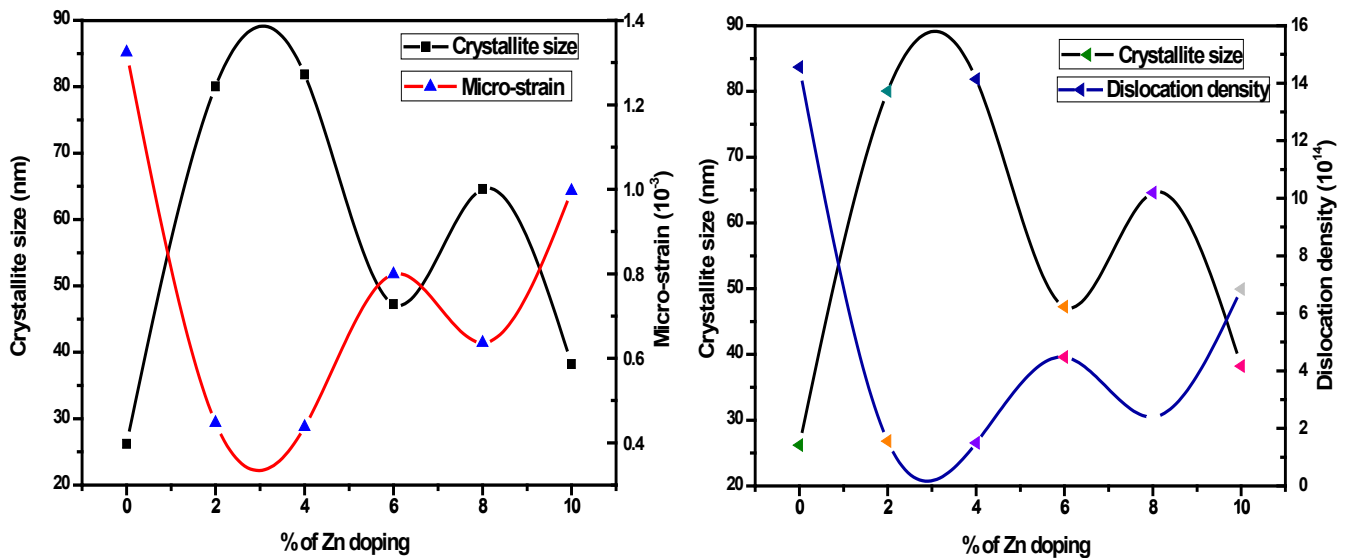**Figure 4.2.3:** Inter-relation between crystallite size, micro-strain and dislocation density of CuO and Zn-CuO (0.00 ≤ x ≤ 0.10) nanoparticles calcinated at 600 ºC.

Table 2. Calculated values of lattice parameters, cell volume, average crystallite size, micro-strain and dislocation density

Property	CuO	$Cu_{0.98}Zn_{0.02}O$	$Cu_{0.96}Zn_{0.04}O$	$Cu_{0.94}Zn_{0.06}O$	$Cu_{0.92}Zn_{0.08}O$	$Cu_{0.90}Zn_{0.10}O$
x (Å)	4.7174	4.6909	4.6807	4.7126	4.6968	4.7030
y (Å)	3.4321	3.4262	3.4204	3.4366	3.4270	3.4357
z (Å)	5.1465	5.1302	5.1265	5.1464	5.1282	5.1443
β (º)	99.693	99.522	99.500	99.628	99.552	99.596
Cell volume $(Å)^3$	82.1388	81.3164	80.9529	82.1748	81.3987	81.9590
Average crystallite size (nm)	26.21	80.04	81.83	47.24	64.57	38.23
Micro-strain (ε) in x 10^{-3}	1.3242	0.4475	0.4380	0.7992	0.6367	0.9965
Dislocation density(δ) in x 10^{14}	14.556	1.561	1.494	4.481	2.398	6.842

4.2.2.2. SEM and EDAX analysis
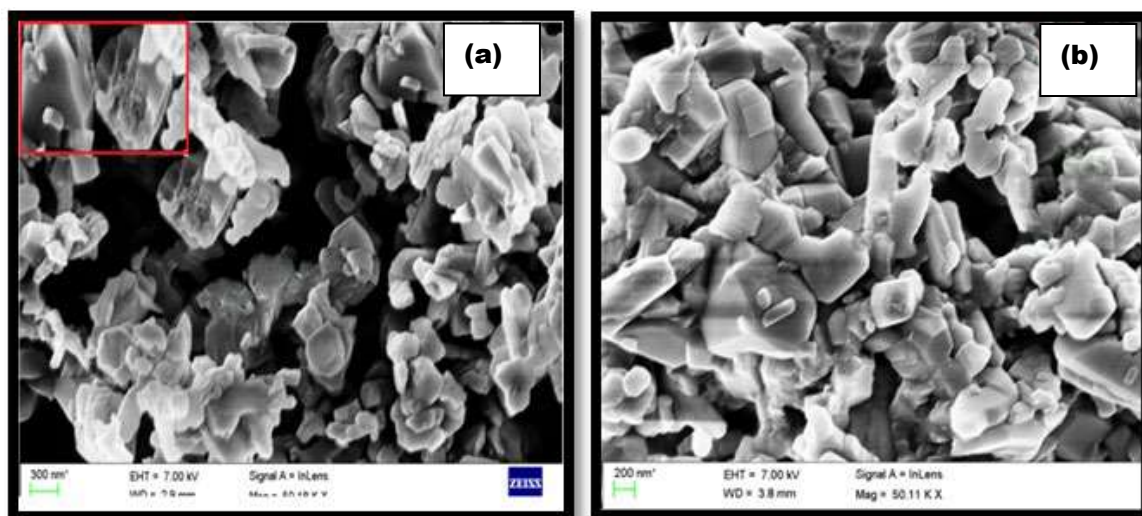
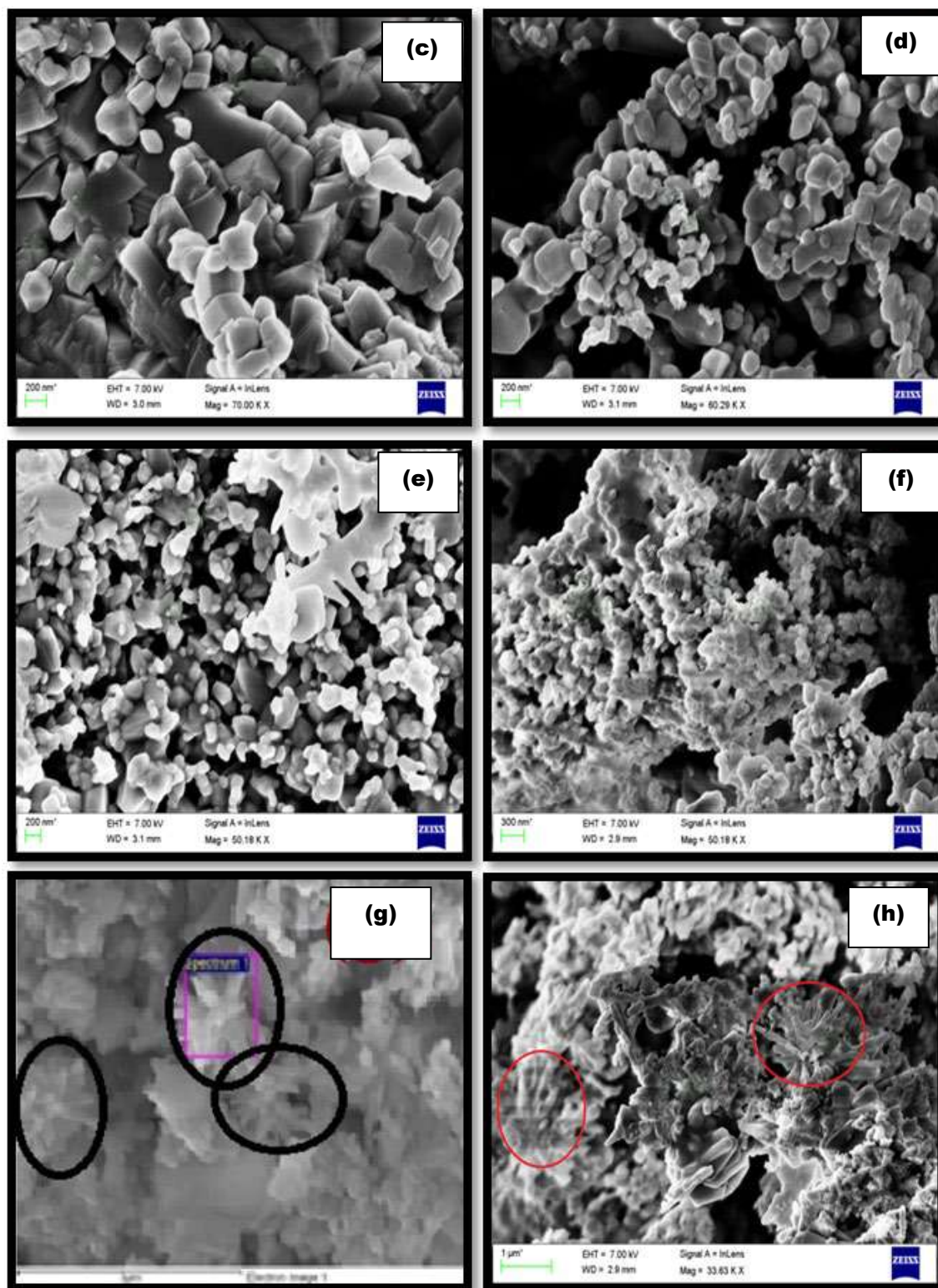**Figure 4.2.4:** FE-SEM images of (a) undoped CuO, (b) 2 mol% of Zn-CuO, (c) 4 mol% of Zn-CuO, (d) 6 mol% of Zn-CuO, (e) 8 mol% of Zn-CuO, (f) 10 mol% of Zn-CuO, (g) flower shaped agglomerated Zn-CuO nanoparticles at 8 mol% Zn, (h) flower shaped agglomerated Zn-CuO nanoparticles at 10 mol% Zn.

The morphological characteristics of CuO and Zn-CuO ($0.00 \leq x \leq 0.10$) nanoparticles are shown in Figure 4.2.4(a-h). Figure 4.2.4(a) shows FE-SEM photomicrograph of synthesized CuO nanoparticles. The image shows that the metal oxide has got a mixture of cubes and rod-like structures with an uneven grain size of 21-100 nm with a better crystalline quality. This is due to the anisotropic growth of monoclinic CuO crystal consisting of alternately arranged O^{2-} and Cu^{2+} ions along the specific directions [42]. In general, Zn doping does not have much influence on the morphology of CuO. But upon Zn doping, variation in the size of the CuO nanoparticles with the formation of elongated and small nanostructures have been observed. Figure 4.2.4(g-h) show the low magnification FE-SEM images of flower shaped Zn-CuO nanostructures. The XRD data revealed that the average size of the particles has been increased upto 4 mol% of Zn and on further increase in the concentration, the size of the particles was found to be varied irregularly due to the induction of micro-strain and lattice mismatch in the lattice [43]. This can also be observed in the SEM photomicrographs. Figure 4.2.5 shows the EDAX spectra of pure CuO and 8 mol% Zn-CuO nanoparticles. The EDAX analysis of Zn-CuO nanoparticles confirmed the presence of Zn in CuO lattice [44].
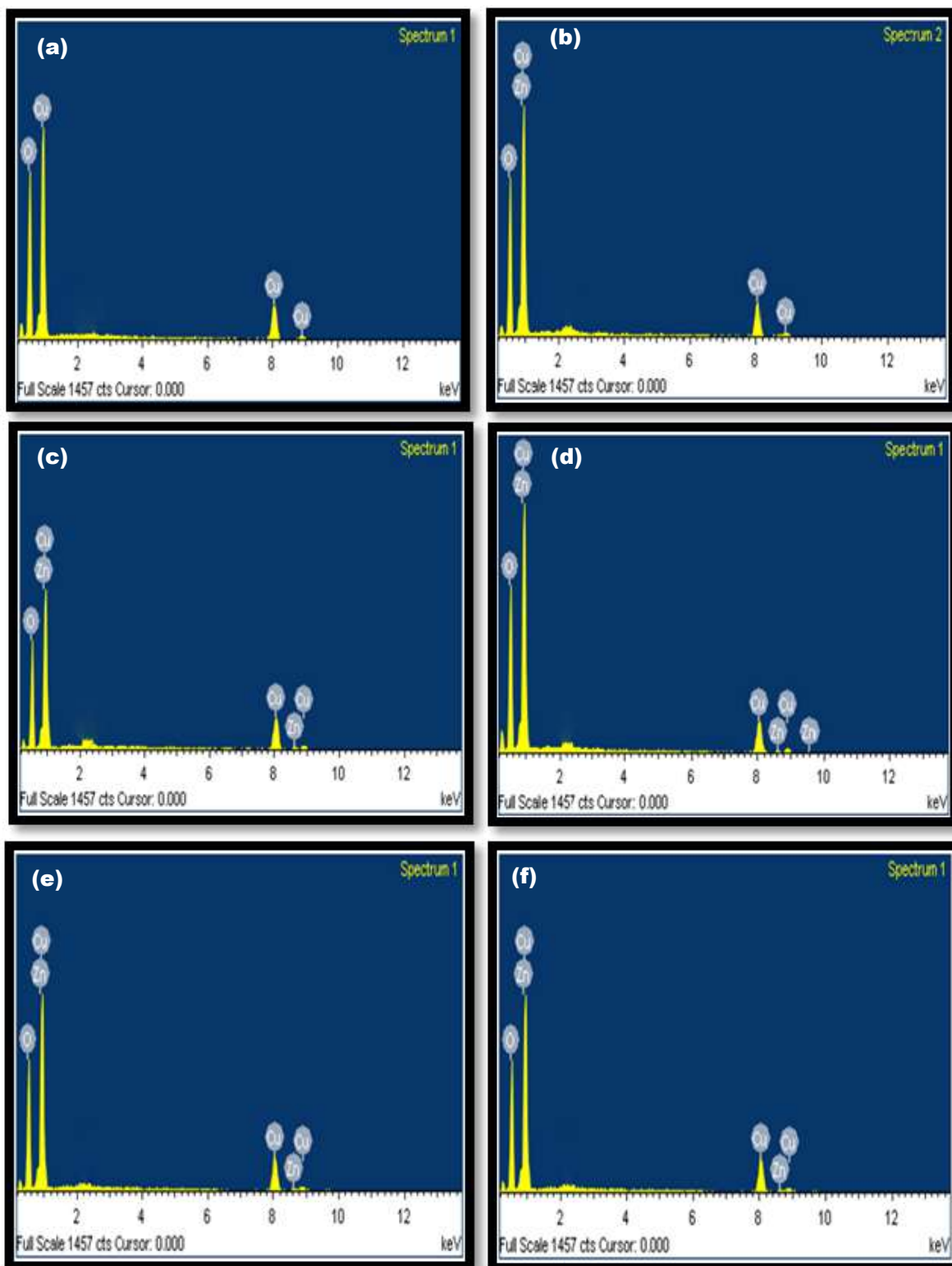
Figure 4.2.5: EDAX spectra of (a) undoped CuO, (b) 2 mol% of Zn-CuO, (c) 4 mol% of Zn-CuO, (d) 6 mol% of Zn-CuO, (e) 8 mol% of Zn-CuO, (f) 10 mol% of Zn-CuO.
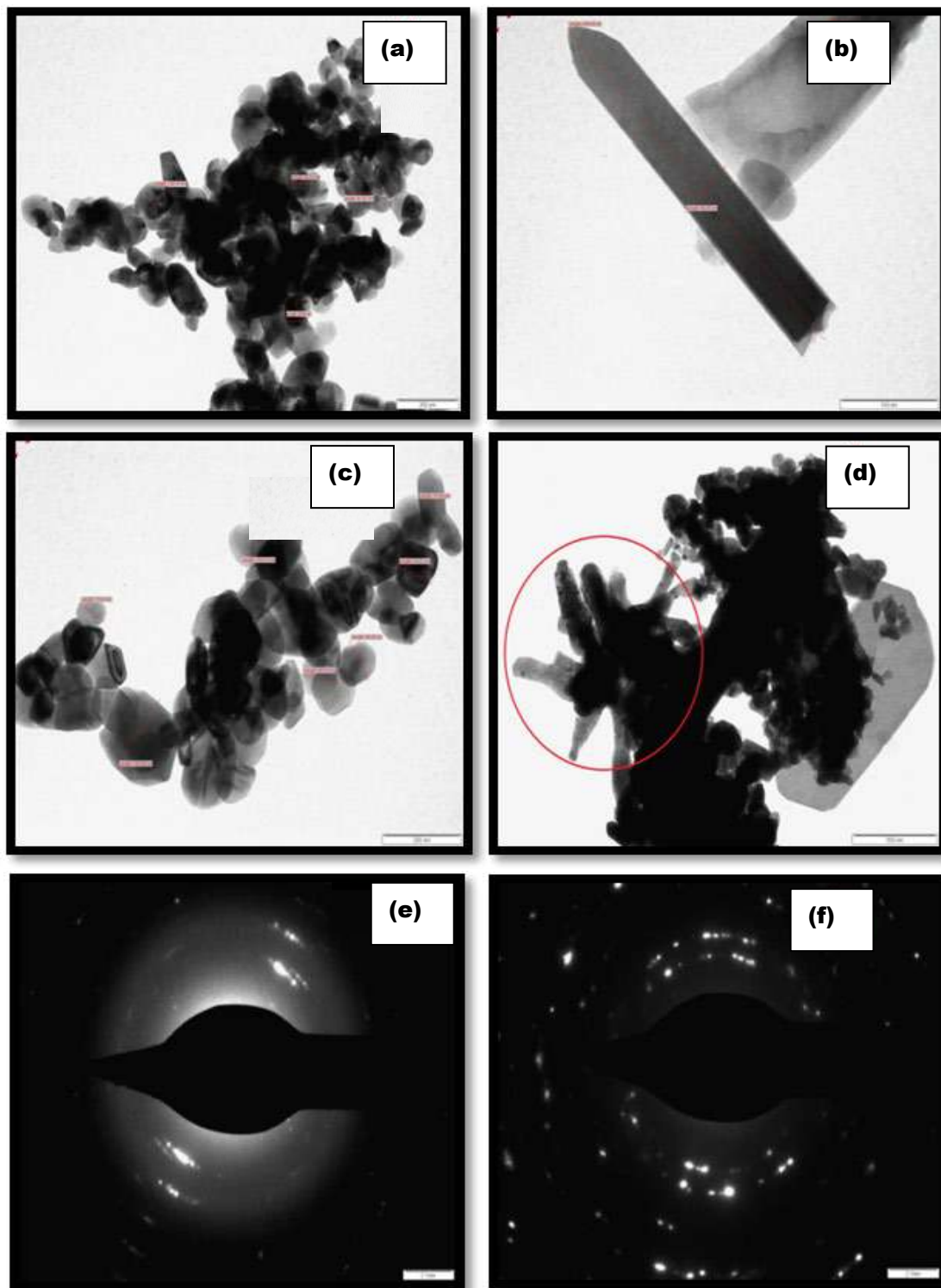
4.2.2.3. TEM analysis

Figure 4.2.6: TEM images and SAED pattern of undoped CuO and 8 mol% Zn-CuO nanoparticles calcinated at 600ºC.

Figure 4.2.6**(a-f)** show the transmission electron microscopic (TEM) images and selected area electron diffraction (SAED) images for CuO and Zn-CuO (8 mol% of Zn) nanoparticles synthesized via microwave combustion method and annealed at 600 ºC. Figure 4.2.6(a) and (c) show the cube-like structures of CuO and Zn-CuO nanoparticles with different particle size. Figure 4.2.6 **(b)** shows the rod-shaped CuO nanocrystals of length 386.45 nm and breadth 59.40 nm. For both CuO and 8 mol% Zn-CuO nanoparticles, the agglomeration of crystals has been observed. The extent of agglomeration is small in pure CuO as compared to 8 mol% of Zn-CuO nanoparticles. Figure 4.2.6 **(**d) shows the agglomeration of individual Zn-CuO nanoparticles forming flower-shaped nanostructures. The particles size have been calculated from TEM images and were found to be in the range of 30-100 nm for CuO and 71-186 nm for 8 mol% Zn-CuO nanoparticles [45]. The SAED pattern of CuO and Zn-CuO is shown in Figure 4.2.6**(e-f)**. The SAED pattern of CuO shows diffused rings, indicating that the synthesized material is polycrystalline in nature. On the other hand, SAED pattern of Zn-CuO confirmed the formation of well-defined single phase crystal with monoclinic structure. Hence, the results of SAED also support the experimental evidences observed from the XRD results [46].

4.2.2.4. UV-Visible spectral analysis

Figure 4.2.7 shows the optical properties of CuO and Zn-CuO nanoparticles. The UV-Vis. spectra have been recorded in the wavelength range 300-800 nm at room temperature. The absorption spectrum has been used to derive the optical bandgaps of CuO and Zn-CuO nanoparticles. The direct band gap of CuO nanoparticles has been found to be 2.31 eV. Upon doping of Zn upto 2-4 mol%, the optical absorption edge has

slightly shifted towards longer wavelength (2.17-2.12 eV) and on further increase in Zn content, the absorption edge has shifted towards shorter wavelength (2.21-2.25 eV). This attribution of absorbance mainly depends upon some of the factors like particle size, oxygen deficiency, lattice strain and thickness [47]. The optical band gap (E_g) of pure CuO and Zn-CuO is derived from the Tauc's formula, $(\alpha h\nu)^{1/n} = A (h\nu - E_g)$, where h is Planks constant (6.626×10^{-34} J s), A is an energy-independent constant, α is the absorption coefficient, E_g is the optical bandgap of valence and conduction band (eV) and *n* is determined the optical transition of semiconductor. On plotting the values of $(\alpha h\nu)^2$ versus $(h\nu)$, a better linearity has been observed for the direct transition (Figure 4.2.8). The band gap of Zn-CuO with different concentration of Zn was found to be 2.17, 2.12, 2.23, 2.21 and 2.25 eV for 2, 4, 6, 8 and 10 mol%, respectively [48].
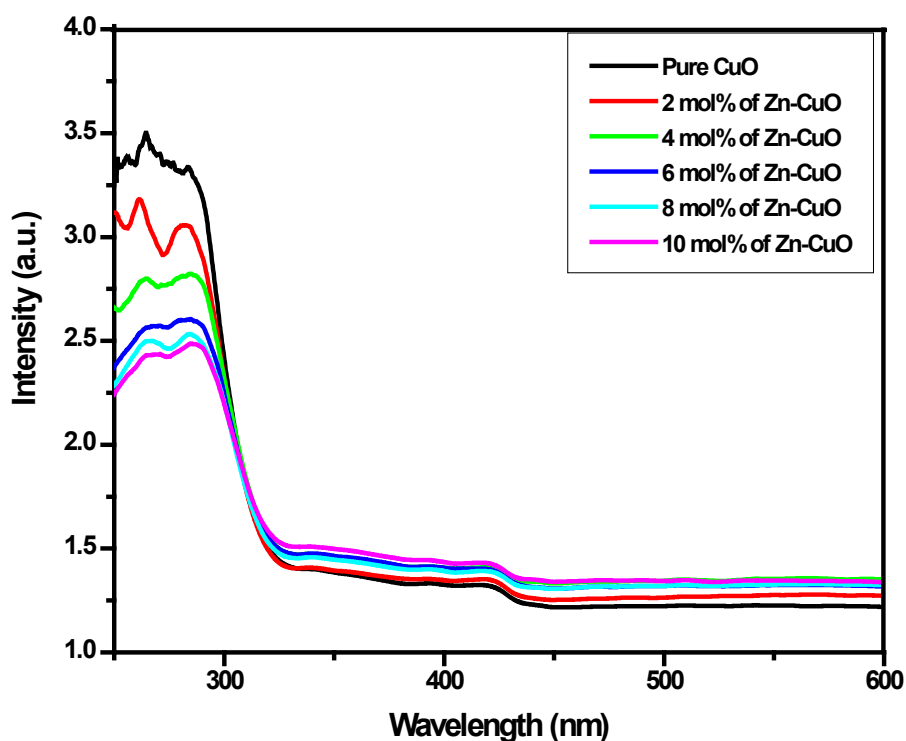

Figure 4.2.7: UV-Visible spectra of CuO and Zn-CuO ($0.00 \leq x \leq 0.10$) nanoparticles.
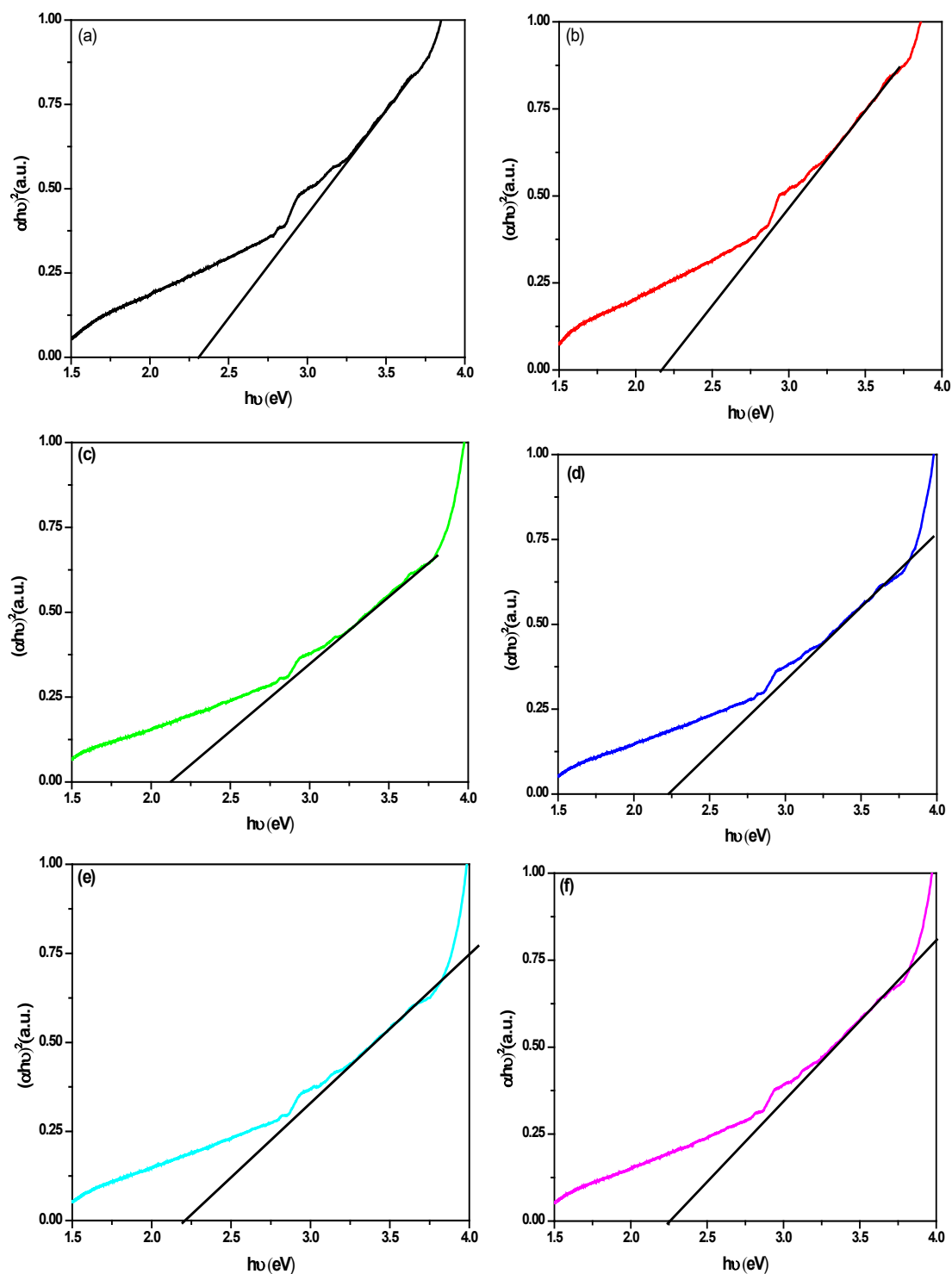
Figure 4.2.8: Tauc plot of (a) undoped CuO (b) 2 mol% of Zn-CuO (c) 4 mol% of Zn-CuO (d) 6 mol% of Zn-CuO (e) 8 mol% of Zn-CuO and (f) 10 mol% of Zn-CuO nanoparticles.

4.2.2.5. Electrical properties of CuO and Zn-CuO nanoparticles
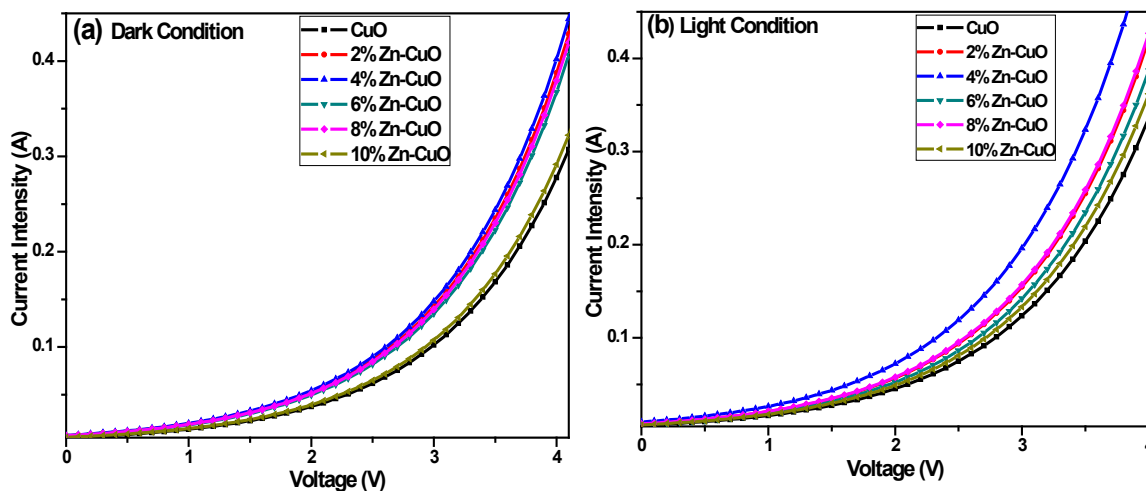
Figure 4.2.9: I-V characteristics of undoped CuO and Zn-CuO nanoparticles calcinated at 600 °C.

The current and resistance are the two parameters play an important role in the investigation of electrical properties of conducting materials [49]. According to Ohm's law, the current in a circuit is directly proportional to the voltage across the circuit and inversely proportional to the total resistance in the circuit [50]. The I-V characteristic studies of CuO and Zn-CuO nanoparticles have been carried out using silver paste to make good electrical contact. Figure 4.2.9 shows the I-V characteristics of CuO and Zn-CuO under the dark and UV-light condition. From the I-V curves, it can be seen that the pure CuO sample shows very high resistance in the dark condition. This may be due to the effect of grain boundaries on the mobility of charge carriers. These boundaries act as dissemination sites and potential walls which lead to a reduction in the carrier mobility by increasing the resistance and decreasing the current [51]. At low concentration of Zn doping (2-4 mol%) into CuO lattice, the decrease in resistance is due to the replacement of Cu^{2+} ($3d^9$) ions by Zn^{2+} ($3d^{10}$) ions which introduce a number of electrons in the doped films and thus the charge carriers. Hence the conductivity of Zn-CuO nanoparticles has

been enhanced. However, with further increase in the doping concentration of Zn, a slight increase in the resistance was observed. This reduction in conductance at higher concentration of Zn dopant could be attributed to the segregation of Zn ions in the grain boundaries. Moreover, at higher concentration of Zn the neutral defect may be observed. As a result of these defects the excess charge carriers get neutralize and leads to an increased resistivity [52]. The prepared CuO and Zn-CuO nanoparticle have shown a considerable enhancement in the conductivity under UV-light condition. This indicated that the motion of charge carriers increases under the light condition and considerably improves the conduction of CuO and Zn-CuO nanoparticles [53]. The remarkable increase in the conductance by these samples may result in higher efficiency of the solar cells [54].

4.2.3. Conclusions

In the present work, synthesis of CuO and Zn-CuO nanoparticles via simple microwave combustion method has been reported. The effect of Zn doping on the structural, optical and electrical properties of CuO nanoparticles have been studied. The SEM and TEM analysis revealed that the size and morphology of Zn-CuO nanoparticles depend on the concentration of Zn dopant. The optical properties of synthesized nanoparticles were studied by measuring of band gap energy. This reveals that with increasing the doping concentration of Zn upto 4 mol%, the band gap edge shifted to longer wavelength region. The I-V characteristic studies of CuO and Zn-CuO nanoparticles in dark and under UV-light illumination have shown the dependency between the conduction and the concentration of dopant. Therefore estimated optical band gap energy, conductance and resistance of Zn-CuO are very useful for the applications in the solar cells and optical devices.

4.3. Structural, Optical and Electrical Properties of CdO and Ni-CdO Nanoparticles

4.3.1. Introduction

Cadmium Oxide (CdO) is an interesting n-type semiconductor, with a direct band gap of 2.3 eV and indirect bandgap of 1.98 eV. It has been studied for a variety of potential applications like organic solar cells [55], eliminating cancer cells [56], photocatalyst [57], light emitting diodes [58], flat display panels [59], photovoltaics [60] electrochemical study of drugs [61] and heat mirrors [62]. However, various nanostructures of pure CdO and transition metal doped CdO nanoparticles (such as nanoprisms, nanorods, nanoflowers, nanosheets, nanospheroids etc.) have drawn more importance compared to other wide bandgap metal oxides (ZnO, TiO_2, SnO_2) because of their structural dependent properties such as narrow band gap, good electrical conductivity, low processing cost and excellent thermal stability [63]. Hence, recent application oriented research is more focussed at controlling the crystallite size and shape to improve the optical absorption and electrical properties of CdO nanostructures [64]. Various efforts have already been made for improvement of physiochemical properties of CdO nanomaterials such as morphological, magnetic, optical and electrical properties by doping with different transition and inner-transition elements [65]. Recently, doping of two or more elements instead of single element has also been adopted to enhance the above properties. The existence of two or more transition elements simultaneously in the host material helps to increase the impurity (electronic) states between the valence and conduction band. Hence, very high enhancement of optical and electrical properties of

nanomaterial was observed [66]. But harsh conditions such as high temperature, high pressure and highly sophisticated instruments are required for multiple elements doping when compared to single element doping process. Due to these reasons, single metal ion doping has been adopted in the present work. Of all the transition metals, Ni is selected as one of the effective dopant material for CdO as the ionic radius of Ni^{2+} ion is smaller than the ionic radius of Cd^{2+} ion. Hence, substitution of Ni^{2+} ion into CdO lattice is more facile. Also, divalent nickel oxide is a p-type semiconductor with a stable wide bandgap of 3.5-4.0 eV. A single crystal of NiO has potential applications in electrochromic films, batteries and extensively studied in dye sensitized solar cells due to its salient characteristics such as electrochemical stability, non-toxicity, thermal stability and low-cost of the starting materials [67]. Hence, it is possible to modify the conducting properties of CdO by doping with Ni^{2+}. The conducting properties of CdO depend on the energy gap formed by the incorporation of Ni^{2+}.

To the best of our knowledge, the preparation of CdO and Ni-CdO nanoparticles using microwave combustion method is very less explored. Hence, we report the synthesis of Ni-CdO using simple micro-wave assisted combustion method. The consequences of Ni^{2+} doping on crystal structure, optical and electrical properties of CdO have been studied with the help of field emission scanning electron microscopy (FE-SEM), X-ray diffractometry (XRD), UV-Visible spectroscopy (UV-Vis.), transmission electron microscopy (TEM) and photoconductivity techniques. The obtained results have been discussed in terms of optical and electrical properties in correlation with structure and microstructure.

4.3.2. Results and discussion

4.3.2.1. XRD analysis

The powder X-ray diffraction study was carried out to investigate the phase purity and structural parameters of CdO and Ni-CdO nanoparticles. Inset Figure 4.3.1(a) illustrates a typical X-ray diffraction spectrum of CdO nanoparticles prepared by the microwave combustion method. The six strong Bragg's reflection peaks are noticed at 32.69°, 38.01°, 54.79°, 65.75°, 68.86° and 81.80° which can be assigned to diffraction from (111), (200), (220), (311), (222) and (400) planes respectively, according to JCPDS Card No. 78-0653. This reveals that the resultant nanoparticles were pure CdO with a face centred cubic structure (space group: Fm-3m) [68]. Figure 4.3.1(b-f) shows the X-ray diffraction patterns of Ni-CdO nanoparticles with varying concentrations ($2 \leq x \leq 10$ wt%) of Ni^{2+}. The peaks appeared in X-ray diffraction pattern of Ni-CdO are well matched with X-ray diffraction pattern of undoped CdO nanoparticles and no additional peaks corresponding to secondary phases were found upto 4 wt% Ni^{2+} doping. The result shows that the generated Ni-CdO nanomaterials have good crystalline phase and high purity. However, on further increasing the doping percentage of Ni^{2+} ($x = 6-8$ wt%), a very small peak of new phase emerges at 43.02° in the X-ray diffraction spectrum. This impurity phase in the X-ray diffraction pattern is assigned to (200) plane (JCPDS Card No. 65-2901, a = 4.194 Å, V = 73.80 $Å^3$) of cubic phase NiO nanocrystals, which may be due to the excess of unreacted Ni^{2+} in the CdO lattice [69]. Figure 4.3.2 shows the broadening of Ni-CdO diffraction peaks as compared to CdO diffraction peaks and the broadening was found to be based on the Miller indices of the crystal plane. In the synthesized materials, the diffraction peak (111) is narrower than (002) peak, and in turn (002) peak is narrower than (220) peak. This clearly indicated the presence of

asymmetry in the crystallite shape. Further Ni^{2+} doping is confirmed by the presence of small deviation in 2θ values of Ni-CdO peaks, which is attributed to the replacement of Cd^{2+} by Ni^{2+} and evidenced with an increase of peaks intensities along (111), (200) and (220) planes. The planes (111), (200) and (220) initially deviated towards higher 2θ side ($\Delta 2\theta \sim 0.35°$) when doping concentration was about 2-4 wt% of Ni^{2+}. The planes further deviated by $0.08°$ (lower 2θ side) in 6 wt% of Ni-CdO and on further doping of Ni^{2+} (8-10 wt%), the angle of planes were slightly deviate towards higher 2θ side ($\Delta 2\theta \sim 0.18°$). The deviation of peak positions suggests that Ni^{2+} ions were successfully incorporated into the CdO lattice which leads to imperfections in crystals [70]. The intensity of the most intense peak (111) was found to be higher in pure CdO sample and for 2-4 wt% of Ni^{2+} doping the intensity of the peak found to be decreased with an improvement in FWHM.
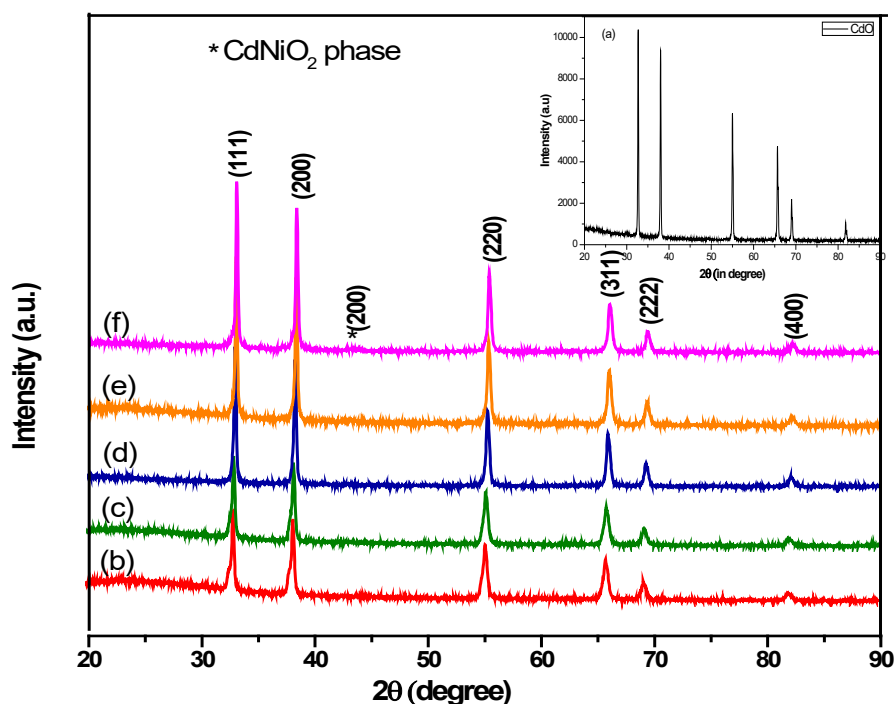
Figure 4.3.1: XRD patterns of (a) pure CdO, (b) 2 wt% of Ni^{2+},(c) 4 wt% of Ni^{2+}, (d) 6 wt% of Ni^{2+}, (e) 8 wt% of Ni^{2+},(f) 10 wt% of Ni^{2+} doped CdO nanoparticles.
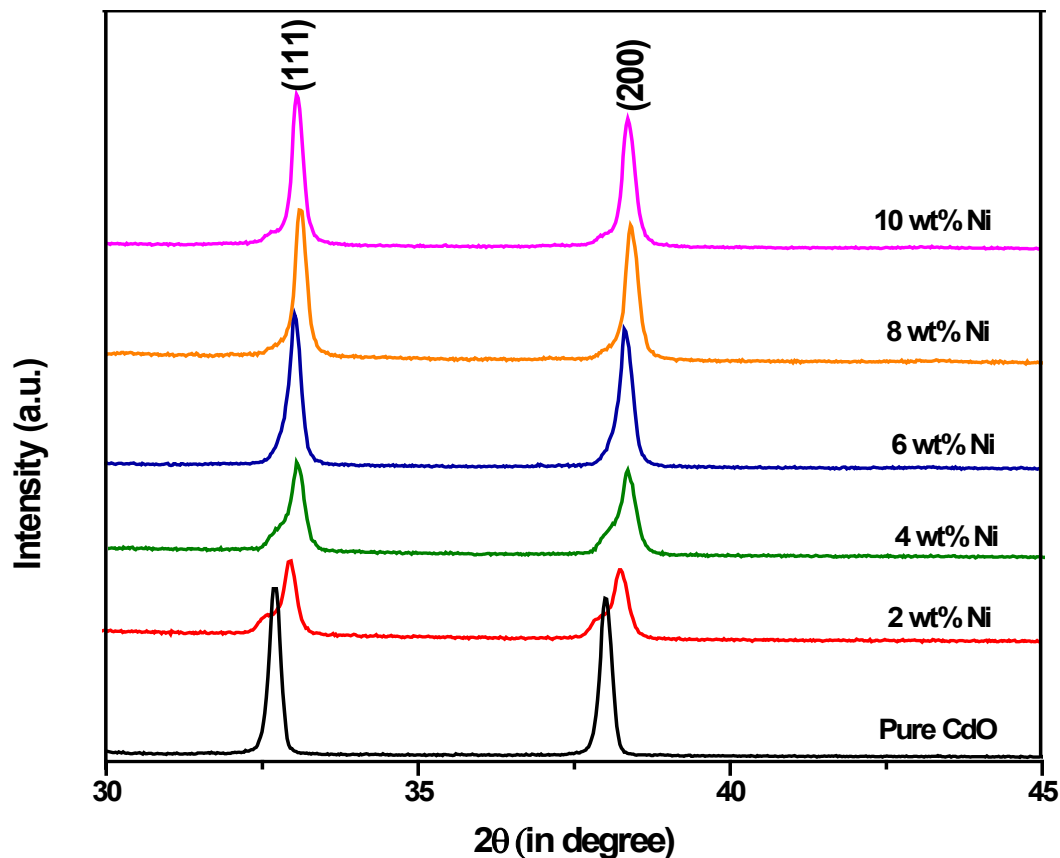
Figure 4.3.2: The shift of peak position of CdO and Ni-CdO ($2 \leq x \leq 10$ wt%) nanoparticles.

However, with further increase of Ni^{2+} concentration, the FWHM narrowed down with an increase in intensity. This may be due to the presence of secondary phase of NiO which generates the micro-strain in the host lattice and compresses the unit volume of Ni-CdO. This shows noticeable changes in lattice parameter (*a*) [71]. The calculated average crystallite size (D), micro-strain (ε) and dislocation density (δ) of pure CdO and Ni-CdO nanoparticles are tabulated in Table 3. The relation between lattice constant, micro-strain, dislocation density and crystallite size for pure CdO and Ni-CdO nanoparticles were calculated from the XRD data are depicted in Figure 4.3.3. The dislocation density and micro-strain are the two parameters to study the change in crystal

nature of CdO nanoparticles upon Ni^{2+} doping. Dislocation density estimates the density of linear defects in the samples and it is defined as the length of dislocation lines per unit volume of the crystal [72]. Generally, dislocation density is directly proportional to micro-strain and inversely proportional to crystallite size, i.e., for all the samples, as the dislocation density of diffraction planes were increased, there was simultaneous increase in the micro-strain and decrease in the crystallite size or vice-versa [73].
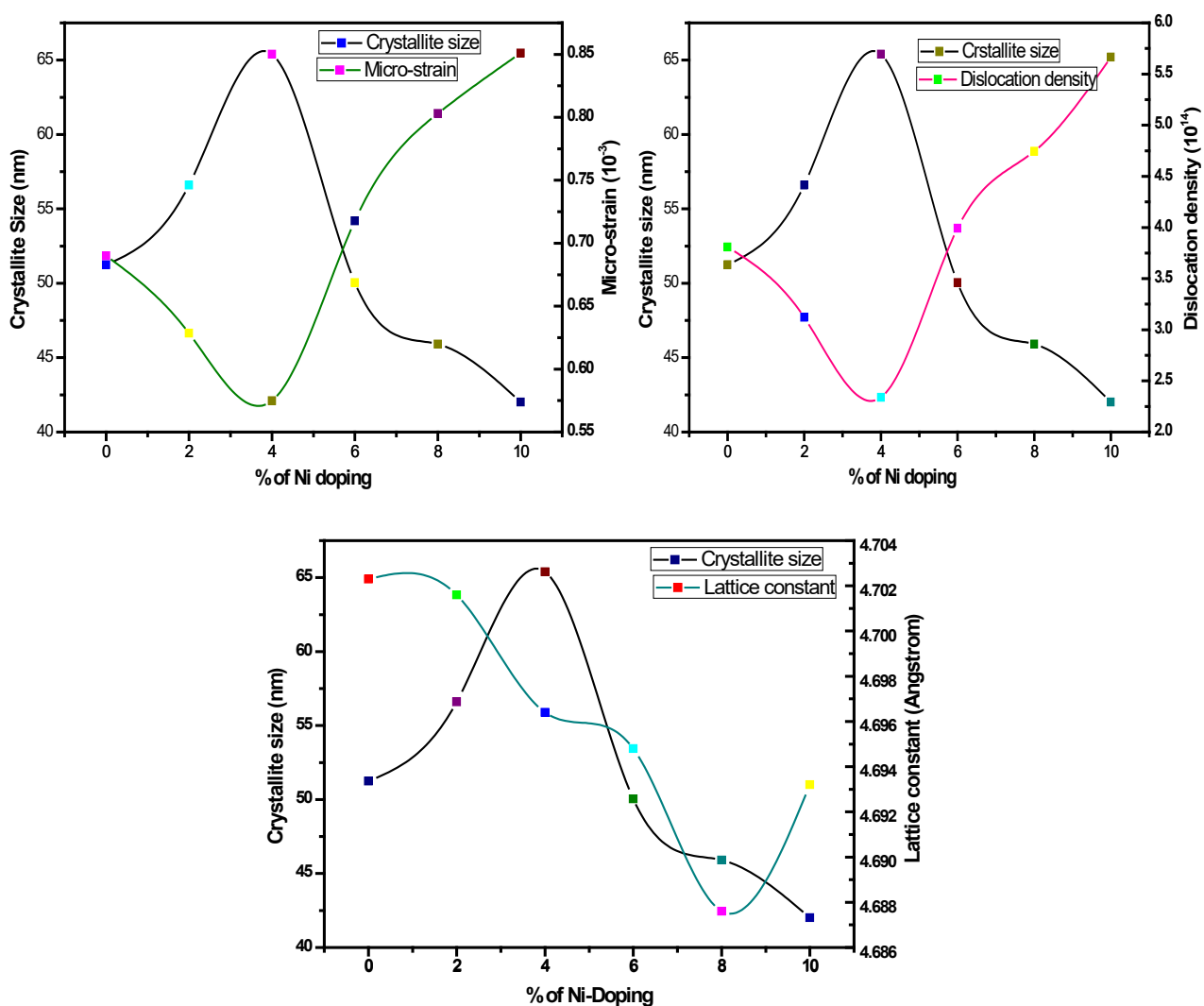

Figure 4.3.3: Variation of crystallite size, micro-strain, dislocation density and lattice constants with respect to Ni^{2+} concentration.

In addition, as observed from the experimental results and calculations, it is concluded that the lattice constants along (111) planes inversely affect the crystallite size. The calculated lattice constant and unit volume are summarized in Table 1. It revealed that there was no considerable variation in the lattice constants for undoped and Ni^{2+} doped CdO. The ionic radii of Ni^{2+} and Cd^{2+} are 0.55Å and 0.95 Å, respectively, and therefore the ionic radius ratio of Ni^{2+}/Cd^{2+} is equal to 0.58. Hence, the smaller sized Ni^{2+} ions could be occupied the interstitial crystalline position of CdO lattice. This also leads to a minor shift in lattice constants and Bragg's angle [74].

Table 3. FWHM, average crystallite size, micro-strain and dislocation density values of CdO and Ni-CdO nanoparticles

Property	CdO	$Cd_{0.98}Ni_{0.02}O$	$Cd_{0.96}Ni_{0.04}O$	$Cd_{0.94}Ni_{0.06}O$	$Cd_{0.92}Ni_{0.08}O$	$Cd_{0.90}Ni_{0.10}O$
a (Å)	4.7023	4.7016	4.6964	4.6948	4.6876	4.6932
Volume (Å)^3	103.98	103.93	103.59	103.48	103.00	103.37
Average crystallite size (nm)	51.24	56.60	65.39	50.05	45.91	42.11
Micro-strain (ε) in x 10^{-3}	0.6901	0.6285	0.5749	0.7177	0.8030	0.8510
Dislocation density (δ) in x 10^{14}	3.8087	3.1215	2.3387	3.9920	4.7444	5.6662

4.3.2.2. FE-SEM and EDAX analysis
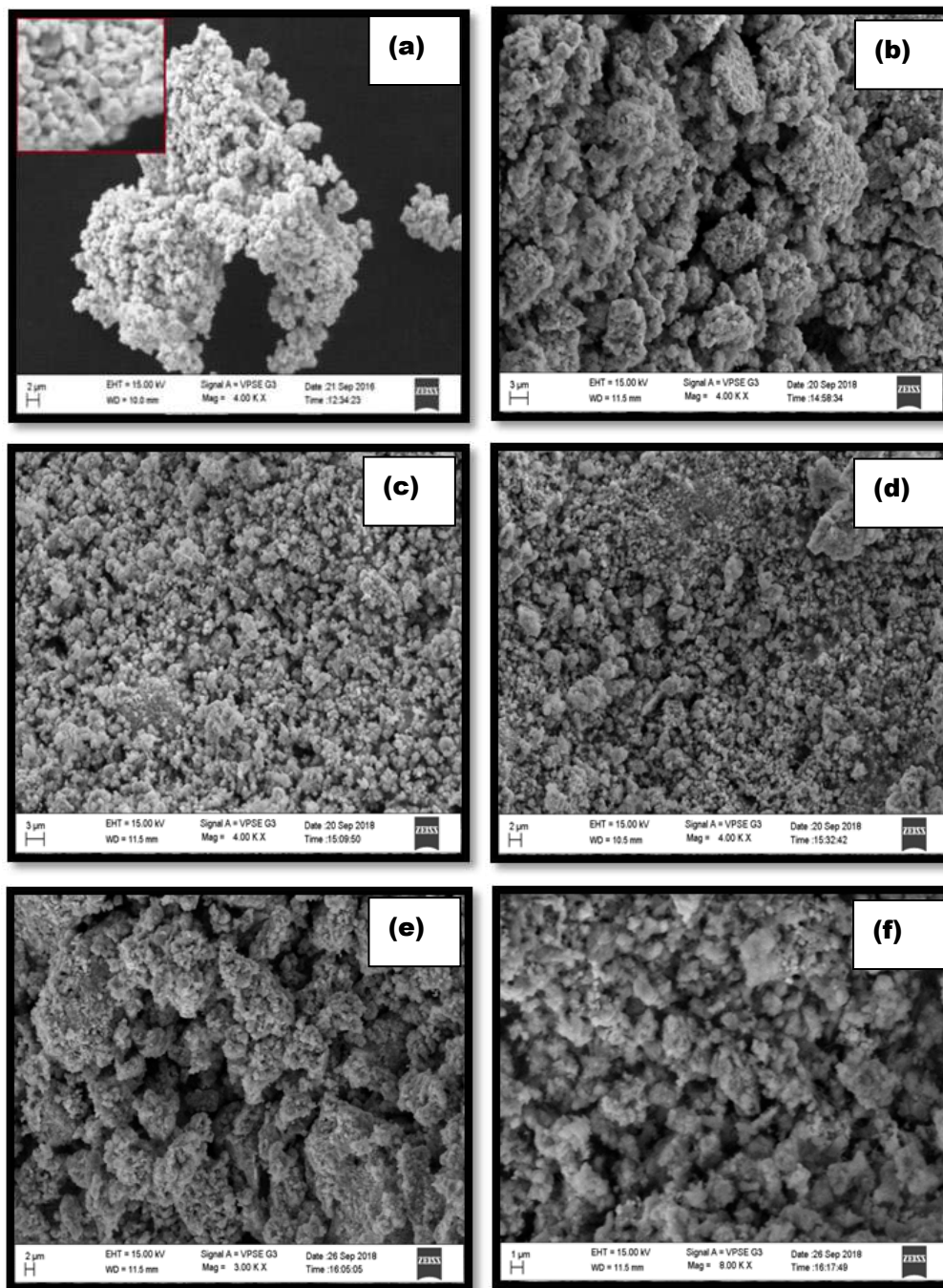
Figure 4.3.4: FE-SEM images of (a) Pure CdO, (b) 2 wt% of Ni^{2+}, (c) 4 wt% of Ni^{2+}, (d) 6 wt% of Ni^{2+}, (e) 8 wt% of Ni^{2+} and (f) 10 wt% of Ni^{2+} doped CdO nanoparticles.

FE-SEM is one of the promising techniques for morphological study of nanomaterials. It gives important information regarding the growth mechanism and shape of the particles. The FE-SEM image presented in Figure 4.3.4(a) shows that the nanoparticles exhibit a well distinguished network of surface features. It was noted that the particles have certain homogeneity in size and nearly prismatic shaped particles. The grain sizes of pure CdO semiconducting nanoparticles were in the range of 30 to 40 nm [75]. Figure 4.3.4(b-f) shows the FE-SEM images of Ni-CdO nanoparticles prepared by microwave combustion route. The images reveal that the particles are homogenous in morphology with prismatic to spherical shape. The grain size seems to be in the nano-meter range. In addition, porosity was observed in the calcinated Ni-CdO samples which are attributed to the release of gaseous products like H_2O, CO_2 and N_2 during microwave heating process. The porosity of generated Ni-CdO nanoparticles increases with increase in Ni^{2+} ion concentration. The grain size varies with increase in the concentration of Ni^{2+}. The increase in dopant concentration causes more defects and deformation in the lattice structures. The existence of more defects greatly degenerates the grain size and shape. Hence, the grain size and shape is larger for the doped samples than the pure samples [76]. Figure 4.3.5(a-f) shows the EDAX images of CdO and Ni-CdO nanoparticles. The typical EDAX spectra of CdO and Ni-CdO nanoparticles clearly shows that the peak intensity of Ni increases with increase in Ni^{2+} ion incorporation into the CdO lattice site. This confirmed the existence of Ni in Ni-CdO nanocrystals [77].
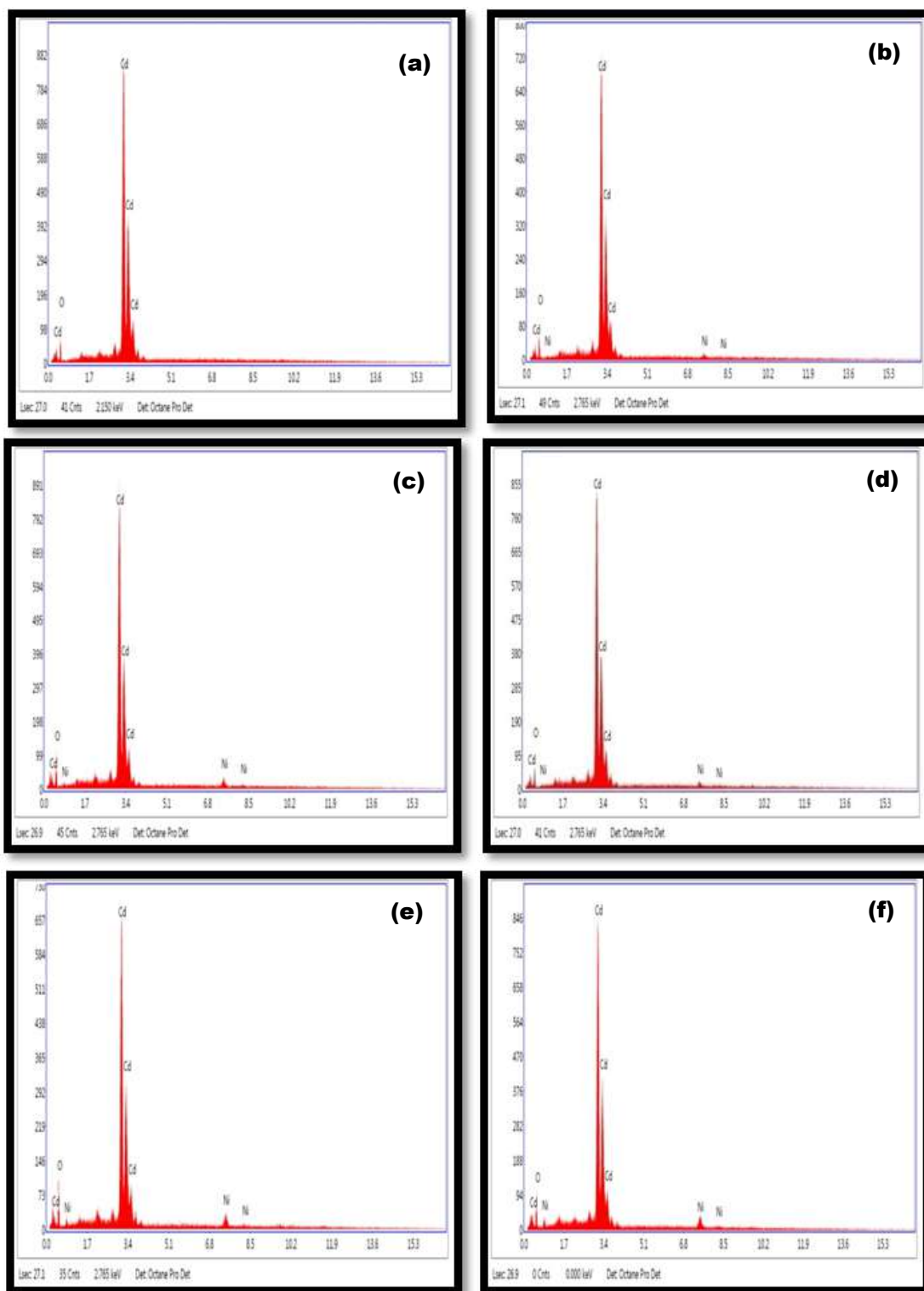
Figure 4.3.5: EDAX pictures of CdO and Ni-CdO nanoparticles calcinated at 500 °C.

4.3.2.3. TEM analysis
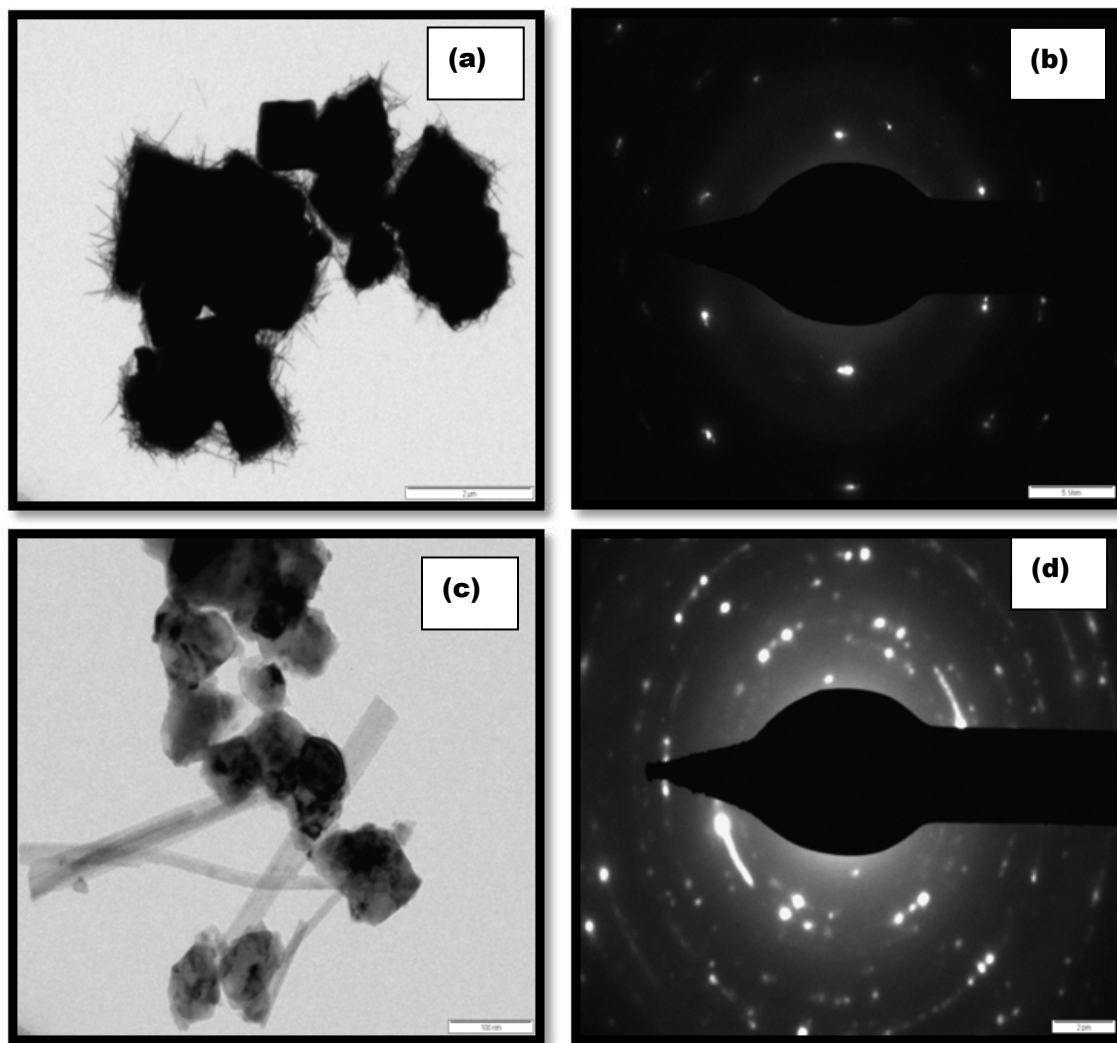
Figure 4.3.6: TEM images and SAED pattern of pure CdO (a, b) and 6 wt% Ni-CdO (c, d) nanoparticles calcinated at 500 °C.

Complementary morphological description can be achieved through TEM along with selected area electron diffraction (SAED) pattern studies. Figure 4.3.6 (a-d) show the TEM images and SAED patterns of CdO and Ni-CdO (6 wt%) nanoparticles synthesized via microwave combustion method and annealed at 500 °C. Figure 4.3.6(a)

86

and 4.3.6(c) depict the morphology of CdO and Ni-CdO nanoparticles, respectively. The images show a mixture of prismatic and spherical like structures. In addition, the micrographs reveal that the grain size ranges from 40-50 nm for CdO and 30-100 nm for Ni-CdO nanoparticles. This matches to the crystallite sizes obtained from XRD [78]. SAED pattern of CdO [Figure 4.3.6(b)] confirms that the product has a well-defined single-phase crystal and cubic phase of CdO. In Figure 4.3.6(d), the ring pattern clearly demonstrates the polycrystalline nature of Ni-CdO, which confirms the formation of secondary phase at 6 wt% of Ni-CdO. All the images of TEM and SAED pattern confirmed that Ni^{2+} is substantially doped in CdO lattice and the particles have several single grains of varying sizes and orientations without any major lattice defects [79].

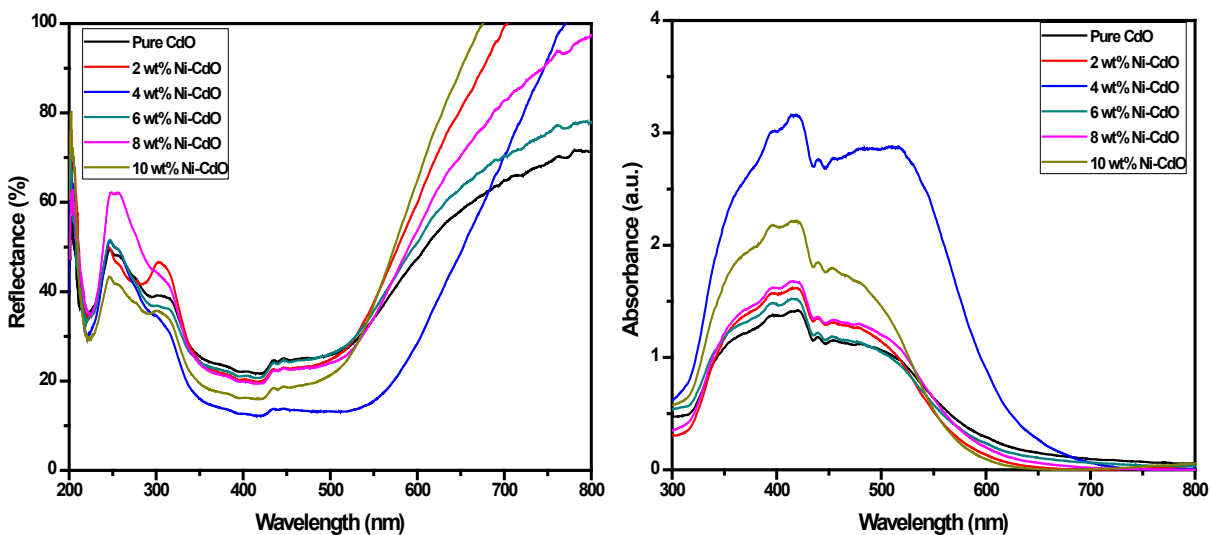### 4.3.2.4. UV-Visible spectral analysis

Figure 4.3.7: UV-Visible absorption spectra of Cdo and Ni-CdO nanoparticles for different Ni^{2+} concentrations.

UV-Vis spectrometry is the most used tool to evaluate the optical properties of pristine and transition metal doped semiconducting nanomaterials, because doped nanostructures show different optical properties compared to pure nanostructures. Usually three forms of spectra are used to analyze the λ_{max} of synthesized samples i.e., absorbance, transmittance and reflectance. In the present work, to estimate the optical energy gap and related properties, the optical reflectance measurements were carried out between 200-800 nm wavelength regions at room temperature [80]. Figure 4.3.7(a) shows the diffused reflectance spectra of CdO and Ni-CdO nanoparticles calcinated at 500 °C. It reveals that all the prepared samples show perfect reflection in the visible region. The reflection (%) of all the Ni-CdO samples increased with increase in the concentration of Ni^{2+}. Figure 4.3.7(b) shows the absorption spectra of CdO and Ni-CdO samples which also show the absorption edge of CdO nanoparticles shifted to visible region (red shift) after doping of Ni^{2+} ions (581 nm for CdO, 593, 626, 604, 620 and 610 nm for 2, 4, 6, 8 and 10 wt% respectively) [81]. The diffused reflectance of CdO and Ni-CdO nanocrystals were analyzed by Kubeluka-Munk method. Figure 4.3.8 shows the plot of photon energy in eV versus $[F(R)h\nu]^2$ for CdO and Ni-CdO nanoparticles [82]. The optical band gap was found to be 2.13 eV for CdO, 2.09, 1.97, 2.05, 2.00 and 2.03 eV for 2, 4, 6, 8 and 10 wt% of Ni-CdO respectively.
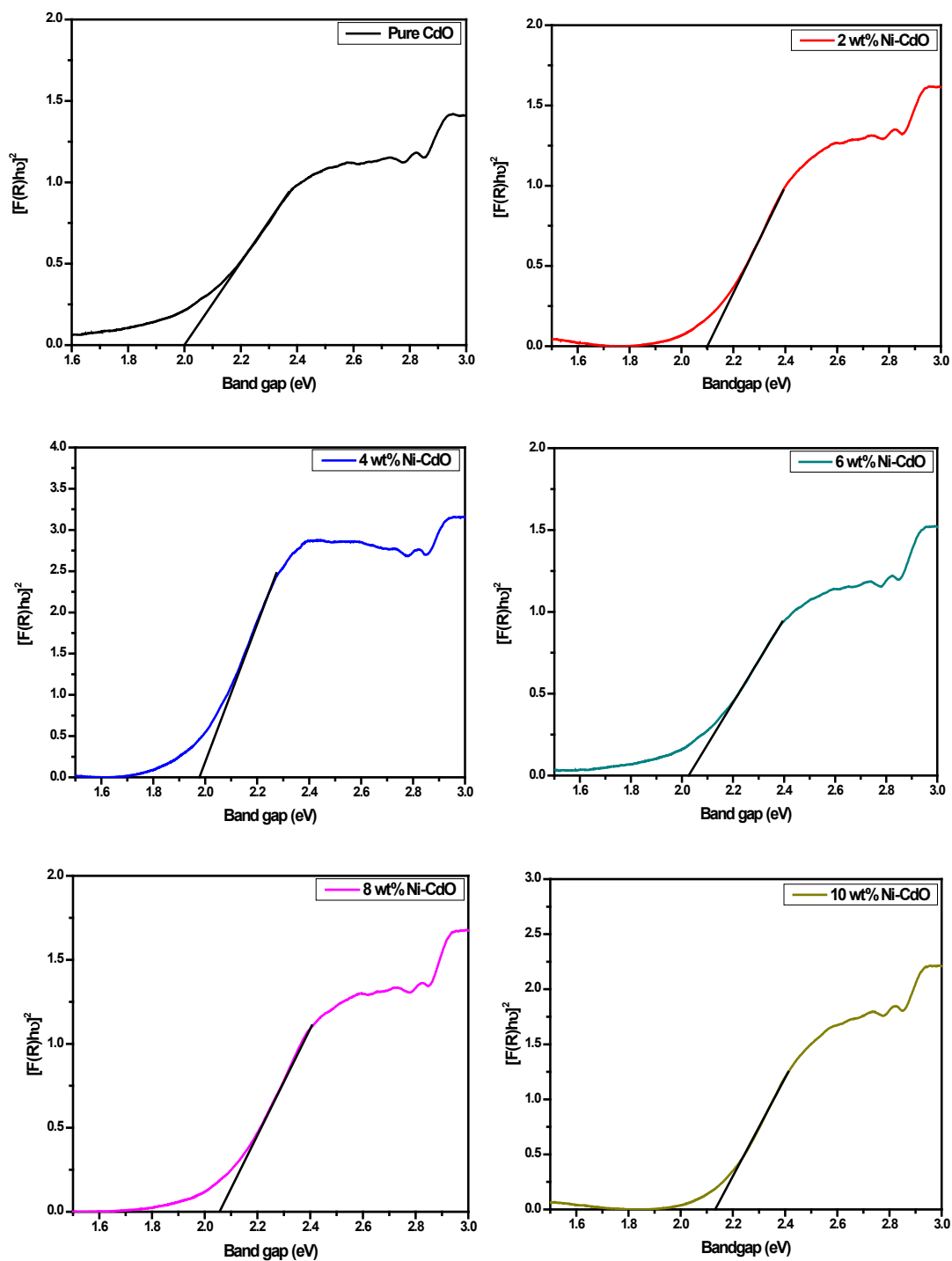
Figure 4.3.8: Tauc plot of (a) CdO, (b) 2 wt% of Ni^{2+}, (c) 4 wt% of Ni^{2+}, (d) 6 wt% of Ni^{2+}, (e) 8 wt% of Ni^{2+} and (f) 10 wt% of Ni^{2+} doped CdO nanoparticles.

4.3.2.5. Electrical properties of CdO and Ni-CdO nanoparticles

I-V characteristic studies of CdO and Ni-CdO nanoparticles under UV-light illumination and in dark were carried out and are shown in Figure 4.3.9. It shows that all the samples have strong nonlinear I-V characteristics. From these results, it can be assumed that the nonlinearity of the system is strongly related to the amount of oxygen and the presence of metal oxide precipitate in the grain boundary. The EDAX spectrum of synthesized sample gave a proof of very high atomic percentage of oxygen and SEM images shows the porous nature [82]. This indicates that the prepared films were metal deficient. Further, the adsorbed oxygen may produce potential barrier which hinders the electrical transport. So, all the samples prepared in the present work shows the non-ohmic and schottky barrier characters. In dark condition, the negatively charged O_2 molecules present in the surface of CdO nanoparticles interact with the free electrons of CdO. This generates the depletion layer close to the surface of CdO, which decreases the current intensity of prepared CdO nanoparticles [83]. The electrical conductivity is increased by intrinsic defects created due to the doping of Ni^{2+}. At low concentration of Ni^{2+} doping (2-4 wt%) in CdO lattice, the current intensity gradually increases due to the replacement of Cd^{2+} ($3d^{10}$) ions by Ni^{2+} ($3d^8$) ions. This replacement of Cd^{2+} by Ni^{2+} introduces more carrier-electrons in the conduction band due to the valency of Ni^{2+}. Further, oxygen vacancies are generated during the combustion processes which are also responsible for the enhancement of conductivity. On the other hand, increase in the doping concentration of Ni^{2+} (6-10 wt%) results in a slight decrease of conductivity [84]. The decrease in current intensity is due to the strain arises at the interface of the adjacent layers on introducing CdO lattice and shows huge lattice discrepancy. Such strain can be removed by mismatch dislocations and systematically arrange themselves by generating a regular network at the interface to influence the stronger ionic conductivity [85].
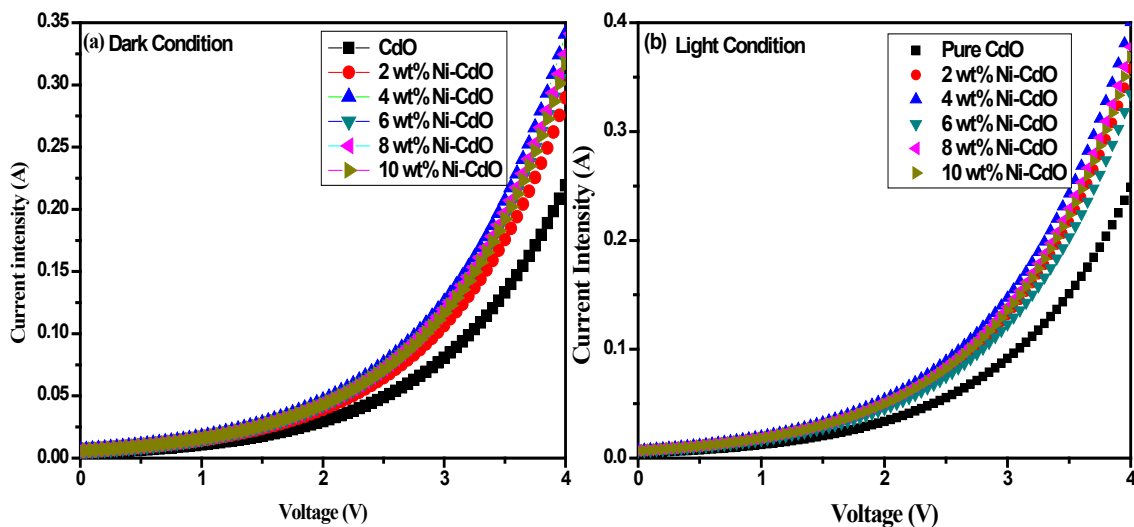
Figure 4.3.9: I-V characteristics of pure CdO and Ni-CdO nanoparticles calcinated at 500 °C.

4.3.3. Conclusions

In this chapter, CdO and Ni-CdO nanoparticles were synthesized by fast, simple and low-cost microwave combustion method. The effects of Ni^{2+} doping on the structural, optical and electrical properties of CdO nanoparticles were studied. The synthesized materials were characterized by XRD analysis and the results showed that the optimum incorporation of Ni^{2+} ions into CdO lattice was in between 4-6 wt%. The FE-SEM and TEM studies revealed that the crystallite size and surface morphology of Ni-CdO nanoparticles depend on the concentration of Ni^{2+} ions. The optical band gaps of pristine CdO and Ni-CdO nanoparticles were estimated through diffuse reflectance spectra which show a significant change with increase in doping concentration of Ni^{2+}. The I-V characteristics measurement shows the photosensitive behaviour of CdO and Ni-CdO nanoparticles under dark and UV-light condition. Therefore estimated band gap, current intensity and resistance of Ni-CdO indicated the possibility of using these nanoparticles in solar cells and optoelectronic devices.

91

4.4. Structural, Optical and Electrical Properties of TiO_2 and $Cr-TiO_2$ Nanoparticles

4.4.1. Introduction

Past few years, researchers worked on solar cells were considered the TiO_2 has a promising photo anodic material. It is because of its wide-energygap, low-cost of preparation, excellent thermal stability, good optical and electrical properties [85]. Due to these properties, TiO_2 nanostructures have attained a large extent of interest owing to their wide potential applications in various fields such as solar devices [90], catalysis [91], electrochemical analysis [92], field emitters [93], gas sensing [94], photo catalytic activity [95], supercapacitor [96], giant magnet resistance materials [97], ceramic pigments [98], electrochromic devices [99] etc. Moreover, more importance has been given to control the crystallite size and shape of TiO_2 nanostructures, which improves the optical and electrical properties. Currently, morphology and size distribution of TiO_2 nanoparticles play an important role in deciding their properties. An important method to modify the properties of nanoparticles is the introduction of dopant in the parent system. Suitable dopants ($Cr^{2+/3+}$, Gd^{3+}, Ni^{2+}, Yb^{3+}, Co^{2+}) are often mixed with the TiO_2 matrix, which modify its microstructure and defect chemistry, resulting in a change in its electrical and optical properties [100]. Among these metal ions, chromium has been used to enhance the optical properties, magnetic properties and luminescent properties of TiO_2 [101]. Chromium Oxide is the one of the important semiconductor, which exists in different phases of chromium oxide, such as Cr_2O, CrO, Cr_3O_4, Cr_2O_3, CrO_2, Cr_8O_{11} and CrO_3. Among these, Cr_2O_3 is the most stable phase under normal conditions. Amorphous and polycrystalline Cr_2O_3 has got an increasing interest in a wide variety of applications, such as solar absorber for thermal collectors, protective coating layers, various catalytic

systems [102]. Hence, it is possible to modify the conducting properties of TiO_2 upon doping with Cr.

In the present work, an effort has been made to realize the distribution of Cr^{3+} ions in the unit cell of TiO_2 nanoparticles synthesized through a simple, versatile and eco-friendly microwave combustion method. In addition, the consequences of Cr^{3+} incorporation on morphology, optical and electrical properties of these nanoparticles have been studied through XRD, FE-SEM, UV-Vis., TEM and photoconductivity techniques. The obtained optical and electrical properties were correlated with crystal morphology and particle size.

4.4.2. Results and discussion
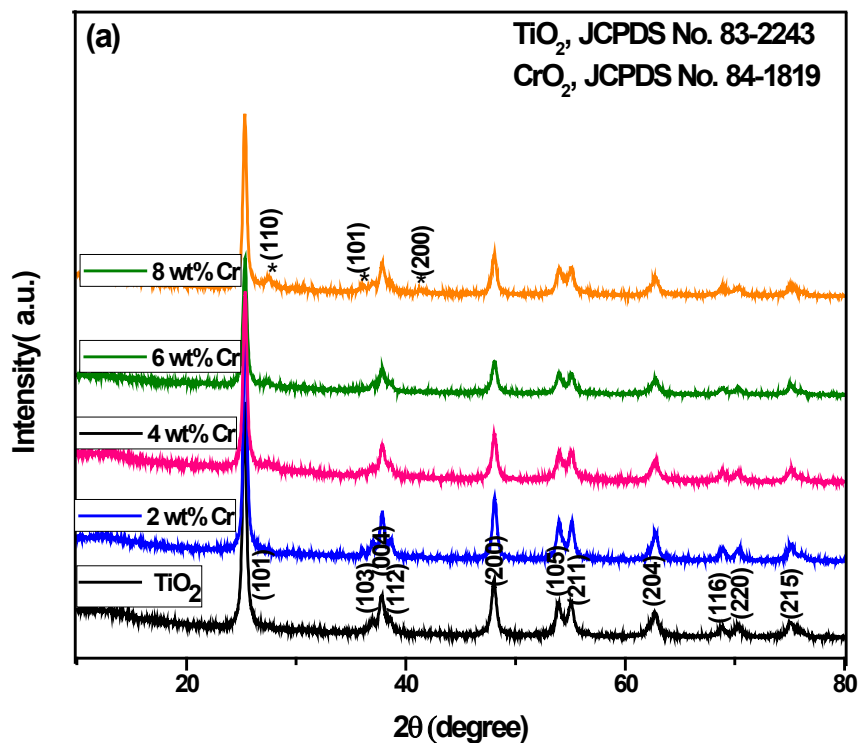
4.4.2.1. XRD analysis

Figure 4.4.1: X-ray diffraction pattern of TiO_2 and $Cr-TiO_2$ (0-8 wt%) nanoparticles calcinated at 500 °C.

The X-ray diffraction study is an important tool to evaluate the crystalline structure, lattice parameters, and whether the synthesized nanomaterials posses single or multi-phase. Figure 4.4.1(a) illustrates the X-ray diffraction pattern of pure TiO_2 and Cr-TiO_2 nanoparticles calcinated at 500 ºC. The existence of sharp peaks in X-ray diffraction pattern reveals the good crystalline nature of tetragonal anatase phase of TiO_2 and Cr-TiO_2. The X-ray diffraction of synthesized samples were compared with standard data (JCPDS Card no. 83-2243) and all the diffraction planes viz., (101), (103), (004), (112), (200), (105), (211), (204), (116), (220), (215) and (301) were exactly matches with the anatase phase of TiO_2 and Cr-TiO_2 nanocrystals [103]. The diffraction model shown that the reflection peaks of Cr-TiO_2 were broadened compared to pristine TiO_2 peaks. The XRD peak (101) is narrower than (004) peak and, in turn (004) peak is broader than (200) peak. This clearly indicated the presence of asymmetry in the crystalline structure and prepared samples were in the nanometre range. In addition, at lower concentrations (0-2 wt%) of Cr^{3+}, no peaks corresponding to secondary phases (CrO_2, Cr_2O_3, $Cr(OH)_2$, $TiCrO_3$) were indexed in the XRD pattern. This clearly confirms that the dissolution limit of Cr^{3+} ion in TiO_2 lattice was below 4 wt% and above 2 wt% [104]. At higher concentration of Cr^{3+} (4-8 wt%), a very small peaks of secondary phases were raised at 27.55º, 36.20º and 41.40º corresponding to CrO_2 along (110), (101) and (200) planes (JCPDS card no. 84-1819). This secondary phase formation may be due to the saturated Cr^{3+} ions present in the reaction solution [105]. The shifting of major (110) diffraction plane as a function of incorporation of Cr^{3+} was observed which further confirmed the distribution of Cr^{3+} ions in the unit cell of TiO_2. These diffraction planes were initially shifted towards higher 2θ values for 2 wt% of Cr^{3+} and achieves maximum shift at 6 wt%

of Cr^{3+}. Afterwards, these planes were shifted slightly towards lower 2θ values upto 8 wt% of Cr^{3+}. The variation in the diffraction angle specified that the lattice parameter, d-spacing and unit volume of Cr-TiO_2 were affected by the extent of Cr^{3+} incorporation. Also, with increase in Cr^{3+} concentration upto 2 wt%, the peak intensity of (110) plane has been increased and above 2 wt% of Cr^{3+} in TiO_2 lattice has resulted in the broadening of FWHM with a subsequent decrease in the peak intensity. It can be concluded that the Cr^{3+} doping can significantly increases the crystallinity and promote the crystal growth along (110) plane [106]. The lattice parameters *a, b* and *c* for TiO_2 and Cr-TiO_2 were estimated from XRD graph. It can be seen that there is no appreciable change in lattice parameter *a,* where as a slight change in lattice parameter *c* is observed [107]. This change may be attributed to the replacement of smaller ionic radii Cr^{3+} (0.64 Å) by larger ionic radii Ti^{4+} (0.68 Å) [108]. Figure 4.4.2(b) shows the decrease in full width at half maxima (FWHM) for Cr-TiO_2 nanoparticles as compared to pure TiO_2 nanoparticles. This is due to the crystallite size induced or micro-strain induced reduction, since (101) peak positions almost have changed as shown in Figure 4.4.2(a) [109]. Figure 4.4.3 is clearly indicated that the micro-strain is directly proportional to the dislocation density and inversely proportional to the crystallite size. Dislocations are the irregularity in a crystal which arises due to the lattice mismatch from one part of the crystal to another part. In this case, the dislocation densities are found to vary along with micro-strain as shown in Figure 4.4.3(a) and 4.4.3(b) [110]. The crystallite size (D), dislocation density (δ) and micro-strain (ε) of TiO_2 and Cr-TiO_2 nanoparticles were calculated and are given in Table 4.
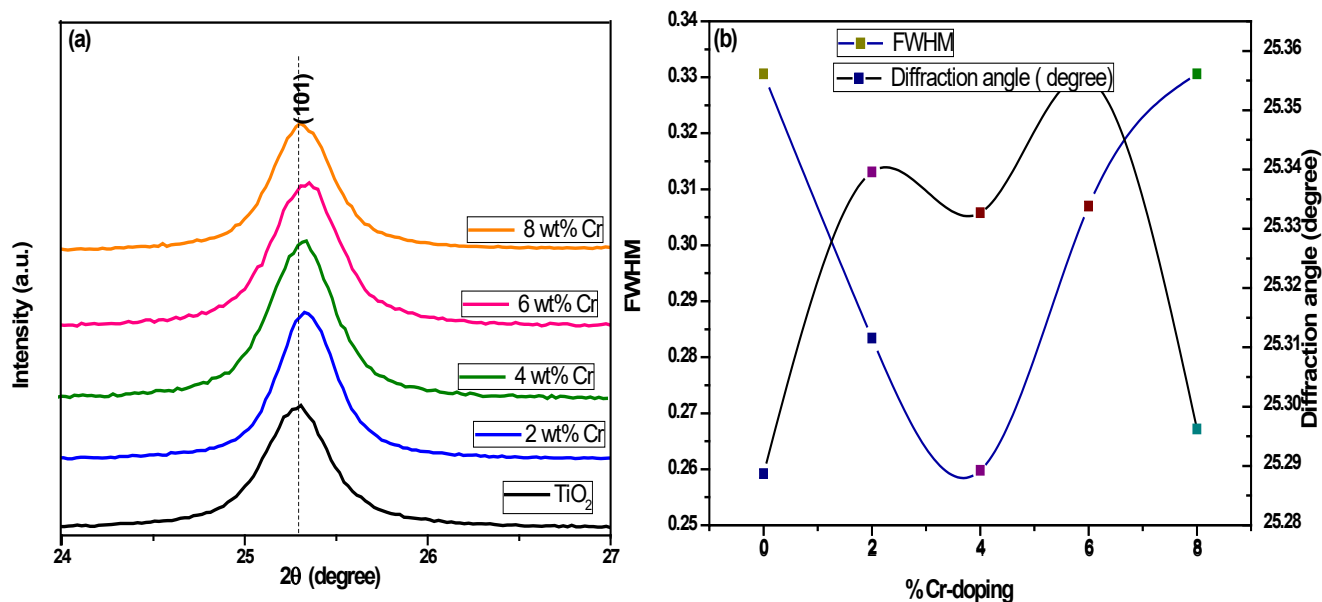
Figure 4.4.2: (a) The shift of peak position of TiO₂ and Cr-TiO₂ (0.00 ≤ x ≤ 0.10) nanoparticles, (b) the change in the FWHM of TiO₂ with different Cr concentration.

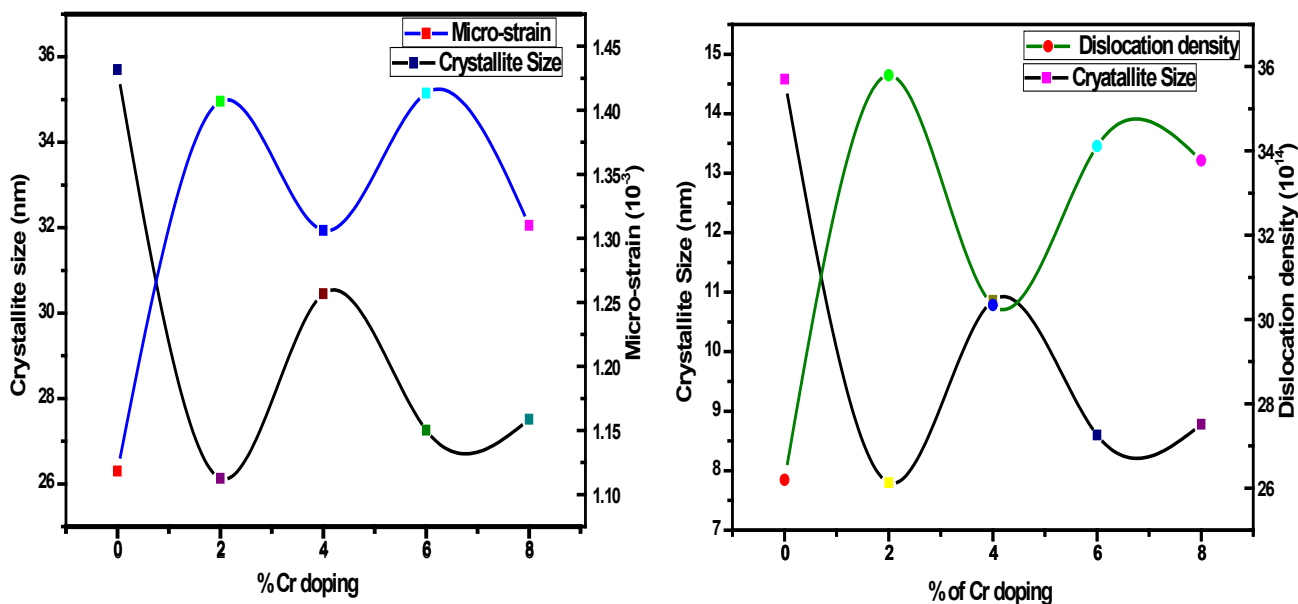**Figure 4.4.3:** Inter-relation between crystallite size, micro-strain and dislocation density of TiO₂ and Cr-TiO₂ (0-8 wt%) nanoparticles calcinated at 500 °C.

Table 4. Calculated values of lattice parameters, cell volume, average crystallite size, micro-strain and dislocation density

Property	TiO_2	$Ti_{0.98}Cr_{0.02}O$	$Ti_{0.96}Cr_{0.04}O$	$Ti_{0.94}Cr_{0.06}O$	$Ti_{0.92}Cr_{0.08}O$
a (Å)	3.7912	3.7878	3.7842	3.7834	3.7833
c (Å)	9.4363	9.5089	9.4480	9.4005	9.6384
Cell volume (Å)^3	135.63	136.43	135.26	134.56	137.95
Average crystallite size (nm)	35.70	26.13	30.45	27.26	27.51
Micro-strain (ε) in x 10^{-3}	1.1183	1.4069	1.3061	1.4134	1.3102
Dislocation density (δ) in x 10^{14}	7.846	14.646	10.785	13.457	13.213

4.4.2.2 FE-SEM and EDAX analysis

FE-SEM is one of the important tools for morphological study of samples and it gives the significant information about the growth mechanism, crystallite shape and size of the particles. Figure 4.4.4(a-e) shows the FE-SEM images of pure TiO_2 and $Cr-TiO_2$ nanoparticles, respectively. Figure 4.4.4(a) it is clearly observed that the pure TiO_2 contains a mixture of self aggregated cube and rods like structures. Figure 4.4.4(b) depicts that the shape of 2 wt% $Cr-TiO_2$ found to be same as that of pure TiO_2 but with a slight increase in the length and width of nanocrystals. This is in good agreement with the calculated values of X-ray diffraction data. Above 2 wt% of Cr^{3+} doping resulted in the morphological distortion of $Cr-TiO_2$ crystal lattice, which is the evidence for the conversion of fully nanorods like $Cr-TiO_2$ into cube like structures [111]. The elemental compositions of synthesized samples were determined by EDAX and are shown in Figure 4.4.5(a-e). The EDAX spectrum indicates the presence of O, Ti and Cr in all the samples of $Cr-TiO_2$. In addition, no extra peaks corresponding to unexpected elements (H, S and C) were observed, thereby confirming the purity of synthesized $Cr-TiO_2$ samples [112].

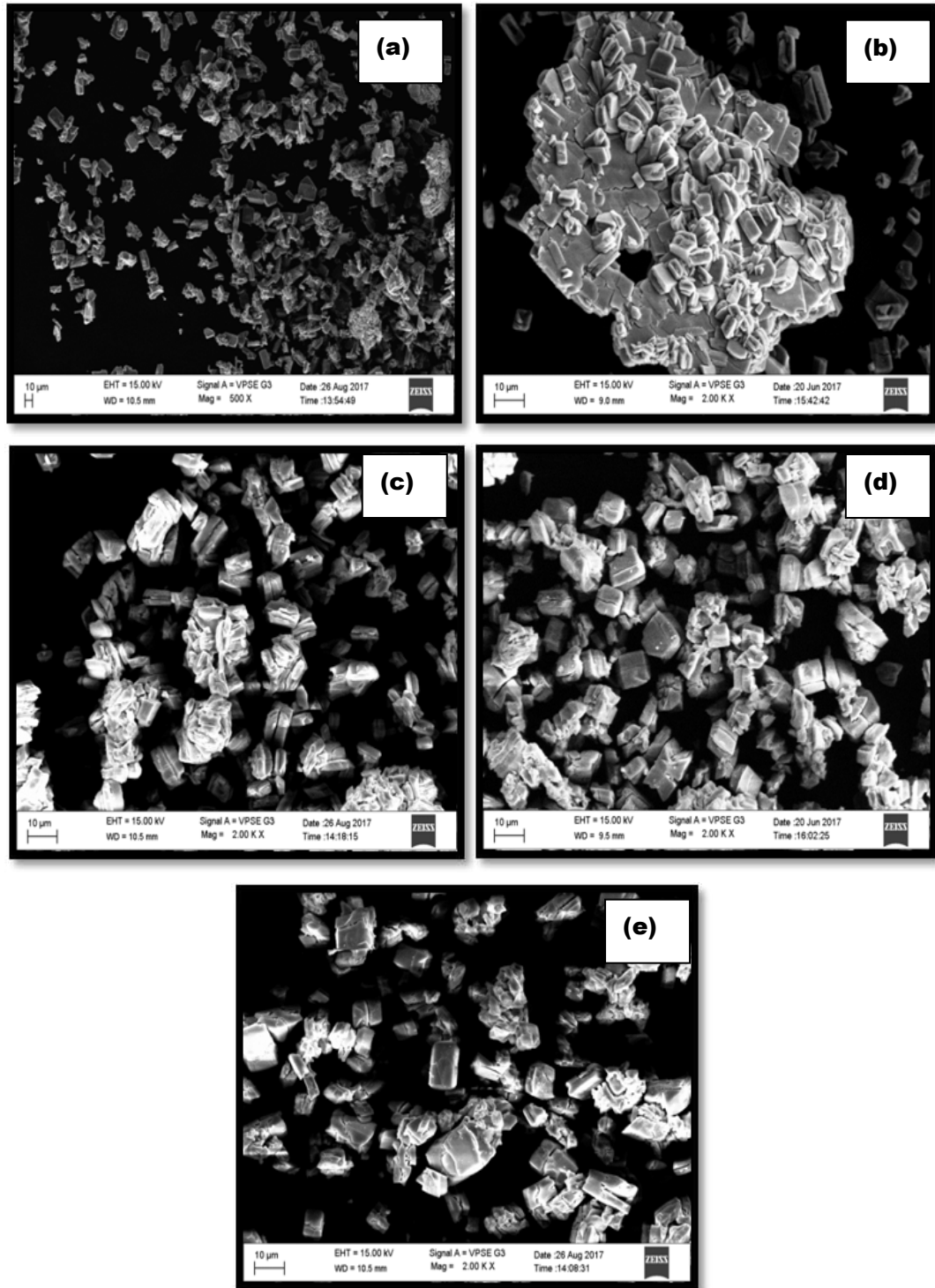**Figure 4.4.4:** FE-SEM images of (a) Undoped TiO_2, (b) 2 wt% of Cr-TiO_2, (c) 4 wt% of Cr-TiO_2, (d) 6 wt% of Cr-TiO_2 and (e) 8 wt% of Cr-TiO_2 nanoparticles.
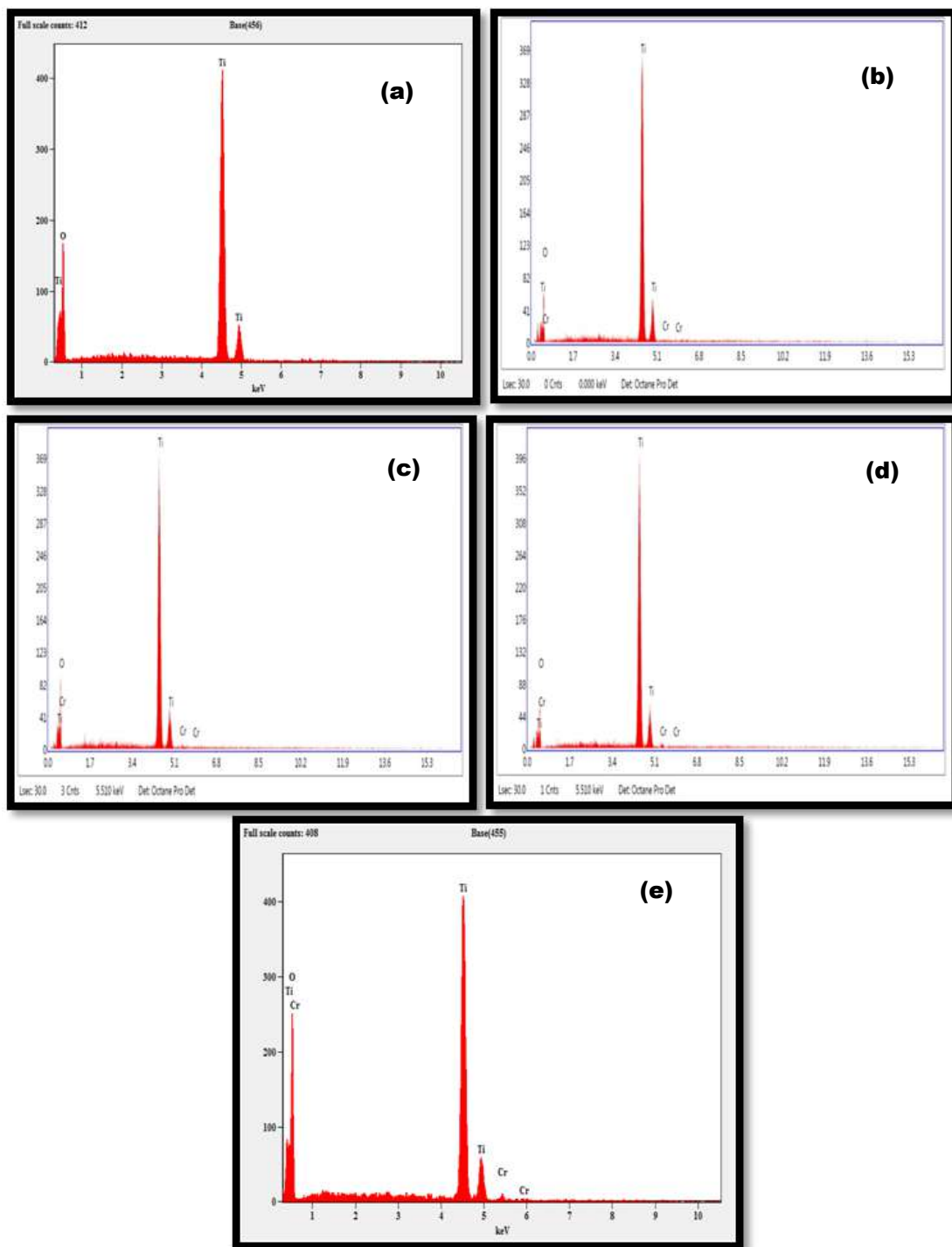
Figure 4.4.5: EDAX pictures of TiO_2 and Cr-TiO_2 nanoparticles calcinated at 500 ºC.

4.4.2.3. TEM and SAED analysis
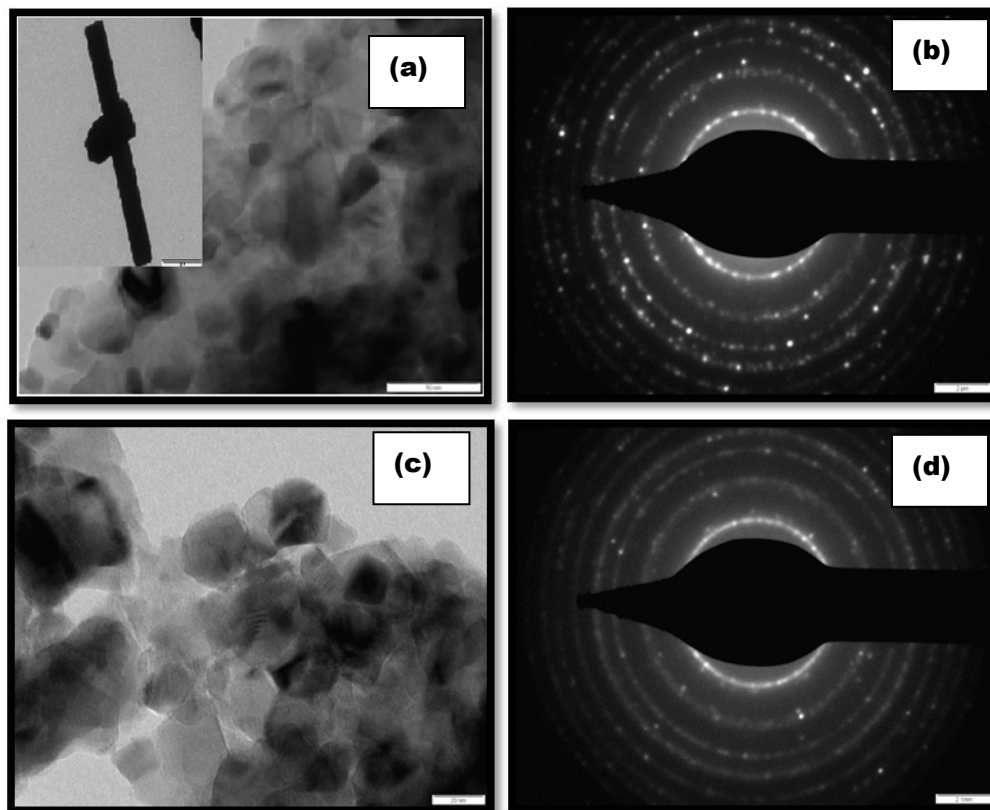
Figure 4.4.6: TEM images and SAED pattern of pure TiO_2 (a, b) and 6 wt% Cr-TiO_2 (c, d) nanoparticles calcinated at 500 °C.

A transmission electron microscopic study (TEM) has been carried out to study the morphology, crystallinity and average crystallite size of prepared samples. Figure 4.4.6 shows the TEM images of TiO_2 (a) and 6 wt% Cr-TiO_2 (c) samples. The average size of TiO_2 nanoparticles was found to be ~ 35 nm and it is well matched with the findings of FE-SEM and XRD values. Although the nanoparticles were slightly agglomerated, their grain boundaries were clearly distinguishable. Here, nano-size crystallites are closely seen as grouping together and forming a mixture of cube and rods like morphologies. But from Figure 4.4.6 (c) it is revealed that the doping of Cr^{3+} ions into TiO_2 lattice, changes the nano-rods shape of TiO_2 nanoparticles into aggregated nano-cubes [113]. The selected area of electron diffraction (SAED) pattern

100

(Figure 4.4.6(b) & (d)) indicates the crystallite nature of TiO_2 and $Cr-TiO_2$ nanoparticles. Careful observation of Figure 4.4.6(b) revealed that the planes corresponding to pure TiO_2 nanoparticles were exactly matched with the XRD model, representing the long range ordering among the unit cells. Similarly, the SAED pattern of 6 wt% of $Cr-TiO_2$ (Figure 4.4.6(d)) shows the diffused type of rings. This is because the short range ordering among the unit cells caused by the incorporation of Cr^{3+} ions which indexed the reduced crystallinity in 6 wt% $Cr-TiO_2$ samples. Thus, SAED results are supported the experimental evidences of XRD studies [114].

4.4.2.4. UV-Visible spectral analysis
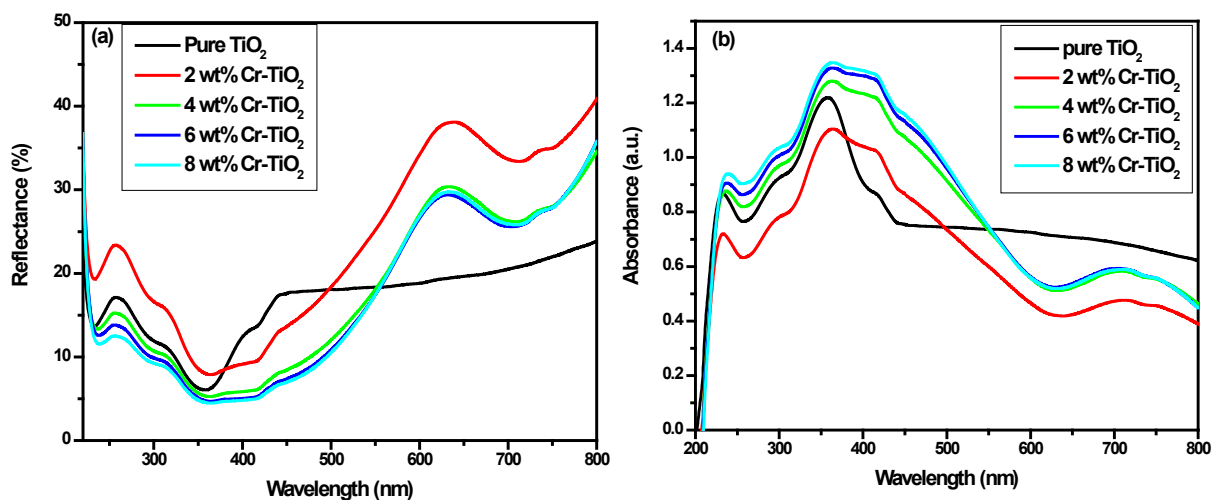
Figure 4.4.7: (a) UV-Visible absorption, (b) reflectance spectra of undoped and $Cr-TiO_2$ nanoparticles for different Cr^{3+} concentrations.

UV-Vis. spectrometry is the most used technique to analyze the optical properties of pristine and transition metal doped semiconducting nanomaterials, since the doped nanostructures show different optical properties compared to pure nanostructures. Usually three forms of spectra are used to analyze the λ_{max} of synthesized samples i.e., absorbance, transmittance and reflectance. In the present work, to estimate the optical energy gap and related properties, the optical reflectance measurements were carried out between 200-800 nm wavelength regions at room temperature [115].
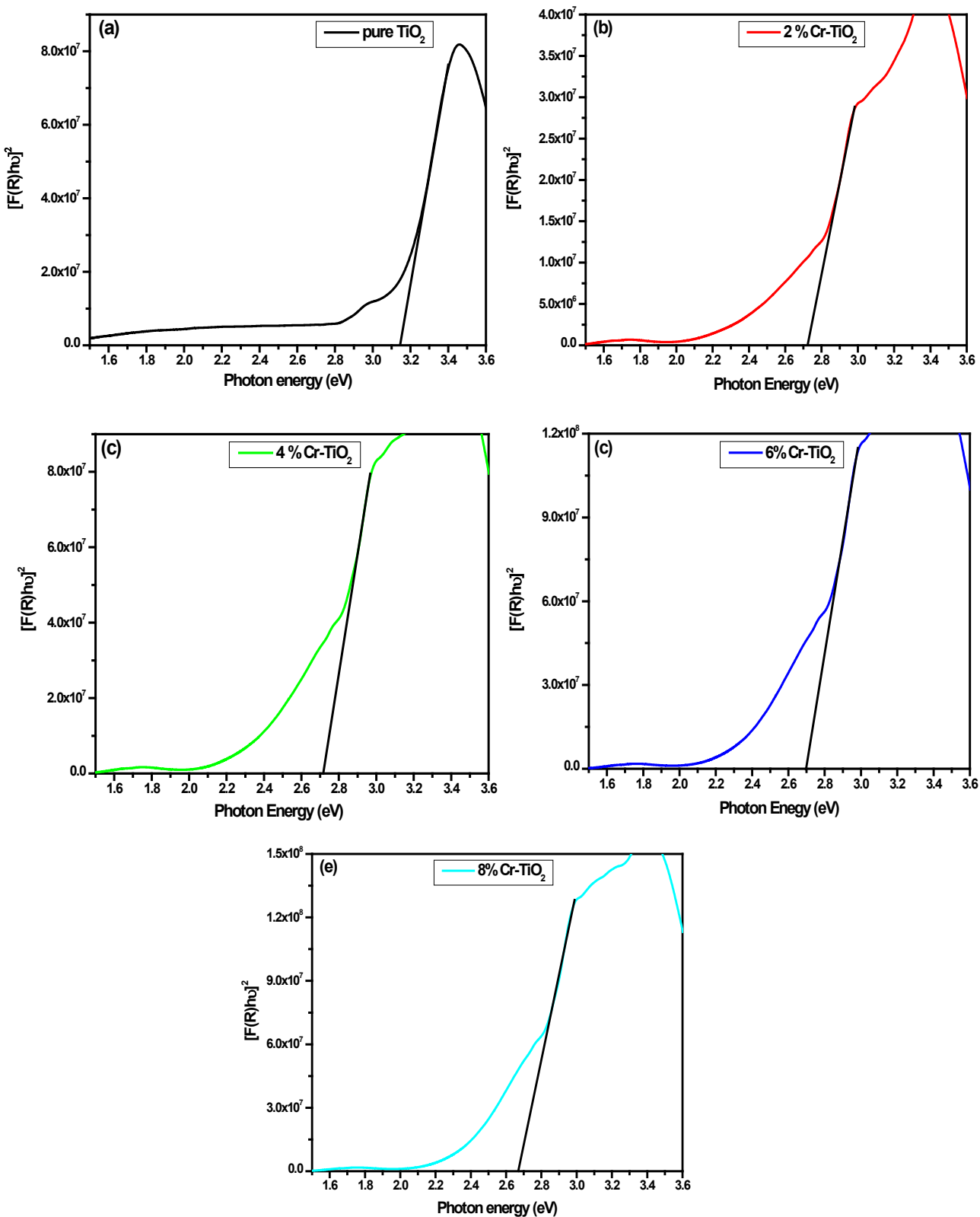
Figure 4.4.8: Kubeluka-Munk's plot of undoped and Cr-TiO₂ nanoparticles.

Figure 4.4.7(a) shows the diffused reflectance spectra of TiO$_2$ and Cr-TiO$_2$ nanoparticles calcinated at 500 °C. It revealed that all the prepared samples show perfect reflection in the visible region. The reflection (%) of all the Cr-TiO$_2$ samples increased with increase in the concentration of Cr^{3+}. Figure 4.4.7(b) shows the absorption spectra of TiO$_2$ and Cr-TiO$_2$ samples which also show the absorption edge of TiO$_2$ nanoparticles shifted towards visible region (red shift) after doping of Cr^{3+} ions [116]. The diffused reflectance of TiO$_2$ and Cr-TiO$_2$ nanocrystals were analyzed by Kubeluka-Munk method. Figure 4.4.8 shows the plot of photon energy in eV versus $[F(R)h\nu]^2$ for TiO$_2$ and Cr-TiO$_2$ nanoparticles [117]. The optical band gap was found to be 3.15 eV for TiO$_2$, 2.72, 2.71, 2.69 and 2.66 eV for 2, 4, 6, 8 and 10 wt% of Cr-TiO$_2$, respectively.

4.4.2.5. Electrical properties of TiO$_2$ and Cr-TiO$_2$ nanoparticles

The properties like conductivity or resistivity are comes under the class of electrical properties. These properties are noticed at nano-scale level by changing the optical properties of nanomaterials. Single crystal semiconductors developed from pure metal salts showed poor conductivity because of their poor carrier density. The latter can be raised by orders of magnitude by doping with right dopant (transition metal ions, rare earth metal ions etc.) [117]. By doping of metal ions into host lattice of nanomaterials, certain changes were observed: (i) the band gap values were decreased with increase in dopant concentration, and this is due the addition of dopant which can cause an increase in density of states in valence band or it can also create the localized states within the forbidden gap itself [118]; (ii) creation of anion or cations vacancies in host lattice. It is well known that the electrical properties of oxide nanomaterials at room temperature is due to intrinsic defects created by anion vacancies and the extrinsic defects created by

adding impurity metal cations. These defects also introduce donor states in the forbidden band slightly below the conduction band. Hence, these properties improve the conductivity of nanomaterials [119]. The I-V characteristic studies of TiO_2 and $Cr-TiO_2$ nanoparticles were carried out using silver paste to make good electrical contact. Figure 4.4.9 (a-b) shows the I-V characteristics of TiO_2 and $Cr-TiO_2$ nanoparticles under the dark and UV-light condition. From Figure 4.4.9(a) it is evident that 8 wt% of $Cr-TiO_2$ sample shows maximum current intensity while pure TiO_2 sample shows minimum current intensity in dark as well as under light condition. It is found that the increase of current intensity is due to incorporation of Cr^{3+} ions into the Ti^{4+} ions site and availability of free charge carriers (electrons). Similarly, I-V curves show a decrease of current intensity and this may attributed to the effect of grain boundaries on the mobility of charge carriers. These boundaries act as dissemination sites and potential walls which lead to a reduction in the carrier mobility by increasing the resistivity [120].
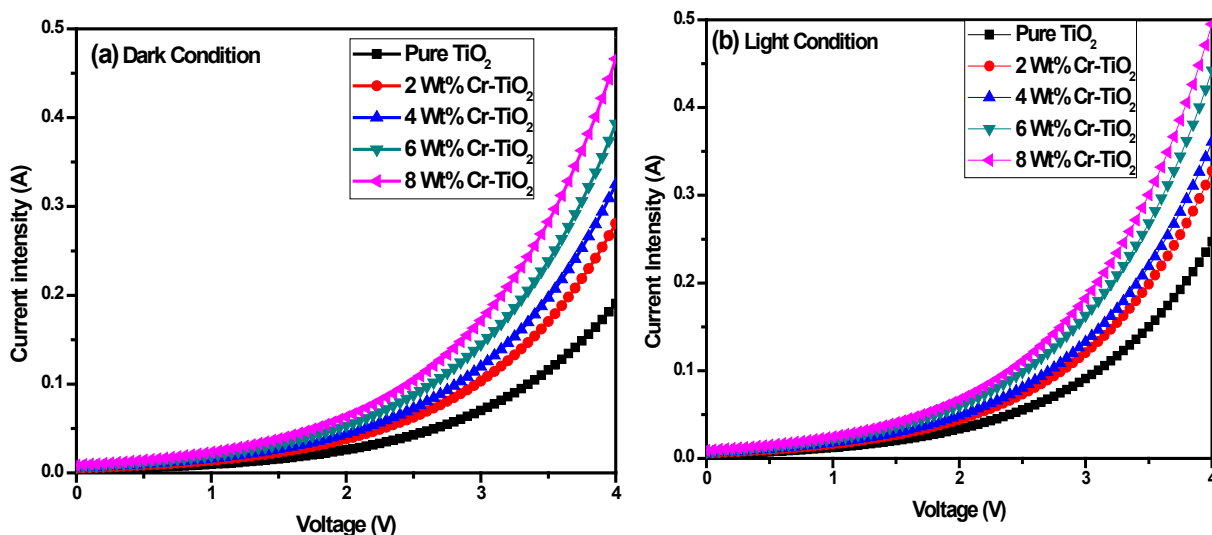

Figure 4.4.9: Current-Voltage (I-V) characteristics of pure TiO_2 and $Cr-TiO_2$ nanoparticle films.

On UV-light illumination the current intensity of TiO_2 and Cr-TiO_2 nanoparticles has found to be enhanced considerably. This indicated that the UV-light illumination has provoked the motion of charge carries faster in the TiO_2 and Cr-TiO_2 lattice and hence increased the current intensity of TiO_2 and Cr-TiO_2 nanoparticles [121].

4.4.3. Conclusions

In the present work, TiO_2 and Cr-TiO_2 nanoparticles have been prepared via microwave combustion method. The samples were characterized by X-ray diffraction studies (XRD), field emission scanning electron microscopy (FE-SEM), energy-dispersive analysis using X-rays (EDAX), UV-Visible spectroscopy (UV-Vis) and photoconductivity technique. The XRD results indicated that Cr^{3+} ions have been incorporated in TiO_2 lattice and secondary phase of CrO_2 has appeared above 4 wt% of Cr^{3+} doping. The FE-SEM images clearly indicated the structural changes which caused due to the effect of Cr doping and EDAX images confirmed the presence of Cr ions in TiO_2 lattice. The band gap of TiO_2 nanoparticles has been determined using Tauc plot and the result showed that the incorporation of Cr^{3+} has decreased the bandgap of TiO_2. The I-V characteristics studies of TiO_2 and Cr-TiO_2 nanoparticles under dark and UV-light illumination have shown the dependency between the conductance and percentage of Cr^{3+} ions concentration in the TiO_2 lattice. Therefore, the predicted optical energy gap and conductance of prepared Cr-TiO_2 nanoparticles are very useful in the field of solar cells and optical devices.

4.5. Structural, Optical and Electrical Properties of MgO and Zn-MgO Nanoparticles

4.5.1. Introduction

Magnesium oxide (MgO) has a rock salt structure with a wide band gap of 7.8 eV [121]. Due to its wide band gap, inexpensiveness and long term stability, MgO is used in potential applications of numerous disciplines. It can be extensively utilized in the fields of translucent ceramics, refractory plasma display panel, absorbents in many pollutants and superconducting products [122]. Due to good photocatalytic properties of MgO, it is being used as ultra-thin shells on the surface of some metal oxides such as SiO_2 [123], ZnO [124] and TiO_2 [125] to improve the efficiency of dye-sensitized solar cells. Magnesium oxide (MgO) has been used as an insulating layer in the TiO_2 based DSSCs because of two important reasons: firstly, the MgO layer protects the back electron transfer from the TiO_2 layer to the electrolyte solution and hence, reduces electron-hole recombination [126]; secondly, the MgO layer improves the dye adsorption, leading to an improved efficiency [127]. Also, it is an eco-friendly material and is extensively used in many medical, industrial and agricultural products [128].

Currently, research is more dedicated towards synthesizing the undoped and transition metal doped semiconducting nanomaterials. For semiconductors, doping is an effective method to improve and control the optical and electrical properties. Now-a-days researchers are selecting simple and cost effective dopant atoms like Cr, Fe, Cu, Ni, Ag, Nd, Eu and Al to develop and modify the unique features of synthesized host nanomaterials [129]. Out of all transition metal ions, zinc has been chosen to improve the optical, electrical and luminescent properties of MgO. It is because; zinc oxide is one of the important n-type semiconductors with a wide-bandgap of 3.17 eV, which shows unique optical and electrical properties. Moreover, the Zn^{2+} doping is expected to alter

the electronic band structure of MgO and hence influence the optical band gap of MgO nanomaterials. Also, similar charge and small differences in ionic radius of Zn and Mg ions (Mg^{2+} = 0.72 Å and Zn^{2+} = 0.74 Å) will result in the incorporation of impurities besides inherent vacancy defects. Due to these features, Zn^{2+} ion has been adapted as one of the important dopant to modify the optical band gap and conductivity of MgO nanoparticles [130].

In the present work, the spherical shape of MgO and Zn-MgO nanoparticles were synthesized by using a microwave combustion method, which is a simple, fast and cost effective route compared to other conventional methods. The consequences of Zn doping were studied through PXRD, FE-SEM, TEM, UV-Vis. and photo-conductivity (I-V) techniques.

4.5.2. Results and discussion

4.5.2.1. XRD analysis

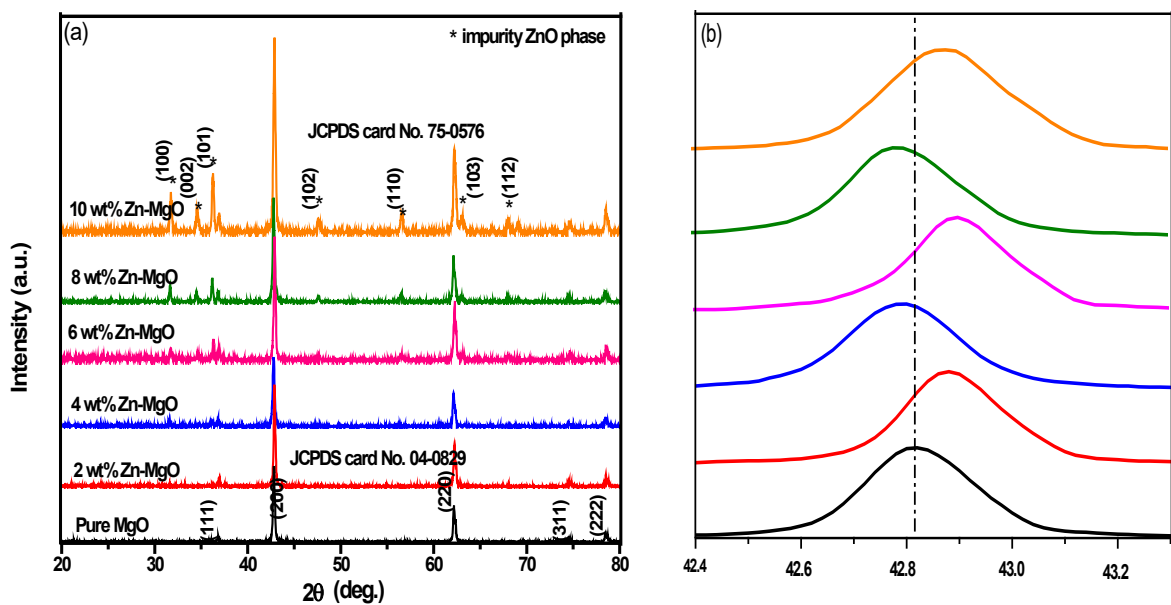**Figure 4.5.1:** (a) X-ray diffractograms of $Mg_{1-x}Zn_xO$ with different Zn^{2+} doping concentration (x = 0-10 wt %), (b) Shifts in peak position and changes in peak broadening are described in the enlarged view of (200) peak for MgO and Zn-MgO nanoparticles.
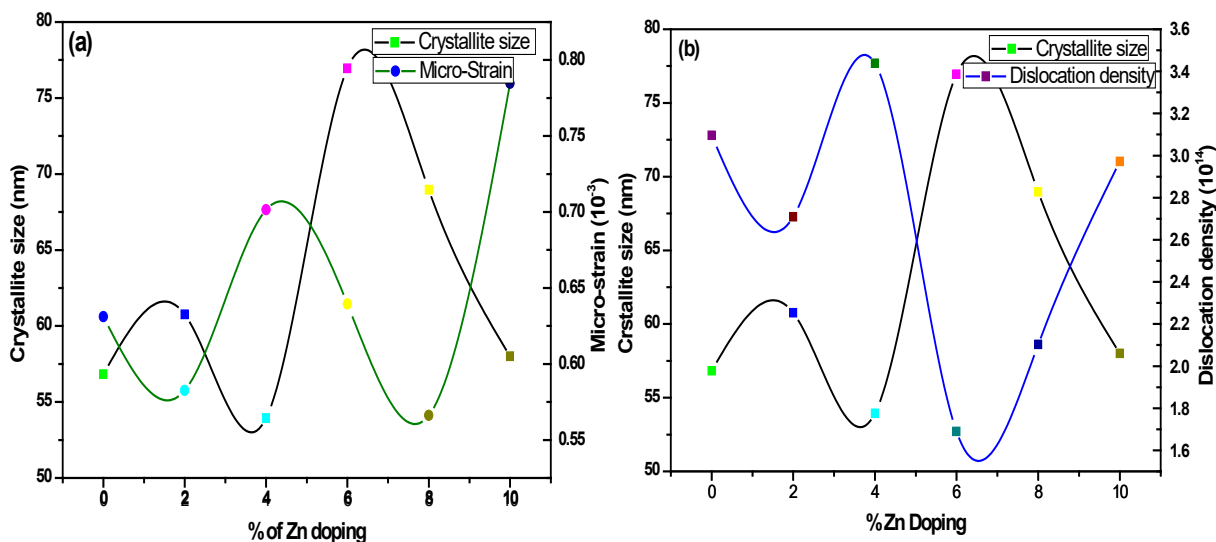
Figure 4.5.2: Inter-relation between crystallite size, micro-strain and dislocation density of MgO and Zn-MgO (0-10wt %) nanoparticles calcinated at 500 °C.

The powder X-rays diffraction (PXRD) studies is a powerful tool to investigate the phase purity and structural parameters of synthesized nano-scale materials. Figure 4.5.2(a) shows the PXRD pattern of microwave combustion synthesis of MgO and Zn-MgO nanoparticles with varying concentration of Zn^{2+} (2-10 wt%). The PXRD pattern illustrates the well defined and sharp Bragg's reflection peaks of the MgO such as (111), (200), (220), (311) and (222). These diffraction peaks clearly indicates that the obtained materials were cubic phase structure and they were free from impurity phases of metal Mg and Mg (OH)2. This is further confirmed by the standard JCPDS Card No. 04-0829 [131]. In addition, for the lower concentration (2 wt%) of Zn^{2+}, no additional peaks corresponding to Mg, Zn, Mg(OH)2, Zn(OH)2 and ZnO are observed in the XRD graph. This clearly indicates the obtained 2 wt% of Zn-MgO nanocrystals show better crystalline phase and high purity [132]. However, further increase in the doping concentration of Zn^{2+} (above 2 wt%) small Bragg's diffraction peaks of ZnO related phase are emerged at 31.97°, 35.20°, 37.20° and 56.65° which can be assigned to the

diffraction from (100), (002), (101) and (110) planes respectively, according to JCPDS Card No. 75-0576. In addition, the impurity phase of ZnO peaks intensity increases with increase in the doping concentration of Zn^{2+} ions. This obviously reveals that the doping limit of Zn^{2+} ions in MgO lattice is favourable upto 2 wt% [133]. Figure 4.5.1(b) shows the peak broadening of MgO and Zn-MgO nanoparticles along (200) diffraction peak and it was found that the broadening was based on the Miller indices of the crystal plane. In the prepared samples, the reflection peak (002) is narrower than (111) peak whereas (220) peak is broader than (002) peak. This clearly indicates the presence of asymmetry in the crystallite shape and size [134]. Further, Zn^{2+} doping was confirmed by supervising the peak position of Zn-MgO diffractions along (200) plane, which are ascribed to the replacement of Mg^{2+} by Zn^{2+}. Notably, the strong peak (200) initially moves forward (right, $\Delta 2\theta \sim 0.07°$) when doping concentration was about 2 wt% of Zn^{2+}. This may be due to the successful incorporation of Zn^{2+} ions into MgO lattice. The peak further move towards lower angle side by ~ 0.02-$0.03°$ in 4 and 8 wt% of Zn-MgO and with a doping of 6 and 10 wt %, the angle of (200) peak slightly shifted towards higher angle side. The alternative shift suggests that there was a lattice contraction and expansion in the MgO lattice by Zn^{2+} (higher concentration) doping, which was due to generation of secondary phase in the MgO lattice. This phenomenon is due to the substitution of Zn^{2+} in the MgO lattice [135]. Meanwhile, it is apparent that the peak intensity corresponds to (200) peak has been increased with a decrease of FWHM (at concentration 2, 6 and 10 wt%). But, at the concentration of 4 wt% and 8 wt% of Zn^{2+} there is a slight decrease in the intensity of (200) peak compared to other Zn-MgO samples. This is due to the segregation of impurity phase on the surface of MgO, which leads to the generation of micro-strain in

109

the host lattice and compress the unit cell volume of Zn-MgO [136]. This shows obvious changes in the values of lattice parameter *'a'* in the cubic phase of MgO. By using the Bragg's law of cubic system ($a = b = c$, $\alpha = \beta = \gamma = 90°$), the lattice parameter *'a'* is calculated and mentioned in the Table 5.

Figure 4.5.2(a,b) illustrates the relation between crystallite sizes, micro-strain and dislocation density of MgO and Zn-MgO nanoparticles. Generally, the micro-strain is directly proportional to the dislocation density and inversely proportional to the crystallite size. Dislocations are the irregularity in a crystal which arises due to the lattice mismatch from one part of the crystal to another part. In this case, the dislocation densities are found to vary along with micro-strain as shown in Figure 4.5.2(a) and 4.5.2(b) [137]. The crystallite size (D), dislocation density (δ) and micro-strain (ε) of MgO and Zn-MgO nanoparticles were calculated and are given in Table 5.

Table 5. Calculated values of lattice parameters, cell volume, average crystallite size, micro-strain and dislocation density

| Property	MgO	$Mg_{0.98}Zn_{0.02}O$	$Mg_{0.96}Zn_{0.04}O$	$Mg_{0.94}Zn_{0.06}O$	$Mg_{0.92}Zn_{0.08}O$	$Mg_{0.90}Zn_{0.10}O$
a (Å)	4.2236	4.2190	4.2220	4.2164	4.2278	4.2182
Cell volume (Å)^3	75.3439	75.0980	75.2583	74.9593	75.5689	75.0553
Average crystallite size (nm)	56.83	60.76	53.93	76.95	68.96	58.01
Micro-strain (ε) in x 10^{-3}	0.6312	0.5824	0.7015	0.6395	0.5662	0.7846
Dislocation density (δ) in x 10^{14}	3.0963	2.7087	3.4383	1.6889	2.1028	2.9716

4.5.2.2. FE-SEM and elemental analysis
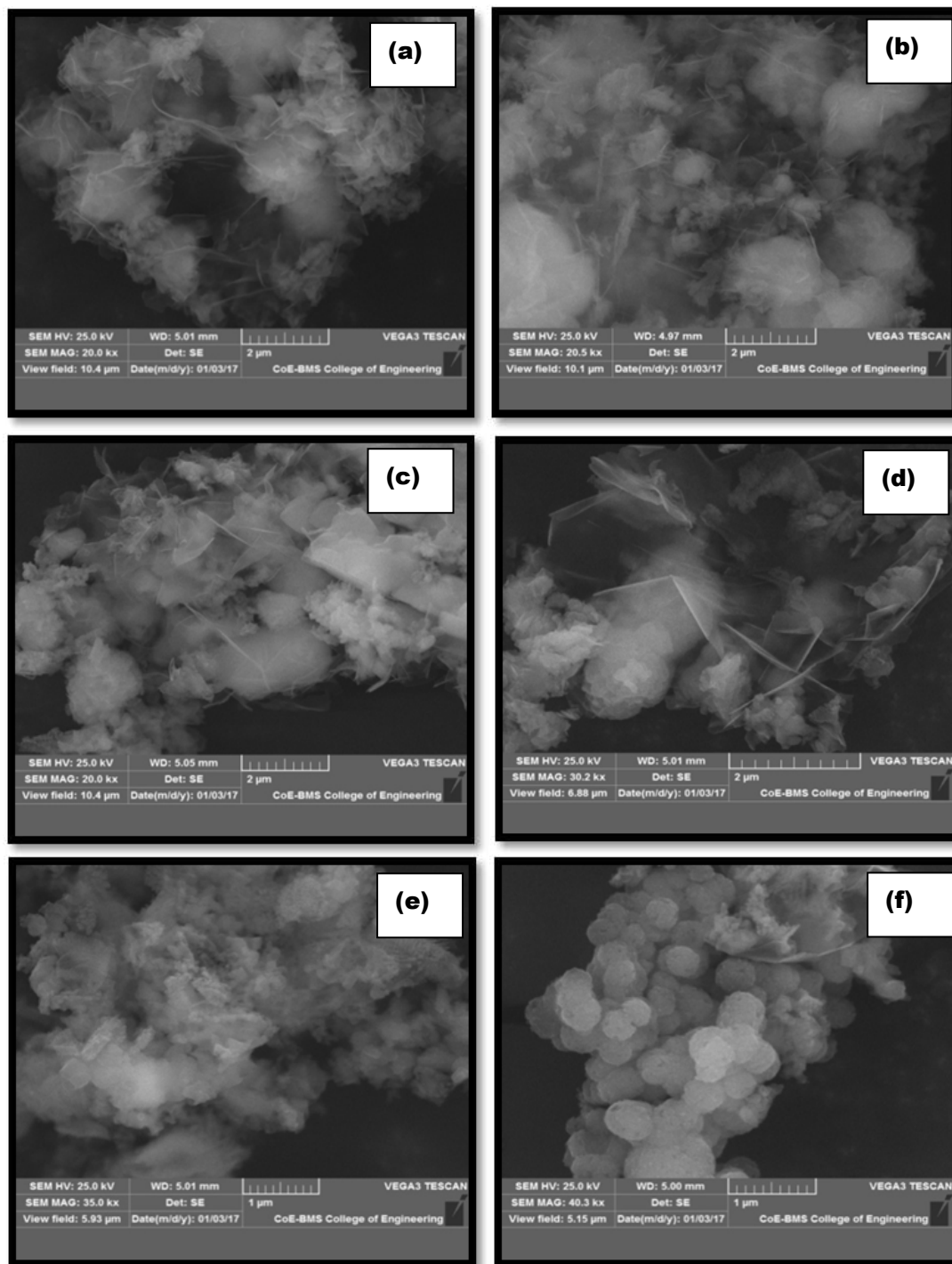
Figure 4.5.3: FE-SEM images of (a) Undoped MgO, (b) 2 wt% Zn-MgO, (c) 4 wt% Zn-MgO, (d) 6 wt% Zn-MgO, (e) 8 wt% Zn-MgO, (f) 10 wt% Zn-MgO nanoparticles.

111

FE-SEM is the technique used for visualizing the morphological picture of undoped and transition metal doped nano scale materials. It provides the significant knowledge of growth mechanism and crystal shape of the synthesized materials. Figure 4.5.3(a-f) shows the FE-SEM images of MgO and Zn-MgO nanoparticles with different weight percentage of Zn^{2+} doping. From the photomicrograph it was noted that all the particles present in the sample were nearly spherical in shape and exhibit nearly homogeneous grain distribution. The rate of grain segregation is a major factor that controls the grain size and shape of the final product [138]. The variation of grain size is observed in Zn-MgO at different weight percent of Zn^{2+} and the obtained grains were in nanometer range [139]. The EDAX is the promising method to estimate the elemental composition of synthesized nanoparticles. It gives the important information regarding to the weight and atomic percentage of elements present in the samples. Figure 4.5.4(a-f) shows the EDAX images of MgO and Zn-MgO nanoparticles. From Figure 4.5.4(a), it is clear that the synthesized MgO nanoparticle comprises only Mg and O elements which indicated that the obtained MgO was pure and single phase. Moreover, Figure 4.5.4(b-f) shows the EDAX spectra of Zn-MgO nanoparticles, which clearly shows that the peak height was improved with different concentration of Zn ions. This confirmed the existence of Zn in Zn-MgO nanocrystals [140].
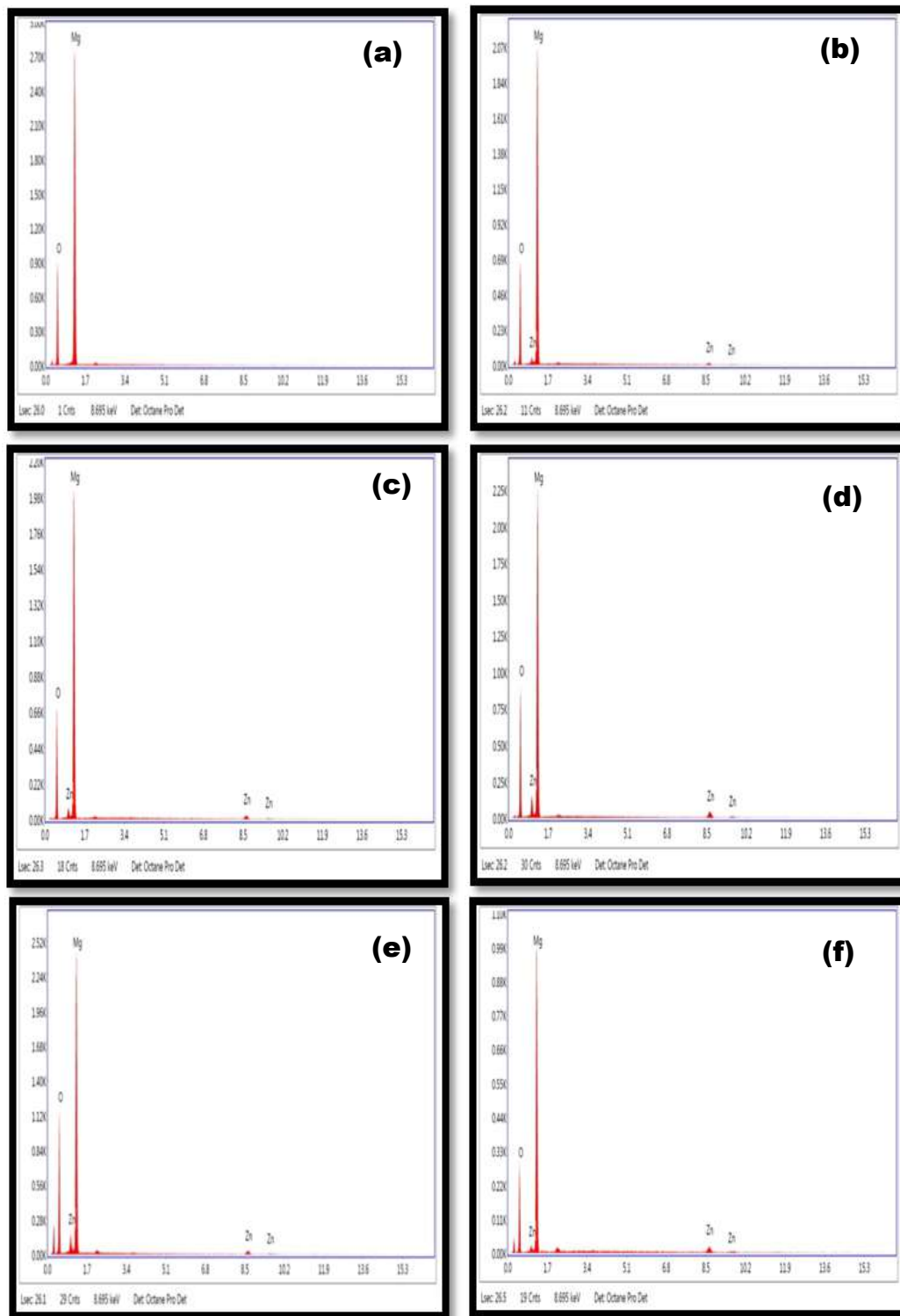
Figure 4.5.4: EDAX micrographs of undoped, 2, 4, 6, 8 and 10 wt% of Zn-MgO nanoparticles.

4.5.2.3. UV-Visible spectral analysis
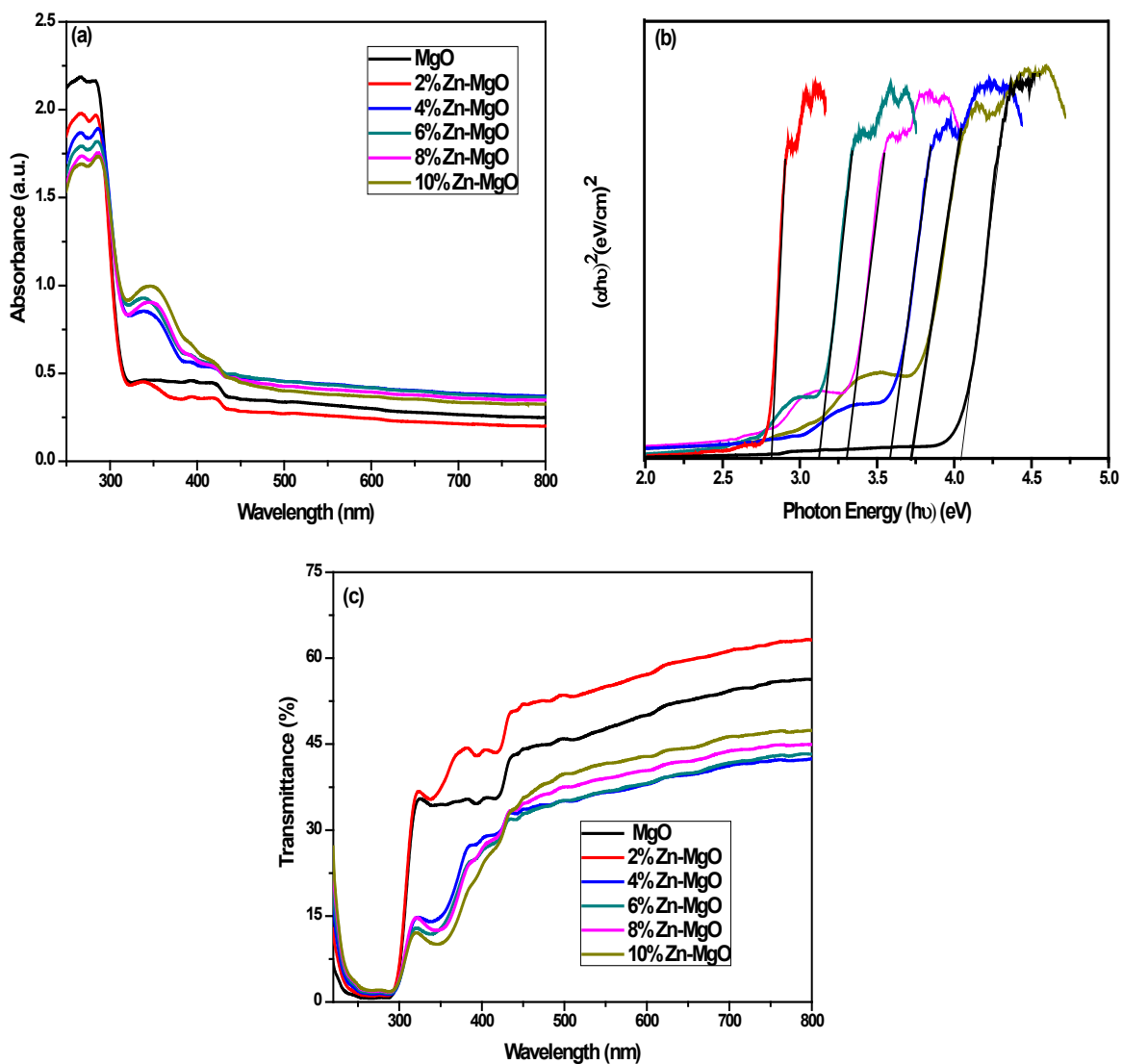
Figure 4.5.5: (a) Optical absorption spectra, (b) Tauc plot, (c) transmittance spectra of undoped MgO and Zn-MgO nanoparticles.

Figure 4.5.5(a) shows the analysis of UV-Visible absorption spectra of synthesized MgO and Zn-MgO nanoparticles. The absorbance of synthesized samples was measured in the wavelength range of 200-800 nm at room temperature [141]. As it is observed from the Figure 4.5.5(a), the absorbance of MgO was lower compared to all Zn-MgO (4-10 wt%) samples except 2 wt% of Zn-MgO. In addition, all the samples

114

show sharp absorption in the UV-region and very weak absorption in the visible region. This is due to the creation of more defects in the MgO lattice upon Zn^{2+} doping [142]. Optical transmittance spectrum of MgO and Zn-MgO nanoparticles in 200-800 nm domain is shown in Figure 4.5.5(c). This obviously shows the inverse trends on absorption spectra of MgO and Zn-MgO nanoparticles. The maximal transmittance was observed in the 2 wt% of Zn-MgO and other samples Zn-MgO (4-10 wt %) showed poor transmittance compared to pure MgO. This is due to absorbance and transmittance of doped samples are generally depends on the numerous factors like oxygen vacancy, grain boundary, thickness and impurity centres. The optical bandgap of MgO and Zn-MgO nanoparticles was calculated from Tauc plot method and it is shown in Figure 4.5.5(b). The energy gap is found to be 4.09 eV for MgO, 2.82, 3.71, 3.12, 3.58 and 3.72 eV for 2, 4, 6, 8 and 10 wt% of Zn-MgO nanoparticles, respectively. These results clearly confirms that the optical band gap of the MgO nanoparticles can tune by Zn^{2+} doping and are promising candidates for DSSCs [143].

4.5.2.4. TEM and SAED analysis

Transmission electron microscopy (TEM) and selected area electron diffraction (SAED) techniques are one of the prominent methods to analyze the morphology of synthesized undoped and doped nanoparticles. Figure 4.5.6(a) and (c) show the TEM micrographs of pure MgO and 6 wt% Zn-MgO nanoparticles. These images reveal that the size of the synthesized samples fall in the nanometre regime and the shape of the particle are spherical in shape. In addition, the particle size distribution of MgO and Zn-MgO nanoparticles is non-uniform and in-homogeneous [144]. Figure 4.5.7(b) shows the SAED pattern of MgO nanoparticles which confirmed that the obtained sample has

cubic phase structure with single crystalline nature. In Figure 4.5.7(d), the diffraction ring spots illustrate the polycrystalline nature of Zn-MgO, which clearly indicates the segregation of nanoparticles and formation of ZnO phase at 6 wt% of Zn-MgO. All the photomicrograph of TEM and SAED confirmed that Zn^{2+} is substantially incorporated in the MgO lattice and the particles have several single grains of varying sizes [145].

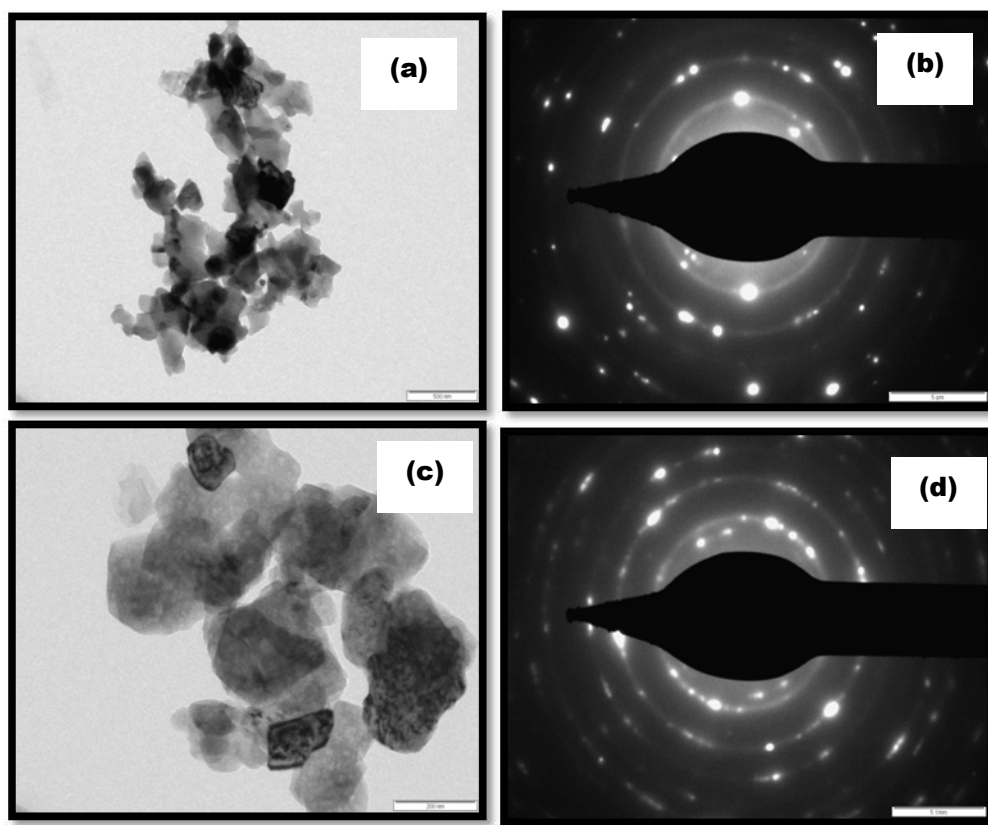**Figure 4.5.6:** TEM and SAED images of undoped MgO (a, b) and 4 wt% Zn-MgO (c, d) nanoparticles calcinated at 500 °C.

4.5.2.5. Electrical properties MgO and Zn-MgO nanoparticles

The I-V characteristics studies of MgO and Zn-MgO nanoparticles synthesized by microwave combustion method have been carried out using Keithley source meter. Figure 4.5.7(a-b) show the I-V characteristics of MgO and Zn-MgO nanoparticles under

the dark and UV-light condition. These figures revealed the non-linear and rectifying nature of the synthesized samples [146]. This confirmed the formation of schottky contact in between the Ag/MgO and Ag/Zn-MgO junction [147]. In I-V curves, the MgO nanoparticles show the low current intensity and high resistance as compared to Zn-MgO (2-6 wt%) nanoparticles in the dark condition. This is because the adsorbed oxygen under dark condition may generate high potential barrier near the surface of MgO, which hinders the electrical transport [148]. The 2 wt% of Zn-MgO nanoparticles shows the high current intensity as compared to MgO nanoparticles, which is due to the increase in the concentration of charge carrier in MgO upon Zn^{2+} doping.
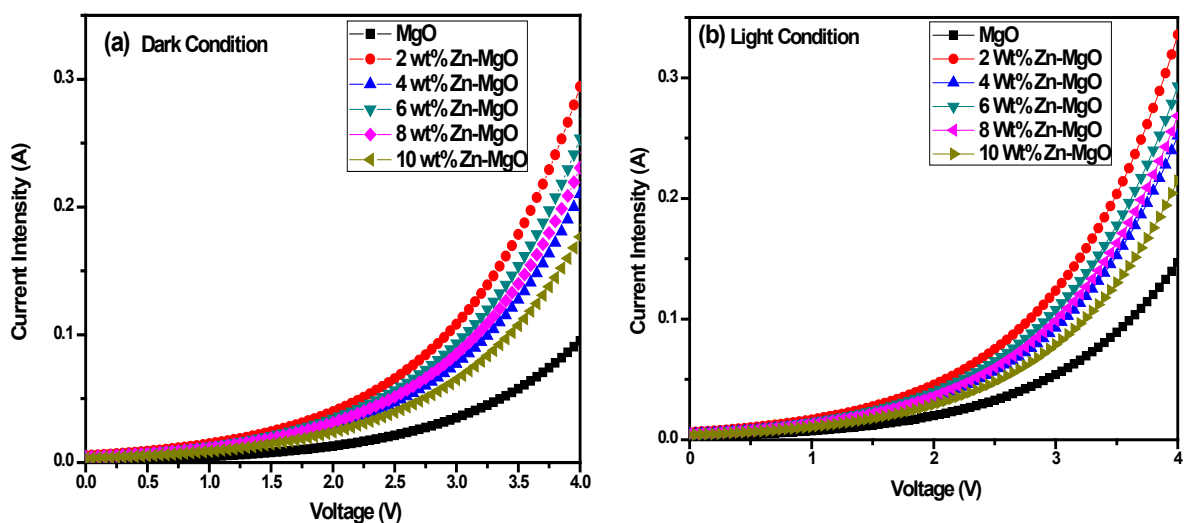
Figure 4.5.7: I-V characteristics of undoped MgO and Zn-MgO nanoparticles in dark and light conditions.

However, with increase in the concentration of Zn^{2+} (> 2 wt%) in MgO lattice, the current intensity was found to be reduced and is attributed to the segregation of Zn^{2+} ions to form grain boundaries or interstices [149]. The MgO and Zn-MgO nanoparticles have considerable enhancement in the current intensity under UV-Vis. light condition. This

indicates that the absorption of UV-Vis. light generates electron-hole pairs and these holes combine with the electrons of adsorbed O^{2-} ions to form O_2 molecules on the surface of MgO and Zn-MgO samples. This leads to a reduction of the depletion barrier thickness and height of the barrier. In the mean time, the unpaired photo-generated electrons are jumped from valence band to conduction band, which enhance the current intensity of MgO and Zn-MgO nanoparticles [150].

4.5.3. Conclusions

The present study demonstrates the successful synthesis of MgO and Zn-MgO nanoparticles via microwave combustion method. The influence of Zn^{2+} doping on structural, optical and electrical properties of MgO nanoparticles was studied. The synthesized samples were characterized by XRD analysis and the results showed that the incorporation of Zn^{2+} did not change the cubic phase of MgO. Nano-sized crystallites with dominant spherical morphology were observed by SEM and TEM analysis. The optical bandgaps of synthesized MgO and Zn-MgO nanoparticles were estimated through optical absorption spectra, which shows a red shift upon substitution of Zn^{2+}dopant. The current-voltage (I-V) measurement under dark and light conditions showed the photosensitive behaviour of MgO and Zn-MgO nanoparticles. Therefore, the increased current intensity of Zn-MgO nanoparticles clearly indicated the possibility of using these nanoparticles in the applications of dye sensitized solar cells (DSSCs).

4.6. Structural, Optical and Electrical Properties of ZnO Nanoparticles Synthesized Under Different Microwave Power

4.6.1. Introduction

Semiconducting metal oxide nanomaterials are recently gained more interest due to their unique properties, novel synthesis route and well shape of materials. Metal oxide semiconductors, such as indium oxide (In_2O_3), zinc oxide (ZnO), copper Oxide (CuO), tin oxide (SnO_2), zirconium oxide (Zr_2O_3) and titanium oxide (TiO_2) etc. have been considered for various scientific applications [151]. Among these materials, ZnO is an important *n*-type transition metal oxide with a wide band gap of 3.37 eV and large exciton binding energy of 60 meV at room temperature. It has paying attention in dye sensitized solar cells [152], electrochemical analysis of drugs [153], batteries [154], super capacitors [155], catalysts in organic reactions [156], sunscreen and cosmetics [157], schottky diodes [158] and hydrogen generation from water splitting [159]. During the past few decades, the researchers have been focused on the fabrication of different structured ZnO nanoparticles such as nano-rods, nano-flowers, nano-flakes, nano-prisms, nano-disks, nano-wires and nano-plates. This is due to the acceptable crystal shape and crystallite size of ZnO nanoparticles, which is the major consideration to control the various structural dependent properties like optical, electrical and magnetic properties [160]. Furthermore, the various morphologies of ZnO nanostructures are expected to use in the build up a well performed optoelectronic devices with special structural design and unique optoelectronic properties. However, achievement of controlling the crystallite size and fabrication of new morphologies of ZnO are more difficult in recent years [161].

119

As of now, various morphologies of ZnO nanostructures were synthesized by different methods like hydrothermal, solvothermal, co-precipitation, thermal evaporation, sonochemical and sol-gel methods [162]. Generally, the above methods require more advanced equipments, relatively more time consumption and also additional solvents for the preparation of ZnO nanoparticles [163]. Out of the various methods, microwave combustion method has recently accepted method because: i) microwave has strong penetrating power into the materials and so the rate of reaction can be increased; ii) microwave radiation can be absorbed only by polarized material; and iii) microwave is a non-thermal reaction. These conditions favour the acceleration in reaction rate, improvement of product yield, increased purity of the material, good control of stoicheometry and well-defined size distribution [164]. Because of these advantages, microwave assisted method can be used for the synthesis of nanoparticles such as CuO nanowires, ZnO, Cu_2O, SnO_2 nano prisms, rods, spheres and stars like Fe_2O_3 with novel structural properties [165].

In this chapter microwave combustion method has been adapted to synthesis the hexagonal prism shaped ZnO nanoparticles. The main goal of this work is to discuss the effect of microwave power on crystal structural, optical and electrical properties with the help of X-ray diffraction studies (XRD), Field emission scanning electron microscopy (FE-SEM), UV-Visible spectroscopy (UV-Vis.) and I-V characterization technique.

4.6.2. Results and discussion

4.6.2.1. XRD analysis

X-ray diffraction (XRD) pattern is the promising method for the identification of micro-structural properties, phase purity and crystal imperfection of the synthesized

metal oxide nanoparticles. Figure 4.6.1 shows the powder XRD patterns of ZnO nanoparticles synthesized under different microwave powers (160, 320, 480, 640 and 800 W). The ten major diffraction peaks were observed in the XRD pattern of ZnO nanoprisms at different Bragg's diffraction angles, corresponding to (100), (002), (101), (102), (110), (103), (200), (112), (201), (004) and (202) directions of ZnO nanoparticles. All the peaks of XRD graph indexed the wurtzite structure and hexagonal phase of ZnO nanoparticles, which is in good agreement with the JCPDS (Joint Committee on Powder X-ray Diffraction Studies) card no. 79-0208 with lattice constants; $a = b = 3.264$ Å, $c = 5.129$ Å . In addition, there were no peaks observed corresponding to the impurities like Zn metal and $Zn(OH)_2$ and so it confirms the high purity of ZnO nanocrystals [166]. Figure 4.6.2(a) shows broadening of peaks at (100), (002) and (101) planes of ZnO with increase in the microwave power. The shifting of major (100), (002) and (101) diffraction planes towards lower 2θ values was observed as a function of microwave power. The broadening and shifting of diffraction planes specifies that the lattice parameter, d-spacing, crystallite size and unit volume of ZnO were affected by the microwave energy [167]. The intensity of XRD peaks were enhanced upto a microwave power of 480 W and this is due to the decrease of FWHM. Above 480 W of microwave power an increase in the FWHM has resulted. This result has shown that the crystalline property of ZnO nanoparticles is dependent on microwave power [168]. In this study, the lattice constants ('*a*' and '*c*') for pure ZnO nanoparticles were calculated using the formula based on Bragg's law. Figure 4.6.2(b) shows that the lattice parameters '*a*' and '*c*' of synthesized ZnO nanoparticles under different microwave power. It demonstrates that there is no considerable variation in the calculated lattice parameters with increase in microwave power (Table 6). Also, the *c*/*a* ratio of unit cell parameters reveals the

hexagonal structure of ZnO which was not affected by different microwave power [169]. The crystallite size, micro-strain and dislocation density are three important parameters to analyze the properties of synthesized nanoparticles, which were determined from the XRD data. Figure 4.6.3 shows the relation between the above parameters of the synthesized ZnO nanoparticles under different microwave power. This reveals that, the parameters like micro-strain and dislocation density are inversely propositional to crystallite size i.e., the micro-strain and dislocation density of synthesized ZnO nanoparticles decreases with increase the crystallite size or vice-versa [170]. The estimated values of micro-strain, dislocation density and crystallite size of all the samples are listed in the Table 7.

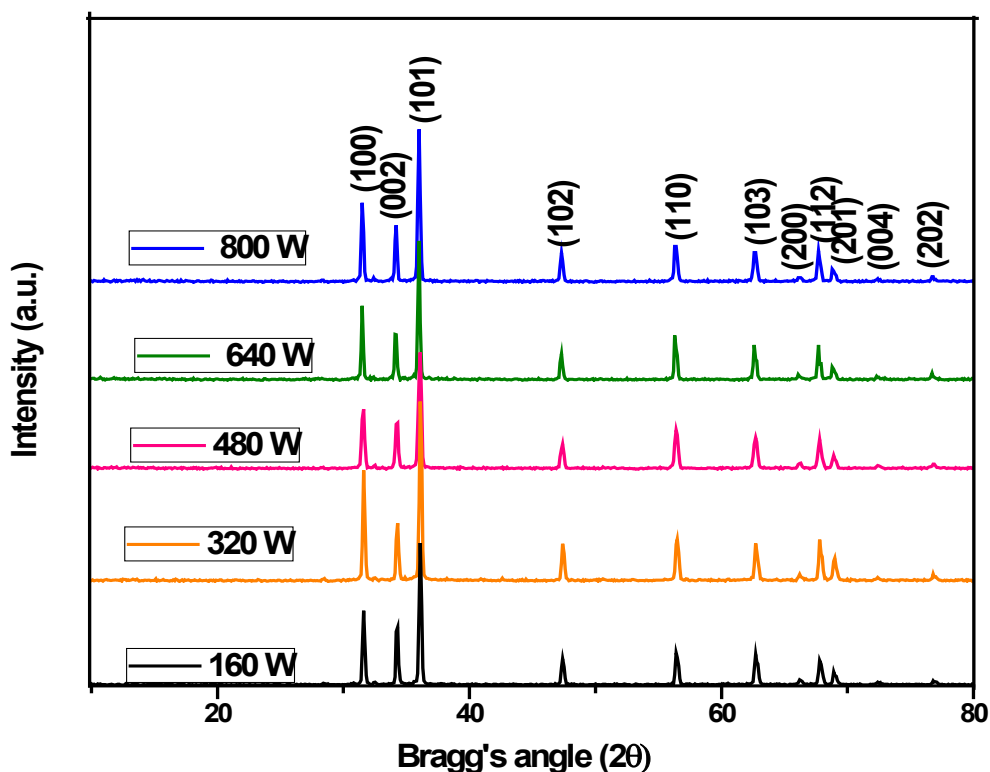**Figure 4.6.1:** Powder X-ray pattern of ZnO nanoparticles synthesized at 160, 320, 480, 640 and 800 W microwave power.
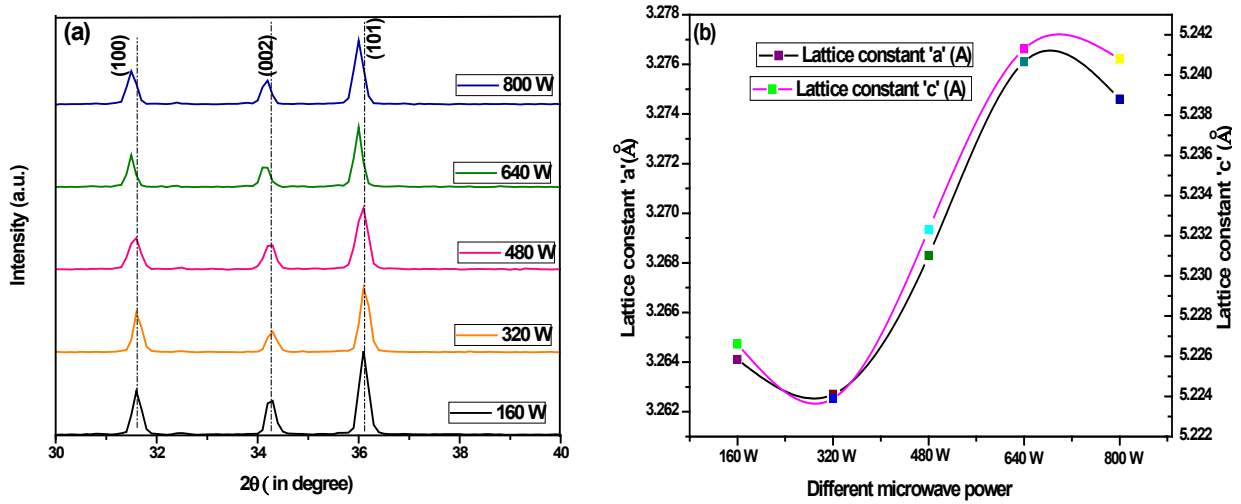
Figure 4.6.2: (a) The shift of peaks positions, (b) the changes in the cell constants '*a*' and '*c*' of ZnO nanoparticles synthesized under different microwave power.
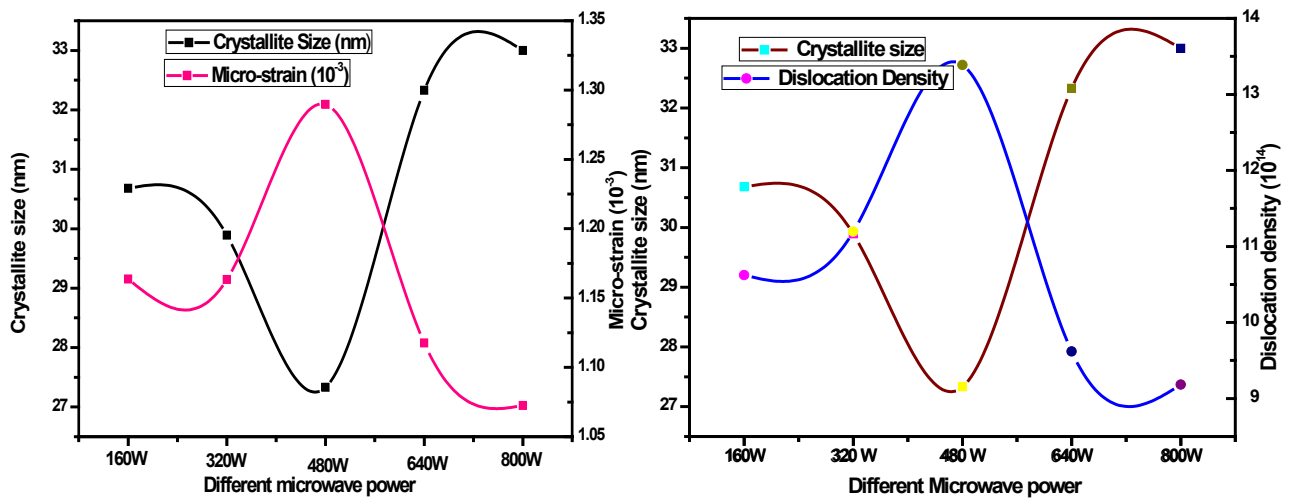
Figure 4.6.3: Crystallite size, micro-strain and dislocation density of ZnO nanoparticles synthesized at different microwave powers.

Table 6. Lattice parameters ('*a*' and '*c*'), unit cell volume, bond length and c/a ratio of synthesized ZnO nanoparticles under different microwave power

Samples	a (Å)	c (Å)	Volume (Å)^3	Bond length (Å)	c/a ratio
ZnO (160 W)	3.2641	5.2266	48.2241	1.9861	1.6012
ZnO (320 W)	3.2627	5.2239	48.1578	1.9853	1.6011
ZnO (480 W)	3.2683	5.2323	48.4010	1.9892	1.6009
ZnO (640 W)	3.2761	5.2413	48.7159	1.9930	1.5998
ZnO (800 W)	3.2746	5.2408	48.6667	1.9928	1.6004

Table 7. Crystallite size, micro-strain and dislocation density of synthesized ZnO nanoparticles under different microwave power

Samples	Crystallite size (nm)	Micro-Strain (10^{-3})	Dislocation density (10^{14})
ZnO (160 W)	30.68	1.1636	10.624
ZnO (320 W)	29.89	1.1633	11.193
ZnO (480 W)	27.33	1.2896	13.388
ZnO (640 W)	32.24	1.1176	09.620
ZnO (800 W)	33.00	1.0725	09.183

4.6.2.2. FE-SEM and EDAX analysis

Figure 4.6.4: FE-SEM images of ZnO nanoparticles synthesized with different microwave power: (a) ZnO-160 W; (b) ZnO-320 W; (c) ZnO-480 W; (d) ZnO-640 W and (e) ZnO-800 W.
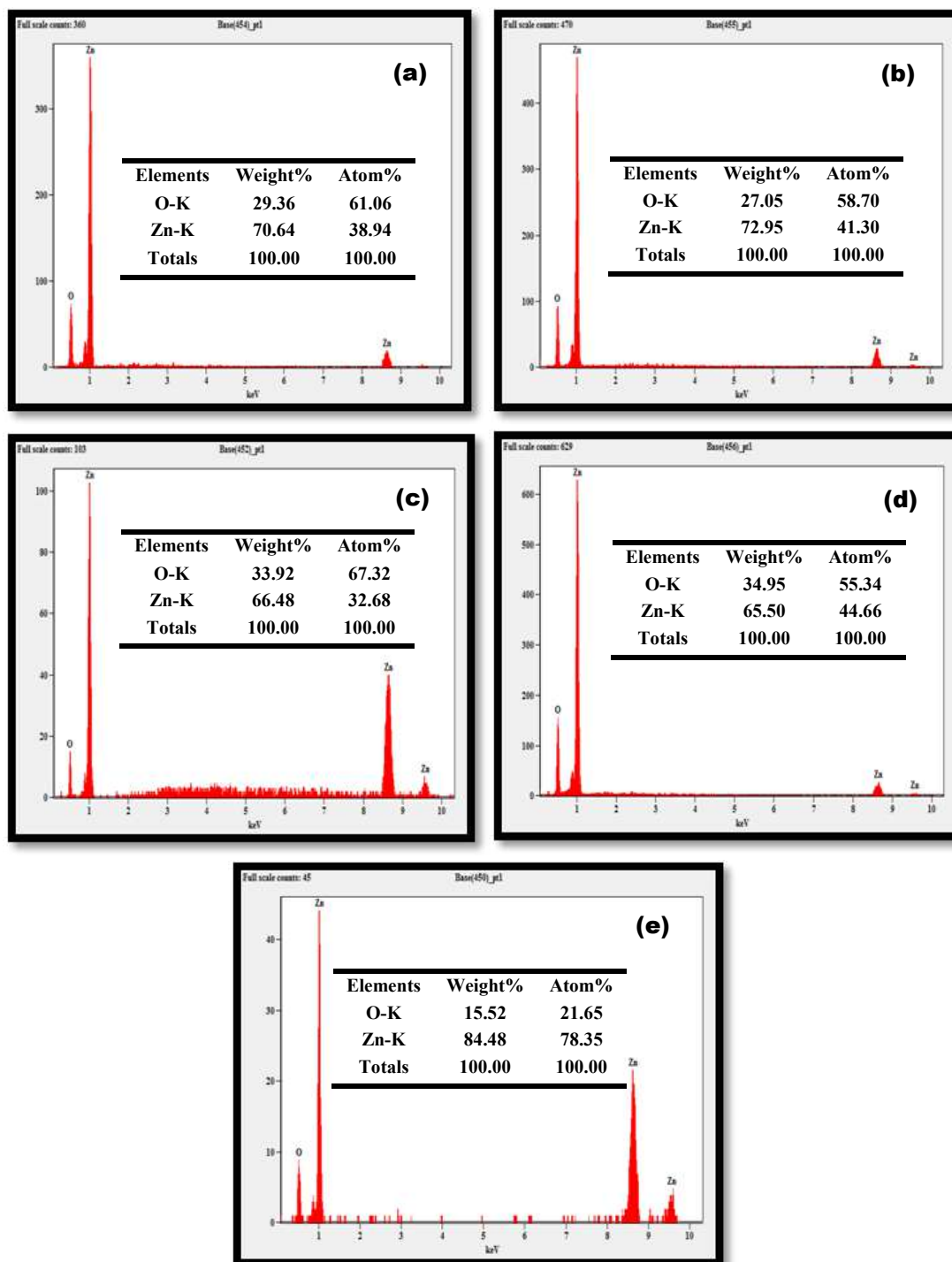
Figure 4.6.5: EDAX of ZnO nanoparticles produced with different microwave power: (a) ZnO-160 W; (b) ZnO-320 W; (c) ZnO-480 W; (d) ZnO-640 W; (e) ZnO-800 W.
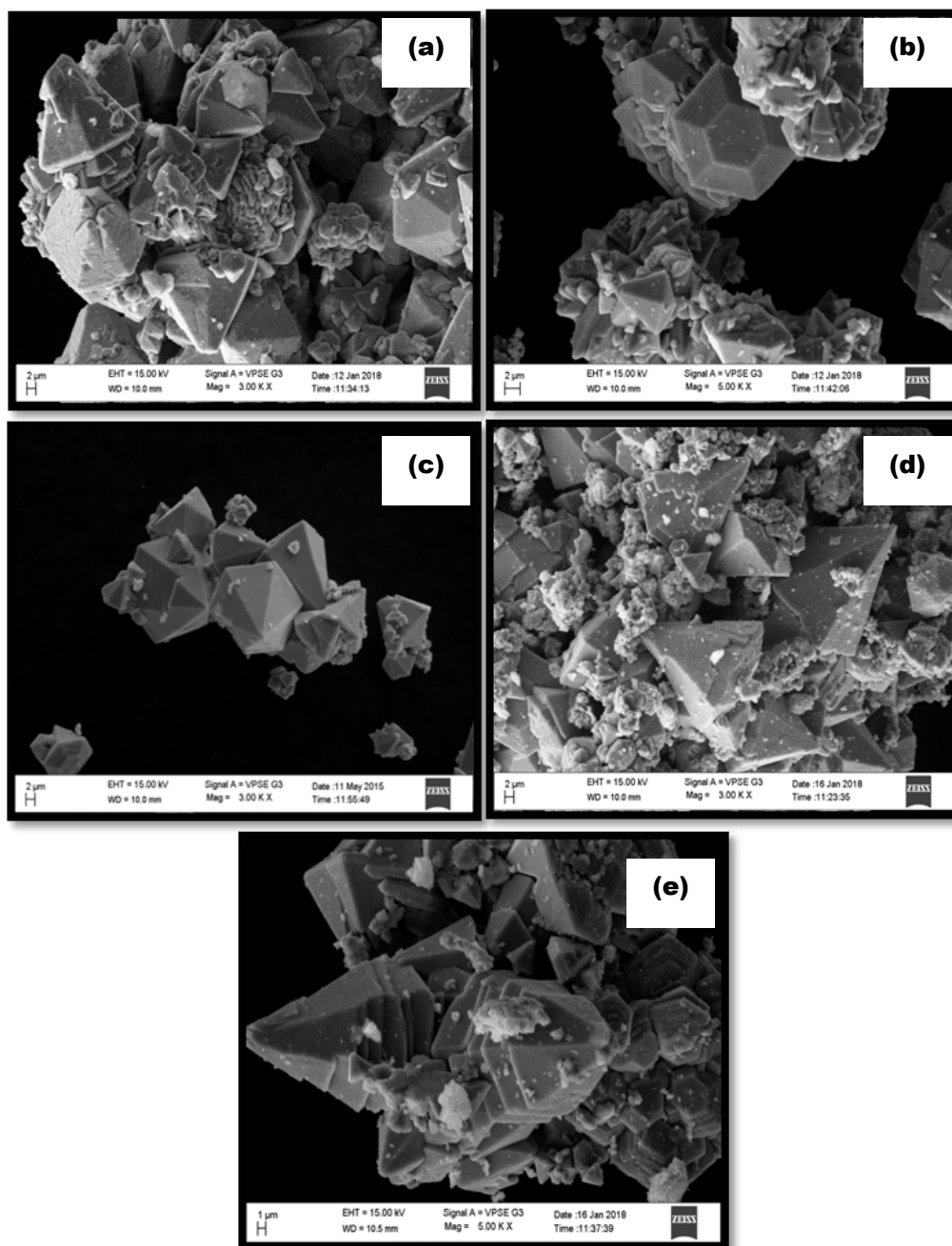
The FE-SEM is one of the most commonly used experimental techniques for morphological identification of synthesized metal oxide nanoparticles. Figure 4.6.4(a-e) represents the FE-SEM photomicrographs of ZnO nanoparticles synthesized under different microwave power. It is evident from the FE-SEM images that the ZnO nanoparticles prepared under different microwave power show almost hexagon prism like structure with sharp tip having good crystalline quality [171-172]. The FE-SEM images of ZnO nanoparticles obtained at different microwave power show the agglomeration of the grains. The grain segregation is a most significant factor that controls the crystallite size and shape of the synthesized materials [173]. Figure 4.6.5(a-e) shows the EDAX spectrum of ZnO nanoprisms. The EDAX spectrum of all the synthesized ZnO nanoparticles shows an evidence for the existence of Zn and O. This indicated that all the prepared ZnO nanoparticles have got well crystalline and high purity nature [174].

4.6.2.3. UV-Visible spectral analysis

Figure 4.6.6: (a) UV-Vis absorbance, (b) reflectance spectra of ZnO nanoparticles obtained at different microwave power.

Figure 4.6.7: Plot of $[F(R)h\nu]^2$ versus energy gap for ZnO nanoparticles synthesized using microwave power : (a) 160 W; (b) 320 W; (c) 480 W; (d) 640 W; (e) 800 W.
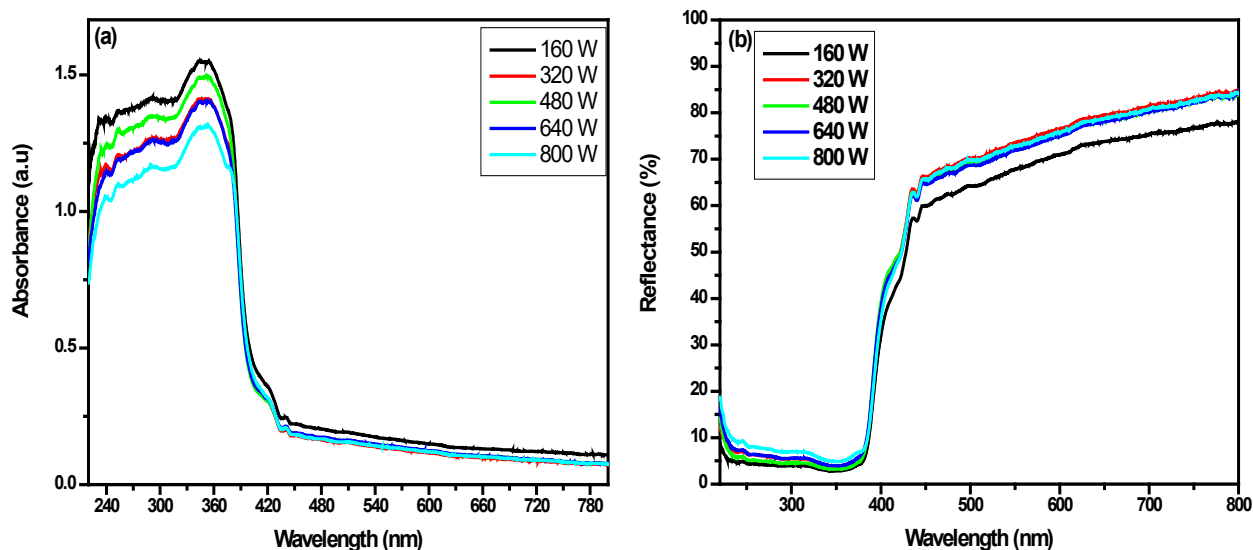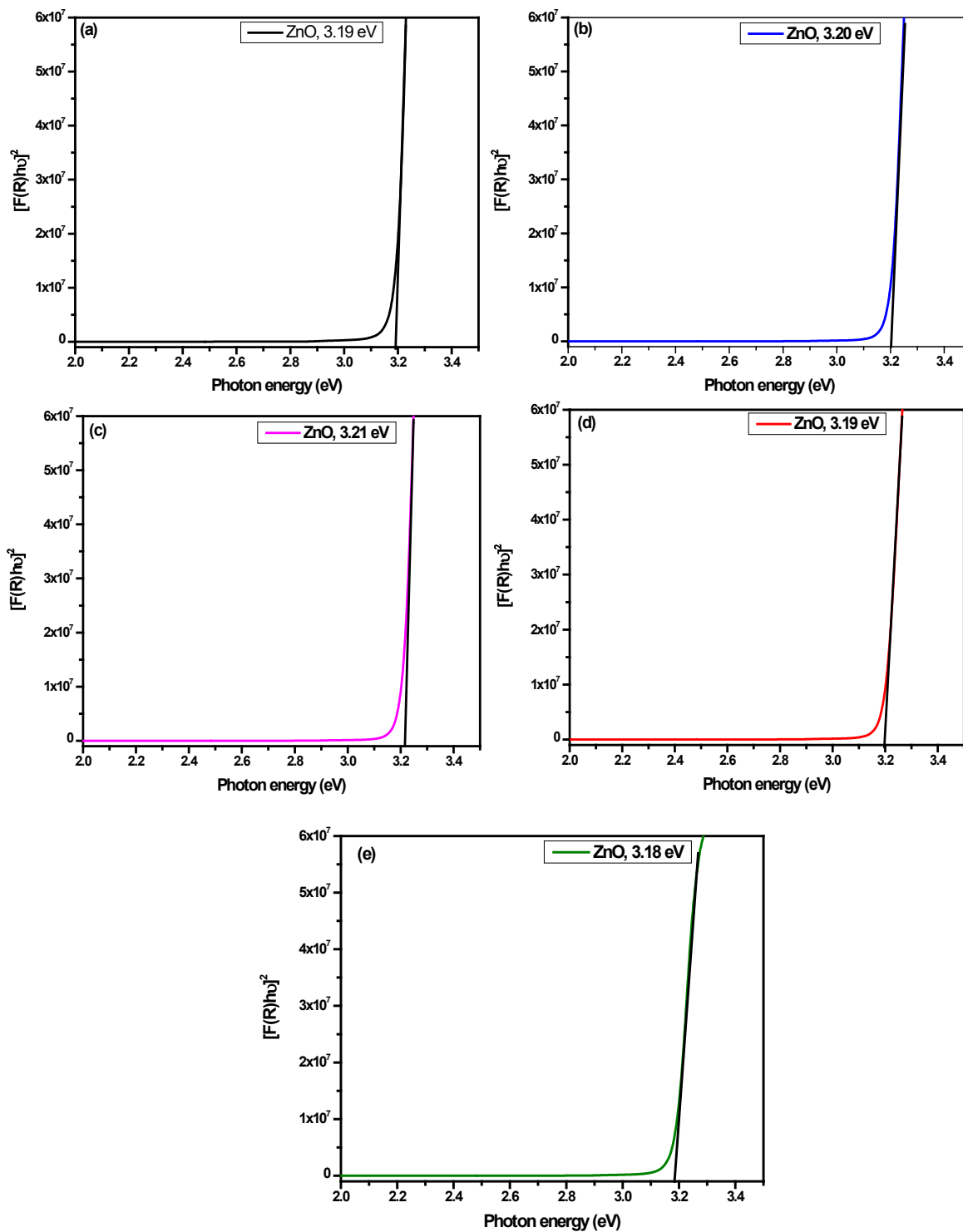
The optical energy gaps of synthesized ZnO nanoparticles at different microwave power have been estimated by optical absorbance and reflectance measurements carried out between 200-800 nm wavelength regions at room temperature [175]. Figure 4.6.6(a) illustrates the absorbance spectra of synthesized ZnO nanoparticles at different microwave power. The optical absorption edge of ZnO nanostructures synthesized at 160-480 W microwave power shows red shift, whereas the ZnO synthesized at high microwave power (640-800 W) shows slight blue shift. Figure 4.6.6(b) shows the diffused reflectance spectra of ZnO nanoparticles synthesized at different microwave power. It reveals that all the prepared samples show perfect reflection in the visible region. The reflection (%) of all the ZnO samples increased with increase in the microwave power upto 480 W. The band gap of ZnO nanoparticles prepared under different microwave power was determined by Kubelka-Munk method. Figure 4.6.7 shows the plot of photon energy in eV versus $[F(R)h\nu]^2$ for ZnO nanoparticles. The optical band gap was found to be 3.19, 3.20, 3.21, 3.19, 3.18 eV for 160, 320, 480, 640 and 800 W respectively [176].

4.6.2.4. Electrical properties of ZnO nanoparticles

The current-voltage (I-V) characteristic studies of ZnO films have been carried out using silver paste to make good electrical contact. Figure 4.6.8(a-b) illustrates the I-V response of ZnO nanostructures synthesized via microwave combustion method at 160, 320, 480, 640 and 800 W of microwave power. From I-V curves, it can be shown that all the synthesized ZnO nanoparticles have non-linear characteristics in dark as well as in light conditions. From these results, it can be assumed that the nonlinear property of the synthesized ZnO samples is related to amount of oxygen and the precipitate of metal

oxide in the grain boundaries. The EDAX spectrum gives a proof for the presence of very high atomic percentage of oxygen in the synthesized ZnO nanoparticles. This represents the prepared ZnO nanoparticles are metal deficient [177].
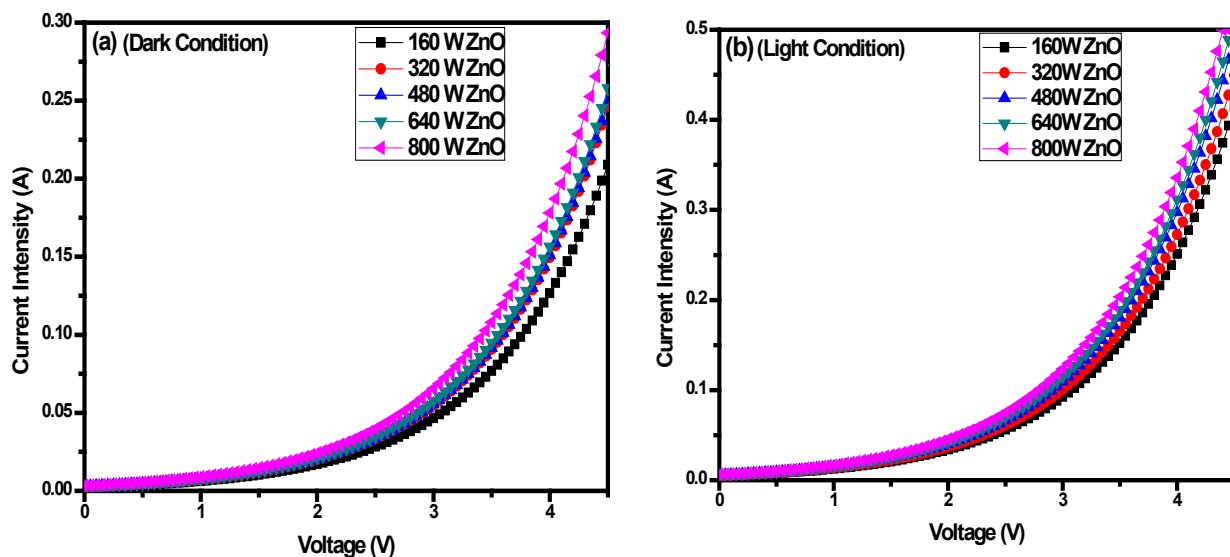
Figure 4.6.8: I-V characteristics of ZnO nanoparticles synthesized under different microwave power in dark and light conditions.

The current intensity of ZnO nanoparticles prepared at the microwave power of 800 W have shown good current intensity and low resistance compared to ZnO nanoparticles prepared at other microwave power of 160, 320, 480 and 640 W (Figure 4.6.8(a)). Smaller the band gap, faster will be transition of electron from valence band to conduction band and hence higher will be the current intensity [178]. Figure 4.6.8(b) shows the current-voltage characteristic of ZnO nanoparticles in UV-light condition. It shows that, all the samples of ZnO have considerable enhancement in the current intensity (Curves moves to lower potential side) under UV-light illumination. This indicated that the motion of charge carriers increases under the light condition and considerably improves the current intensity of ZnO nanoparticles [179].

4.6.3. Conclusions

In this chapter, pure hexagonal phase and wurtzite structure of ZnO nanoparticles were successfully synthesized by an inexpensive microwave combustion route at 160, 320, 480, 640 and 800 W. The XRD shows that microwave power affect the crystallite size of synthesized ZnO nanoparticles. The FE-SEM analysis showed the hexagon prism structure of ZnO nanoparticles. The optical bandgap of synthesized ZnO nanostructures were estimated through diffused reflectance spectra which shows a red shift upon increasing the microwave power. The current-voltage characteristic of ZnO nanoparticles obtained from different microwave power showed the photosensitive behaviour under dark as well as UV-light conditions.

4.7. Structural, Optical and Electrical Properties of Synthesized ZnO Nanoparticles by Microwave Combustion Method Using Different Solvents

4.7.1. Introduction

Zinc oxide (ZnO) is an important n-type semiconductor nanoparticle, which shows unique optical and electronic properties due to its wide bandgap of 3.37 eV and the large exciton binding energy (60 eV) at room temperature [180]. Moreover ZnO is a commercially available material with the advantage of non-toxicity, low-cost, high chemical stability and environmental friendly. Because of these properties, ZnO nanoparticles possess many interesting applications in transparent conductive coatings, electrode materials for dye-sensitized solar cells, gas sensors and electro-photo luminescent materials [181]. Recently, ZnO can be prepared in different morphologies including nano-flowers, nano-rods, nano-plates, nano-wires, nano-prisms, nano-disks and so forth [182]. The chemical and physical properties of ZnO nanoparticles depend on structural properties like crystallite size, shape and surface structures. Furthermore, the ZnO with different morphologies can be prepared by following certain reaction conditions. Also the reaction temperature, pH of the reaction mixture, time, reactants stoichiometry and the use of specific zinc ion salt will significantly alters the morphologies of synthesized ZnO nanoparticles [183-184].

The solvent phase synthesis of nanoparticles is more familiar compared to the solid phase and other types of syntheses. The organic solvents are more frequently being used in the synthesis of metal oxide nanoparticles [185]. The point in choosing the organic solvents for the preparation of metal oxides nanoparticles is because of their good

stabilizing ability that facilitates better crystal growth without abnormal segregation of particles. Furthermore, the synthesis steps are easy to perform and require neither multi-steps nor an advanced experimental condition or equipment [186]. The organic solvents like high boiling polyols such as ethylene glycol (EG), di-ethylene glycol (DEG), tetra ethylene glycol (TEG) and glycerol have been used.

In this chapter, a simple microwave method has been used to synthesize the hexagonal prism shaped ZnO nanoparticles. The main goal of this work was to discuss the effect of solvents on structural, optical and electrical properties of synthesized ZnO nanoparticles.

4.7.2. Results and discussion

4.7.2.1. XRD analysis
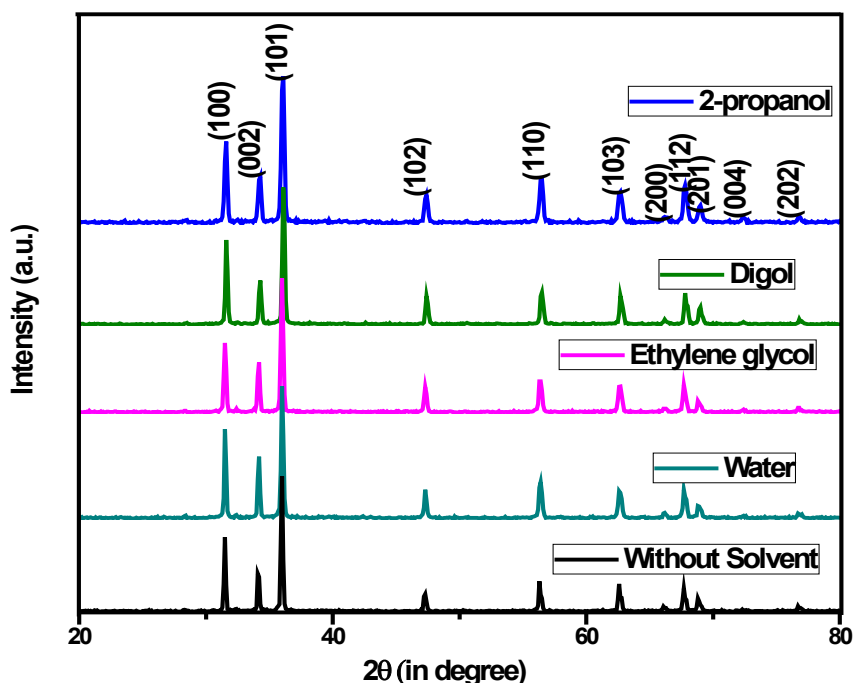
Figure 4.7.1: X-ray diffraction pattern of ZnO nanoparticles synthesized using different solvents.
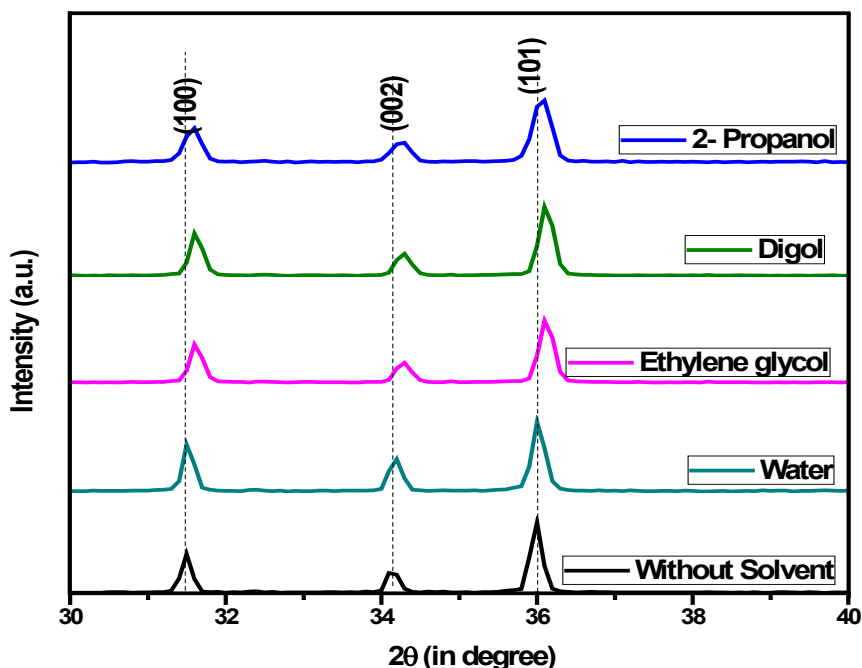
Figure 4.7.2: Shifting and broadening of (100), (002) and (101) peaks for ZnO nanoparticles synthesized using different solvents.

Figure 4.7.1 illustrates a typical X-ray diffraction pattern of synthesized ZnO nanoparticles prepared by microwave combustion method using different solvents. The major XRD peaks were observed at 2θ value of 31.49°, 34.17°, 35.99°, 47.29°, 56.37°, 62.66°, 67.74°, 68.88°, 72.36° and 76.77° which can be assigned to (100), (002), (101), (102), (110), (103), (200), (112), (201), (004) and (202) planes respectively, according to JCPDS Card No. 79-0208 (Lattice parameters: $a = b = 3.264$ Å, $c = 5.219$ Å). This clearly shown that all the diffraction peaks in the XRD pattern belongs to hexagonal phase of ZnO with a wurtzite type of structure (space group: P6$_3$mc) [187]. No additional peaks corresponding to Zn metal, Zn(OH)$_2$ and ZnO$_2$ were observed, which confirmed that the ZnO nanoparticles obtained with and without solvents have got same type of morphology [188]. Figure 4.7.2 shows the enlarged view of major (100), (002) and (101) diffraction planes for ZnO nanoparticles synthesized using different solvents. It reveals

the diffraction peaks of ZnO nanoparticles synthesized at different solvents are slightly broadened as compared to the peaks synthesized without solvent. Further, the shifting of major (100), (002) and (101) diffraction planes towards higher 2θ values was observed as a function of solvents used. The broadening and shifting of diffraction planes specifies that the lattice parameter, d-spacing, crystallite size and unit volume of ZnO were slightly affected by the solvents [189]. In this study, the lattice constants ('*a*' and '*c*') for pure ZnO nanoparticles were calculated using the formula based on Bragg's law.
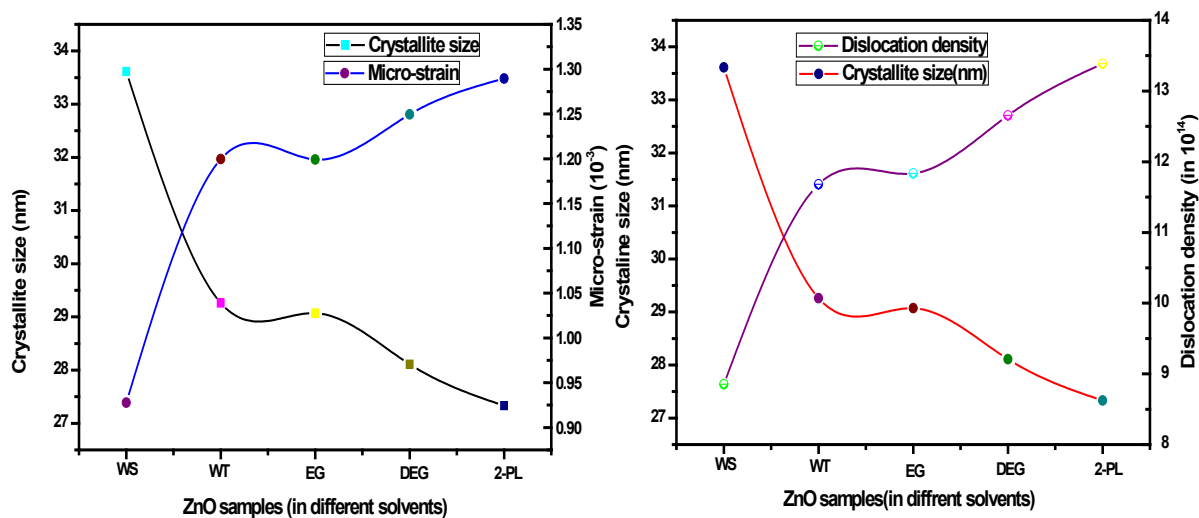
Figure 4.7.3: Variation of crystallite size, micro-strain and dislocation density of ZnO nanoparticles synthesized using different solvents.

Table 8 shows the calculated values of lattice parameters of ZnO nanoparticles synthesized using different solvents. The calculated values of lattice parameters shows a slight deviation compared to standard values which may attributed to the existence of various defects in the ZnO lattice such as surface defects and Zn interstitials [190]. Figure 4.7.3 illustrates the relationship between micro-strain, dislocation density and average crystallite size of ZnO nanoparticles synthesized using different solvents. Figures revealed that, the parameters like micro-strain and dislocation density are inversely

proportional to crystallite size i.e., the micro-strain and dislocation density of synthesized ZnO nanoparticles decreases with increase the crystallite size or vice-versa [191]. Calculated values of crystallite size, dislocation density and micro-strain of ZnO nanoparticles are listed in Table 9.

Table 8. Lattice parameters ('*a*' and '*c*'), unit cell volume, bond length and *c/a* ratio of synthesized ZnO nanoparticles under different microwave power

Samples	*a* (Å)	*c* (Å)	Volume (Å)^3	Bond length (Å)	*c/a* ratio
ZnO(WS)	3.2764	5.2424	48.7351	1.9931	1.6000
ZnO(WT)	3.2731	5.2394	48.6091	1.9914	1.6007
ZnO(EG)	3.2627	5.2239	48.1578	1.9853	1.6011
ZnO(DEG)	3.2677	5.2304	48.3656	1.9881	1.6006
ZnO(2-PL)	3.2683	5.2323	48.4010	1.9892	1.6009

Table 9. Crystallite size, micro-strain and dislocation density of synthesized ZnO nanoparticles using different solvents

Samples	Crystallite size (nm)	Micro-Strain (10^{-3})	Dislocation density (10^{14})
ZnO(WS)	33.61	0.9278	8.8524
ZnO(WT)	29.26	1.1996	11.6802
ZnO(EG)	29.07	1.1991	11.8334
ZnO(DEG)	28.11	1.2456	12.6555
ZnO(2-PL)	27.33	1.2895	13.3880

4.7.2.2. FE-SEM and EDAX analysis

Figure 4.7.4. FE-SEM images of ZnO nanoparticles synthesized using different solvents: (a) without solvent; (b) water; (c) ethylene glycol; (d) digol and (e) 2-propanol.
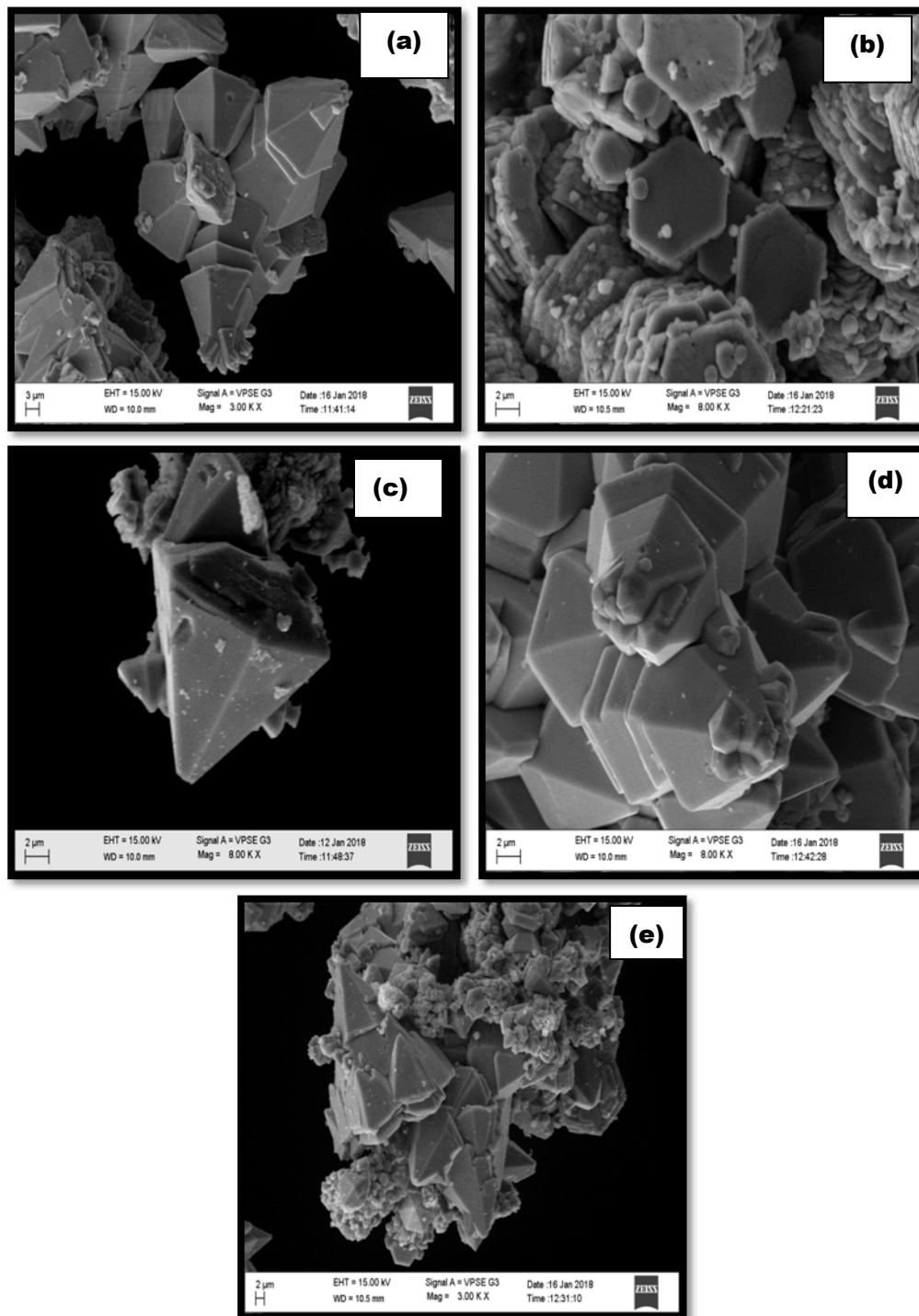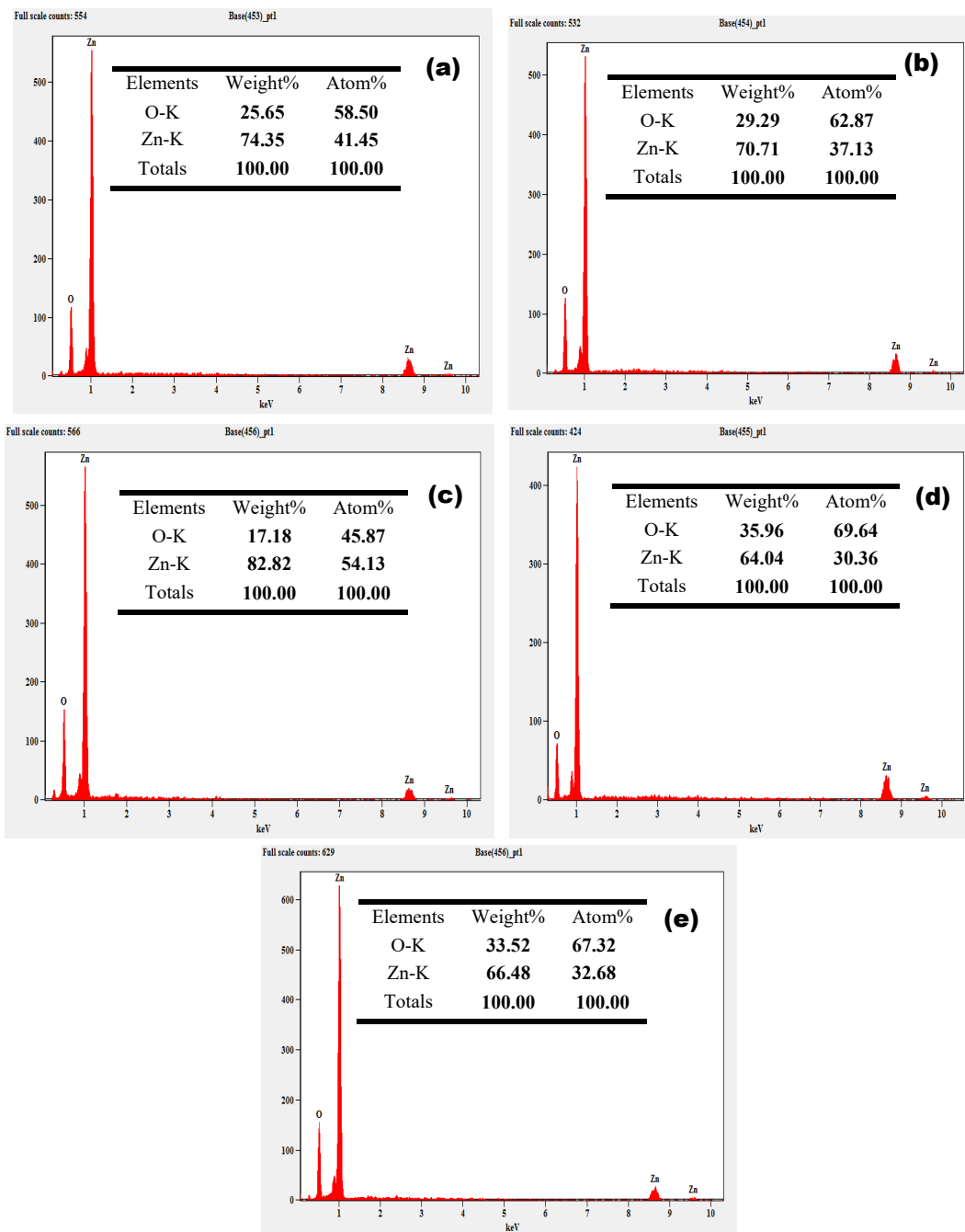
Figure 4.7.5. EDAX images of ZnO nanoparticles synthesized using different solvents: (a) without solvent; (b) water; (c) ethylene glycol; (d) digol; (e) 2-propanol.

The field emission scanning electron microscopes (FE-SEM) is one of the prominent tools for the identification of crystalline shape and sizes of the synthesized metal oxide nanostructures [192]. Figure 4.7.4(a-e) show the FE-SEM photomicrographs of ZnO nanoparticles synthesized using with and without solvents. It can be observed that the ZnO nanoparticles prepared using different solvents (except in water) and without solvent show almost hexagon prism like structure with sharp tip having good crystalline quality. Figure 4.7.4(b) shows the FE-SEM images of ZnO nanoparticles synthesized using water as a solvent, which shows the hexagonal plate like structure. The FE-SEM images of ZnO nanoparticles obtained at with and without solvents display the agglomeration of the grains. The grain agglomeration is a most important factor that controls the crystalline shape and size of the synthesized nanomaterials [193]. Figure 4.7.5(a-e) show the EDAX spectrum of ZnO nanoparticles obtained from different solvents. The EDAX spectra of all the synthesized ZnO nanoparticles show an evidence for the presence of Zn and O. This indicated that all the prepared ZnO nanoparticles have got good crystalline nature and high purity [194].

4.7.2.3. UV-Visible spectral analysis

The optical energy gaps of synthesized ZnO nanoparticles at different solvents have been estimated by optical absorbance and reflectance measurements carried out between 200-800 nm wavelength region at room temperature. Figure 4.7.6(a) illustrates the absorbance spectra of ZnO nanoparticles synthesized through microwave combustion method using different solvents. All the samples of ZnO nanoparticles show the optical absorption at UV-region. The absorption maxima (λ_{max}) were observed at 348, 350, 348, 358 and 350 nm for without solvent, water, ethylene glycol, digol and 2-propanol,

respectively [195]. The absorption spectrum in the UV-region is attributed to the presence of intrinsic band gap of ZnO nanoparticles. Figure 4.7.6(b) shows the reflectance spectra of ZnO nanoparticles obtained from different solvents. It reveals that all the prepared samples show perfect reflection in the visible region. The optical energy gap of ZnO nanostructures was determined using Kubelka-Munk method. Figure 4.7.7 shows the plot of photon energy in eV versus $[F(R)h\nu]^2$ for ZnO nanoparticles. The optical band gap was found to be 3.18, 3.19, 3.21, 3.21 and 3.19 eV for ZnO nanoparticles synthesized without solvent and with water, ethylene glycol, digol and 2-propanol, respectively [196].
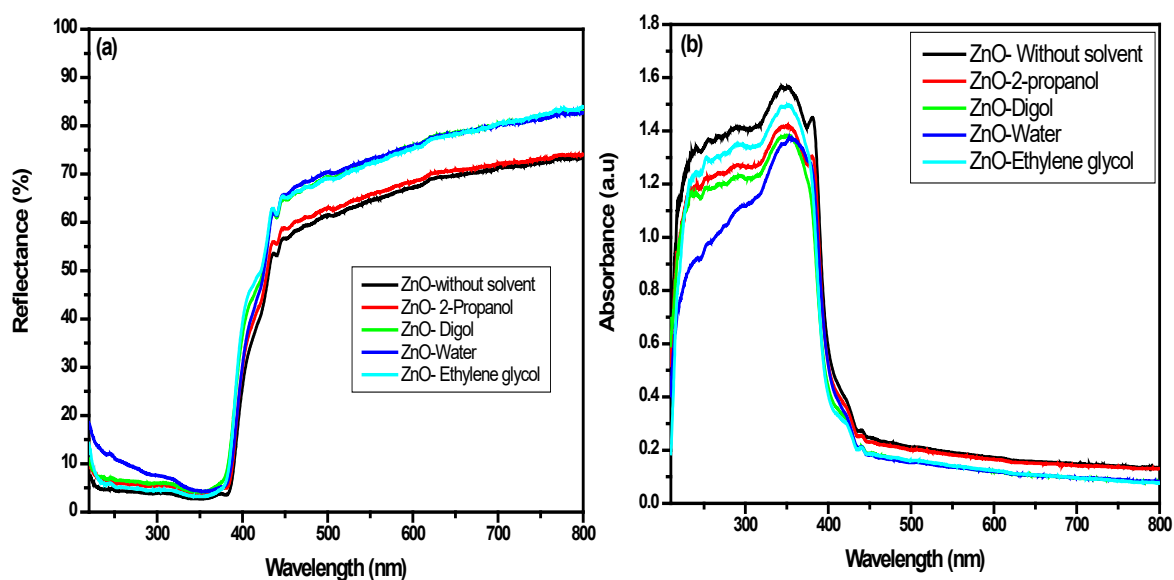
Figure 4.7.6: (a) UV-Visible reflectance spectra; (b) UV-Visible absorbance spectra of ZnO nanoparticles synthesized using different solvents.
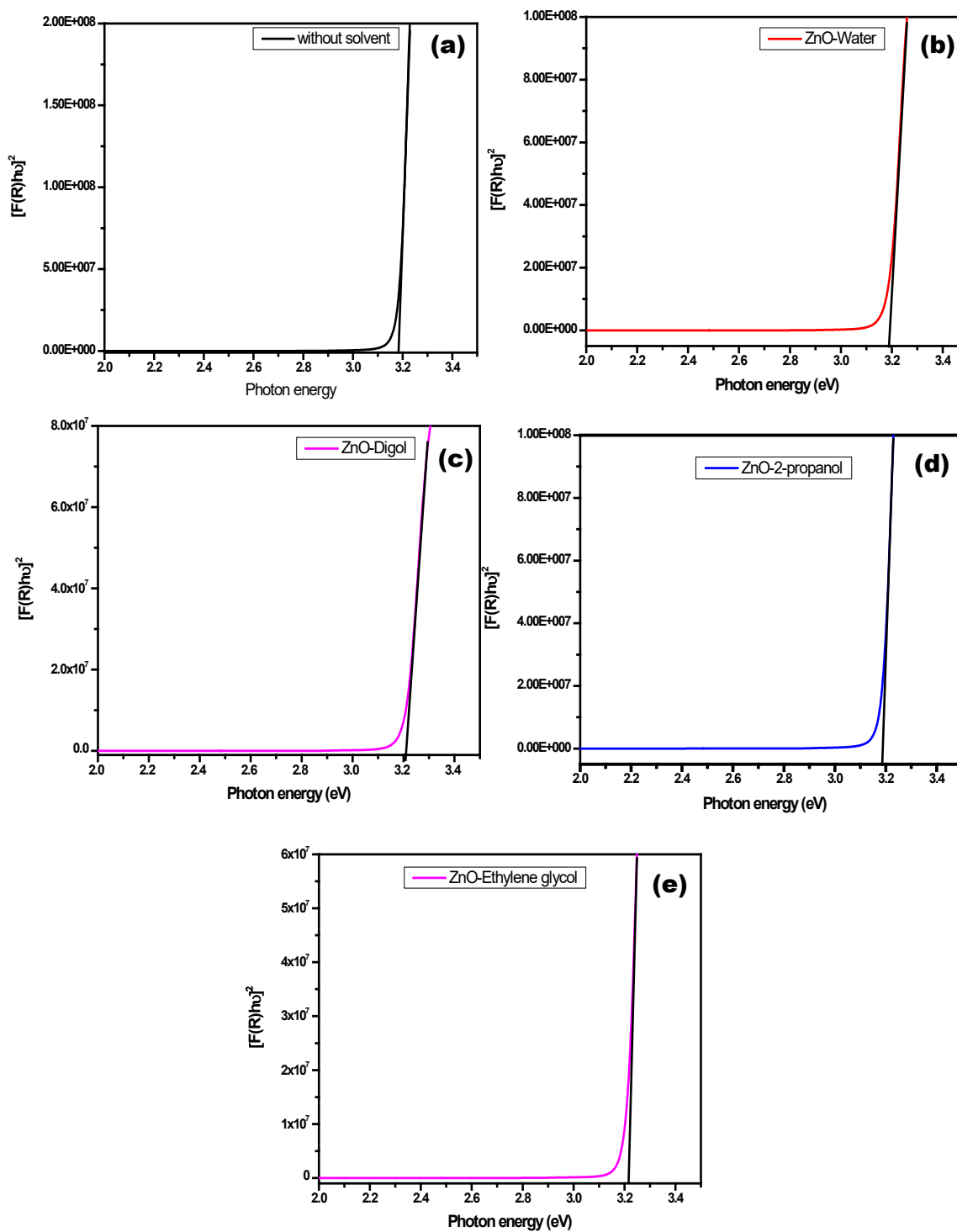
Figure 4.7.7: Plot of $[F(R)h\nu]^2$ versus energy gap for ZnO nanoparticles synthesized using different solvents: (a) without solvent; (b) water; (c) digol; (d) 2-propanol and (e) Ethylene glycol.

4.7.2.4. Electrical properties of ZnO nanoparticles
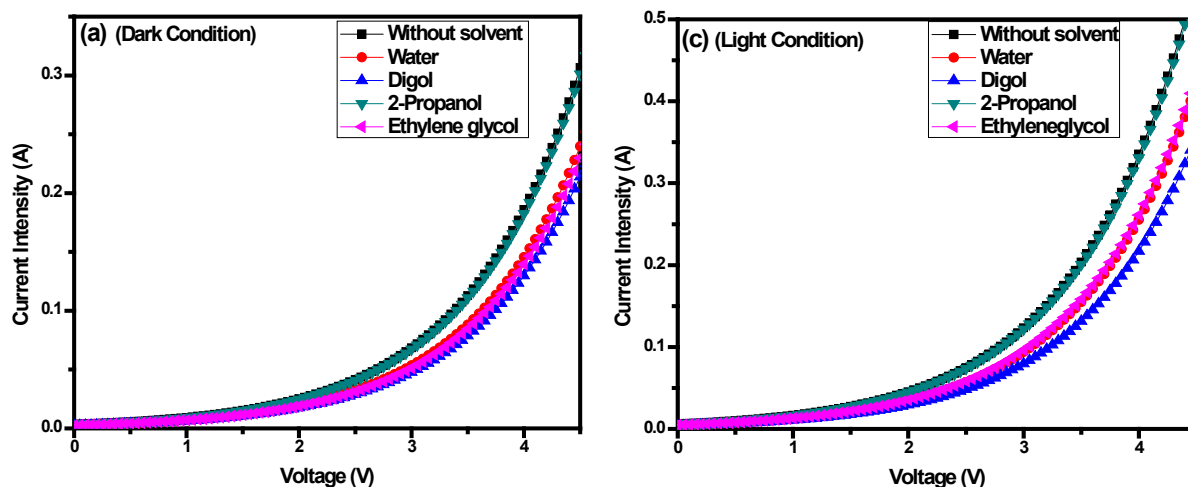
Figure 4.7.8: I-V characteristics of ZnO nanoparticles synthesized using different solvents in dark and light conditions.

The current-voltage (I-V) characteristic studies of ZnO films prepared from doctor blade method have been carried out using silver paste to make good electrical contact. Figure 4.7.8(a-b) illustrates the I-V response of ZnO nanostructures synthesized using different solvents. The resistance and current intensity are the two important factors to study the electrical properties of ZnO nanoparticles synthesized using different solvents. It shows that all the synthesized ZnO nanoparticles have non-linear characteristics in dark as well as in light conditions [198]. In dark condition, the current intensity of ZnO nanoparticles prepared without solvent and with solvent 2-propanol have shown good current intensity and low resistance compared to ZnO prepared using other solvents (Figure 4.7.8(a)). Smaller the band gap, faster will be transition of electron from valence band to conduction band and hence higher will be the current intensity [199]. Figure 4.7.8(b) shows the I-V characteristic of ZnO nanoparticles under UV-light condition. It shows that, all the samples of ZnO nanoparticles have considerable

enhancement in the current intensity (Curves moves to lower potential side) under UV-light illumination. This indicates that the absorption of UV-Vis. light generates electron-hole pairs and these holes combine with the electrons of adsorbed O^{2-} ions to form O_2 molecules on the surface of ZnO nanoparticles. However, the rest of electrons present in the conduction band cause an increase in the current intensity [200].

4.7.3. Conclusions

In the present study, the pure ZnO nanoparticles were successfully synthesized using different solvents such as water (WT), ethylene glycol (EG), digol (DG) and 2-propanol (2-PL) through microwave combustion method. The effects of solvents on structural, optical and electrical properties of ZnO nanoparticles were studied. The synthesized ZnO nanoparticles were characterized by XRD and the results shows that the ZnO nanostructures displayed hexagonal wurtzite structure. The FE-SEM images were showed the surface morphology of the ZnO nanoparticles. The optical band of ZnO materials were calculated through diffused reflectance spectra, which shows ZnO nanoparticles obtained without solvent, and with water and 2-propanol exhibit similar energy gap of 3.18 eV. The ZnO nanoparticle synthesized using ethylene glycol and digol show the energy gap of 3.21 eV which may be due to the surface-related fluctuations. The I-V characteristics of synthesized ZnO nanoparicles using different solvents showed photosensitive behaviour under dark and UV-light conditions.

References

[1]   P. Wu, N. Du, H. Zhang, L. Jin, D. Yang, Mater. Chem. Phys., 124, 908, **(2010)**.

[2]   Y.R. Sui, Y. Cao, X.F. Li, Y.G. Yue, B. Yao, X.Y. Li, J.H. Lang, J.H. Yang, Ceram. Int., 41, 587, **(2015)**.

[3]   D. Rajesh, B. Varalakshmi, C.S. Sunandana, Phy. B, 407, 4537, **(2012)**.

[4]   M. Arshad, M.M. Ansari, A.S. Ahmed, P. Tripathi, S.S.Z. Ashraf, A.H. Naqvi, A. Azam, J. Lumin., 161, 275, **(2015)**.

[5]   L. Chow, O. Lupan, G. Chai, H. Khallaf, L.K. Ono, B.R. Cuenya, I.M. Tiginyan, V.V. Ursaki, V. Sontea, A. Schulte, Sens. Actuators, A, 189, 399, **(2013)**.

[6]   Y.X. Liua, Y.C. Liua, D.Z. Shena, G.Z. Zhonga, X.W. Fana, X.G. Konga, R. Muc, D.O. Hendersonc, J. Cryst. Growth, 240, 152, **(2002)**.

[7]   M.A. Ciciliati, M.F. Silva, D.M. Fernandes, A.C. Demelo, Mater. Lett., 159, 84, **(2015)**.

[8]   G. Qin, G. Fang, N. Sun, X. Fan, Q. Zheng, F. Chen, J. Wan, X.Z. Zhao, Thin Solid Films, 519, 4334, **(2011)**.

[9]   N.H. Al-Hardana, M.J. Abdullah, A.A. Aziz, Appl. Surf. Sci., 270, 480, **(2013)**.

[10]   L. El Mir, Z.B. Ayadi, H. Rahmouni, J.E. Ghoul, K. Djessas, H.J.V. Bardeleben, Thin Solid Films, 517, 6007, **(2009)**.

[11]   R. Bhargava, P.K. Sharma, S. Kumar, A.C. Pandey, N. Kumar, J. Solid State Chem., 183, 1400, **(2010)**.

[12]   M.A. Kumar, S. Muthukumaran, Opt. Mater., 37, 671, **(2014)**.

[13]   J.A. Wibowo, N.F. Djaja, R. Saleh, Adv. Mater. Phys. Chem., 3, 48, **(2013)**.

[14]   M.A. Kumar, S. Muthukumaran, J. Lumin., 162, 97, **(2015)**.

[15]   C.C. Vidyasagar, Y.A. Naik, T.G. Venkatesh, R. Viswanatha, Nanosci. Nanotech. Int. J., 2, 18, **(2012)**.

[16]   M. Shahmiri, N. Ibrahim, N. Zainuddin, N. Asim, B. Bakhtyar, A. Zaharim, K Sopian, WSEAS Trans. Envi. Dev., 9, 137, **(2013)**.

[17]   M.M. Hassan, W. Khan, A. Azam, A.H. Naqvi, J. Ind. Eng. Chem., 21, 283, **(2015)**.

[18]   S. Vempati, A. Shetty, P. Dawson, K.K. Nanda, S.B. Krupanidhi, Thin Solid Films, 524, 137, **(2012)**.

[19]   Y.R. Sui, Y. Cao, X.F. Li, Y.G. Yue, B. Yao, X.Y. Li, J.H. Lang, J.H. Yang, Ceram. Int., 41, 587, **(2015)**.

[20]   S. Fareed, A. Jamil, N. Tiwari, M.A. Rafiq, Micro. Nano. Eng., 2, 49, **(2019)**.

[21]   S.U. Kumar, V. Renuka, K. Kavitha, J. Chem. Pharm. Res., 4, 1279, **(2012)**.

[22]   A.A. Yosif, Int. J. Emer. Trends Tech. Comp. Sci., 3, 164, **(2014)**.

[23]   P. Samarashekara, U. Wijesinghe, E.N. Jayaweera, GESJ: Phys., 1(13), 3, **(2015)**.

[24]   K. Nishimura, J.L.C. Huaman, M. Hiroshi, T. Akiyama, T. Oku, B. Jeyadevan, Mat. Res. Exp., 1, 015032, **(2014)**.

[25]   T.K. Pathak, R. Kumar, L.P. Purohit, Int. J. Chem. Tech. Res., 2, 987, **(2015)**.

[26]   A.D. Dhondge, S.R. Gosavi, N.M. Gosavi, C.P. Sawant, A.M. Patil, A.R. Shelke, N.G. Deshpande, Condens. Matter Phys., 5, 4, **(2015)**.

[27]   T. Jiang, Y. Wang, D. Meng, X. Wu, J. Wang, J. Chen, Appl. Surf. Sci., 311, 602, **(2014)**.

[28]   A. El-Trass, H.E. Shamy, I.E. Mehasse, M.E. Kemary, Appl. Surf. Sci., 258, 2997, **(2012)**.

[29]   A. Sharma, M. Varshney, H.T. Kyun, K.H. Chae, H.J. Shin, Curr. Appl. Phys., 15, 1148, **(2015)**.

[30]   X. Li, W. Guo, Y. Liu, W. He, Z. Xiao, Elect. Chim. Acta, 116, 278, **(2014)**.

[31]   J. Lee, A. Katoch, J. Kim, S. Kim, Sen. Actuators B-Chem., 222, 307, **(2016)**.

[32] H. Siddiqui, M.S. Qureshi, F.Z. Haque, Optik, 127, 3713, **(2016)**.

[33] R. Etefagh, E. Azhir, N. Shahtahmasebi, Sci. Iranica, 20, 1055, **(2013)**.

[34] M. Ahmad, E. Ahmed, Z.L. Hong, X.L. Jiao, T. Abbas, N.R. Khalid, Appl. Surf. Sci., 285P, 705, **(2013)**.

[35] I. Singh, R.K. Bedi, Appl. Surf. Sci., 257, 7592, **(2011)**.

[36] D.C. Agarwal, U.B. Singh, S. Gupta, R. Singhal, P.K. Kulriya, D.K. Avasthi, Sci. Reports, 9, 4, **(2019)**.

[37] S.A. Ansari, A. Nisar, B. Fatma, W. Khan, A.H. Naqvi, Mater. Sci. Eng. B, 177, 428, **(2012)**.

[38] C.C. Vidyasagar, H.B. Muralidhara, Y.A. Naik, G. Hosamani, M.S. Ilango, Energy Environ. Focus, 4, 54, **(2015)**.

[39] O.A. Yildirim, C. Durucan, Cerm. Inter., 42, 3229, **(2016)**.

[40] G. Viruthagiri, P. Praveen, S. Mugundan, E. Gopinathan, Ind. J. Adv. Chem. Sci., 1, 132, **(2013)**.

[41] K. Venkateswarulu, M. Sandyarani, T.A. Nellaippan, N. Rameshbabu, Proc. Mater. Sci., 5, 212, **(2014)**.

[42] Q. Ahsanulhaq, J.H. Kim, J.S. Lee, H.B. Hahn, Electrochem. Comms., 12, 475, **(2010)**.

[43] M. Vaseem, A. Umar, S.H. Kim, Y.B. Hahn, J. Phys. Chem. C, 112, 5729, **(2008)**.

[44] S. Muthukumaran, R. Gopalakrishnan, Opt. Mater., 34, 1946, **(2012)**.

[45] R. Bhargava, P.K. Sharma, S. Kumar, A.C. Pandey, N. Kumar, Mat. Chem. Phys., 125, 664, **(2011)**.

[46] B.G. Ganga. M.R. Verma, P.N. Santhosh, Cry. Eng. Comm., 17, 7088, **(2015)**.

[47] C. Yang, X. Su, F. Xiao, J. Jian, J. Wang, Sen. Actuators B- Chem., 158, 299, **(2011)**.

[48]   P. Sathishkumar, R. Sweena, J.J. Wub, S. Anandana, Chem. Eng. J., 171, 138, **(2011)**.

[49]   T. Li, H. Qiu, P. Wu, M. Wang, Thin Solid Films, 515, 3905, **(2007)**.

[50]   K.L. Foo, M. Kashif, U. Hashim, M.E. Ali, Curr. Nanosci., 9, 003, **(2013)**.

[51]   B. Chavillon, L. Cario, A. Renaud, F. Tessier, F. Chevire, M. Boujtita, Y. Pellegrin, E. Blart, A. Smeigh. L. Hammarstrom, F. Odobel, S. Jobic, J. Am. Chem. Soc., 134, 467, **(2012)**.

[52]   W.J. Jeyarani, T. Tenkyong, N. Bachan, D.A. Kumar, J.M. Shyla, Adv. Powder Technol., 27 338, **(2016)**.

[53]   S. Tewari, A. Bhattacharjee, Pramana. J. Phys., 76, 153, **(2011)**.

[54]   R.O. Yathisha, Y.A. Nayaka, C.C. Vidyasagar, Mater. Chem. Phys., 18, 167, **(2016)**.

[55]   D.M. Yufanyi, J. F. Tendo, A. M. Ondoh, J. K. Mbadcam, J. Mater. Sci. Res., 3, 5, **(2014)**.

[56]   A. Heidari, C. Brown, J. Nanomedicine Res., 2, 8, **(2015)**.

[57]   J. Li, Y. Ni, J. Liu, J. Hong, J. Phy. Chem. Sol., 70, 1285, **(2009)**.

[58]   K. Kaviyarasu, E. Manikandan, J. Kennedy, M. Jayachandran, Mater. Lett., 120, 243, **(2014)**.

[59]   T. Yesudoss, Inter. J. Inform. Res. Rev., 4, 4244, **(2017)**.

[60]   C.C. Vidyasagar, Y.A. Naik, T.G. Venkatesh, R. Viswanatha, Powder Technol., 214, 337, **(2011)**.

[61]   L.A. Saghatforoush, S. Sanati, R. Mehdizadeh, M. Hasanzadeh, Superlattices Microstruct., 52, 885, **(2012)**.

[62]   B. Sahin, Y. Gulen, F. Bayansal, H.A. Cetinkara, H.S. Guder, Superlattices Microstruct., 65, 56, **(2014)**.

[63]   B. Sahin, F. Bayansal, M. Yuksel, N. Biyikli, H.A. Çetinkara, Ceram. Int., 40, 5237, **(2014)**.

[64]   Y. Yang, S. Jin, J.E. Medvedeva, J.R. Ireland, A.W. Metz, M.C. Hersam, A.J. Freeman, T.J. Marks, J. Am. Chem. Soc., 127, 8796, **(2005)**.

[65]   S. Phokha, D. Prabhakaran, A. Boothroyd, S. Pinitsoontorn, S. Maensiri, Microelectron. Eng., 126, 93, **(2014)**.

[66]   M.F. Elkady, M.A. Alrafaa, N.A. El Essawy, Beni-Suef Uni. J. Basic Appl. Sci., 3, 229, **(2014)**.

[67]   A.A. Dakhel, Bull. Mater. Sci., 36, 819, **(2013)**.

[68]   V.K. Gupta, A. Fakhri, S. Tahami, S. Agarwal, J. Colloid Interface Sci., 504, 164, **(2017)**.

[69]   P.K. Sharma, R.K. Dutta, R.J. Choudhary, A.C. Pandey, Cryst. Eng. Comm., 15, 4438, **(2013)**.

[70]   C.C. Vidyasagar, G. Hosamani, P. Kariyajjanavar, R.O. Yathisha, Y.A. Nayaka, Mater. Today: Proceedings, 5, 22173, (2018).

[71]   I. Singh, R. K. Bedi, Appl. Surf. Sci., 257, 7592, **(2011)**.

[72]   A. Mesaros, D. Toloman, M. Nasui, R.B. Mos, T. Petrisor, B.S. Vasile, V.A. Surdu, J. Mater. Sci., 50, 6075, **(2015)**.

[73]   R. Jeyachitra, V. Senthilnathan, T.S. Senthil, J. Mater. Sci.: Mater. Electron., 29, 1189, **(2018)**.

[74]   A.A. Dhakel, Microelectron. Reliab., 79, 278, **(2019)**.

[75]   F. Yakuphanoglu, J. Sol-Gel. Sci. Technol., 59, 570, **(2011)**.

[76]   C.S. Naveen, M.L. Dinesha, H.S. Jayanna, J. Mater. Sci. Technol., 29, 898, **(2013)**.

[77]   A. Samanta, M.N. Goswami, P.K. Mahapatra, J. Alloys Compond., 730, 402, **(2018)**.

[78]   S. Kuriakose, B. Satpati, S. Mohapatra, Phys. Chem. Chem. Phys., 16, 12741, **(2014)**.

[79]   A. Mason, S.C. Mukhopadhyay, K.P. Jayasundera, N. Bhattacharyya, Sensing Technology: Current Status and Future Trends I, Springer International Publishing, Heidelberg, **(2014)**.

[80]   N.M. Al-Hada, E.B. Saion, A.H. Shaari, M.A. Kamarudin, M.H. Flaifel, S.H. Ahmad, A. Gene, Mater. Sci. Semicond. Process., 26, 464, **(2014)**.

[81]   C.R. Foschini, B. Hangai, C.S. Cavalcante, A.Z. Simoes, M. Cilense, E. Longo, J. Mater. Sci.: Mater. Electron., 28, 15685, **(2017)**.

[82]   M. Munirah, Z. R. Khan, M. S. Khan, A. Aziz, Mater. Sci.-Poland, 32(4), 688, **(2014)**.

[83]   T. P. Rao, M.C. Santhosh kumar, App. Surf. Sci., 255, 4579, **(2009)**.

[84]   M. Benhaliliba, C. E. Benouis, A. Tiburcio-Silver, F. Yakuphanoglu, A. Avila-Garc, J. Lumin., 132, 2653, **(2012)**.

[85]   A. Tavira, R.R. Trujillo, Z. Mouffak, J. Lumin., 132, 2653, **(2012)**.

[86]   J. Tang, F. Redl, Y. Zhu, T. Siegrist, L. E. Brus, M. L. Steigerwald, Nano Lett., 5, 543, **(2005)**.

[87]   M.M. Viana, V.F. Soares, N.D.S. Mohallem, Ceram. Inter., 36, 2047, **(2010)**.

[88]   U. Nwankwo, R. Bucher, A.B.C. Ekwealor, S. Khamlich, M. Maaza, F.I. Ezema, Vacuum, 161, 49, **(2019)**.

[89]   M. Guang, Y. Xia, D. Wang, X.F. Zeng, J.X. Wang, J.F. Chen, Mater. Chem. Phys., 224, 100, **(2019)**.

[90]   V.A.Z. Ibarra, S. Shaji, B. Krishnan, J. Johny, S.S. Kanakkillam, D.A. Avellaneda, J.A. Martinez, T.K.D. Roy, N.A.R. Delgado, Appl. Surf. Sci., 483, 156, **(2019)**.

[91]   M. Morozova, P. Kluson, J. Krysa, M. Vesely, P. Dzik, O. Solcova, Proc. Eng., 42, 573, **(2012)**.

[92] J. Lim, S.Y. Ryu, J. Kim, Y. Jun, Nanoscaled Res. Lett., 8, 227, **(2013)**.

[93] X. Xu, C. Tang, H. Zeng, T. Zhai, S. Zhang, H. Zhao, Y. Bando, D. Golberg, Appl. Mater. Interfaces, 3, 1352, **(2011)**.

[94] J. Bai, B. Zhou, Chem. Rev., 114, 10131, **(2014)**.

[95] B.A. Van Driel, P.J. Kooyman, K.J. Van den Berg, A.S. Ott, J. Dik, Microchem. J., 126, 162, **(2016)**.

[96] A. Hodaei, A.S. Dezfuli, H. R. Naderi, J. Mater. Sci.: Mater. Electron., 29, 14596, **(2018)**.

[97] R. Zahid, M. Manzoor, A. Rafiq, M. Ikram, M. Nafees, A.R. Butt, S.G. Hussain, S. Ali, Electr. Mater. Lett., 14, 587, **(2018)**.

[98] F.T. G. Vieira, D.S. Melo, S.J.G. Lima, E. Longo, C.A. Paskocimas, Mater. Res. Bulletin, 44, 1086, **(2009)**.

[99] A.K. Bhosale, S.R. Kulal, V.M. Gurame, P.S. Patil, Bull. Mater. Sci., 38, 483, **(2015)**.

[100] M. Khairy, W. Zakaria, Egypt. J. Petroleum, 23, 419, **(2014)**.

[101] L. Kernazhitsky, L. Kernazhitsky, V. Shymanovska, T. Gavrilko, V. Naumov, L. Fedorenko, V. Kshnyakin, J. Lumin., 166, 253, **(2015)**.

[102] A. Khana, D.G. Bhat, J. Vac. Sci. Technol. A, 24, 1870, **(2006)**.

[103] Y. Bessekhouad, D. Robert, J.V. Weber, J. Photochem. Photobio., A: Chem., 157, 47, **(2003)**.

[104] X. Li, Z. Guoa, T. He, Phys. Chem. Chem. Phys., 15, 20037, **(2013)**.

[105] H.M. Yadav, T.V. Kolekar, A.S. Barge, N.D. Thorat, S.D. Delekar, B.M. Kim, B.J. Kim, J.S. Kim, J. Mater. Sci.: Mater. Electron., 27, 526, **(2016)**.

[106] M. Ahamed, M.A.M. Khan, M.J. Akhtar, H.A. Alhadlaq, A. Alshamsan, Sci. Reports, 6, 1, **(2016)**.

[107] T.B. Nguyen, M.J. Hwang, K.S. Ryu, Bull. Korean Chem. Soc., 33, 243, **(2012)**.

[108]   K.B. Jaimy, S. Ghosh, S. Sankar, K.G.K. Warrier, Mater. Res. Bulletin, 46, 914, **(2011)**.

[109]   N. Bsiri, M.A. Zrir, A. Bardaoui, M. Bouaicha, Ceram. Inter., 42, 10599, **(2016)**.

[110]   B. Parveen, M. Hassan, Z. Khalid, S. Riaz, S. Naseem, J. App. Res. Technol., 15, 132, **(2017)**.

[111]   S.P. Takle, O.A. Apine, J.D. Ambekar, S.L. Landge, N.N. Bhujbal, RSC Adv., 9, 4226, **(2019)**.

[112]   D.V. Aware, S.S. Jadhav, Appl. Nano Sci., 6, 965, **(2016)**.

[113]   J.C. Colmenares, A. Magdziarz, K. Kurzydlowski, J. Grzonka, O. Chernyayeva, D. Lisovytskiy, Appl. Catalysis B: Environ., 135, 136, **(2013)**.

[114]   A. Chanda, K. Rout, M. Vasundhara, S.R. Joshic, J. Singh, RSC Adv., 8, 10939, **(2018)**.

[115]   S. Mathew, A.K. Prasad, T. Benoy, P.P. Rakesh, P. Radhakrishnan, J. Fluorescence, 22, 1563, **(2012)**.

[116]   S.A. Ahmed, J. Magn. Magn. Mater., 442, 152, **(2017)**.

[117]   A.T. Zajac, M. Radecka, M. Jasinski, K.A. Michalowa, M. Rekas, E. Kusior, J. Power Sources, 194, 104, **(2009)**.

[118]   S.N.R. Inturi, M. Suidan, P.G. Smirniotis, Appl. Catal., B: Environ., 180, 351, **(2016)**.

[119]   B. Choudhury, A. Choudhury, Mater. Sci. Eng.: B, 178, 794, **(2013)**.

[120]   M. Asemi, A. Suddar, M. Ghanaatshoar, J. Mater. Sci: Mater. Electron., 28, 15233, **(2017)**.

[121]   T. Sharifi, Y. Ghayeb, T. Mohammadi, M.M. Momeni, Dalton Trans., 48, 11593, **(2013)**.

[122]   P.B. Devaraja, D.N. Avadhani, S.C. Prashantha, S.C. Sharma, B.M. Nagabhushana, H.P. Nagaswarupa, B.D. Prasad, J. Rad. Res. Appl. Sci., 8, 364, **(2015)**.

[123] M.R. Anilkumar, H.P. Nagaswarupa, H. Nagabhushana, S.C. Sharma, Y.S. Vidya, K.S. Anantharaju, S.C. Prashantha, C. Shivakuamra, K. Gurushantha, Spectrochim. Acta A: Mol. Biomol. Spect., 149, 703, **(2015)**.

[124] M.K.I. Senevirathna, P.K.D.D.P. Pitigala, E.V.A. Premalal, K. Tennakone, G.R.A. Kumara, A. Konno, Sol. Energy Mater. Sol. Cells, 91, 544, **(2007)**.

[125] N.O.V. Plank, H.J. Snaith, C. Ducati, J.S. Bendall, L. Schmidt-Mende, M.E. Welland, Nanotechnol., 19, 4, **(2008)**.

[126] B. Li, G. Lu, L. Luo, Y. Tang, Wuhan Univer. J. Natural Sci., 15, 325, **(2010)**.

[127] E. Palomares, J.N. Clifford, S.A. Haque, T. Lutz, J.R. Durrent, J. Am. Chem. Soc., 125, 475, **(2003)**.

[128] A. Kay, M. Gratzel, Chem. Mater., 14, 2930, **(2002)**.

[129] T. Berger, J. Schuh, M. Sterrer, O. Diwald, E. Knozinger, J. Catal., 247, 63, **(2007)**.

[130] A.A. Tedstone, D.J. Lewis, P.O. Brien, Chem. Mater., 28, 1965, **(2016)**.

[131] J. Jayaprakash, N. Srinivasan, P. Chandrasekaran, E.K. Girija, Spectrochem. Acta A: Mol. Biomol. Spect., 136, 1803, **(2015)**.

[132] P.B. Devaraja, D.N. Avadhani, S.C. Prashantha, H. Nagabhushana, S.C. Sharma, B.M. Nagabhushana, H.P. Nagaswarupa, Spectrochim. Acta A: Mol. Biomol. Spect., 118, 847, **(2014)**.

[133] U. Sharma, P. Jeevanandam, J. Sol-Gel. Sci. Technol., 75, 7, **(2015)**.

[134] D. Zhen, Z. Jiang, J. Geng, Q. Wang, D. Yang, Ind. Eng. Chem. Res., 46, 2741, **(2007)**.

[135] D. Dai, Q. Ma, Y. Pei, Z. Zheng, L. Yuan, Dalton Trans., 47, 17423, **(2018)**.

[136] D. Anbuselvan, S. Muthukumaran, Opt. Mater., 42, 124, **(2015)**.

[137] M.M. Obeid, S.J. Edrees, M.M. Shukur, Superlattices Microstruct., 122, 126, **(2018)**.

[138] N.J. Sushma, D. Prathyusha, G. Swathi, T. Madhavi, B.D.P. Raju, K. Mallikarjuna, H.S. Kim, Appl. Nanosci., 6, 441, **(2016)**.

[139] T.A. Vijayan, R. Chandramohan, S. Valanarasu, J. Thirumalai, S.P. Subramanian, J. Mater. Sci., 43,1776, **(2008)**.

[140] S. Das, V.M. Srivasatava, Smart Sci., 4, 193, **(2016)**.

[141] J. Kulkarnia, R. Ravishankara, H. Nagabhushana, K.S. Anantharaju, R.B. Basavaraj, M. Sangeeta, H.P. Nagaswarupa, L. Renuka, Mater. Today: Proceedings, 4, 11760, **(2017)**.

[142] S. Suresh, D. Arivuoli, Digest J. Nanomater. Biostruct., 6, 1600, **(2011)**.

[143] T. Ohira, M. Kawamura, M. Fukuda, K. Alvarez, B.O. Zkal, O. Yamamoto, JMEPEG, 19, 374, **(2010)**.

[144] K. Badreddine, I. Kazah, M. Rekaby, R. Awad, J. Nanomater., 7096195, 5, **(2018)**.

[145] J. Sivasankari, S. Sellaiyan, S. Sankar, L.V. Devi, K. Sivaji, Physica E, 85,152, **(2017)**.

[146] A.M. Salehi, G. Moussavi, K. Yaghmaeian, Chem. Eng. J., 310, 157, **(2017)**.

[147] R.L.Z. Hoye, S. Heffernan, Y. Ievskaya, A. Sadhanala, A. Flewitt, R.H. Friend, J.L.M. Driscoll, K.P. Musselman, Appl. Mater. Interfaces, 6, 22196, **(2014)**.

[148] T. Dixit, I.A. Palani, V. Singh, RSC Adv., 8, 6829, **(2018)**.

[149] Y.J. Chen, Y.C. Cheng, L.Y. Lin, W.C. Chang, S.M. Chang, Electrochem. Acta, 178, 414, **(2015)**.

[150] M. Sharon, An Introduction to the Physics and Electrochemistry of Semiconductors: Fundamentals and Applications, Scrivener Publishing, Canada, **(2016)**.

[151] A. Venkatanarayanan, E. Spain, Compress. Mater. Processing, 13, 47, **(2014)**.

[152] R.Y. Hong, J.H. Li, L.L. Chen, D.Q. Liu, H.Z. Li, Y. Zheng, J. Ding, Powder Technol., 189, 426, **(2009)**.

[153] J. Singh, T. Dutta , K.H. Kim, M. Rawat, P. Samddar, P. Kumar, J. Nanobiotechnol., 16, 17, **(2018)**.

[154] B.S. Han, S. Caliskan, W. Sohn, M. Kim, J.K. Lee, H.W. Jang, Nanoscale Res. Lett., 11:221, 1, **(2016)**.

[155] H.K. Maleh, K. Ahanjan, M.Taghavi, M. Ghaemy, Anal. Methods, 8, 1780, **(2016)**.

[156] J. Zhang, P. Gu, J. Xu, H. Xue, H. Pang, Nanoscale, 8, 18578, **(2016)**.

[157] X. He, J. E.Yoo, M.H. Lee, J. Bae, Nanotechnology, 28, 245402, **(2017)**.

[158] Suresh, J.S. Sandhu, Inter. J. Org. Chem., 2, 305, **(2012)**.

[159] M.J. Osmond, M.J. Mccall, Nanotoxicol., 4(1), 15, **(2010)**.

[160] R. Yatskiv, J. Grym, K. Zdansky, K. Piksova, Carbon, 50, 3928, **(2012)**.

[161] A. Steinfeld, Inter. J. Hydrog. Energy, 27, 611, **(2002)**.

[162] S. Ghosh, D. Majumder, A. Sen, S. Roy, Mater. Lett., 130, 215, **(2015)**.

[163] A.B. Djurisic , A.M.C. Ng, X.Y. Chen, Prog. Quant. Electron., 34, 191, **(2010)**.

[164] U. Pal, P. Santiago, J. Phys. Chem. B, 109, 15317, **(2005)**.

[165] N.M. Shamhari, B.S. Wee, S.F. Chin, K.Y. Kok, Acta Chim. Slov., 65, 579, **(2018)**.

[166] D. Sharma, S. Sharma, B.S. Kaitha, J. Rajput, M. Kaur, Appl. Surf. Sci., 257, 9661, **(2011)**.

[167] Y. Zhao, J.J. Zhu, J.M. Hong, N. Bian, H.Y. Chen, Eur. J. Inorg. Chem., 2004, 4073, **(2004)**.

[168] M. Darwish, A. Mohammadi, N. Assi, Q.S. Manuchehri, Y. Alahmad, S. Abuzerr, J. Alloys Compds. 703, 399, **(2017)**.

[169] B.J. Zhang, J.S. Lian, L. Zhao, Q. Jiang, Appl. Surf. Sci., 257, 5659, **(2011)**.

[170] B.D. Cullity, Elements of X-ray Diffraction, Addison-Wesley, Reading, MA, **(1978)**.

[171] P.M. Shafi, A.C. Bose, AIP Advs., 5, 057137, 2, **(2015)**.

[172] N.P. Herring, L.S. Panchakarla, M.S. El-Shall, Langmuir, 30, 2233, **(2014)**.

[173] W. Peng, S. Qu, G. Cong, Z. Wang, Cryst. Growth Design, 6, 1521, **(2006)**.

[174] D.S.Y. Jayathilake, T.A. Nirmal Peiris, J.S. Sagu, D.B. Potter, K.G.U. Wijayantha, C.J. Carmalt, D.J. Southee, ACS Sustainable Chem. Eng., 5, 4824, **(2017)**.

[175] P.P. Mahamuni, P.M. Patil, M.J. Dhanvade, M.V. Badiger, P.G. Shadija, A.C. Lokhande, R.A. Bohara, Biochem. Biophys. Reports, 17, 74, **(2019)**.

[176] N.A. Bakr, Z.T. Khodair, S.M. A. Hassan, Res. J. Chem. Sci., 5(10), 54, **(2015)**.

[177] P.K. Giri, S. Bhattacharya, D.K. Singh, R. Kesavamoorthy, B.K. Panigrahi, K.G.M. Nair, J. Appl. Phys., 102, 5, **(2007)**.

[178] M.N.H. Mia, M.F. Pervez, M.K. Hossin, M.R. Rahman, H.K. Ghosh, Results Phys., 7, 2689, **(2017)**.

[179] R.O. Yathisha, Y.A. Nayaka, P. Manjunatha, M.M. Vinay, H.T. Purushothama, Microchem. J., 145, 638, **(2014)**.

[180] R.O. Yathisha, Y.A. Nayaka, P. Manjunatha, H.T. Purushothama, M.M. Vinay, K.V. Basavarajappa, Physica E, 108, 266, **(2019)**.

[181] N. Kamarulzaman, M.F. Kasim, R. Rusdi, Nano Scale Res. Lett., 10, 1, **(2015)**.

[182] S. Xu, Z.L. Wang, Nano Res., 4, 1013, **(2011)**.

[183] N. Mir, M.S. Niasari, F. Davar, Chem. Eng. J., 181, 779, **(2012)**.

[184] J. Xiong, W. Li, Y. Gan, Y. Wei, G. Cheng, S. Dou, Z. Li, Inorg. Chem. Front., 5, 2432, **(2018)**.

[185] D. Cao, S. Gong, X. Shu, D. Zhu, S. Liang, Nanoscale Res. Lett., 14, 1, **(2018)**.

[186] P. Lidstrom, J. Tierney, B. Wathey, J. Westman, Tetrahedron, 57, 9225, **(2001)**.

[187] B.G. Nemmaniwar, N.V. Kalyankar, P.L. Kadam, Orbital, 5, 2, **(2013)**.

[188] V.P. Dinesh, P. Biji, A. Ashok, S. K. Dhara, M. Kamruddin, A.K. Tyagi, B. Raj, RSC Adv. (Supplementary Data), 4, 58940, **(2014)**.

[189] V. Koutu, L. Shastri, M.M. Malik, Mater. Sci. -Poland, 34, 820, **(2016)**.

[190] S. Kumar, K. Asokan, R.K. Singh, S. Chatterjee, D. Kanjilal, A.K. Ghosh, RSC Adv., 4, 62123, **(2014)**.

[191] K.C. Verma, N. Goyal, R.K. Kotnala, Phys. Chem. Chem. Phys., 21, 12543, **(2019)**.

[192] A. Antony, P. Poornesh, I.V. Kityk, K. Ozga, J. Jedryka, P. Rakus, A. Wojciechowski, IOP- Laser Phys., 28, **(2018)**.

[193] Y. Sui, W. Fu, H. Yang, Y. Zeng, Y. Zhang, Q. Zhao, Y. Li, X. Zhou, Y. Leng, M. Li, G. Zou, Cry. Growth Design, 10, 100, **(2010)**.

[194] L.N. Dem'yanets, L.E. Li, T.G. Uvarova, J. Mater. Sci., 41, 1440, **(2006)**.

[195] S. Saif, A. Tahir, T. Asim, Y. Chen, M. Khan, S.F. Adil, Saudi J. Biol. Sci., (In Corrected Proof), **(2019)**.

[196] P. Mallick, Ind. J. Pure & Appl. Phys., 55, 190, **(2017)**.

[197] S.S. Kumar, P. Venkateswarlu, V. R.Rao, G.N. Rao, Inter. Nano Lett., 3, 4, **(2013)**.

[198] R.O. Yathisha, Y.A. Nayaka, Inter. J. Nanoelect. Mater., 11, 237, **(2018)**.

[199] S. Ilican, Y.Coglar, J. Optoelect. Adv. Mater., 10, 2578, **(2008)**.

[200] N. Lupu, Nanowires Science and Technology, Intech, Croatia, **(2010)**.

Chapter 5

DYE SENSITIZED TARNSTION METAL DOPED SEMICONDUCTING NANOPARTICLES

In an efficient dye sensitized solar cell (DSSC), a sensitizer (dye) is one of the important key components which improve the efficiency of solar energy conversion. Over the past decades, the Ruthenium (Ru) complex based DSSCs were developed by researchers, which have shown high light to energy conversion efficiencies of over 11% [1]. However, high cost of synthesis, problematical steps of compound purification, very less yield of product and environmental concern have limited the potential applications of Ru complexes. These disadvantages of Ru based complexes have given an insight for the development of metal free organic sensitizers. These dyes are used in the DSSCs due to their various significant advantages such as high absorption co-efficient, easy for synthesis and purification, less toxic, affordable cost and eco-friendliness [2]. The recent reports highlighted the highest photo conversion efficiency of DSSCs from organic sensitizers is greater than 13.5% indicates that the organic dye sensitizers are also proves to be the significant materials for DSSCs compared to Ru, Ce and Zn transition metal sensitizers. The anchoring modes of the dye molecules to the crystalline semiconductor surface are of essential significance, the interaction and the extent of electronic coupling between the lower unoccupied state (LUMO) of dye and the conduction band of semiconductor influencing directly the overall cell performance [3]. Anchoring with wide band gap semiconductor surface (ZnO, TiO_2, SnO_2) has been achieved by using a number of essential functional groups present in the dye molecules, such as carboxylic acid (-COOH), sulfonic acid ($-SO_3H$), Nitro ($-NO_2$), acetylacetonate derivatives ($-CH_3COCHCOCH_3^-$) and salicylate ($-C_7H_5O_3^-$). Among these, the sensitizers with

functional group -SO$_3$H gained more prominence due to the different possibilities of binding modes (mono-dentate or bi-dentate) on the surface of semiconductors [4]. Generally, the electronic and optical properties of dye molecules have contributed to understanding the type of dye-semiconductor interaction. It was observe that dyes having a sulphonic acid group as an anchoring group, the absorption of dye molecule was preferred by bidentate bridging with transfer of proton to nearby oxygen. The dye anchoring on surface of semiconductor by monodentate was found less stable compared to other forms of binding. [5]. But several researchers were used -SO$_3$H contained dyes and achieved better efficiency of Gratzel cell. R. Parthiban *et al*. were revealed that the Evans blue sensitized ZnO device has shown the efficiency of 0.1% and it depends on the electronic structure of dye and semiconductor used [6]. S.A. Kazmi *et al*. reported that the 2.5% of efficiency was achieved by methyl orange anchor-TiO$_2$ Ag DSSCs [7].

In the present study, azo chromophore (-N=N-) based organic dyes (Trypan blue, SPDANS and Evans blue) have been used for the sensitization of transition metals doped nanoparticles. The main aim of this chapter was to study the effect of dyes on the optical and electrical properties of transition metal doped semiconducting nanoparticles. The semiconducting doped metal oxide nanoparticles, Cr-ZnO, Zn-CuO, Ni-CdO, Cr-TiO$_2$ and Zn-MgO have been selected for the study.

5.1. Optical and Electrical Properties of Dye Sensitized Cr-ZnO Nanoparticles

5.1.1. Results and discussion

5.1.1.1. Cyclic voltammetric studies of dyes
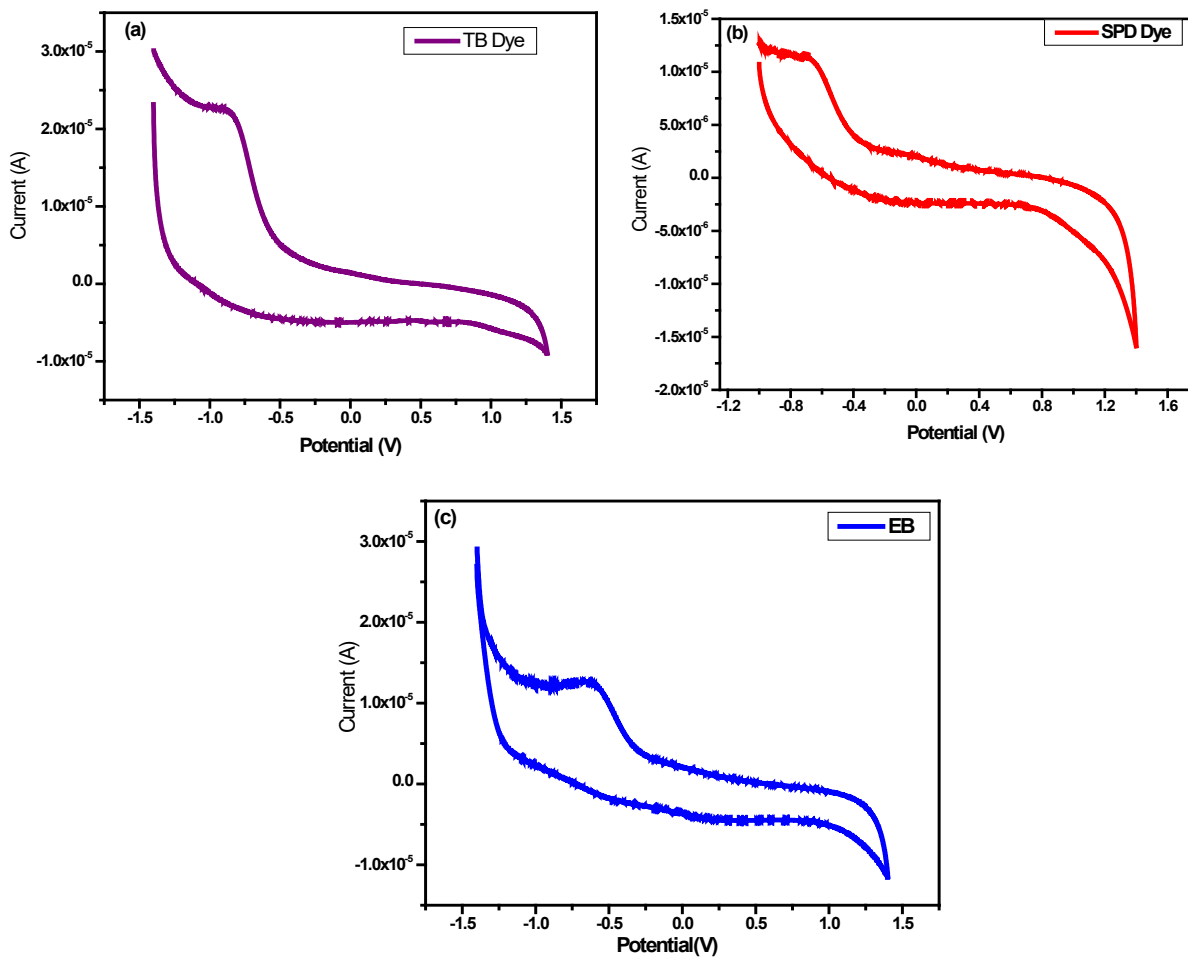

Figure 5.1.1: Cyclic voltammograms of (a) Trypan blue (b) SPADNS (c) Evans blue dyes in   0.1 M KCl solution.

The electrochemical properties measured from cyclic voltammetry have been used to identify the molecular orbital energy levels of dye molecules. The molecular orbital energy levels of organic dye molecules consist of two major energy levels i.e., highest

occupied molecular orbital (HOMO) and lowest unoccupied molecular orbital (LUMO). The HOMO is an outer energy level that acts as electron donor and LUMO is the innermost energy level that acts as electrons acceptor (from HOMO level). While selecting the organic dyes for DSSCs, the following points, viz., band gap energy, HOMO and LUMO energy levels of dye have to be considered [8]. Figure 5.1.1 shows the cyclic voltammograms of 0.1 mM solutions of Trypan Blue (TB), SPADANS (SPD) and Evans Blue (EB) in 0.1 M of KCl solution in the potential range from -1.4 to 1.4 eV versus saturated calomel electrode (SCE). The cyclic voltammograms of dyes shows irreversible cathodic peaks at -0.84, -0.67 and -0.60 V for TB, SPD and EB dyes, respectively (Figure 5.1.1(a-c)). The energy gap, LUMO and HOMO energy levels of the dyes have been calculated using the following equations [9]:

$$E_{LUMO} / E_{HOMO} = - (4.8 + E_{onset}^{red} / E_{onset}^{oxd})$$

$$E_g = E_{LUMO} - E_{HOMO}$$

$$E_{HOMO} = E_{LUMO} - E_g$$

$$E_g = \frac{1240}{\lambda_{onset}} \ eV$$

where, E_{onset}^{oxd} is the onset oxidation potential and E_{onset}^{red} is the onset reduction potential of the dyes and E_g is the energy level of ferrocene (4.8 eV), a standard reference. The E_{LUMO}/E_{HOMO} of TB, SPD and EB dyes were found to be - 3.93 eV / - 6.02 eV, - 4.13 eV / - 6.56 eV and - 4.18 eV / - 6.22 eV, respectively.

5.1.1.2. UV-Visible absorption analysis of dye sensitized Cr-ZnO nanoparticles
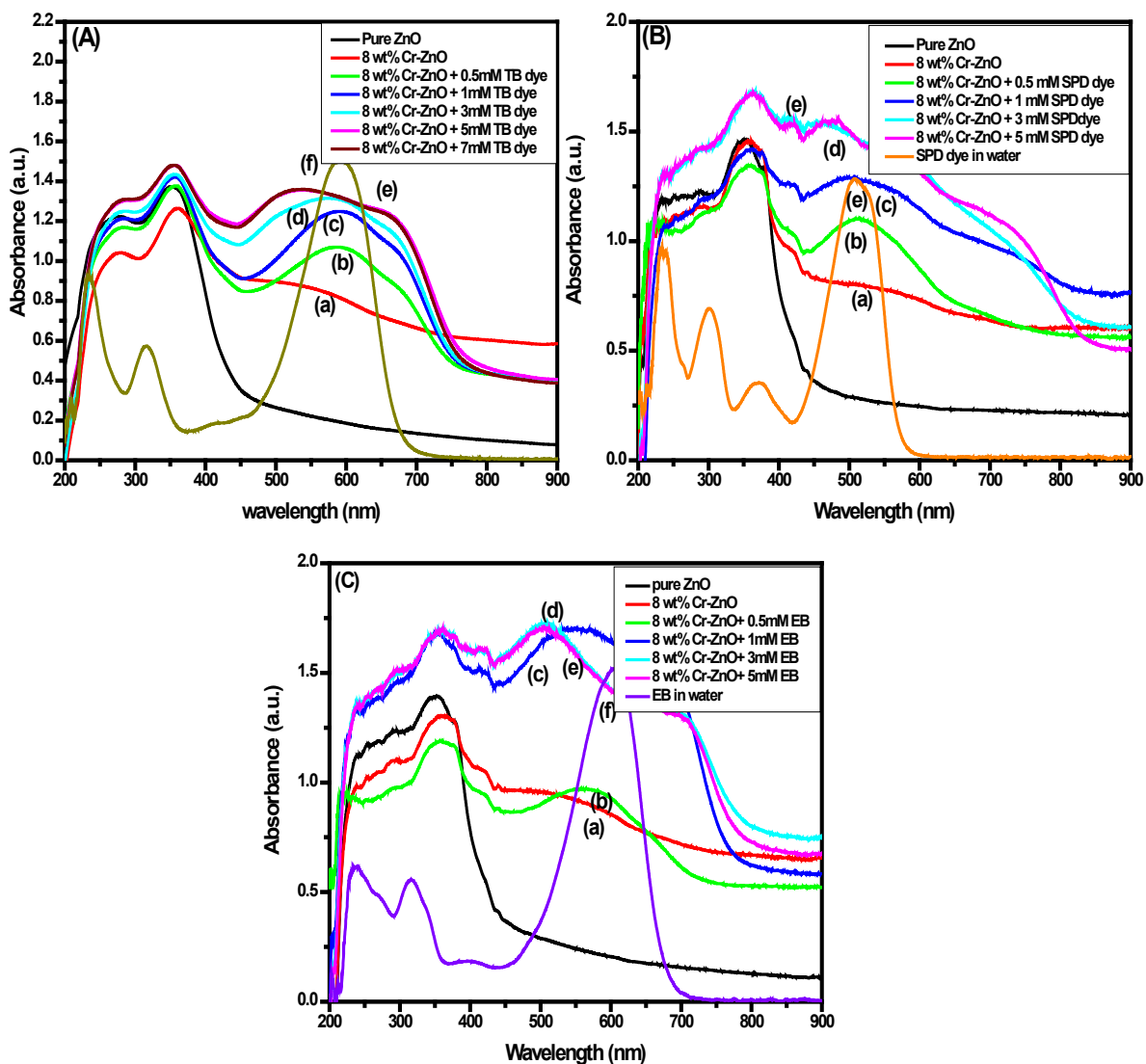
Figure 5.1.2: Optical absorption spectrum of (A) Trypan blue (B) SPADNS (C) Evans blue dyes sensitized Cr-ZnO nanoparticles.

Figure 5.1.2(A-C) shows the optical absorption spectra of dyes (TB, SPD and EB) in solution, 8 wt% Cr-ZnO nanoparticles (solid) and dyes sensitized 8 wt% Cr-ZnO nanoparticles (solid). From these figures, a significant difference between the optical absorption spectra of dyes and dyes sensitized 8 wt% Cr-ZnO nanoparticles was observed. Figure 5.1.2A(f)-C(f) represents the absorption spectra of dyes in solution,

which show the stronger absorption peaks at 597, 603 and 607 nm for TB, SPD and EB dyes, respectively. It reveals that the absorption maxima for all the dyes are in the visible range [10-11]. In addition, the absorption spectrum of individual dye in solution shows the different bands at lower wavelength region (UV) and one significant sharp band at higher wavelength region (Visible). The bands at lower wavelength region are assigned to $\pi \rightarrow \pi^*$ transition of the aromatic ring. A sharp band at visible region is assigned to $n \rightarrow \pi^*$ transition of lone pair of electrons present in the azo group (-N=N-) of dyes [12]. Figure 5.1.2A(a)-C(a) show the UV-Visible spectra of 8 wt% Cr-ZnO nanoparticles, which reveal that, the 8 wt% Cr-ZnO nanoparticles shows the highest absorption maximum at 390 nm. Figure 5.1.2A-C(b-e) show the absorption for different concentration (0.5-7 mM for TB, 0.5-5 mM for SPD, EB) of dyes sensitized 8 wt% Cr-ZnO nanoparticles. The broadening in the absorption spectra (compared to dyes in solution) of dye sensitized 8 wt% Cr-ZnO nanoparticles clearly confirmed the anchoring of dyes on the surface of Cr-ZnO nanoparticles [13]. The Cr-ZnO nanoparticles sensitized with 3 mM TB, 3 mM SPD and 1 mM EB have shown strong optical absorption compared to the other concentration of dyes. At higher concentrations of dyes, no further increase in the optical absorption was observed and hence the adsorption saturation limit of TB, SPD and TB dyes on Cr-ZnO has been fixed at 3, 3 and 1 mM, respectively [14].

5.1.1.3. I-V characteristics of dye sensitized Cr-ZnO nanoparticles

Figure 5.1.3(a-b) illustrates the current-voltage (I-V) characteristics of TB, SPD and EB dyes sensitized 8 wt% Cr-ZnO nanoparticles under dark and UV-light conditions.

Figure 5.1.3(a) shows the current intensity of dyes sensitized 8 wt% Cr-ZnO nanoparticles under dark condition. From these curves, it can be seen that the dyes sensitized Cr-ZnO samples shows low current intensity compared to bare Cr-ZnO nanoparticles. This decrease in current intensity after dye sensitization is due to the blocking effect of the dye and as well as surface relaxation effect [15]. On UV-light illumination the current intensity of dyes sensitized Cr-ZnO nanoparticles has found to be enhanced considerably. This is due to the photo exited charge carriers (electrons) present in the LUMO levels of dyes are easily jumped into the conduction band (CB) of Cr-ZnO (E_{CB} = -4.194 eV) nanoparticles. The mobility of these charge carriers increases under UV-light condition and hence increases the current intensity of dye sensitized Cr-ZnO nanoparticles [16].
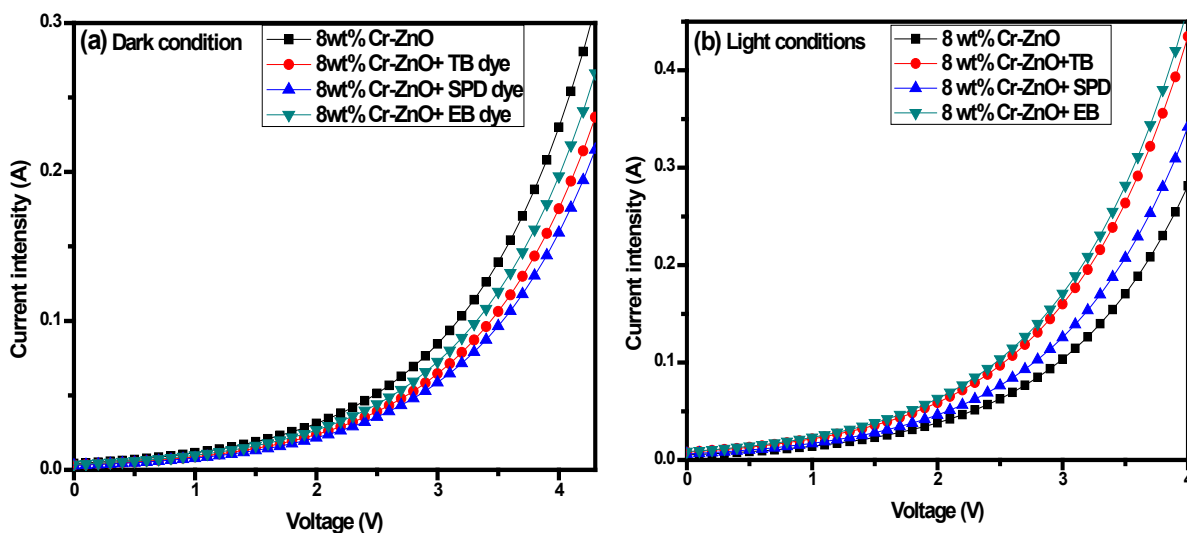
Figure 5.1.3: I-V characteristics of Trypan blue, SPADNS and Evans blue dyes sensitized 8 wt% Cr-ZnO in dark condition and UV-light condition.

163

5.2. Optical and Electrical Properties of Dye Sensitized Zn-CuO Nanoparticles

5.2.1. Results and discussion

5.2.1.1. UV-Visible absorption analysis of dye sensitized Zn-CuO nanoparticles

Figure 5.2.1: UV-Visible spectrum of (A) Trypan blue (B) SPADNS (C) Evans blue dyes sensitized 4 mol% Zn-CuO nanoparticles.

Figure 5.2.1(A-C) show the UV-Visible absorption spectra of Trypan blue (TB), SPADNS (SPD) and Evans blue (EB) dyes and dyes sensitized monoclinic 4 mol% Zn-CuO nanoparticles. The absorption of dyes sensitized samples is due to the combined effect of transition metal doped semiconductors and dye molecules [17]. Figure 5.2.1A(f)-C(f) show the optical absorption maxima at (λ_{max}) 597 nm, 603 nm and 607 nm for TB, SPD and EB dyes, respectively. The λ_{max} for all the dyes are in the visible region [18]. Figure 5.2.1(A) displays the absorption spectra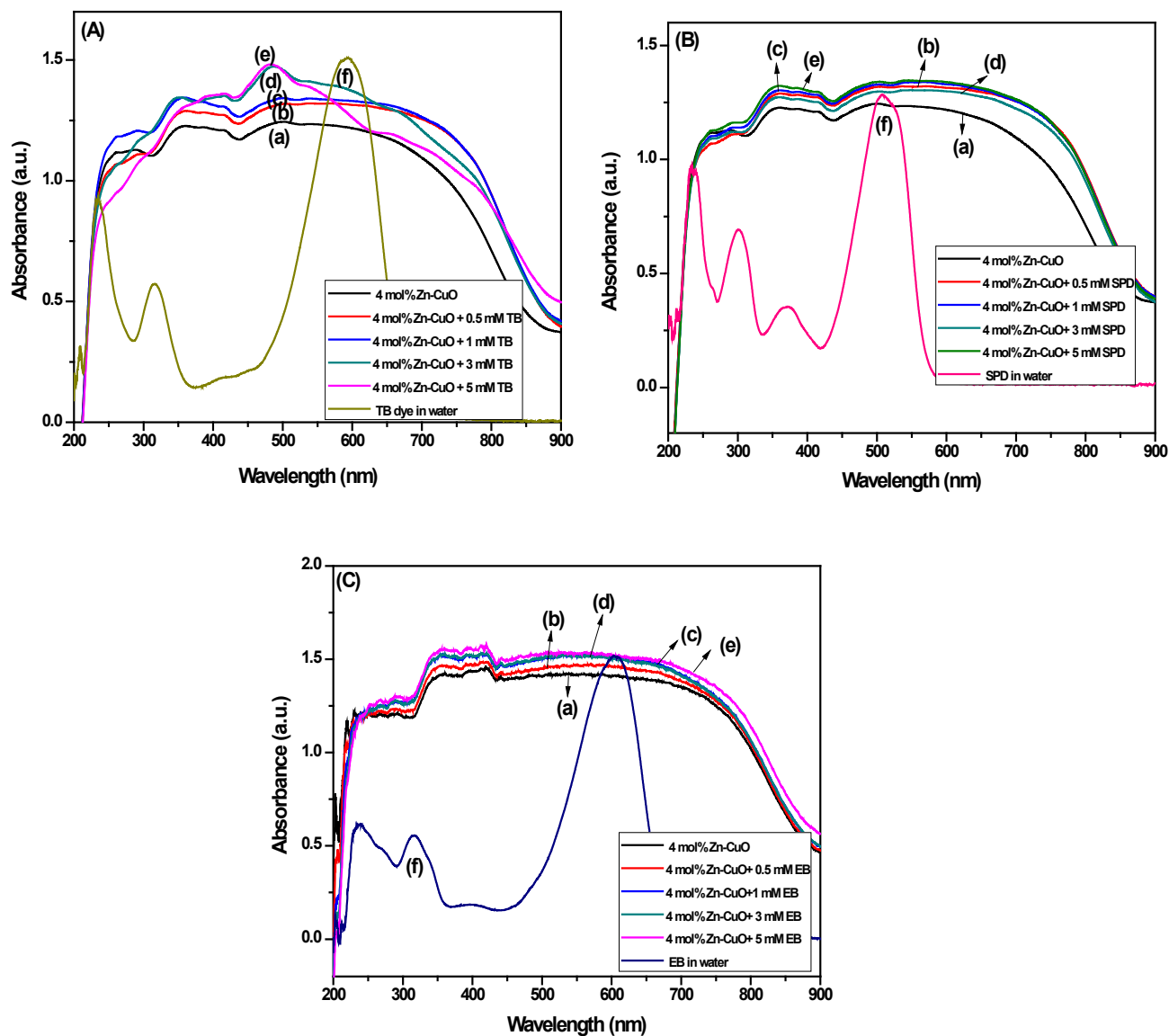 of TB sensitized (0.5-5 mM) 4 mol% Zn-CuO nanoparticles. It is found that the absorption of dye sensitized Zn-CuO nanoparticles was increased with increase in the concentration of dye with a small broadening in absorption maxima. It reveals the cooperative mechanism of TB dye molecule and Zn-CuO towards the optical absorption [19]. The similar result was observed in the SPD and EB dyes sensitized 4 mol% of Zn-CuO nanoparticles (Figure 5.2.1(B-C)). Among these samples, EB sensitized Zn-CuO nanoparticles show well broadening (441-874 nm) compared to TB (440-841 nm) and SPD (438-865 nm) sensitized Zn-CuO nanoparticles. The Zn-CuO nanoparticles sensitised with 1 mM TB, 1 mM SPD and 5 mM EB have shown strong optical absorption and at higher concentrations of the dyes, no further increase in the optical absorption was observed. This indicated that the adsorption saturation limit of TB, SPD and EB dyes on Zn-CuO was 1, 1 and 5 mM, respectively [20].

5.2.1.2. I-V characteristics of dye sensitized Zn-CuO nanoparticles

Figure 5.2.2(a-b) shows the I-V response of TB, SPD and EB dye sensitized 4 mol% of Zn-CuO nanoparticles under dark and UV-light conditions. At dark condition,

the 4 mol% Zn-CuO nanoparticles show low current intensity compared to TB, SPD and EB dyes sensitized Zn-CuO nanoparticles. The low current intensity of dye sensitized Zn-CuO nanoparticles may be attributed to the blocking effect of dyes [15]. Figure 5.2.2(b) shows the I-V curves of 4 mol% Zn-CuO nanoparticles and dye sensitized 4 mol% Zn-CuO nanoparticles under UV-light condition, which indicates a considerable enhancement in the current intensity upon dye sensitization. This is due to the transfer of photo electrons from the innermost energy (LUMO) levels of dyes to the conduction band (CB) of Zn-CuO (E_{CB} = -4.35 eV) nanoparticles. The mobility of these charge carriers in the dye sensitized Zn-CuO nanoparticles increases under UV-light condition and responsible for the considerable enhancement in the current intensity of dye sensitized Zn-CuO nanoparticles [21].
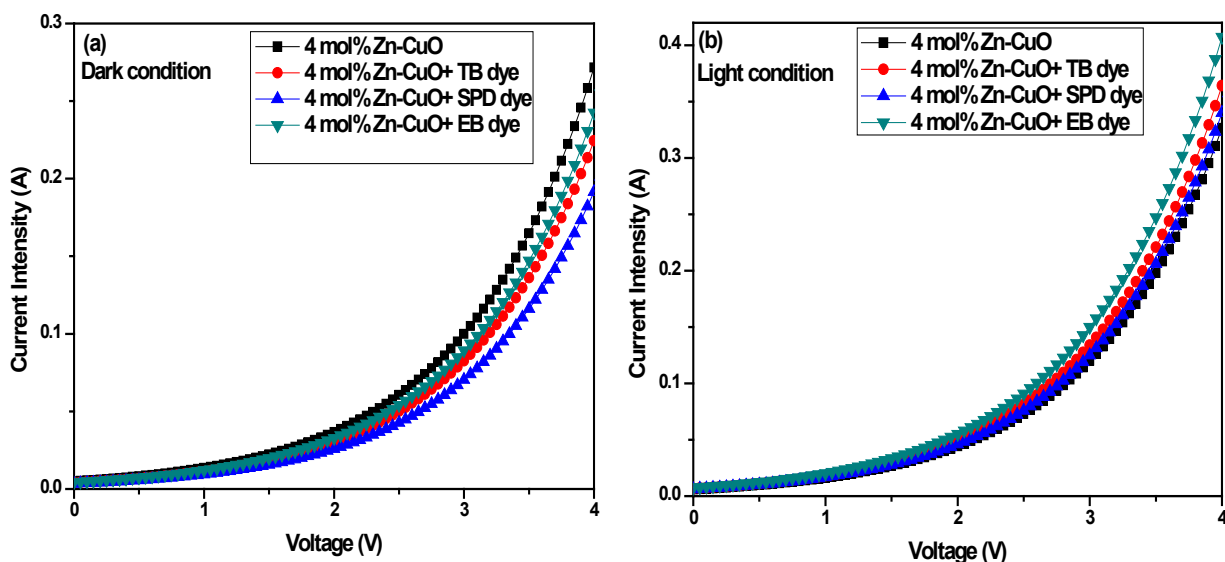
Figure 5.2.2: I-V characteristics of Trypan blue, SPADNS and Evans blue dyes sensitized 8 wt% Zn-CuO nanoparticles in dark and UV-light condition.

5.3. Optical and Electrical Properties of Dye Sensitized Ni-CdO Nanoparticles

5.3.1. Results and discussion

5.3.1.1. UV-Visible absorption analysis of dye sensitized Ni-CdO nanoparticles
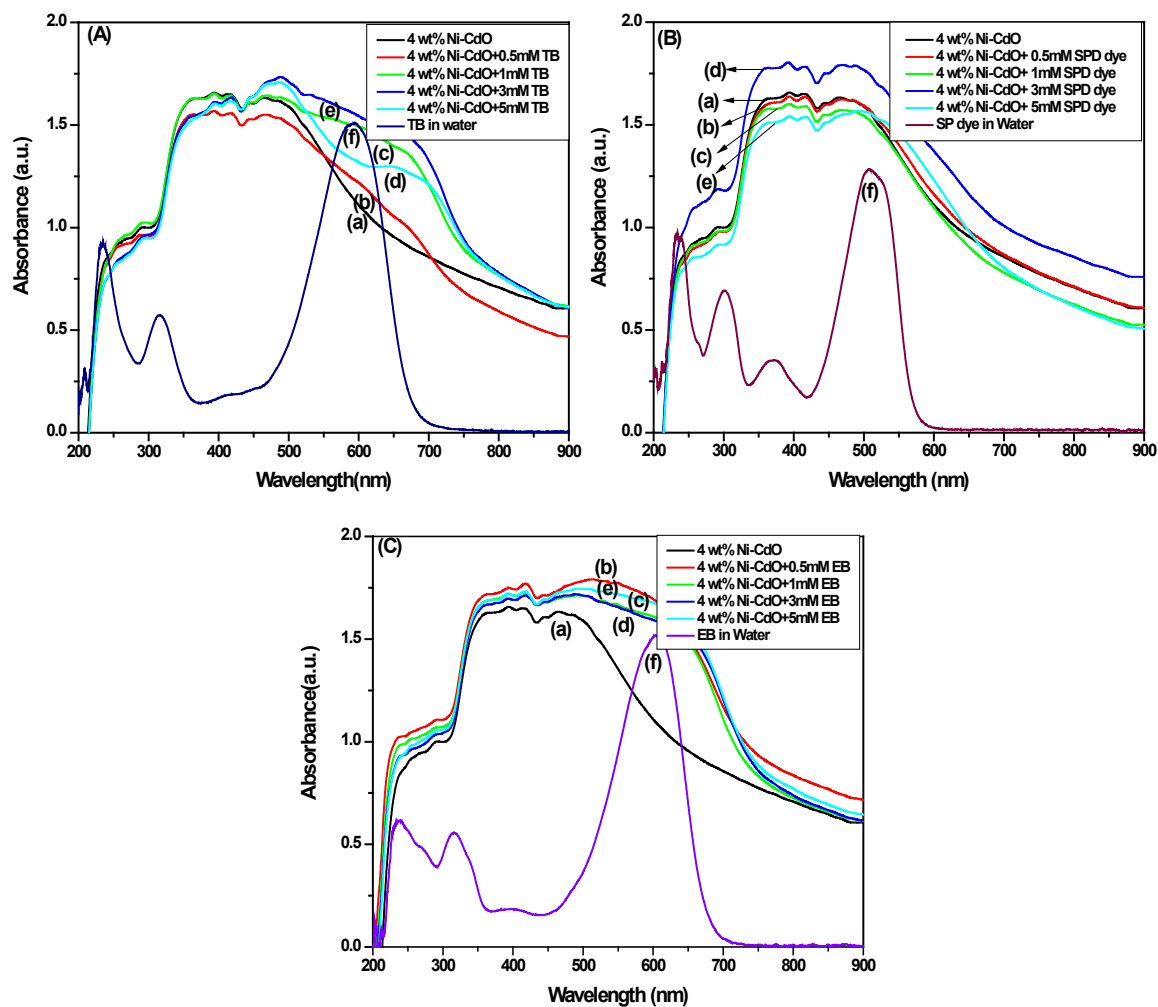
Figure 5.3.1: UV-Visible absorbance spectrum of (A) Trypan blue (B) SPADNS and (C) Evans blue dyes sensitized 4 wt% Ni-CdO nanoparticles.

To improve the power conversion efficiency of dye sensitized solar cells (DSSCs) optical properties of each material are very significant. Hence, the optical absorbance measurement of semiconducting nanomaterials, dyes and dyes coated nanomaterials were carried out using UV-Visible spectrophometer [22]. Figure 5.3.1A(f)-C(f) show the

optical absorption maxima at (λ_{max}) 597 nm, 603 nm and 607 nm for TB, SPD and EB dyes, respectively. In addition, the absorption spectrum of individual dye in solution shows a sharp absorption peak at visible region and the small absorption peaks at UV- region. The absorption peak at visible region is attributed to n→π* transition of lone pair of electrons present in the azo group (-N=N-) of dyes and the absorption peaks at UV-region are attributed to π→π* transition of the aromatic rings [23]. Figure 5.3.1A(a)-C(a) display the optical absorption spectra of 4 wt% Ni-CdO, which reveal that the 4 wt% of Ni-CdO nanoparticles shows a strong absorption maxima in visible-region (481 nm). Figure 5.3.1A-C(b-e) represents the TB, SPD and EB dyes sensitized (0.5-5 mM) 4 wt% Ni-CdO nanoparticles. It is found that the optical absorption of TB, SPD and EB sensitized 4 wt% Ni-CdO nanoparticles were increased with increase in the concentration of dyes with a small broadening in absorption maxima. This indicated that the anchoring of dyes on the surface of 4 wt% Ni-CdO nanoparticles are responsible for broadening of absorption maxima. Among the dyes sensitized samples, the TB and EB sensitized Ni-CdO nanoparticles shows more broadening of absorption edge in the wavelength range of 435-754 and 433-716 nm, respectively [24]. On the other hand the SPD dye sensitized Ni-CdO nanoparticles shows less broadening. The Ni-CdO nanoparticles sensitized with 3 mM TB, 3 mM SPD and 0.5 mM EB have shown strong optical absorption and above these concentrations, no further increase in the optical absorption was observed. This indicated that the adsorption saturation limit of TB, SPD and EB dyes on Ni-CdO was 3, 3 and 0.5 mM, respectively [25].

5.3.1.2. I-V characteristics of Ni-CdO nanoparticles with and without dye sensitization

Figure 5.3.2 (a-b) show the I-V response of TB, SPD and EB dyes sensitized 4 wt% of Ni-CdO nanoparticles under dark and UV-light conditions. Figure 5.3.2(a)

shows I-V curves of dye sensitized 4 wt% Ni-CdO nanoparticles under dark condition. It can be seen that the TB, SPD and EB dyes sensitised 4 wt% Ni-CdO nanoparticles exhibits poor current intensity compared pure 4 wt% Ni-CdO nanoparticles. The decrease in the current intensity of dye sensitized Ni-CdO nanoparticles may be attributed to the blocking effect of the dye and as well as surface relaxation effect [26].
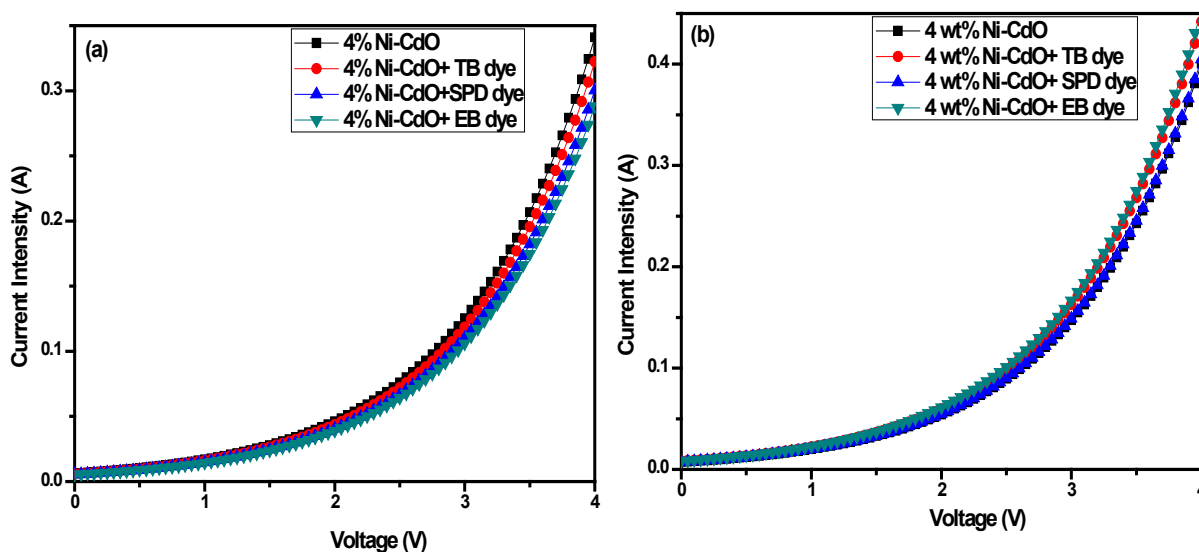
Figure 5.3.2: I-V characteristics of Trypan blue, SPADNS and Evans blue dyes sensitized 4 wt% Ni-CdO nanoparticles in dark and light condition.

Figure 5.3.2(b) shows the I-V curves of TB, SPD and EB dyes sensitized 4 wt% Ni-CdO nanoparticles under UV-light condition. It is found that the current intensity of dye sensitized nanoparticles shows considerable enhancement compared to bare 4 wt% of Ni-CdO nanoparticles. This is due to the transfer of photo exited charge carrier (electrons) from LUMO levels of dyes to the conduction band (CB) of Ni-CdO (E_{CB} = -4.315 eV) nanoparticles. An increase in the mobility of these charge carriers under UV-light condition is responsible for the increase in current intensity for the dye sensitized Ni-CdO nanoparticles [27].

5.4. Optical and Electrical Properties of Dye Sensitized Cr-TiO₂ Nanoparticles

5.4.1. Results and discussion

5.4.1.1. UV-Visible absorption analysis of dye sensitized Cr-TiO₂ nanoparticles

Figure 5.4.1. Optical absorption spectrum of (A) Trypan blue (B) SPADNS (C) Evans blue dyes sensitized Cr-TiO₂ nanoparticles.

Figure 5.4.1(A-C) illustrates the UV-Visible absorption spectra of 8 wt% Cr-TiO₂, dyes coated 8 wt% Cr-TiO₂ and dyes in solution. From these figures, a significant difference between the optical absorption spectra of dyes coated 8 wt%
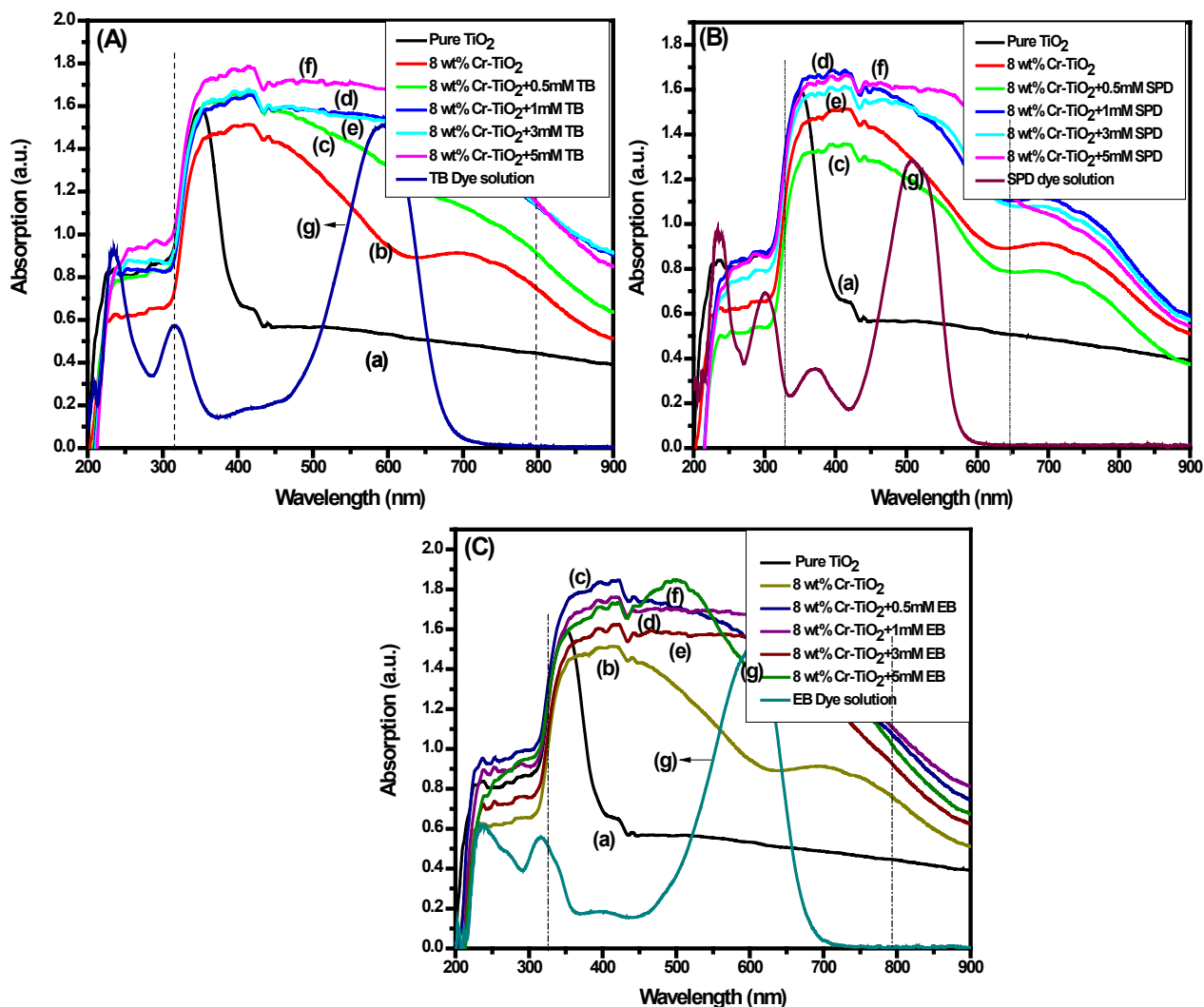
Cr-TiO$_2$ nanoparticles and TB, SPD, EB dyes was observed. Figure 5.4.1A(g)-C(g) shows the UV-Visible absorption spectra of TB, SPD and EB dyes in solution, which exhibit sharp absorption band at visible-region (597 nm for TB, 603 nm for SPD and 607 nm for EB) and two to three week absorption band at UV-region (233 nm, 315 nm for TB, 235 nm, 301 nm, 371 nm for SPD, 316 nm, 396 nm for EB) [28]. The absorption maximum at higher wavelength region (Vis.) is corresponds to n→π* transition of lone pair of electrons present in the azo group. The absorption maxima at lower wavelength region (UV) are corresponds to π→π* transition of the conjugated aromatic system of the dyes [29]. Figure 5.4.1A(b)-C(b) show the absorbance spectra of 8 wt% Cr-TiO$_2$ nanoparticles and it has strong optical absorbance at UV-region (394 nm). Figure 5.4.1A-C(c-f) shows the absorbance spectra of TB, SPD and EB dyes sensitized Cr-TiO$_2$ nanoparticles. From these figures, the broadening of absorption maxima was observed at TB, EB and SPD dyes sensitized Cr-TiO$_2$ nanoparticles. It clearly reveals the cooperative mechanism of dye molecules and Cr-TiO$_2$ nanoparticles towards the optical absorption [30]. The 4 wt% Cr-TiO$_2$ nanoparticles sensitized with 5, 5 and 1 mM have shown strong optical absorption compared to the other concentration of dyes. At higher concentration of dyes, no further increase in the optical absorption was observed, which confirmed the adsorption saturation limit of TB, SPD and TB dyes on Cr-TiO$_2$ [31].

5.4.1.2. I-V characteristics of Cr-TiO$_2$ nanoparticles with and without dye sensitization

Figure 5.4.2 (a-b) displays the current-voltage (I-V) characteristic studies of with (TB, SPD and EB) and without dye sensitized 8 wt% of Cr-TiO$_2$ nanoparticles under dark and UV-light conditions. At dark condition, the 8 wt% Cr-TiO$_2$ exhibits very low current

intensity compared TB, SPD and EB dye sensitized Cr-TiO$_2$ nanoparticles. The decrease in current intensity after dye sensitization is due to the blocking effect of dye and surface relaxation effect [32-33]. Figure 5.4.2(b) displays the I-V curves of dyes (TB, SPD and EB) sensitized 8 wt% Cr-TiO$_2$ nanoparticles under UV-light condition. On UV-light illumination the current intensity of TB, SPD and EB dyes sensitized Cr-TiO$_2$ nanoparticles has found to be improved considerably. This may be due to the easy transfer of photo exited electrons from the LUMO levels of dyes into the conduction band (CB) of Cr-TiO$_2$ (E_{CB} = -4.3143 eV) nanoparticles. The increase in the charge carrier density and mobility upon light illumination enhances the current intensity of dye sensitized Cr-TiO$_2$ nanoparticles [33].

Figure 5.4.2: I-V characteristics of Trypan blue, SPADNS and Evans blue dyes sensitized 8 wt% Cr-TiO$_2$ nanoparticles in dark and light condition.

5.5. Optical and Electrical Properties of Dye Sensitized Zn-MgO Nanoparticles

5.5.1. Results and discussion

5.5.1.1. UV-Visible absorption analysis of dye sensitized Mg-ZnO nanoparticles
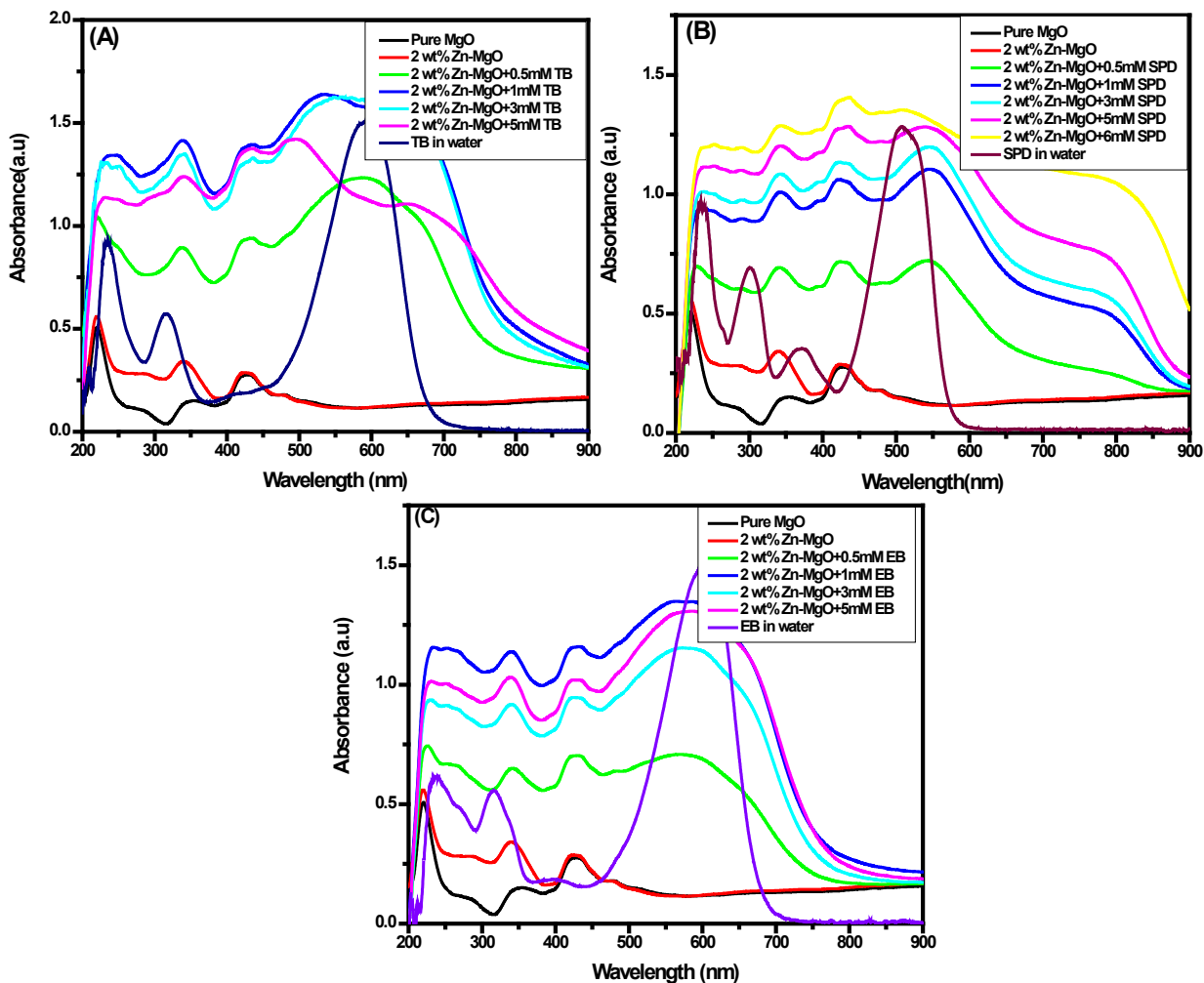
Figure 5.5.1: Optical absorption spectrum of (A) Trypan blue (B) SPADNS (C) Evans blue dyes sensitized 2 wt% Zn-MgO nanoparticles.

Figure 5.5.1(A-C) shows the absorption spectra of dyes (TB, SPD and EB) in solution and dyes coated 2 wt% Zn-MgO nanoparticles. The absorption spectra of TB, SPD and EB dyes in solution show the stronger absorption peaks at 597, 603 and 607 nm, respectively. It reveals that the absorption maxima for all the dyes are in the visible

range. The Zn-MgO nanoparticles sensitized with different concentration (0.5-5 mM TB, EB and 0.5-6 mM SPD) of dyes show the broadening of absorption edge as compared to the dyes in solution. In this case, the Zn-MgO nanoparticles sensitized with 1mM TB, 1mM EB and 5 mM SPD dyes showed strong optical absorption compared to the other concentrations of dyes. At higher concentrations of dyes, no further increase in the optical absorption was observed. This revealed the adsorption saturation limit of TB, SPD and TB dyes on Zn-MgO was at 1, 1 and 5 mM, respectively [34]. The optical absorption spectra of all the dyes sensitized Zn-MgO nanoparticles illustrates that the TB, SPD and EB dyes are completely chemisorbed with Zn-MgO nanoparticles. The overall results indicate that the selected dyes TB, SPD and EB can be used as photo-sensitizers in wide band gap semiconductors [35].

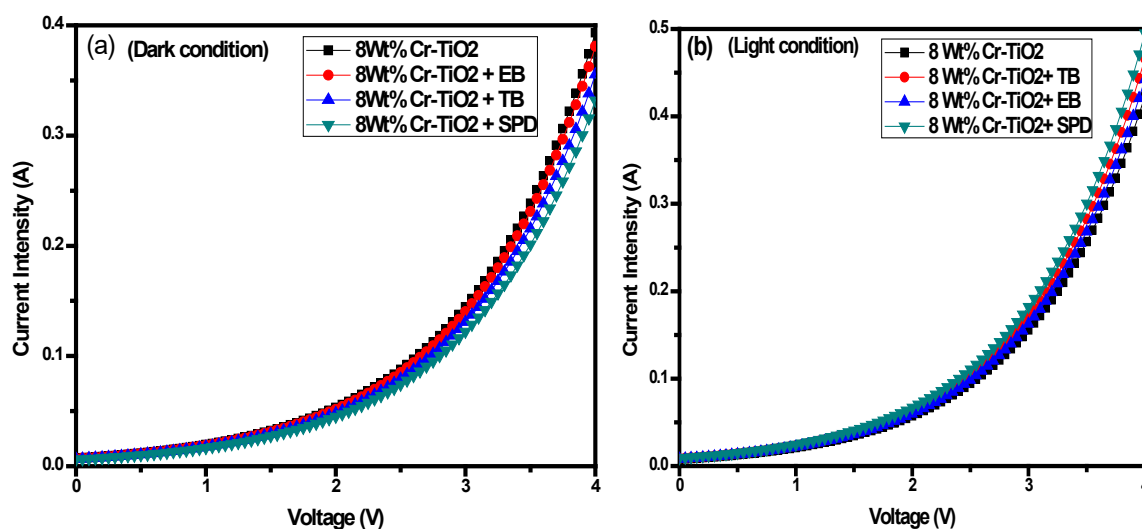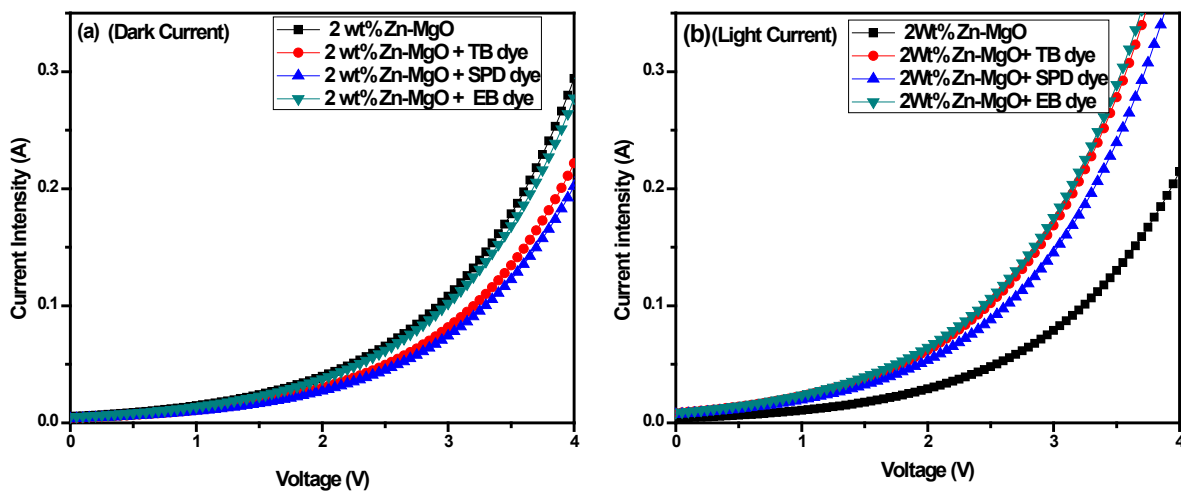### 5.5.1.2. I-V characteristics of Zn-MgO nanoparticles with and without dye sensitization

Figure 5.5.2: I-V characteristics of Trypan blue, SPADNS and Evans blue dyes sensitized 2 wt% Zn-MgO nanoparticles in dark and light condition.

Figure 5.5.2(a-b) illustrates the current-voltage (I-V) characteristics of TB, SPD and EB dyes sensitized 2 wt% Zn-MgO nanoparticles under dark and light conditions.

Figure 5.5.2(a) shows the current intensity of dyes sensitized Zn-MgO nanoparticles under dark condition. From these curves, it can be seen that the dyes sensitized Zn-MgO nanoparticles shows low current intensity compared to bare Zn-MgO nanoparticles. The decrease in current intensity after dye sensitization is due to the blocking effect of the dye [36]. Upon UV-light illumination on the surface of dyes sensitized Zn-MgO nanoparticles, the electrons present in the dyes were promoted from HOMO (- 6.02, - 6.56 and - 6.22 eV) level to LUMO (- 3.93, - 4.13 and - 4.18 eV) level of the dyes. Subsequently, these exited electrons are impinged to the conduction band of Zn-MgO (E_{CB} = - 4.24 eV, E_{VB} = - 7.05 eV) nanoparticles [37]. The increase in the charge carrier density and mobility upon light illumination is responsible for the enhancement of current intensity of Zn-MgO nanoparticles. This remarkable increase in the current intensity of dyes coated Zn-MgO nanoparticles made them to use in photovoltaic applications [38].

5.6. Conclusions

The effect of dyes on the optical and electrical properties of Cr-ZnO, Zn-CuO, Ni-CdO, Cr-TiO₂ and Zn-MgO nanoparticles were studied. The absorption spectrum of TB, SPD and EB dyes sensitized 8 wt% Cr-ZnO, 4 mol% Zn-CuO, 4 wt% Ni-CdO, 8 wt% Cr-TiO₂ and 2 wt% Zn-MgO nanoparticles show the broader peaks compared to bare 8 wt% Cr-ZnO, 4 mol% Zn-CuO, 4 wt% Ni-CdO, 8 wt% Cr-TiO₂ and 2 wt% Zn-MgO nanoparticles. The current-voltage (I-V) measurement under dark as well as UV-Vis. light illumination conditions showed the photosensitive behaviour of dye sensitized Cr-ZnO, Zn-CuO, Ni-CdO, Cr-TiO₂ and Zn-MgO nanoparticles. The increased current intensity of dye sensitized Cr-ZnO, Zn-CuO, Ni-CdO, Cr-TiO₂ and Zn-MgO nanoparticles was clearly indicated the possibility of using these nanoparticles in the fabrication of dye sensitized solar cells (DSSCs).

References

[1]   S. Bose, V. Soni, K.R. Genewa, Inter. J. Sci. Res. Publications, 5, 2, **(2015)**.

[2]   A. Mishra, M.K.R. Fischer, P. Bauerle, Angew. Chem. Int. Ed., 48, 2475, **(2009)**.

[3]   J.K. Roy, S.Kar, J. Leszczynski, Sci. Reports, 8 (10997), 1, **(2018)**.

[4]   L. Zhang, J.M. Cole, Appl. Mater. Inter., 7, 3427, **(2015)**.

[5]   K. Ladomenou, T. N. Kitsopoulos, G. D. Sharma, A. G. Coutsolelos, RSC Adv., 4, 21399, **(2014)**.

[6]   R. Parthiban, B. Balamurugan, B.G. Jeyaprakash, Spectrochem. Acta A: Mol. Biomol. Spect., 136, 992, **(2015)**.

[7]   S.A. Kazmi, S. Hameed, A. Azam, Propspect. Sci., 8, 579, **(2016)**.

[8]   M.A. Stevens, A.C. Arango, Org. Electron., 37, 80, **(2016)**.

[9]   A. Amacher, C. Yi, J. Yang, M.P. Bircher, Y. Fu, M. Cascella, M. Gratzel, S. Decurtinsa, S.X. Liu, Chem. Commun., 50, 6541, **(2014)**.

[10]   Y. Liao, J. Hu, C. Zhu, Y. Liu, X. Chen, C. Chen, C. Zhang, J. Mol. Struct., 1108, 472, **(2016)**.

[11]   U. Mehmood, I.A. Hussein, A.A. Ahmed, S. Ahmed, J. Photovolt., 6, 2, **(2016)**.

[12]   Y.G. Sidir, I. Sidir, H. Barber, E. Tasal, J. Mol. Liquids, 162, 150, **(2011)**.

[13]   W. A. Ayalew, D. W. Ayele, J. Sci.: Advance Mater. Devices, 1, 490, **(2016)**.

[14]   M.Y.A. Rahman, A.A. Umar, R. Taslim, M.M. Salleh, Electrochim. Acta, 88, 646, **(2013)**.

[15]   A. Stanley, D. Mathews, Aust. J. Chem., 48, 1297, **(1995)**.

[16]   Z.Q. Bai, Z.W. Liu, Scientific Reports, 7: 11384, 11160, **(2017)**.

[17]   Y.J. Chen, Y.C. Cheng, L.Y. Lin, W.C. Cheng, S.M. Chang, Electrochem. Acta, 178, 417, **(2015)**.

[18]   M. Gratzel, J. Photochem. Photobiol. C Photochem. Rev., 4, 150, **(2003)**.

[19]   B.P. Kafle, B.R. Pokhrel, R. Gyawali, A. Kafle, T.M. Shrestha, R. Shrestha, R.M. Adhikari, Adv. Appl. Sci. Res., 5, 10, **(2014)**.

[20]   P.K. Baviskar, J. Solid State Electrochem., 21, 2702, **(2017)**.

[21]   Z.Q. Bai, Z.W. Liu, Sci. Reports, 7, 4, **(2017)**.

[22]   M.S. Jo, J.S. Cho, X.L. Wang, E.M. Jin, S.M. Jeong, D.W. Kang, Nanomaterials, 9, 5, **(2019)**.

[23]   M.K. Hossain, M.F. Pervez, M.N.H. Mia, M.S. Rahaman, M.R. Kavin, M.A. Khan, Results Phys., 7, 1520, **(2017)**.

[24]   L.Q. Bao, P. Ho, R.K. Chitumalla, J. Jang, S. Thogiti, J. H. Kim, Dyes Pigments, 149, 31, **(2018)**.

[25]   P.N. Didwal, K.S. Pawar, P.R. Chikate, A.C. Abyankar, H.M. Pathan, J. Mater. Sci.: Mater. Electron., 27, 12449, **(2016)**.

[26]   K. Hara, T. Horiguchi, K. Sayama, T. Kinoshita, H. Sugihara, H. Arakawa, Sol. Energy Mater. Sol. Cells, 64, 120, **(2000)**.

[27]   J. Reemts, A. Kittel, J. Appl. Phys., 101, 4, **(2007)**.

[28]   A. Dumbrava, G. Prodan, A. Georgescu, F. Moscalu, Bull. Mater. Sci., 38, 71, **(2015)**.

[29]   N. Ruangsupapichat, M. Ruamyart, P. Kanchanarugee, C. Boonthum, N. Prachumark, T. Sudyoadsuk, V. Promarak, Dyes Pigments, 151, 153, **(2018)**.

[30]   M. Mao, Q.S. Li, X.L. Zhang, G.H. Wu, C.G. Dai, Y. Ding, S.Y. Dai, 117, 34, **(2015)**.

[31]   K. Kasinathan, J. Kennedy, M. Elayaperumal, M. Henini, M. Malik, Sci. Reports, 6, 7, **(2016)**.

[32]   K. Pomoni, M.V. Sofianon, T. Georgakopoulos, N. Boukos, C. Trapalis, J. Alloys Compd., 548, 198, **(2013)**.

[33]   M. Sheinkman, A.Y. Shik, Sov. Phys. Semicond., 10, 141, **(1976)**.

[34]   J. Lim, A. D. Bokare, W. Choi, RSC Adv., 7, 32493, **(2017)**.

[35]   S. Suresh, A. Pandikumar, S. Murugesan, R. Ramaraj, S.P. Raj, Sol. Energy, 85, 1789, **(2011)**.

[36]   Z.H. Liang, Y.J. Zhu, G.F. Huang, J. Mater. Sci., 42, 480, **(2007)**.

[37]   M. Rani, S.K. Tripathi, J. Elect. Mater., 43, 430, **(2014)**.

[38]   M. Rani, S.J. Abbas, S.K. Tripathi, Mater. Sci. Eng.: B, 187, 80, **(2014)**.

Research Publications

1. **R.O. Yathisha,** Y. Arthoba Nayaka and C.C. Vidyasagar**,** Microwave combustion synthesis of hexagonal prism-shaped ZnO nanoparticles and effect of Cr on structural, optical and electrical properties of ZnO nanoparticles, Mater. Chem. Phys., 181(2016) 167-175.

2. **R.O. Yathisha** and Y. Arthoba Nayaka, Structural, optical and electrical properties of zinc incorporated copper oxide nanoparticles: doping effect of Zn, J. Mat. Sci. 53 (2018) 678-691.

3. **R.O. Yathisha** and Y. Arthoba Nayaka, Synthesis of copper oxide nano-rods by microwave-assisted combustion route and their characterization studies, Inter. J. Nanoelect. Mater. 11(2018) 233-240.

4. **R.O. Yathisha,** Y. Arthoba Nayaka, P. Manjunatha, M.M. Vinay and H.T. Purushothama, Doping, structural, optical and electrical properties of Ni^{2+} doped CdO nanoparticles prepared by microwave combustion route, Micro-chemical Journal, 145 (2019) 630-641.

5. **R.O. Yathisha,** Y. Arthoba Nayaka, P. Manjunatha, H.T. Purushothama, M.M. Vinay and K.V. Basavarajappa, Study on the effect of Zn^{2+} doping on optical and electrical properties of CuO nanoparticles, Physica E: Low-dimensional Systems and Nanostructures 108 (2019) 257–268.

6. **R.O. Yathisha,** Y. Arthoba Nayaka, P. Manjunatha, H.T. Purushothama, M.M. Vinay and K.V. Basavarajappa, Influence of Zn^{2+} doping and organic dyes as sensitizers on MgO nanoparticles synthesized by microwave combustion route, Powder technology (Under review).

7. **R.O. Yathisha** and Y. Arthoba Nayaka, Optical and electrical properties of dye-sensitized Cr-TiO_2 nanoparticles (Under preparation).

8. **R.O. Yathisha** and Y. Arthoba Nayaka, Optical and electrical properties of metal free organic dyes-sensitized Cr-ZnO Ni-CdO and Zn-CuO nanoparticles (Under preparation).

9. **R.O. Yathisha** and Y. Arthoba Nayaka, Structural, optical and electrical properties of ZnO nanoparticles synthesized under different microwave power (Under preparation).

10. **R.O. Yathisha** and Y. Arthoba Nayaka, Structural, optical and electrical properties of synthesized ZnO nanoparticles by microwave combustion method using different solvents (Under preparation).

Papers Presented in Internal and National Conferences

1. Two days National conference on "Recent Advances in Chemical Science Research", during 14-15th March 2015, held at Department of Chemistry, Kuvempu University, Shankaraghatta, Shivamogga, Karnataka, India.

2. International Conference on "Chemistry for Renewable Energy (ICCRE)", during 25-26th February 2016, held at Bishop Heber College (Autonomous), Tiruchirappalli, Tamil Nadu, India.

3. Chemical and Bio-Chemical aspects in pharmaceutical applications (NCCBAPA), during 23rd April 2016, held at Department of Pharmaceutical Chemistry, Kuvempu University, P.G, Centre, Kadur, Chikkamagalur, Karnataka, India.

4. National Conference on "Mechanical, Materials and Manufacturing Engineering (NCMMME)", during 23-24th May 2016, held at The National Institute of Engineering, Mysuru, Karnataka, India.

5. 9th KSTA Annual Conference on "Science, Technology, and Innovations in the 21st Century", during 20-21st December 2016, held at Christ University, Bangalore, Karnataka, India.

6. 35th Annual National Conference on "Indian Council of Chemists", during 22-24th December 2016, held at Haribhai V. Desai College, Pune, Maharashtra, India.

7. International Conference on "Green Chemistry and Nanotechnology Opportunities and Challenges", during 27-28th, St. Aloysius College (Autonomous), Mangaluru, Karnataka, India.

8. Two Days National Conference on "Recent Advances in Chemical Biology and Material Science for Industry and Society (RACBMS)", during 9-10th February 2018, Department of Industrial chemistry, Shivamogga, Kuvempu University, Karnataka, India.

9. Two days National Conference on "Exploring Innovative Research and Developments in Chemical Sciences (EIRDCS)", during 1-2nd March 2019, held at Department of Chemistry, Shivamogga, Kuvempu University, Karnataka, India.

Seminars and Workshops Attended

1. One Day National Level Seminar on "Advances and Challenges in Biological Research", during 17th March 2016, held at Department of Biochemistry, Kuvempu University, Shivamogga, Karnataka, India.

2. Two Days National Seminars on "Recent Developments in Nano Materials and Their Applications", during 18-19th March 2016, held at Department of Physics, Kuvempu University, Shivamogga, Karnataka, India.
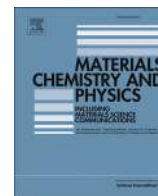
CrossMark

Microwave combustion synthesis of hexagonal prism shaped ZnO nanoparticles and effect of Cr on structural, optical and electrical properties of ZnO nanoparticles

R.O. Yathisha [a], Y. Arthoba Nayaka [a, *], C.C. Vidyasagar [b]

[a] Department of Chemistry, School of Chemical Sciences, Kuvempu University, Jnanasahyadri, Shankaraghatta 577 451, Karnataka, India
[b] Department of Chemistry, School of Basic Sciences, Ranichannamma University, Belgaum 591156, Karnataka, India

HIGHLIGHTS

- The prism shaped $Zn_{1-x}Cr_xO$ $(0 \leq x \leq 0.15)$ was prepared by microwave combustion method.
- Effect of Cr on the properties of ZnO was reported.
- Change in crystal size was explained by lattice strain and Zener-Pinning effect.
- The optical measurements shows up to 8 wt% of Cr doping had more efficient.
- Compared to ZnO, Cr doped ZnO enhance the photo voltaic activity.

GRAPHICAL ABSTRACT
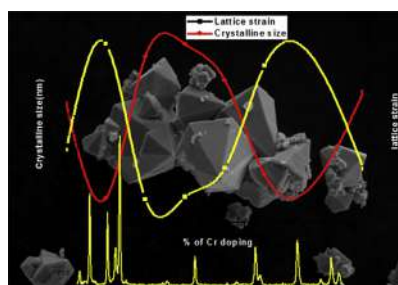
ARTICLE INFO

ABSTRACT

The synthesis and study of semiconducting nanostructure materials have become a considerable interdisciplinary area of research over the past few decades. The control of morphologies and effective doping by right dopant are the two tasks for the synthesis of semiconducting nanoparticles. The present work outlines the synthesis of ZnO and Cr-ZnO nanoparticles via microwave combustion method without using any fuel. The crystal morphology, optical and electrical properties were characterized by X-ray diffraction study (XRD), UV—Visible spectroscopy (UV—Vis), Scanning electron microscopy (SEM), Energy-dispersive analysis using X-rays (EDAX), Transmission electron microscopy (TEM) and Keithley source meter. The crystal size was determined from XRD, whose values were found to be decreased with increase in the concentration of Cr up to 2 wt% and further increase in the dopant concentration resulted the formation secondary phase ($ZnCr_2O_4$). Scanning electron micrographs shows the hexagonal prism structure of ZnO and Cr-ZnO nanoparticles. EDAX shows the existence of Cr ion in the Cr-ZnO. The optical properties and bandgap studies were undertaken by UV—Visible spectroscopy. I-V characterization study was performed to determine the electrical property of ZnO and Cr-ZnO films.

© 2016 Published by Elsevier B.V.

1. Introduction

Nanotechnology is an emerging field with its varied applications in science and technology for the manufacturing of new materials at the nanoscale level [1]. The development of nano-sized metal

Electronic materials

Structural, optical and electrical properties of zinc incorporated copper oxide nanoparticles: doping effect of Zn

R. O. Yathisha[1] and Y. Arthoba Nayaka[1,*]

[1] Department of Chemistry, School of Chemical Sciences, Kuvempu University, Jnanasahyadri, Shankaraghatta, Karnataka 577 451, India

ABSTRACT

The present paper demonstrates the effect of Zn ion doping on structural, electrical and optical properties of monoclinic CuO nanoparticles prepared via microwave combustion method. The crystal structure, optical and electrical properties of synthesized CuO and Zn-doped CuO samples were characterized by X-ray diffraction study, field emission scanning electron microscopy, energy-dispersive X-ray diffraction study, UV–Visible spectroscopy, transmission electron microscopy and photoconductivity technique. The XRD values show that the crystalline size of Zn-doped CuO nanoparticles was varied with Zn concentration and also it depends on the micro-strain and dislocation density of CuO lattice. FE-SEM and TEM images indicated that the synthesized samples are of the cube and rod-like structures in nature. The band gap of CuO nanoparticles has been calculated using Tauc's plot and the result showed that the incorporation of Zn has decreased the bandgap of CuO. The *I–V* characterization study was performed to determine the electrical property of CuO and Zn-doped CuO films. From the results, it is observed that the photocurrent of CuO and Zn-doped CuO films is found to be greater in UV-light as compared to dark.

Introduction

In recent years, the nanometer sized semiconducting metal oxides and transition metal-doped metal oxides have become subject of interest [1]. Currently, the research is focussed on the synthesis of various nanostructures of semiconducting metal oxides (such as nanorods, nanowires, nanoflowers, nanoprisms, nanoplates, etc.), because of their structural dependent properties. In the oxides of copper family, cuprous oxide (Cu_2O) and cupric oxide (CuO) are the most selected metal oxides to prepare nanoparticles with different morphologies [2]. A number of CuO nanostructures have been synthesized in different morphologies through various methods like hydrothermal [3], solvothermal [4], co-precipitation

Synthesis of Copper Oxide Nano-Rods by Microwave-Assisted Combustion Route and their Characterization Studies

Yathisha R O[a] and Y. Arthoba Nayaka[a]*.

[a]Department of Chemistry, School of Chemical Sciences, Kuvempu University, Jnanasahyadri, Shankaraghatta-577 451, Karnataka, India.

ABSTRACT

The present study demonstrates how petal-shaped copper oxide (CuO) nano-rod structures were fabricated using the microwave-assisted combustion method. The prepared material was annealed at a temperature of 500°C and characterized by means of optical absorption spectroscopy (UV–Vis), X-ray diffraction (XRD), Field emission scanning electron microscopy (FE-SEM), and Photo-conductivity technique (I-V characteristics). The optical energy gap of CuO nano-rods was analysed through the UV–Vis NIR spectroscopic technique and the result illustrates that the energy gap of synthesised CuO nano-rods is found to be 1.44 eV. The XRD of the synthesised sample confirms that copper oxide nano-rods are in pure monoclinic phase with lattice parameters x=4.675 Å, y=3.343 Å, z=5.183 Å. Energy dispersive analysis using X-rays confirms the existence of copper and oxygen atoms in synthesised CuO nanocrystals. FE-SEM micrographs specify that the synthesised material contains nanostructured nano-rods with a small amount of agglomeration in the product. The electrical properties of CuO film were studied through I-V characterization and the results depict that the conductance of CuO film is found to be superior under UV- light compared to in the dark.

Keywords: Crystalline size, Energy gap, Morphology, Petal shaped rods, Tenorite.

1. INTRODUCTION

Synthesis of metal-oxide and transition metal doped semiconducting nanomaterials provide opportunities for improved applications in different areas of science and technology due to their unique physical and chemical properties caused by their nano-sized dimension and large surface/volume ratio [1]. One-dimensional nanomaterial such as nano-ribbons, nano-belts, nano-cubes, and nano-prisms have become the focus of intensive research due to their distinctive properties and their significance for fabrication into high-density nanoscale devices [2]. The transition metal oxides such as copper sulphide (CuS), cerium oxide (CeO_2), nickel oxide (NiO), ferrous oxide (Fe_2O_3), and Titania (TiO_2) are an important class of semiconductors. Among these metal-oxides, Copper (I) oxide (Cu_2O) and copper (II) oxide (CuO) have been gaining more popularity in recent years due to properties such as excellent thermal stability, easily available reactant materials, non-toxic, and exhibits good optical and electrical properties [3]. Due to these properties, recently most research work is mainly focused on the synthesis of different CuO nanostructures, such as nano-flowers, nano-flakes, nano-pyramid, nano-plates, and nano-bats [4].

Corresponding Author: drarthoba@yahoo.co.in

Doping, structural, optical and electrical properties of Ni^{2+} doped CdO nanoparticles prepared by microwave combustion route

R.O. Yathisha, Y. Arthoba Nayaka*, P. Manjunatha, M.M. Vinay, H.T. Purushothama

Department of Chemistry, School of Chemical Sciences, Kuvempu University, Jnanasahyadri, Shankaraghatta 577 451, Karnataka, India

ABSTRACT

This work outlines the synthesis of pure CdO and Ni-CdO nanoparticles with different weight percentage (2, 4, 6, 8 and 10 wt%) of Ni^{2+} through microwave combustion route using cadmium nitrate and nickel nitrate as precursors and ethylene glycol as solvent. The morphological, optical and electrical properties of the material obtained after calcination was systematically characterized for various physicochemical properties and photo-conductivity characteristics. The X-ray diffraction study of the synthesized and calcined CdO and Ni-CdO nanoparticles confirms the existence of cubic phase with no impurity peaks (up to 4 wt%). The average crystalline size is found to be in the range of 41–47 nm based on Debye-Scherrer formula calculation. The scanning electron micrograph reveals that the synthesized samples are prismatic to spherical shaped and also it is observed that, the porosity enhances with increase in the concentration of Ni^{2+} ions. Energy dispersive X-ray micrographs show the existence of Ni^{2+} in the Ni-CdO samples. The optical bandgaps of synthesized samples are determined by Tauc's plot. Transmission electron microscope images are in accordance with the surface morphologies of scanning electron micrographs. The current-voltage characteristic (I–V) of CdO and Ni-CdO films shows that the photo current of CdO and Ni-CdO films is greater in UV-light as compared to dark.

1. Introduction

Semiconductor nanoparticles have been extensively studied from both experimental and theoretical viewpoints because of their potential applications in solar energy conversion, photocatalysis and in optoelectronics devices [1]. Nanoscale materials have unusual optical and electronic properties and wide potential uses as optoelectronic devices. The desire for miniaturization is the driving force behind nanoparticles synthesis [2]. Since the shape, size, and dimensionality of semiconductors are vital parameters for their properties, developing facile methods to prepare nanomaterials with well-defined structures are of great interest and importance. One-dimensional nanostructures of semiconductor materials have received much attention because they offer superior opportunities for both fundamental research and technological applications [3–6]. More recently, the transparent semiconducting nanomaterials have attracted attention due to its excellent properties arising out of large surface-to-volume ratio, quantum confinement effect [7] etc. CdO is an interesting n-type semiconductor, with a direct band gap of 2.3 eV and indirect bandgap of 1.98 eV. It has been studied for a variety of potential applications like organic solar cells [8], eliminating cancer cells [9], photocatalyst [10], light emitting diodes [11], flat display panels [12], photovoltaic's [13]

electrochemical study of drugs [14] and heat mirrors [15]. However, various nanostructures of pure CdO and doped CdO nanoparticles (such as nanoprisms, nanorods, nanoflowers, nanosheets, nanospheroids etc.) have drawn more importance compared to other wide bandgap metal oxides (ZnO, TiO$_2$, SnO$_2$ etc.) because of their structural dependent properties such as narrow band gap, good electrical conductivity, low processing cost and excellent thermal stability [16]. Hence, recent application oriented research is more focussed at controlling the crystalline size and shape to improve the optical absorption and electrical properties of CdO nanostructures [17].

A substantial number of studies have reported that the properties of CdO and transition metal (Cr, Cu, Ni etc.) doped CdO nanoparticles are extremely dependent on their conditions and methods of preparation [18]. Desirable properties have been achieved by doping with the right dopant and using appropriate preparation methods such as mechanochemical, simple thermal evaporation, solvothermal, template hydrothermal and solid vapour methods [19–22]. Although these methods are proven to be useful, they encounter some disadvantages such as consuming large amount of solvents, requirement of high-cost instruments, high processing cost and need for long reaction completion time. Further, some of these synthesis routes require very high temperature, involve multiple steps of procedure and

---
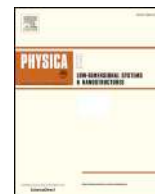
Study on the effect of Zn^{2+} doping on optical and electrical properties of CuO nanoparticles

R.O. Yathisha, Y. Arthoba Nayaka*, P. Manjunatha, H.T. Purushothama, M.M. Vinay, K.V. Basavarajappa

Department of Chemistry, School of Chemical Sciences, Kuvempu University, Jnanasahyadri, Shankaraghatta, Karnataka 577 451, India

ARTICLE INFO

ABSTRACT

The present work outlines the synthesis of CuO and Zn-CuO nanoparticles via microwave combustion method using urea as a fuel. The structural, optical and electrical properties of the CuO and Zn-CuO nanoparticles were systematically characterized through UV–Visible spectroscopy (UV–Vis), Field-emission scanning electron microscopy (FE-SEM), Photoconductivity technique (I-V study), X-ray diffraction studies (XRD), Transmission electron microscopy (TEM) and Energy dispersive analysis X-rays spectrometer (EDAX). The average crystalline size and micro-strain of pure CuO and Zn-CuO nanoparticles were calculated using Debye-Scherrer and William-Hall (W-H) plot methods. The crystalline size was found to be decreased with increase in the concentration of Zn^{2+} up to 6 mol% and a further increase in the Zn^{2+} concentration resulted in the formation impurity phase. Field emission scanning electron micrographs show the monoclinic rod-like structure of CuO and Zn-CuO nanoparticles. Energy dispersive X-ray spectra display the existence of Zn^{2+} in Zn-CuO nanoparticles. The optical band gap values of CuO and Zn-CuO nanoparticles were determined by optical absorption method and the results show a slight decrease in the optical band gap with Zn^{2+} doping. Electrical properties of CuO and Zn-CuO films were performed using I-V characterization studies and the results shown that the enhancement of photocurrent is more in UV-light as compared to dark.

1. Introduction

Intense research is being carried on the synthesis of different transition metal oxide nanostructures (ZnO, SnO_2, CdO, V_2O_5, TiO_2 and Fe_2O_3) because of their special properties such as large surface to volume ratio, quantum size effect, magnetic, optical and electrical properties [1]. In addition, these materials are dependent upon other properties like crystalline size, structure of particles and their surface conditions [1]. These properties are achieved through preparation of different active nanostructures (nanorods, nanoflower, nanoprism etc.) using different experimental techniques [2]. Among the transition metal oxides, a lot of research has been carried out on different nanostructured cupric oxide (CuO) and cuprous oxide (Cu_2O). It is because of their small energy gap, low cost of preparation, excellent thermal stability, good optical and electrical properties [3–5]. Due to these properties, CuO nanostructures have attained a large extent of interest owing to their wide potential applications in various fields such as solar devices [6], catalysis [7], electrochemical analysis [8], field emitters [9], gas sensing [10], photo catalytic activity [11], supercapacitor [12],

giant magnet resistance materials [13], ceramic pigments [14], electrochromic devices [15] etc. Moreover, more importance has been given to control the crystalline size and shape of CuO nanostructures, which improves the optical and electrical properties [16].

Currently, morphology and size distribution of CuO nanoparticles play an important role in deciding their properties. An important method to modify the properties of nanoparticles is the introduction of dopant in the parent system. Suitable dopants ($Cr^{2+/3+}$, Gd^{3+}, Ni^{2+}, Yb^{3+}, Co^{2+} etc.) are often mixed with the CuO matrix, which modify its microstructure and defect chemistry, resulting in a change in its electrical and optical properties [17]. Among these transition metal ions, Zn^{2+} ion has been used to improve the optical, electrical and magnetic properties of CuO nanoparticles. ZnO is an important p-type semiconductor nanoparticle, which shows unique optical and electronic properties due to its wide bandgap of 3.37 eV and the large exciton binding energy (60 eV) at room temperature [18]. In addition, ZnO possesses salient characteristics such as high stability, non-toxic nature, good optoelectronic properties and low cost of synthesis. Hence, Zn^{2+} has been chosen as a right dopant to modify the band gap and improve

---

* Corresponding author.
E-mail address: drarthoba@yahoo.co.in (Y. Arthoba Nayaka).

GENERATION OF DYE-SENSITIZED TRANSITION METAL DOPED SEMICONDUCTORS FOR EFFICIENT SOLAR ENERGY HARVESTING – A LOW-COST METHOD

A thesis submitted to the Faculty of Science

KUVEMPU UNIVERSITY

for the award of degree of

DOCTOR OF PHILOSOPHY
IN
CHEMISTRY

By

Mr. YATHISHA R.O. M.Sc.

Under the guidance of

Dr. Y. ARTHOBA NAYAKA
Professor
Department of Chemistry

Department of P.G. Studies and Research in Chemistry
Kuvempu University
Jnana Sahyadri, Shankaraghatta - 577 451
Shivamogga Dist., INDIA

August-2019

SYNOPSIS

The look for renewable sources of energy is a most important thrust area as an alternative to conventional energy sources due to very high emission levels of environmental polluted gases (greenhouse gases) like carbon dioxide (CO_2), carbon monoxide (CO), nitrogen oxides (NOx), sulphur dioxide (SO_2), phosphorous pentaoxide (P_2O_5) and other traditional fossil fuels like hydrocarbons [1]. Furthermore, the processing cost for the generation of electrical energy from conventional sources like fossil fuels and nuclear elements increases significantly. In addition to this, the social and environmental considerations, such as the cost for securing reliable oil supplies, process nuclear wastes, and to relief disasters caused by global climate changes, etc, are increasing day-by-day [2]. While the generation of electricity from non-renewable energy sources is released a large amount of CO_2 and nuclear radiations, which affects the big environmental issues like global warming and health issues for human beings. So it is necessary to replace these conventional sources with non-conventional one [3]. Among the various renewable energies, solar energy is considered as the most favourable for its usefulness. Moreover, the solar ultraviolet radiations striking on the earth's surface have no cost, clean, sustainable, eco-friendly and commonly dispersed over the entire global [4]. So the light conversion route of these solar radiations into electrical power by using the optical and electronic properties of appropriate materials shows to be a graceful energy conversion process and an ideal alternative to conventional energy sources. This clearly confirms the solar modules are the best solution for converting solar energy into useful electrical energy [5].

During the past few decades, nanomaterials have emerged as the new building blocks to construct solar energy harvesting assemblies. Nanotechnology is believed to revolutionize the industry in the coming years and will have a significant economic impact allowing a considerable cost reduction of the photovoltaic energy, both by reducing the cost of the devices and by increasing efficiencies [6]. Size-dependent properties such as size quantization effect in semiconductor nanoparticles and quantized charging effect in metal nanoparticles provide the basis for developing new and effective light energy harvesting systems [7]. These nanostructures provide innovative strategies for designing next-generation energy conversion devices. Tailoring the optoelectronic properties of metal oxide nanoparticles by organizing chromophores of specific properties and functions on nanoparticles can yield photoresponsive inorganic nanohybrid materials. Amongst the various types of nanomaterials, semiconductor nanoparticles have been widely investigated in recent years [8].

In order to improve the photo-efficiency of photovoltaic devices (solar cells), various methods are used such as doping of right dopant ions (transition and inner transition metal ions) into bare nanomaterial lattice [9]. Doping the impurity ion is known as one of the effective ways to manipulate the internal properties of host material such as crystalline structure and crystallite size. Many attempts have been made to tune the band gap by varying the composition of transition metal ions. It is possible to decrease the band gap by using right dopants [10]. In addition, a few reports of present years suggested that transition metal doped semiconductors could possess interesting optical properties. The origin of these improved photo-reactivities is clearly related to the efficiencies of the doping centers in trapping charge carriers and interceding in the

interfacial transfer. Trapping either an electron or hole alone is ineffective for the generation of photocurrent because immobilized charge species quickly recombines with mobile counterpart. Thus, metal ions can also serve as charge trapping sites and thus reduce electron-hole recombination rate [11]. In order to reduce the band gap of semiconductors, incorporation of certain amount of transition and rare earth metal such as Cr, Er, Ce, Cu, Gd, Mn and V has extensive importance. Doping of these metals essentially reduces the band gap of semiconductors for the photo-excitation and simultaneously reduces the recombination rate of photogenerated electron-hole pairs [12]. The effect of doping on the activity of semiconducting nanomaterials depends on number of key factors, e.g. the method of doping, synthesis route and the concentration of dopant [13]. Therefore, looking for a simple method and appropriate metal dopants are necessary for the large-scale synthesis of metal-doped nano semiconductors.

Recently, numerous methods, such as electrochemical [14], solvothermal [15], solid-state [16], hydrothermal [17], sol-gel [18] have been developed for synthesizing uniform nano-sized pure and doped metal oxide particles. The metal oxide nanoparticles exhibit novel electrical, mechanical, chemical and optical properties due to the larger surface area and quantum confinement effects [19]. Among these methods, the microwave-assisted synthesis has gained more importance due to its advantages of being fast, simple and more energy efficient [20-21]. Compared to the conventional heating process, (a) microwaves generate high power densities, enabling increased production speeds and decreased production costs, (b) microwave energy is precisely controllable and can be turned on and off instantly, eliminating the need for warm-up and cool-down, (c) microwave energy is selectively absorbed by areas of greater moisture resulting in more uniform temperature and moisture profiles, and d) microwave method gives

improved yields and enhanced product performance [22]. Therefore, the fabrication of transition metal oxides with different morphology for the solar energy harvesting has been the target of scientific interests in recent years because of their unique properties and fascinating applications in optoelectronics [23].

Dye-sensitized solar cells (DSSCs) are the most promising photovoltaic devices in the third generation solar cells for achieving good energy conversion efficiency at low cost [24]. It was firstly reported by the Michael Gratzel and Brian O'Regan in 1991, so it is also called as "Gratzel cell". After this invention, DSSCs have gained more importance in the various fields like chemistry, physics and materials science due to their low processing cost and easy fabrication method compared to Si-based conventional solar cells [25].

In DSSCs, the heart of the system is a mesoporous oxide layer composed of metal oxide nanoparticles sintered on a transparent conductive glass substrate, such as indium-doped tin oxide (ITO) or fluorine-doped tin oxide (FTO) glass. This mesoporous oxide film acts as a high surface area support for the sensitizer, a pathway for electron transportation and a porous membrane for the diffusion of the redox couple [26]. Specifically, nanocrystalline semiconductor oxide (typically TiO_2) nanoparticles, which adsorb dye molecules onto their surface and transport photo-generated electrons to the outer circuit, serve as electron conductors and state the efficiency of electron transport and collection [27]. By this, the solar energy-to-electricity conversion efficiency for the best DSSCs has now been enhanced from 12 to 14%, with various recent efforts directed mainly towards developing better inorganic electrode materials and organic sensitizers [28].

Zinc oxide (ZnO) is one of the significant metal oxide semiconductors with a wide energy gap of 3.31 eV and large excitation binding energy (60 eV) [29]. These unique characteristics make it suitable to various applications, such as optical coating, solar cells, gas sensors and photocatalyst [30]. In fact, doping of right dopant, structure, and size play a vital role in the optical and electrical properties of ZnO nanostructures, which can be controlled by the different routes of the nanostructure growth. Therefore, many methods have been created to synthesize ZnO nanostructures including microwave combustion method, solvothermal method, sol-gel method, hydrothermal method, an auto combustion method, ultrasonic and chemical vapor deposition methods [31]. As mentioned above, the doping of ZnO with right dopants offers an effective method to enhance and control its electrical properties. The elements such as Au^{2+}, Ce^{3+}, Eu^{3+}, In^{3+}, Cu^{2+} and Cr^{3+} have been doped in order to control the optical and electrical properties of host ZnO materials. Moreover, undoped and doped ZnO has considered being a potential commercial material due to its low-cost, non-toxicity, and abundant availability in nature. By this, ZnO is being used in the fabrication of third-generation dye-sensitized solar cells (DSSCs) [32].

Copper oxide (CuO) is an important semiconducting transition metal oxide with a monoclinic crystal structure and it has been studied as a p-type semiconducting metal oxide with a bandgap of 1.7 eV [33]. The CuO is being used as a novel material because of the ease of availability of raw materials, low processing cost, non-toxic nature, excellent thermal stability, good optical and electrical properties [34]. The unique physical, chemical and electrical properties of CuO nanoparticles have many potential applications in the fields of photocatalyst, batteries, gas sensing, solar cells and biosensors [35]. It has been highlighted that the crystal shape and size are the two

important considerations to control the optical and catalytic properties of CuO nanoparticles [36]. Furthermore, in the recent research the main focus is given to tune the energy gap of CuO. Doping of several metal ions into the host lattice of CuO is one of the significant routes to alter the energy gap of CuO [37]. Chiang *et al*. reported the effects of Ni doping on the photoelectrochemical properties of CuO thin film photo-electrode. They found that the photocurrent density was decreased with the improved conductivity [38], M. Iqbal *et al*. reported that the band gap of CuO increased upon Mn doping and they proved that the Mn-doped CuO nanowires are much photoactive than the undoped CuO nanowires [39].

Cadmium oxide (CdO) is transparent conducting oxides materials that hold both high electrical conductivity and high optical transparency (>80%) in the visible light region of the electromagnetic spectrum [40]. CdO is an *n*-type semiconductor with nearly metallic conductivity. Its indirect and direct bandgaps of are in the range of 2.2-2.5 eV and 1.3-1.98 eV respectively. Such a difference in both direct and indirect bandgaps is attributed to intrinsic cadmium and oxygen vacancies [41]. Due to its ionic nature coupled with its low electrical resistivity and high optical transmission in the visible region. Nanoscaled CdO has extensive applications as solar cells, windows, IR reflector, transparent electrodes, flat panel display and photo-transistor. It was proven that the structural, electrical and optical properties are very sensitive to the film structure and deposition conditions. Such transparent conductors are being used to comprehensively in thin films solar cells and optoelectronic devices [42].

Titanium oxide (TiO$_2$) nanoparticle is one of the promising materials for the fabrications of dye-sensitized solar cells (DSSCs). Because it has special properties like wide bandgap, suitable band edge levels for charge injection and extraction, the long

lifetime of excited electrons, exceptional resistance to photo-corrosion, non-toxicity and low cost [43]. TiO_2 occurs naturally in three different forms; anatase (tetragonal), rutile (tetragonal) and brookite (orthorhombic). For DSSCs, anatase is the most commonly used phase due to its superior charge transport. The tetragonal anatase crystal structure is made up of a chain of distorted TiO_6 octahedrons, which results in a unit cell containing four titanium atoms and eight oxygen atoms [44]. In addition, TiO_2 is one of the most attractive wide bandgap transition metal semiconductor, non-toxic, highly stable and low commercial cost. Due to these properties, TiO_2 gain more importance in the fabrication of photo-anode for dye-sensitized solar cells (DSSCs) with different structures such as nanotubes, nano-rods, nano-flower and nanofibers [45]. Most of the research focused on the modification of properties of TiO_2 by changing the morphology, tuning of the phase or external doping by different approaches. Also, morphology, specific surface area, crystal phase and crystalline structure of TiO_2 nanoparticles plays important role in solar cell performance [46].

Magnesium oxide (MgO) has a rock salt structure with Mg^{2+} and O^{2-} ions are octahedrally coordinated, making bulk magnesium oxide a diamagnetic material with a wide band gap of 7.8 eV [47]. Due to its wide band gap, inexpensiveness, and long term stability, MgO is used in potential applications of numerous disciplines. It can be extensively utilized in the fields of translucent ceramics, refractory, plasma display panel, absorbents in many pollutants and superconducting products [48]. Due to good photocatalytic properties of MgO, it is being used in the form of an ultra-thin shell on the surface of some metal oxides such as SiO_2, ZnO, and TiO_2 to improve the efficiency of dye-sensitized solar cells. Magnesium oxide (MgO) has been used as an insulating layer in the TiO_2 based DSSCs because of two important reasons: firstly, the MgO layer

protects the back electron transfer from the TiO₂ layer to the electrolyte solution and hence, reduces electron-hole recombination; secondly, the MgO coating layer improves the dye adsorption, leading to an improved efficiency. Also, it is an eco-friendly material and is extensively used in many medical, industrial and agricultural products [49].

Similar to photo-anode materials, many organic dyes are taking a significant role in the applications of dye-sensitized solar cells. The process of photosensitization play a vital role in absorbing some amount of visible light and photo exited electrons in the dye molecules that impinge into the conduction band of metal surfaces [50]. To achieve these functions, the dye molecules have to meet several conditions such as; the excited energy level (LUMO) of the dye should be slightly higher compared to conduction band of semiconductors, forming strongly bond with semiconductor surface, high absorption coefficient, wide spectrum of absorption in the visible region (redshift) and long term stability [51]. However, in past few years, most of the researchers have used ruthenium-based complexes as effective sensitizers, due to their intense charge absorption capacity in the whole visible range and more efficient in metal-to-ligand charge transfer rate. But, in recent days the metal-free organic dyes are used as a sensitizer in the alternative to ruthenium related complexes. Because the ruthenium complex includes heavy metal, which is undesirable from the point of view of eco-friendly aspects and it has high price [52]. By this, the metal-free organic dyes of Eosin-Y, Fast Sulphon Black-F, Solochrome Black-T, Orange IV, SPDANS and Evans blue are used as sensitizers with acceptable efficiency. These metals free organic dyes have more absorption coefficient compared to transition metal complexes due to π-π^* transition. Due to these features, most researchers have used metal-free organic dyes instead of metal complexes to improve the efficiency of DSSCs [53].

The present work is mainly focused on the synthesis and characterization of purely advanced semiconducting metal oxide nanoparticles, transition metal doped nanoparticles and their usage in low-cost dye-sensitized solar cells. The metal oxide nanostructures were synthesized by microwave combustion method with two different modes, such as solution and solid state mode. These metal oxide nanoparticles can exhibit an array of unique novel properties such as large surface area, high specificity, good reactivity and other properties, which can be an added advantages for industrial applications. The main aim of this work includes,

- Synthesis of undoped (ZnO, CuO, CdO, TiO_2 and MgO) and transition metal doped metal oxide (Cr-ZnO, Zn-CuO, Ni-CdO, Cr-TiO_2 and Zn-MgO) nanoparticles.

- Studies on the effect of doping on structural, optical and electrical properties of ZnO, CuO, CdO, TiO_2 and MgO nanoparticles.

- Sensitization of transition metal doped metal oxide nanoparticles (Cr-ZnO, Zn-CuO, Ni-CdO, Cr-TiO_2 and Zn-MgO).using Eosin-Y, SPADANS, Trypan blue and Evan's blue dyes.

- Evaluation of the consequence of dye sensitization on optical and electrical properties of synthesized transition metal doped semiconducting nanoparticles.

The thesis entitled **"Generation of dye-sensitized transition metal doped semiconductors for efficient solar energy harvesting - A Low-Cost method"** comprises five chapters.

Chapter-1 deals with the general introduction about nanomaterials and dye sensitized solar cells. It covers the literature review on history of solar energy conversion, DSSCs and their working principle, metal oxides for fabrication of DSSCs, nanomaterials

and their types, and various methods of synthesis of nanomaterials. At the end, the properties and applications of metal oxide nanomaterials were also described in detail.

Chapter-2 outlines the broad aim and scope of the work. It highlights the significance and comprehensive approaches to the synthesis of semiconducting nanoparticles and their applications for DSSCs.

Chapter-3 furnishes the methods and materials adopted in this work. This includes;

- Preparation of ZnO, CuO, CdO, MgO, TiO$_2$, Cr-ZnO, Zn-CuO, Ni-CdO, Cr-TiO$_2$, and Zn-MgO nanoparticles using microwave combustion method.

- Characterization of synthesized ZnO, CuO, CdO, MgO, TiO$_2$, Cr-ZnO, Zn-CuO, Ni-CdO, Cr-TiO$_2$ and Zn-MgO nanoparticles using X-Ray diffraction studies (XRD, Model: Bruker D8 Advance), Field-emission scanning electron microscopy (FE-SEM, Model: Nova Nano SEM600-FEI and FE-SEM Carl Zeiss AG-ULTRA 55), Energy dispersive X-ray diffraction spectroscopy (EDAX, Nova Nano SEM 600-FEI), Transmission electron microscopy (TEM, Model: Philips CM 200), Fourier transform infrared spectroscopy (FT-IR, Model: Bruker Alpha-T FT-IR Instruments), UV-Vis. spectroscopy (UV-Vis., Model: USB 4000, Ocean Optics) and photoconductivity method (I-V, Model: Kiethley Instruments Inc.2401).

- Calculation of Crystalline size, Micro-Strain, Dislocation density and lattice constants of nanomaterials using XRD data.

- Estimation of bandgap of nanomaterials using Tauc plot and Kubelka-Munk plot methods.

- Preparation of Eosin-Y, Trypan Blue, SPADANS and Evans blue dye solutions at different concentrations.

- Calculation of HOMO and LUMO of dye molecules using cyclic voltammetry.

- Fabrication of dye sensitized nanoparticle films using doctor blade method.

- Measurement of optical absorption of dye sensitized nanoparticle films using UV-Visible spectral data.

- Measurement of conductivity of dye sensitized nanoparticle films using Kiethley source meter.

Chapter-4 includes synthesis, characterization and properties of ZnO, Cr-ZnO, CuO, Zn-CuO, CdO, Ni-CdO, TiO_2, Cr-TiO_2, MgO and Zn-MgO nanoparticles. This chapter is sub-divided into chapter 4.1- 4.7.

Chapter-4.1 pertains to the synthesis, characterization and properties of ZnO and Cr-ZnO semiconducting nanoparticles. The lattice constants and band gap of synthesized ZnO and Cr-ZnO nanoparticles were calculated. The crystallinity of the samples was analyzed by X-ray diffraction studies (XRD). The doping property was analyzed by EDAX and UV-Visible spectrum for undoped and doped samples.

Chapter-4.2 deals with the characterization and properties of CuO and Zn-CuO nanoparticles by microwave combustion method. The surface morphology was studied by SEM and TEM techniques. EDAX confirms the presence of Zn in Zn-CuO lattice. Optical properties and photoresponse of these materials have been studied.

Chapter-4.3 presents the synthesis and characterization of CdO and Ni-CdO semiconducting nanoparticles synthesized by microwave combustion method. The prepared nanoparticles were characterized by XRD, FESEM, EDAX, UV-Vis. and I-V techniques. Effect of dopant on the optical and electrical properties of synthesized samples was studied.

Chapter-4.4 focused on the characterization of semiconducting TiO_2 and $Cr-TiO_2$ nanoparticles. The surface morphology was studied by FE-SEM and TEM. The optical and electrical properties synthesized TiO_2 and $Cr-TiO_2$ was studied using UV-Vis. spectroscopy and I-V characteristic studies.

Chapter-4.5 pertains to the characterization and properties of MgO and Zn-MgO nanoparticle synthesized by microwave combustion route. The structural, optical and electrical properties of these materials have been studied.

Chapter-4.6 describes the synthesis, characterization and results of synthesized ZnO nanoparticles using different solvents by microwave combustion route. The prepared ZnO nanoparticles were characterized by XRD, FE-SEM, UV-Vis. and I-V techniques. The effect of solvents on optical and electrical properties was studied.

Chapter-4.7 illustrates the structural, optical and electrical properties of synthesized ZnO nanoparticles under different microwave power via microwave combustion route. The structural morphology and elemental composition of synthesized ZnO samples were analyzed by FE-SEM and EDAX.

Chapter-5 focused on the study of optical and electrical characterization of dye-sensitized Cr-ZnO, Zn-CuO, Ni-CdO, $Cr-TiO_2$ and Zn-MgO nanoparticles. This chapter presents the selection of various dyes for sensitization of synthesized nanoparticles to enhance optical absorption band. The dyes Trypan blue, SPADANS and Evans blue were selected and their respective LUMO and HOMO levels were studied through cyclic voltametry. The synthesized doped nanoparticles were coated with these dyes and subjected for optical absorption studies. The optical and electrical properties of dye sensitized Cr-ZnO, Zn-CuO, Ni-CdO, $Cr-TiO_2$ and Zn-MgO were studied via UV-Vis. spectroscopy and I-V characteristic studies.